



**Andreas Michael Josef Goss**

**Generation of high-resolution global  
and regional multi-scale B-spline models  
of the vertical total electron content  
based on low-latency GNSS data**

**München 2022**

**Bayerische Akademie der Wissenschaften**

ISSN 0065-5325

ISBN 978-3-7696-5298-7

---





Generation of high-resolution global  
and regional multi-scale B-spline models  
of the vertical total electron content  
based on low-latency GNSS data

Vollständiger Abdruck  
der von der Fakultät für Luftfahrt, Raumfahrt und Geodäsie  
der Technischen Universität München  
zur Erlangung des akademischen Grades eines  
Doktor-Ingenieurs (Dr.-Ing.)  
genehmigten Dissertation

von

M.Sc. Andreas Michael Josef Goss

München 2022

Bayerische Akademie der Wissenschaften

**Adresse der DGK:**



Ausschuss Geodäsie der Bayerischen Akademie der Wissenschaften (DGK)

Alfons-Goppel-Straße 11 • D – 80 539 München

Telefon +49 – 89 – 23 031 1113 • Telefax +49 – 89 – 23 031 - 1283 / - 1100

e-mail [post@dgk.badw.de](mailto:post@dgk.badw.de) • <http://www.dgk.badw.de>

Prüfungskommission:

Vorsitzender: Prof. Dr.-Ing. Uwe Stilla

Prüfer der Dissertation: 1. apl. Prof. Dr.-Ing. habil. M. Schmidt  
2. Prof. Dr. phil. nat. U. Hugentobler  
3. Prof. Dr. M. Hernández-Pajares

Die Dissertation wurde am 22.04.2021 bei der Technischen Universität München eingereicht  
und durch die Fakultät für Luftfahrt, Raumfahrt und Geodäsie am 02.09.2021 angenommen



# Abstract

The ionosphere describes the charged part of the atmosphere that extends the altitude range between 50 km and 1500 km above the Earth's surface. It is characterised by an increased concentration of charged particles, such as electrons, which influence the propagation of electromagnetic signals through the atmosphere. The ionosphere is considered as one of the largest sources of error in the use of Global Navigation Satellite Systems (GNSS). Since the end of the last century, the International GNSS Service (IGS) and in particular the Ionosphere Working Group have been producing so-called global ionosphere maps (GIM), which represent the Vertical Total Electron Content (VTEC), in order to correct the influence of the ionosphere on geodetic measurements. At the beginning in 1998, there were five Ionosphere Associated Analysis Centers (IAAC), which routinely provided their GIM to the IGS. While in 2002 the number was reduced to four IAACs, there are currently four more institutes that have joined the group of IAACs, including the one that left. The GIMs are published individually and as a combination product on the servers of the IGS.

The processing of the GIMs is based on observations of the global IGS network of ground stations, which receive signals from GNSS and provide the observations via the IGS servers. The majority of the terrestrial GNSS stations in the IGS network are located on continents in the northern hemisphere. Consequently, the observations are inhomogeneously distributed across the globe. In order to create GIMs from the inhomogeneously distributed observations, suitable parameterisation methods are required. Therefore, series expansions of analytical functions on a sphere or discretisation techniques are applied. Most of the IAACs use a series expansion in terms of Spherical Harmonics (SHs). As a matter of fact, SHs require a homogeneously distributed database. Since this is not available, the parameterisation of VTEC by means of SHs is usually limited to a maximum degree of  $n = 15$ . With the further development and expansion of the IGS station network over the last two decades, more stations have been added to the network, but the homogeneity of the global distribution has not improved significantly. On the contrary, some continental regions are equipped with dense station clusters, whereas oceans still exhibit large data gaps and the problem of the inhomogeneous distribution of observations still currently exists.

Even though the provision of GNSS observations has improved over the last decade, most observations are still only available with a large delay. A distinction is made between observations that are provided in the form of hourly or daily data blocks with the corresponding latency, or that are only available at a later point in time. Only about a third of the stations can stream observations in real time (RT). GIMs are usually categorised according to the observations used for modelling: *final* GIMs can – due to their data basis – be made available after a few days to three weeks, approximately, and *rapid* or *ultra-rapid* already after one day, or after a few hours. Using observations via RT-streams, so-called *real-time* GIMs are created, which can be made available for real-time applications. In recent years, IAACs have been generating forecast GIMs with two horizons of one and two days ahead, but unfortunately with a lack of accuracy.

Modern GNSS applications, as well as autonomous driving or GNSS-based drones and agricultural machines, require highly accurate information about the state of the ionosphere, which must be available within the shortest possible time in order to correct the resulting errors in positioning and navigation. The ionospheric products to be provided for this purpose must also

describe small-scale ionospheric variations in the spatial domain in order to enable the most precise positioning possible. In this publication-based dissertation, methods are presented on how to meet these requirements.

In order to avoid the disadvantages of VTEC modelling by means of SHs, a series expansion by means of B-splines is used for this purpose in this thesis. Compared to SHs, B-splines have the advantage of a compact support, hence, they are different from zero only in a spatially limited range. Each B-spline function contributes to the modelling only in this area, which means that inhomogeneously distributed data can be handled appropriately. B-splines are generally defined as a one-dimensional series expansion along bounded intervals or along circles, but they can also be implemented as multi-dimensional representations. Consequently, they are applicable for both regional and global representations.

In addition to the localising features, B-splines also provide a multi-scale representation (MSR) with the fundamental feature of splitting a target function into a smoothed, i.e. low-pass filtered version and a number of detail signals – band-pass filtered versions – through successive low-pass filtering. P-I (Goss et al., 2019) presents how the spatial MRS can be applied to a global VTEC representation to adapt the model resolution to the data distribution. As a matter of fact, the development of high-resolution models is only possible where densely distributed observations are available. Some continental regions are additionally covered by regional networks with particularly dense station clusters and allow the generation of Regional Ionosphere Maps (RIM). In **P-II** (Goss et al., 2020b), a two-step B-spline model has been developed to generate high-resolution GIMs and RIMs using all available global and regional observations.

In order to finally be able to use the developed VTEC maps to correct ionospheric disturbances in GNSS applications, appropriate data formats for the dissemination are required. Currently, two data formats are available: (1) the IONEX (IONosphere EXchange Format) Format, which is commonly used for post-processing, or (2) the RTCM/SSR VTEC (Radio Technical Commission for Maritime Services/ State Space Representation) message, which is currently the only available data format to disseminate ionospheric corrections in real time. However, the SSR VTEC message only allows SH coefficients to be transmitted, thus a transformation of the B-spline model is required to make them available in RT. In **P-III** (Goss et al., 2020a), an efficient method is presented on how to transform a B-spline model for dissemination using SSR VTEC messages. In addition, a comparison of the original model with the transformed model, as well as with prominent GIMs of the IAA Cs, is carried out for the correction of ionospheric disturbances in positioning. Based on the excellent results for positioning using the B-spline models developed in this work, a recommendation for more flexible provision of ionospheric correction data can be discussed.

# Kurzfassung

Die Ionosphäre beschreibt den geladenen Teil der Atmosphäre, der sich über den Höhenbereich zwischen 50 km und 1500 km über der Erdoberfläche erstreckt und durch eine erhöhte Konzentration von geladenen Teilchen gekennzeichnet ist. Freie Elektronen in der Ionosphäre haben einen Einfluss auf die Ausbreitung elektromagnetischer Signale durch die Atmosphäre und gelten als eine der größten Fehlerquellen bei der Nutzung von globalen Navigationssatellitensystemen (engl.: Global Navigation Satellite System, GNSS). Um den Einfluss der Ionosphäre auf geodätische Messungen zu korrigieren, erstellt der Internationale GNSS Service (IGS) und insbesondere die Ionosphären-Arbeitsgruppe (Ionosphere Working Group) seit 1998 sogenannte globale Ionosphärenkarten (engl.: Global Ionosphere Maps, GIM), welche den vertikalen absoluten Elektronengehalt (engl.: Vertical Total Electron Content, VTEC) darstellen. Zu Beginn gab es fünf Analysezentren für die Ionosphäre (engl.: Ionosphere Associated Analysis Center, IAAC), welche routinemäßig ihre GIMs dem IGS zur Verfügung stellten. Im Jahr 2002 hat sich die Anzahl auf vier reduziert, mittlerweile jedoch zählen acht Institute zu den IAACs. Die GIMs werden sowohl einzeln, als auch Kombinationsprodukt auf den Servern des IGS veröffentlicht.

Die Erstellung der GIMs basiert auf Beobachtungen global verteilter Bodenstationen des IGS Netzwerks, welche GNSS Signale empfangen und die Beobachtungen über die Server des IGS bereitstellen. Der überwiegende Teil der terrestrischen GNSS-Stationen im IGS Netzwerk befindet sich auf Kontinenten der nördlichen Hemisphäre, woraus sich eine inhomogene Verteilung der Beobachtungen über die Erdkugel ergibt. Um aus den inhomogen verteilten GNSS Beobachtungen GIMs zu erstellen bedarf es geeigneter Parametrisierungsmethoden. Dazu werden üblicherweise Reihenentwicklungen von Basisfunktionen auf einer Kugel oder Diskretisierungstechniken verwendet.

Die Mehrzahl der IAACs nutzen dazu eine Reihenentwicklung basierend auf Kugelflächenfunktionen (engl.: Spherical Harmonics, SHs), welche eine homogen Datenverteilung benötigen. Da diese jedoch nicht vorliegt, wird die Reihenentwicklung üblicherweise bei einem Maximalgrad von  $n = 15$  begrenzt. Durch die Weiterentwicklung und den Ausbau des IGS Stationsnetzwerkes in den letzten zwei Jahrzehnten wurden weitere Stationen zum Netzwerk hinzugenommen, jedoch verbesserte sich deren inhomogene Verteilung nicht. Im Gegenteil, einige Kontinentalregionen sind mit dichten Stationsclustern versehen, wohingegen Ozeane große Datenlücken in der globalen Verteilung aufweisen. Das Problem der inhomogenen Verteilung der Beobachtungsstationen besteht noch heute.

Auch wenn sich im letzten Jahrzehnt die Bereitstellung der GNSS Beobachtungen verbessert hat, stehen die meisten Beobachtungen dennoch erst mit großer zeitlicher Verzögerung zur Verfügung. Man unterscheidet zwischen Beobachtungen, die in Form von stündlichen oder täglichen Datenblöcken mit entsprechender Latenz bereitgestellt werden, oder erst zu einem späteren Zeitpunkt zur Verfügung stehen. Nur etwa ein Drittel der Stationen können ihre Beobachtungen bereits in Echtzeit (engl.: real-time, RT) mittels Streaming verbreiten. Die GIMs werden üblicherweise anhand der für die Modellierung verwendeten Beobachtungen kategorisiert; *finale* GIMs werden aufgrund ihrer Datenbasis zumeist erst nach wenigen Tagen bis drei Wochen bereitgestellt, *rapid* oder *ultra-rapid* GIMs bereits nach einem Tag, bzw. nach wenigen Stunden. Unter Verwendung von Beobachtungen mittels RT-Streams werden sogenannte *real-time* GIMs erstellt, welche für Echtzeitanwendungen bereitgestellt werden können. In den letzten Jahren haben die IAACs be-

gonnen Vorhersage-GIMs für ein bis zwei Tage in die Zukunft zu generieren, jedoch aber mit geringer Genauigkeit.

Moderne GNSS Anwendungen, wie autonomes Fahren oder GNSS gesteuerte Drohnen und Landwirtschaftsmaschinen bedürfen hochgenauer Informationen über den Zustand der Ionosphäre mit möglichst geringer Latenz, um die dadurch entstehenden Fehler in der Positionierung und Navigation zu korrigieren. Die dafür notwendigen Ionosphärenprodukte müssen zudem auch räumlich kleinskalige Variationen in der Ionosphäre beschreiben, um eine möglichst präzise Positionierung zu ermöglichen. In dieser kumulativen Dissertation werden basierend auf drei Publikationen Methoden vorgestellt, wie man den genannten Anforderungen gerecht werden kann.

Um die Nachteile der VTEC Modellierung mittels SHs zu vermeiden, wird dazu in dieser Arbeit eine Reihenentwicklung mittels B-Splines verwendet. Die Verwendung von B-Splines als Basisfunktionen hat gegenüber SHs den Vorteil, dass sie einen kompakten Träger besitzen und daher nur in einem räumlich begrenzten Bereich von Null verschiedene Werte aufweisen. Jede B-Spline Funktion trägt daher auch nur in diesem Bereich zur Modellierung bei, wodurch inhomogen verteilte Daten besser behandelt werden können als durch SHs. B-Splines sind generell als eindimensionale Reihenentwicklung entlang von begrenzten Intervallen oder Kreisen definiert, jedoch lassen sie sich als Tensor-Produkte in mehreren Dimensionen entwickeln. Dies hat zur Folge, dass B-Splines sowohl für regionale als auch globale Repräsentationen Verwendung finden.

Neben den lokalisierenden Merkmalen erzeugen B-Splines zusätzlich eine Multiskalendarstellung (engl.: Multi-Scale Representation, MSR), mit dem wesentlichen Merkmal der Aufspaltung einer Zielfunktion in eine geglättete, d.h. tiefpassgefilterte Version und eine Anzahl von Detailsignalen – bandpassgefilterte Versionen – durch sukzessive Tiefpassfilterung. In **P-I** (Goss et al., 2019) wird vorgestellt, wie die räumliche MSR für eine globale VTEC Repräsentation angewandt werden kann, um die Modellauflösung an die Datenverteilung anzupassen. Fakt ist, dass die Entwicklung hochauflösender Modelle nur dort möglich ist, wo entsprechend dicht verteilte Beobachtungen vorliegen. Einige Kontinentalregionen sind zusätzlich durch regionale Netzwerke, mit besonders dichten Stationsclustern versehen und erlauben die Erstellung von regionalen Ionosphärenkarten (engl.: Regional Ionospher Map, RIM). In **P-II** (Goss et al., 2020b) wird deshalb ein Zwei-Schritt B-Spline Model (engl.: Two-Step Model, TSM) entwickelt, um mittels aller global und regional zur Verfügung stehenden Beobachtungen hochaufgelöste GIMs und RIMs zu erstellen.

Um schlussendlich die entwickelten VTEC Karten dafür verwenden zu können, den Einfluss der Ionosphäre auf GNSS Anwendungen zu korrigieren, bedarf es entsprechender Datenformate, mittels derer die Karten an Nutzer verbreitet werden können. Derzeit stehen zwei Datenformate zur Auswahl; (1) das IONEX (IONosphere EXchange Format) Format, welches üblicherweise im Post-Processing Verwendung findet, oder (2) die RTCM/SSR VTEC Message (Radio Technical Comission for Maritime Services/ State Space Representation), welche derzeit die einzige Möglichkeit bietet, Ionosphäreninformationen in Echtzeit an Nutzer zu verbreiten. Da die SSR VTEC Message jedoch ausschließlich die Verbreitung von Kugelfunktionskoeffizienten ermöglicht, bedarf es für die in dieser Arbeit entwickelten B-Spline Modelle einer Transformation. In **P-III** (Goss et al., 2020a) wird eine effiziente Methode vorgestellt, wie ein B-Spline Modell für die Verbreitung mittels SSR VTEC Message in ein SH Modell transformiert werden kann. Zusätzlich wird ein Vergleich des originären Modells mit dem transformierten Modell, sowie mit etablierten GIMs für die Korrektur des Ionosphäreinflusses auf die Positionsbestimmung durchgeführt. Auf Basis der herausragenden Ergebnisse für die Positionsbestimmung unter Verwendung der in dieser Arbeit entwickelten B-Spline Modelle kann eine Empfehlung zur flexibleren Bereitstellung von Ionosphärenkorrekturdaten diskutiert werden.

# Preface

This cumulative dissertation is composed of the following three published first-author papers:

- P-I** Andreas Goss, Michael Schmidt, Eren Erdogan, Barbara Görres, Florian Seitz (2019): **High-resolution vertical total electron content maps based on multi-scale B-spline representations** In: *Annales Geophysicae*, 37(4), 699–717, 10.5194/angeo-37-699-2019
- P-II** Andreas Goss, Michael Schmidt, Eren Erdogan, Florian Seitz (2020): **Global and Regional High-Resolution VTEC Modelling Using a Two-Step B-Spline Approach** In: *Remote Sensing*, 12(7), 1198, 10.3390/rs12071198
- P-III** Andreas Goss, Manuel Hernández-Pajares, Michael Schmidt, David Roma-Dollase, Eren Erdogan, Florian Seitz (2020): **High-Resolution Ionosphere Corrections for Single-Frequency Positioning** In: *Remote Sensing*, 13(1), 12, 10.3390/rs13010012

Within this thesis, the findings published in the first-author publications are set into context. Thereby, the publications are cited within this dissertation and each is marked with the letter P and the respective Roman number. Furthermore, parts of the first-author publications are cited in direct form with adapted numbering for equations, figures and tables to fit in the scope of this thesis. These direct citations are written indented in the main body of the thesis.

In addition to the first-author publications, the findings of the following co-author publications are incorporated into this dissertation:

- C-I** Eren Erdogan, Michael Schmidt, Andreas Goss, Barbara Görres, Florian Seitz (2020): **Adaptive Modeling of the Global Ionosphere Vertical Total Electron Content** In: *Remote Sensing*, 12(11), 1822, 10.3390/rs12111822
- C-II** Qi Liu, Manuel Hernández-Pajares, Haixia Lyu, Andreas Goss (2021): **Influence of temporal resolution on the performance of global ionospheric maps** In: *Journal of Geodesy*, 95(3), 1–16, 10.1007/s00190-021-01483-y

These publications are cited in this work using the usual citation style.

Starting with the description of the field of research and the related underlying physical relationships and key parameters of the ionosphere, the background and the motivation for this thesis is provided. Thereafter, the generation of high-resolution global and regional multi-scale B-spline Models for modelling the Vertical Total Electron Content (VTEC) is derived, based on the first-author publications **P-I**, **P-II**. Subsequently, different VTEC product types are defined which result from the multi-scale modeling approach. As the final step, the dissemination strategies published in **P-III** complete the entire process chain for the generation of high-resolution VTEC models.



# Contents

<b>Abstract</b>	<b>iii</b>
<b>Kurzfassung</b>	<b>v</b>
<b>Preface</b>	<b>vii</b>
<b>1 Introduction</b>	<b>1</b>
1.1 Motivation . . . . .	1
1.2 Research Topic and Research Questions . . . . .	3
<b>2 The Earth Atmosphere</b>	<b>9</b>
2.1 The Neutral Atmosphere . . . . .	9
2.2 The Charged Atmosphere . . . . .	10
2.2.1 Space Weather . . . . .	10
2.2.2 Spatial and Temporal Variations of the Ionosphere . . . . .	12
2.2.3 Ionospheric Key-Quantities . . . . .	14
<b>3 Global Navigation Satellite Systems</b>	<b>17</b>
3.1 Global Positioning System . . . . .	17
3.2 GLONASS . . . . .	19
3.3 Other GNSS Systems . . . . .	20
3.4 Global and Regional GNSS Networks . . . . .	21
<b>4 VTEC Modelling by Means of GNSS Observations</b>	<b>23</b>
4.1 Sun-Fixed Coordinate System . . . . .	23
4.2 Parameterisation . . . . .	25
4.3 Spherical Harmonic Expansion . . . . .	25
4.4 B-spline Series Expansion . . . . .	26
4.4.1 1-D Polynomial B-splines Expansion . . . . .	26
4.4.2 1-D Trigonometric B-splines Expansion . . . . .	28
4.5 GNSS Data Acquisition and Processing . . . . .	29
4.5.1 GNSS Data Selection Step . . . . .	31
4.5.2 GNSS Pre-Processing Step . . . . .	34
4.6 Multi-Scale Modelling of the Ionosphere . . . . .	36
4.6.1 Global B-spline VTEC Model . . . . .	38
4.6.2 Regional B-spline VTEC Model . . . . .	41
4.7 Estimation of Model Parameters . . . . .	45
4.7.1 Global Measurement Model of the Kalman Filter . . . . .	46
4.7.2 Regional Measurement Model of the Kalman Filter . . . . .	47
4.7.3 Kalman Filter . . . . .	48
4.7.4 Global and Regional Prediction Model . . . . .	48
4.7.5 Two-Step Model Outputs . . . . .	49

<b>5</b>	<b>Ionosphere Products and Validation</b>	<b>51</b>
5.1	Data Types and Products . . . . .	51
5.1.1	Ionosphere Products Type 1 . . . . .	52
5.1.2	Ionosphere Products Type 2 . . . . .	54
5.2	Data Formats . . . . .	57
5.2.1	IONosphere EXchange Format . . . . .	58
5.2.2	SSR VTEC - Message . . . . .	59
5.2.3	Real-Time Dissemination of High-Resolution B-spline Products . . . . .	60
5.3	Validation and Assessment . . . . .	65
5.3.1	Self-Consistency Validation . . . . .	65
5.3.2	Single-Frequency Positioning . . . . .	67
<b>6</b>	<b>Summary and Conclusions</b>	<b>71</b>
6.1	Primary Results of the Research Questions . . . . .	71
6.2	Outlook . . . . .	78
<b>7</b>	<b>Content of the Publications</b>	<b>83</b>
7.1	P-I . . . . .	83
7.2	P-II . . . . .	105
7.3	P-III . . . . .	128
7.4	Co-Author Publications . . . . .	149
	<b>List of Figures</b>	<b>151</b>
	<b>List of Tables</b>	<b>155</b>
	<b>Acronyms</b>	<b>157</b>
	<b>Bibliography</b>	<b>161</b>



# 1 Introduction

## 1.1 Motivation

‘Turn left in three meters’ ... but the route in question does not exist.

Today, the use of Global Navigation Satellite Systems (GNSS) for positioning with a smartphone or for navigation of cars, airplanes and drones is firmly anchored in our everyday life. But what if the calculated position does not correspond to the real one? The consequences would be fatal for applications such as autonomous passenger vehicles or agricultural machines.

Positioning using GNSS suffers from many different disturbances, with the ionosphere being one of the largest. The ionosphere describes the charged part of the atmosphere and is defined in a height between 50 km and 1500 km above the Earth’s surface. Due to ionisation processes caused by the Sun’s radiation, charged particles are produced in the ionosphere, namely ions and electrons, whose density and distribution is highly variable, see, e.g. Hernández-Pajares et al. (2012a); Monte-Moreno and Hernández-Pajares (2014); Jacobi et al. (2016).

The electrons have a significant impact on applications such as positioning, navigation, telecommunication and aviation since they are responsible for disturbances on the propagation of electromagnetic signals. Due to the dispersive property of the ionosphere, signals are affected differently depending on their frequency (Seeber, 1989; Wanninger, 1994). Signals up to 30 MHz are blocked, while signals with higher frequencies are disturbed and suffer from ray path bending and a signal delay, which accounts for 99.9 % of the ionospheric disturbances (Langley, 1998). Dual- and multi-frequency GNSS users can compute the ionospheric delay by applying the ionospheric linear combination (LC), using the dispersive characteristics of the ionosphere (Seeber, 1989; Mannucci et al., 1998; Hernández-Pajares et al., 1999; Ciraolo et al., 2007). However, for real-time (RT) GNSS applications with dual- or multi-frequency receivers on moving platforms, external information on the state of the ionosphere is needed to have a fast convergence. The same applies to users of single-frequency receivers, who cannot determine the ionospheric delay and are fully dependent on external information as well.

The ionospheric delay mainly depends on the signal frequency, the integral of the electron density  $N_e$  along the ray path, i.e. the Slant Total Electron Content (STEC), as well as the elevation angle at which the signal is received. With decreasing elevation, the influence of the ionosphere increases due to the longer signal path through the ionosphere. At an elevation angle of  $15^\circ$ , it is about 2.5 times as large as for signals in the zenith direction (Wanninger, 1994). Consequently, the electron density is the most important quantity for describing the state of the ionosphere and to determine the STEC.

Since the information about the state of the ionosphere must be made available to users within a limited time for positioning and navigation, a simplification is carried out, which is based on the Single Layer Model (SLM) (Schaer, 1999). The SLM is based on the simple assumption that all electrons are concentrated on a shell of infinitesimal thickness at a certain height above the spherical Earth. It allows for the transformation of STEC into the vertical direction by means of a zenith angle depending mapping function and yields the Vertical Total Electron Content (VTEC), see e.g. Beutler et al. (1999); Schaer (1999); Dach et al. (2015); Lyu et al. (2018). The relationship between the electron density  $N_e$ , the STEC and the VTEC is shown in Fig. 1.1. The



Figure 1.1: Relation between ionospheric key-quantities; the left part presents the integration of  $N_e$  along the ray path of a signal which leads to the STEC. The right part indicates a projection of the STEC into the vertical direction by means of a mapping function, leading to the VTEC.

mapped VTEC refers to the Ionospheric Pierce Point (IPP) as the intersection point of the signal path and the single layer and is expressed in so-called Total Electron Content Units (TECU) as  $1 \text{ TECU} = 10^{16} \text{ el/m}^2$  (Schaer, 1999).

The ionosphere may be considered as an error source for observations and for many space geodetic techniques, but on the other hand their dual- or multi-frequency observations provide precise information about the state of the ionosphere along the signal path. These data are often used to generate models of the ionosphere, which are utilised to correct for ionospheric delay for positioning and navigation. In fact, representations of VTEC as a function of latitude, longitude and time have proven to be reliable models for determining STEC by means of mapping, and for correcting the ionospheric delay. Since the VTEC model must be provided at time to correct the ionospheric delay for positioning and navigation, the data for their generation must be available with low latency as well. However, most of the geodetic observations are usually available after days or weeks. Terrestrial GNSS is the only observation technique whose observations are accessible with low latency or even in RT and which are characterised by a global distribution. Hence, terrestrial GNSS data typically serve as the basis for the low-latency models of the ionospheric VTEC. However, one disadvantage arises if solely GNSS observations are used for VTEC modelling, as they have large data gaps where no terrestrial observing stations are available, i.e. over the oceans and in distant areas. On the other hand, continental regions often have dense station clusters that allow for high-resolution modelling of the VTEC within the areas.

For more than two decades, the International GNSS Service (IGS) and in particular the Ionosphere Associated Analysis Centers (IAAC) have been producing so-called Global Ionospheric Maps (GIM), which represent the VTEC globally using GNSS observations (Feltens and Schaer, 1998; Schaer, 1999; Hernández-Pajares et al., 2009; Roma-Dollase et al., 2017). Other institutions utilise the dense distribution of GNSS observations over the continents to generate Regional Ionosphere Maps (RIM), see e.g. (Nohutcu et al., 2010), (Bergeot et al., 2014), (Krypiak-Gregorczyk et al., 2017). However, most of these models are not suitable for modern GNSS applications such as autonomous driving or precision agriculture, as they are distributed with a large delay or do not have sufficient resolution to meet the accuracy requirements.

In the context of the requirements for precise positioning and navigation for many applications in our daily lives, the main motivation of this work was the development of high-resolution global and regional models with low latency up to the correction of the ionospheric delay in the application case. Within this thesis, a modelling approach based on series expansions in tensor products of one-dimensional B-spline functions is applied. B-splines are particularly advantageous compared to other modelling methods for VTEC, since they are localising basis functions and thus can be adapted to the distribution of the input data, as well as to the signal to be modelled (Schmidt et al., 2011, 2015a). In addition, B-splines can be used to generate VTEC representations at different scales, i.e. global and regional or at different levels of detail with respect to the spectral

resolution of spatial signal variations. The flexibility of the chosen modelling approach allows for the creation of various VTEC products that can be made available for use.

In view of the motivation outlined above, the major objectives of the present thesis are

- (1) the generation of novel global and regional models for the representation of VTEC with high spatio-temporal resolution based on localising B-spline functions,
- (2) which are based on low-latency GNSS observations from global and regional networks and
- (3) which can be used to provide corrections of the ionospheric delay to users for positioning and navigation.

## 1.2 Research Topic and Research Questions

This cumulative dissertation is based on the three first-author articles listed in the preface. These papers have been published in peer-reviewed journals. In the scope of this thesis, the three papers are set in context as represented in the flowchart shown in Fig. 1.2. The overview of the processing chain for the low-latency generation of VTEC models is shown in the left-hand column. The three publications **P-I**, **P-II** and **P-III** are depicted in the middle column, as well as the basic research questions **Q-1**, **Q-2**, **Q-3** and **Q-4** that are answered in this thesis. The right-hand column shows the different sections in this thesis, in which the respective part of the processing chain is discussed and the corresponding research questions are answered.

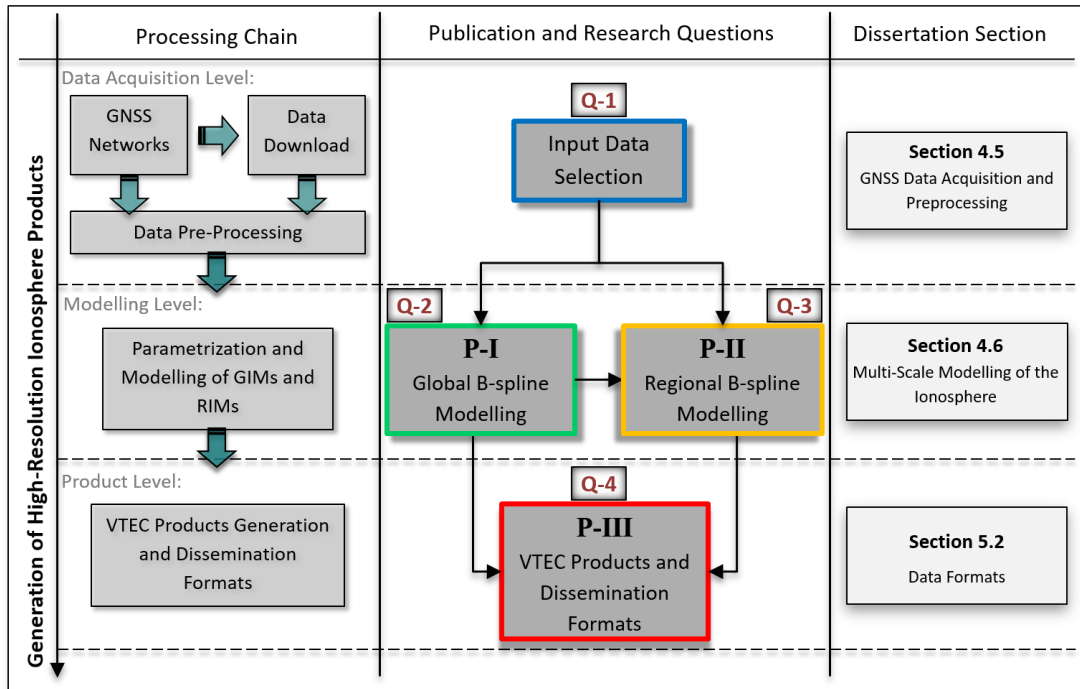


Figure 1.2: Flowchart for the generation of ionosphere products with reference to the three publications and to the respective sections that represent the individual contents.

Following the processing chain, three processing levels can be indicated where the developments within this thesis interfere: (1) the data acquisition level, (2) the modelling level, and (3) the product level.

The data acquisition level comprises the download step and the pre-processing of selected observations to form an appropriate data base for VTEC modelling. The IGS provides observations from several hundred globally distributed GNSS receiver stations at present, of which 280 stations receive multi-GNSS signals. In this context, a distinction is made at which latency the data can be obtained (numbers are taken from Villiger and Dach (2018)); the so-called *daily*-data ( $\approx 599$  stations within the IGS network) are provided after collection of a full day of GNSS observations, *hourly*-data ( $\approx 393$  stations within the IGS network) are provided after the collection of one hour of data and the *high-rate*-data ( $\approx 307$  stations within the IGS network) are provided in irregular sub-hourly time steps. Currently, there are about 195 stations that provide (RT)-streams.

A similar distinction is made for the satellite orbits with *broadcast*, *ultra-rapid*, *final* orbits, and for the clock information of the satellite and receiver clocks. Depending on the latency of the input data used for VTEC modelling, the resulting maps are classified of different latencies. A list of these latency types, the data latency as well as the product latency defining the time after the data acquisition at which the VTEC information can be disseminated was made in **P-III** and is adapted in Tab. 1.1. The IAACs use mostly final data provided by the IGS network

Table 1.1: Product types defined by means of the latency of the input data adapted from **P-III**.

Latency Type	final	rapid	ultra-rapid	near real-time	real-time
Data	post-processed	daily	hourly	high-rate	data-streams
Data Latency	2-3 weeks	> 1 day	> 2 hour	real-time	real-time
Product Latency	2-3 weeks	> 1 day	> 2 hour	< 15 minutes	< 1 minute

and generate so-called final products. Some of them are already generating rapid or real-time products Villiger and Dach (2018); Li et al. (2020). Within this dissertation, explicitly hourly data are acquired, to generate the so-called ultra-rapid products, which are characterised with low product latency, cf. Tab. 1.1. In addition to the observations of the stations from the IGS network, observations from other regional networks, such as the European REference Frame (EUREF) network or the UNAVCO<sup>1</sup> network are included. Figure 1.3 shows the distribution of the stations from the IGS, EUREF and UNAVCO networks, providing hourly-data with a globally inhomogeneous distribution.

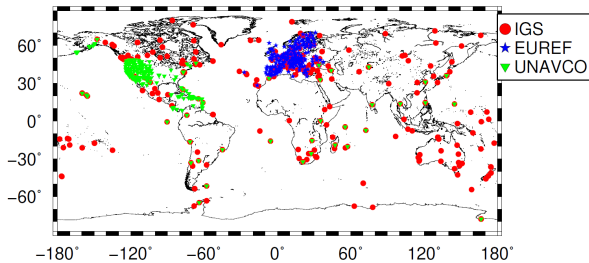


Figure 1.3: Distribution of the stations of the global IGS and the regional EUREF and UNAVCO networks providing hourly data.

As can be seen, there is an inhomogeneous distribution of stations with dense clusters for some continental regions such as Europe or North America and large gaps over the oceans. This can lead to a redundancy of observations for the global model over the continental regions and slowdown the modelling process. However, the densely distributed observations over the continents allow for the generation of regional models to represent the VTEC with higher spectral and spatial resolution. In this thesis, both global and regional models are created, therefore a data separation is applied to define independent data sets, which

serve both global and regional models. The data selection is part of the data acquisition level, as indicated with the blue-bounded box in the middle column of Fig. 1.2, and corresponds to the

<sup>1</sup>UNAVCO is a community of scientists, educators and professionals working together to better understand Earth processes and hazards using geodesy.

research questions **Q-1**.

**Q-1** Selection of input data for global and regional high-resolution VTEC modelling

- a) How can a data selection be performed in order to serve both global and regional modelling procedures?
- b) What are the criteria for the input data to allow high-resolution ionosphere modelling?

**Goal:** Development of a procedure for the data selection.

The largest difference between the VTEC models of the IAACs can be found in the modelling level (cf. Fig. 1.2). They all use data-driven models based on GNSS observations and represent VTEC as a 2-D function – depending on the latitude  $\varphi$  and the longitude  $\lambda$  – or a 3-D function – depending on  $\varphi$ ,  $\lambda$  and time  $t$  – by means of a suitable discretization technique or by means of a series expansion.

The IAACs' *Center for Orbit Determination, Berne, Switzerland (CODE)*, *European Space Operation Center of the European Space Agency (ESOC-ESA)*, *Canadian Geodetic Survey of Natural Resources Canada (NRCan)*, *Wuhan University (WHU)* and *Chinese Academy of Science (CAS)* use series expansions in terms of Spherical Harmonic (SH) functions (Roma-Dollase et al., 2017). The use of SHs for the generation of GIMs representing VTEC globally was first introduced by Schaer (1999) and is well known. The ionosphere research group of *Deutsches Geodätisches Forschungsinstitut der Technischen Universität München (DGFI-TUM)* uses series expansions in terms of B-splines (Schmidt, 2007; Schmidt et al., 2015a; Erdogan et al., 2017), while the *Jet Propulsion Laboratory (JPL)* relies on a three-layer model (Mannucci et al., 1998). In case of a discretization, the *Universitat Politècnica de Catalunya (UPC)* applies a tomographic model based on voxels (Hernández-Pajares et al., 1999; Orus et al., 2005) to generate VTEC maps. A list of the different modelling approaches and a comparison of the maps can be found in the work of Hernández-Pajares et al. (2009, 2017a); Roma-Dollase et al. (2017).

Since the distribution of GNSS stations and thus also the distribution of corresponding observations is generally quite inhomogeneous, with large data gaps over the oceans and dense observation clusters over continental regions (see the distribution of network stations in Fig. 1.3), the different approaches include different strategies to overcome the problem of determining the unknown model parameters. SHs, for example, are globally defined basis functions, and require a homogeneous data distribution over the globe Schmidt et al. (2011). With the given inhomogeneous observation distribution and following Nyquist's sampling theorem on a sphere, the highest degree of the corresponding series expansion has to be chosen accordingly low and is typically set to  $n = 15$  (Li et al., 2015). This value corresponds to a spatial resolution of  $12^\circ \times 12^\circ$  for latitude and longitude.

To avoid the disadvantages of SHs for VTEC modelling, other approaches have been proven in order to be appropriate candidates for modelling VTEC with an enhanced and adapted resolution. Within this dissertation, the series expansion in terms of B-splines is applied. B-spline are localising basis functions, which are more suitable for processing heterogeneous data and allow for appropriate handling of data gaps (Mößmer, 2009; Schmidt et al., 2011, 2015a). Besides this, the spatial resolution of the VTEC model with respect to latitude and longitude can be adapted to both the data distribution and the signal structure. The VTEC signal generally has finer structures in the latitudinal direction than in the longitudinal direction, since the distribution of electrons is influenced by the geomagnetic field and oriented parallel to the geomagnetic equator. In this regard, B-splines allow an increase of the spectral resolution related to the spatial frequencies, as shown in **P-I**. The use of B-splines to model functions on a sphere was published by

Dierckx (1984); Lyche and Schumaker (2001) and applied to VTEC by Schmidt (2007); Schmidt et al. (2011); Erdogan et al. (2017).

Furthermore, B-splines generate a Multi-Scale Representation (MSR), also known as Multi-Resolution Representation (MRR) (Stollnitz et al., 1995a,b; Schumaker and Traas, 1991; Mertins, 1999; Lyche and Schumaker, 2001). The MSR allows splitting the modelled VTEC into a smoothed, i.e. low-pass filtered version and a number of detail signals, i.e. bandpass filtered versions. In this way multiple spectral resolutions can be generated (Schmidt, 2007, 2012; Schmidt et al., 2015a; Liang, 2017).

Within this dissertation, methods are developed to generate and disseminate VTEC maps with low latency by means of a continuously running operational process. Therefore, a Kalman filter (KF) is applied for the sequential estimation of the series coefficients of B-splines and for the generation of ultra-rapid products, as developed by Erdogan et al. (2017). Following Tab. 1.1, ultra-rapid products are based on hourly data, which can be obtained from the data centres of the networks with a minimum data latency of 2 hours. The KF allows for an immediate processing of the data after the acquisition. Thereby, the step size of the KF defines at which temporal intervals a new set of parameters are estimated and thus the temporal output resolution of consecutive VTEC maps.

The generation of global VTEC maps by means of a multi-scale B-spline representation corresponds to the green-bounded box in the middle column of Fig. 1.2 and addresses the research questions **Q-2**.

#### **Q-2** Global high-resolution modelling of the Vertical Total Electron Content

- a) What is the advantage of using B-splines for sequential modelling of VTEC globally compared to traditional modelling methods on a sphere?
- b) How can the spectral resolution of the global B-splines series expansion be related to the maximum degree of a SH expansion?

**Goal:** Generation of high-resolution global VTEC products.

The publication **P-I** *High-resolution vertical total electron content maps based on multi-scale B-spline representations* addresses these questions. Within this thesis, the developed MSR for high-resolution VTEC representations is summarised in Section 4.6.1 and put in context with the related research questions.

As a matter of fact, finer ionosphere structures can only be modelled where high-resolution input data are available. Some continental regions, such as Europe, North America or Australia, are characterised by a particularly dense coverage of GNSS stations. As mentioned above, some continents have regional GNSS networks that provide additional observations within the respective area. This dense observation coverage allows for the modelling of high-resolution RIMs for these specific regions. Different methods for modelling the RIMs have been published (Krypiak-Gregorczyk et al., 2017; Nohutcu et al., 2010; Li et al., 2018; Liu et al., 2010; Schmidt, 2007; Dettmering et al., 2011), but the models are mostly not applied operationally. At least the RIMs are not publicly available. The Royal Observatory of Belgium (ROB) is the sole provider of RIMs for Europe operationally (Bergeot et al., 2011, 2014).

The models mentioned are stand-alone representations of VTEC within selected regions. Within this dissertation, the aforementioned global model will be combined with a regional B-spline representation. Thereby, the global model is estimated in the first step and is used as background model for the regional densification in the second step, as shown in Fig. 1.2 with the yellow-bounded box. This so-called Two-Step Model (TSM) is based on two parallel running KFs, which



are adapted to the signal that will be modelled and the data distribution according to Erdogan et al. (2020). The data sets used for the estimation within each of the KFs are defined beforehand by the data separation (cf. **Q-1**) and can be seen as independent GNSS data sets. Both modelling steps are based on B-spline basis functions. As shown in **P-II**, this method enables a particularly high resolution of the VTEC representation within the regions.

The higher the resolution of the models, the more small-scale variations can be represented. This is not only a great advantage for positioning applications but also for scientific purposes to detect ionospheric irregularities. The possibilities offered by regional densification will be clarified in the research questions **Q-3**.

### **Q-3** Regional high-resolution modelling of the Vertical Total Electron Content

- a) What are the advantages of using RIMs compared to GIMs and which improvements in the representation of VTEC can be achieved?
- b) What is the scientific benefit of generating high-resolution regional models and what can they be used for?

**Goal:** Development of a regional densification by means of a regional B-spline expansion and a global background model.

In **P-II** *Global and Regional High-Resolution VTEC modelling Using a Two-Step B-spline Approach*, the TSM with a global B-spline model as the first step and a regional densification as the second step was published. Section 4.6.2 addresses the development of the regional densification and the two-step B-spline approach and summarises the responses to questions a).

Following the generation of the high-resolution global and regional VTEC maps in the modelling level, the question remains of how they can be disseminated. Within the product level (cf. Fig. 1.2), different product types are defined. As published in **P-III**, a typical distinction is made between coefficient-based and grid-based product types. The selected product type determines the data format used for dissemination. A further distinction has to be undertaken related to the use of the estimated VTEC information, namely

1. for precise positioning or research in post-processing mode:  
as long as the data is not immediately used, the VTEC information can be prepared with highest resolution and quality and be disseminated by means of any appropriate data format and platform (File Transfer Protocol (FTP));
2. for precise navigation and positioning or for early warning with regard to space weather events:  
thereby the selection of possible dissemination formats is limited because the user must receive the ionospheric information within seconds and with high precision, in order to correct the GNSS measurements used, e.g. for positioning.

The IONosphere EXchange (IONEX) data format is commonly used for the dissemination of GIMs and RIMs for post-processing applications. It provides VTEC values on regular grids with arbitrary sampling intervals. A distinction is made between epoch IONEX files, which contain only one grid for a specific time moment, and multi-epoch IONEX files, which contain several VTEC grids with arbitrary temporal sampling intervals. Typically, the spatial sampling of the grid points is fixed with  $2.5^\circ \times 5^\circ$  in latitude and longitude for GIMs, while it varies between  $1^\circ$  or  $0.5^\circ$  in both directions for RIMs, see e.g. Bergeot et al. (2014). The temporal sampling for consecutive epochs between the VTEC maps within the daily IONEX files is usually set to 1–2

h for final products and to 15 min for rapid product. The ultra-rapid products generated in **P-I** and **P-II** and used in **P-III** were set to a temporal sampling of 10 min.

However, the IONEX ASCII file format is not the most adequate for the RT dissemination of ionospheric maps. Currently, only the State Space Representation (SSR) VTEC message – following the RTCM<sup>2</sup> standard – can be used for this purpose. It is designed for the dissemination of SH coefficients up to highest degree  $n = 16$ . Models of a higher spectral resolution cannot be distributed to the user via this message. Another restriction is that models not based on SHs cannot be disseminated in RT by means of this data format. For the B-spline models generated within this thesis, a transformation has to be applied to convert the relevant model parameters to SH coefficients.

Each of the different product types and applications require an individually adapted strategy for the dissemination, which will be clarified by answering the following research questions **Q-4**.

### **Q-4** Strategy for the dissemination and use of high-resolution VTEC products

- a) Which different kinds of ionosphere products can be defined and what is the related appropriate dissemination strategy?
- b) How can the VTEC products be disseminated to users within the required time using typical data formats and what are the limitations in terms of accuracy?

**Goal:** Recommendation to modify the available formats for dissemination of high-resolution products.

The publication **P-III** *High-Resolution Ionosphere Corrections for Single-Frequency Positioning* comprises a case study for the transformation of the B-spline coefficients to SH coefficients and addresses the questions above. In Section 5.2, findings are set into context with the developments in **P-I** and **P-II** and further validated in Section 5.3.

It needs to be noted, that all studies and publications that are part of this dissertation are based on the *hourly* GNSS data. However, the main focus of this thesis lies on the development of up-to-date VTEC models and the dissemination of the resulting products to designated users for RT navigation and positioning applications. Currently, access to RT GNSS data is limited and sometimes not free of charge. Furthermore, only a predefined number of stations can be used to stream the RT observations. With the further expansion of the RT networks, it is assumed that the number of RT stations will increase so that the developed models can also be applied in RT.

---

<sup>2</sup>Radio Technical Commission for Maritime Services



## 2 The Earth Atmosphere

The atmosphere is a complex system with a shell-like structure. In general, a distinction is made between the temperature domain, which divides the atmosphere into different layers based on the temperature along the altitude, and the ionisation domain which describes the existence of charged particles. This is also referred to as the natural atmosphere or the charged atmosphere.

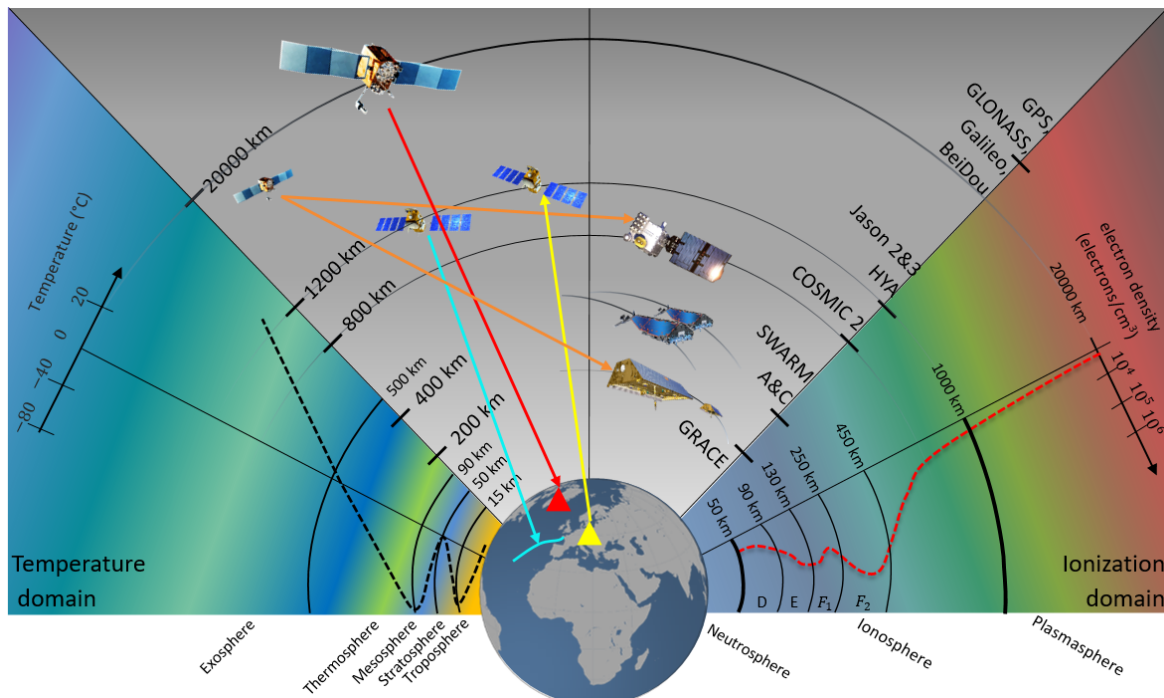


Figure 2.1: Schematic representation of the structuring of the atmosphere in the temperature domain on the left side and the ionisation domain on the right side. Known geodetic space techniques, as well as their observation geometry are represented in the middle. In the temperature domain, the structuring of the neutral atmosphere depends on the temperature as represented with the dashed line on the left. The charged atmosphere is defined in the ionisation domain and thus depends on the number of charged particles. The red dashed line shows the idealised profile of the electron density distribution starting with the ionosphere from 50 km up to approximately 1000 km with the transition to the charged plasmasphere.

### 2.1 The Neutral Atmosphere

The neutral atmosphere is typically described by its chemical composition (oxygen, hydrogen, nitrogen etc.) and the density of the atmospheric gas. The density of the atmosphere decreases with increasing altitude, i.e. the highest gas density is near the Earth's surface. About 99.9 % of the total mass of the atmosphere is present within the first 50 km altitude (Heise, 2002). Above 100 km there is only 0.001 ‰ of the total mass left. The vertical structure of the neutral

atmosphere is usually determined by the temperature, which yields a spherical layering. The left part of Fig. 2.1 shows the horizontal layers with black arcs, visualising the boundaries between the consecutive layers. The boundaries are called pauses. Starting from the Earth's surface up to 15 km, the troposphere is located. Changes in the troposphere determine our weather on the Earth. Within the troposphere, the temperature decreases steadily by about  $6.5^{\circ}\text{C}$  per kilometer. In the tropopause the temperature reaches about  $-65^{\circ}\text{C}$  (Zolesi and Cander, 2007). In the stratosphere above, however, the temperature begins to rise again until it reaches  $0^{\circ}\text{C}$  in the stratopause at an altitude of 50 km. The third layer is called the mesosphere and covers altitudes between 50 km and 90 km. The temperature decreases again and reaches  $-80^{\circ}$  in the mesopause. Above the mesosphere, the thermosphere spreads out until 500 – 1000 km as the temperature increases. Temperatures in the higher thermosphere increase and can reach  $500^{\circ}\text{C}$  and  $1000^{\circ}\text{C}$  or higher. The highest layer is called the exosphere with a gas density which almost reaches the vacuum level.

## 2.2 The Charged Atmosphere

By classifying the atmosphere according to the charged state, three parts are distinguished. The neutral atmosphere (also known as neutrosphere) and an ionized part, including the ionosphere and above the plasmasphere, as the transition to the outer space. The ionosphere extends between 50 km and approximately 1500 km above the Earth's surface and merges there into the plasmasphere, wherein the number of charged particles steadily decreases with increasing altitude (Schaer, 1999). As can be seen in Fig. 2.1, the thermosphere covers a part of the ionosphere but is contrarily defined by the density of neutral particles. The ionosphere and the thermosphere form a coupled system in which physical processes influence each other (Heelis, 2014). Thereby, the Sun is the main driver of the electron density.

### 2.2.1 Space Weather

#### Main Source of Ionisation

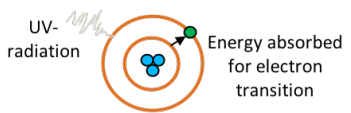

The radiation of the Sun is the main source of ionisation processes in the atmosphere. A correlation between the intensity of solar radiation and ionisation can be found in Jacobi et al. (2016). An important measure for determining the solar activity is the appearance of so-called sunspots. These are cooler regions on the surface of the Sun that emit less visible light, which means that they appear as black spots when viewed from Earth. The number of sunspots has been continuously recorded since the 19th century. Thereby, it was found that the activity of the Sun follows a periodic cycle of 11 years, with daily variations of about 10 to 100 sunspots (Limberger, 2015). Extreme Ultraviolet (EUV) radiation and X-ray are correlated with the number of sunspots and follow the solar cycle. Since the sunspots are not homogeneously distributed on the solar surface, the radiation intensity of EUV and the intensity of the X-rays interacting with the Earth's atmosphere reflect the solar rotation with periods of about 27 days (Bothmer and Daglis, 2007; Schunk and Nagy, 2009).

#### Ionisation and Recombination

An accumulation of sunspots is often associated with solar events. One phenomenon is called solar flare and cause a rapid increase in the EUV radiation and the X-ray. Since EUV radiation and X-ray travel at the speed of light  $c \approx 300000 \text{ km/s}$ , it takes about 8 minutes for them to spread over the distance of 150 million km between the Sun and Earth, and the increased radiation intensity can be observed. Stronger solar radiation causes stronger ionisation within

the Earth's atmosphere. Table 2.1 summarises the phenomena of ionisation by means of EUV radiation and X-ray. The radiation affects the neutral atoms, whereby the energy input changes their charge state and leads to splitting into electrons and positively charged ions. A simplified representation of the ionisation process is given in the third column of Tab. 2.1. The opposite process to ionisation is called recombination. Thereby free electrons recombine with the ions and form again neutral atoms.

Table 2.1: The influence of solar radiation on the neutral particles in the atmosphere.

Phenomenon	Velocity	Propagation	Interaction
EUV	$\approx 300000$ km/s	<ul style="list-style-type: none"> <li>reaches the Earth within 8 minutes</li> <li>causes ionisation</li> </ul>	
X-Ray	$\approx 300000$ km/s	<ul style="list-style-type: none"> <li>reaches the Earth within 8 minutes</li> <li>causes ionisation</li> </ul>	

The degree of ionisation depends on two factors:

1. The neutral density in the atmosphere, which decreases with increasing altitude.
2. The intensity of the radiation, which increases with the height above the Earth's surface. In other words, the intensity decreases due to absorption when entering the atmosphere, and consequently less radiation energy is received at lower altitudes.

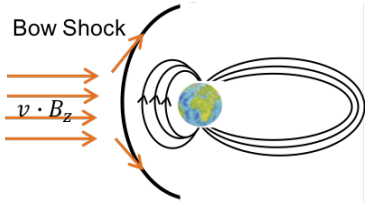
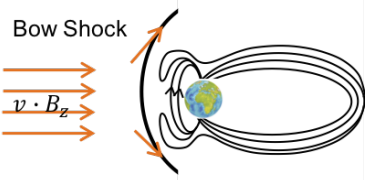
This yields a maximum concentration of electrons in the altitudes between 200 km and 400 km (Schunk and Nagy, 2009). Due to the low gas density at these altitudes, a recombination of the charged particles does not necessarily and immediately occur. Thus, there is a constant presence of electrons and ions.

### Plasma Transportation

The corona of the Sun is characterised by a continuous plasma flow. Due to the gravitation of the Sun, only very fast-moving particles escape into space. The necessary escape velocity for this is 618 km/s (Moldwin, 2008). Due to the high temperature in the corona, a large number of particles move fast enough, causing a constant flux of escaping particles. This flux is known as solar wind and means magnetised plasma, which transports the solar magnetic field into the solar system. As depicted in Tab. 2.2 the propagation speed of the solar wind through space varies typically between 200 km/s and 900 km/s and interacts with the magnetic field of the Earth (Schunk and Nagy, 2009). According to Bothmer and Daglis (2007), the wind is classified as a slow solar wind ( $\leq 450$  km/s) and a fast solar wind ( $\geq 450$  km/s - 900 km/s). The magnetic field of the Earth can be assumed to be a dipole with an axis inclined about  $11^\circ$  to the Earth's rotation axis and the magnetic field direction being from South to North. Due to the constant impact of the solar wind on the Earth's magnetic field, its field lines are compressed on the day side of the Earth (Tsurutani and Gonzalez, 1997; Tsurutani et al., 2006), causing the magnetic field to deform and take the form of a bow shock like a ship sailing through the water. The strength of the deformation on the day side depends on the speed of the solar wind and the transported magnetic field of the solar wind. On the night side of the Earth, however, the magnetic field lines

form a long tail. A schematic representation of the magnetic field is shown in the first row of Tab. 2.2.

Table 2.2: Phenomenon of solar wind and CME interacting with the ionosphere

Phenomenon	Velocity	Propagation	Interaction
solar wind	200–900 km/s	<ul style="list-style-type: none"> <li>• charged particle flow emitted from the Sun</li> <li>• moderate density and speed</li> <li>• compresses the magnetic field</li> </ul>	
CME	> 1000 km/s	<ul style="list-style-type: none"> <li>• charged plasma cloud of enhanced velocity</li> <li>• deforms Earth's magnetic field lines</li> <li>• reaches the Earth in 2–3 days</li> </ul>	

A further phenomenon associated with an accumulation of sunspots are eruptions of hot plasma from the solar surface. Extreme eruptions can lead to Coronal Mass Ejections (CME), in which large amounts of plasma are ejected into space (Bothmer and Daglis, 2007; Moldwin, 2008; Schunk and Nagy, 2009; Tsurutani et al., 2009). The probability of occurrence of these phenomena is related to the number of sunspots, but it does not mean that they cannot occur during the solar minimum. A CME is defined as a dense and fast-moving plasma cloud transporting a strong magnetic field. The velocity of the plasma cloud can reach more than 1000 km/s (Bothmer and Daglis, 2007; Moldwin, 2008). The interaction with the Earth's magnetic field can cause enormous deformations of its field lines. This can even lead to the splitting of the outer lines, if the magnetic field within the solar plasma is counter directed. A schematic sketch is shown in the second column of Tab. 2.2. This phenomenon is called a geomagnetic storm. One consequence is the injection of solar plasma into the Earth's atmosphere and a so-called ionospheric storm with a strong increase of the electron density within the ionosphere (Tsurutani et al., 2009).

## 2.2.2 Spatial and Temporal Variations of the Ionosphere

### Vertical Structure of the Ionosphere

An idealised profile of the vertical electron density distribution is depicted in the right part of Fig. 2.1. The ionosphere itself is usually divided into different layers with different altitude ranges (Schaer, 1999; Dettmering, 2003; Schunk and Nagy, 2009; Limberger, 2015; Liang, 2017). The D-layer expands between 50 km to 90 km, the E-layer between 90 km and 130 km, the F1-layer between 130 km and 250 km, and the F2-layer, which usually contains the maximum values of the electron density in the ionosphere and expands from 250 km up to 450 km. The altitudes range are approximate estimates, as the real ranges depend on solar activity, the solar cycle, the time of day and also the seasons (Schaer, 1999). Neither the solar radiation nor the gas density in the atmosphere is constant, hence the electron density in the ionosphere varies with time, resulting in periodic and recurring variations as well as short-term changes. An overview about some of the regular and irregular variations is given in the following section.

### Regular Variations

Due to the ionisation process on the day side, there is a clear difference in the electron density compared to the night side. These diurnal variation is expressed by electron density maxima in the range of about  $\pm 20^\circ$  around the geomagnetic equator. The so-called Equatorial Ionisation Anomaly (EIA) is caused when ionised gas at the equator rises up in the atmosphere and is transported to North and South along the magnetic field lines by winds (Schunk and Nagy, 2009). Due to gravity and pressure, it accumulates in the geomagnetic latitudes of  $\pm 15^\circ$ . This effect is also called the equatorial fountain.

### Irregular Variations

Irregular ionospheric disturbances occur particularly in the area around the equator and in the higher geomagnetic latitudes. Ionospheric irregularities include small-scale disturbances, which can cause scintillations, as well as so-called Travelling Ionospheric Disturbances (TID) (Hernández-Pajares et al., 2006; Zolesi and Cander, 2007; Belehaki et al., 2020), and also ionospheric irregularities due to solar activity (Monte-Moreno and Hernández-Pajares, 2014; Wang et al., 2016a; Hernández-Pajares et al., 2012a).

Scintillations mostly occur during high solar activity. These cause rapid variations of the ionospheric state, which can lead to extreme disturbances in the propagation of electromagnetic signals or even to the loss of track. An example of this is the degradation of satellite navigation.

TIDs are mainly caused by density variations in the F-region and occur as slowly oscillating variations in the electron density which are decaying with the time. Generally, TIDs can be classified as Large-Scale TIDs (LSTID) with wavelengths of 1000 km and a velocity of 300–1000 m/s (Zolesi and Cander, 2007), Medium-Scale TIDs (MSTID) with wavelengths of 50–300 km and velocity of 100–300 m/s (Hernández-Pajares et al., 2017b, 2011, 2012b), as well as Small-Scale TIDs (SSTID) with smaller wavelengths.

Probably the largest irregularities in terms of electron density variations are caused by ionospheric storms. Ionospheric storms are usually caused by CMEs and often occur after solar flares, i.e. strong eruptions over sunspots that radiate energetic particles into space and appear as bright flashes of light. As described above, CMEs cause extreme spatial and temporal variations in electron density due to increased ionisation processes and the injection of solar plasma into the atmosphere. Probably the most famous and strongest solar storm on record is called the Carrington event, after the astronomer Richard Carrington. Several strong solar flares and a CME with a propagation speed of 2000 m/s occurred between 28 August and 4 September 1859 with extreme impact (Cliver and Dietrich, 2013). The aurora borealis were even observed at medium latitudes, i.e. in Rome, Havana and Hawaii. The increased electron density in the atmosphere induced such strong voltages in telegraph lines that their paper bands caught fire due to sparks. Nowadays, however, the impact on the technical developments were even more significant (Oughton et al., 2017; Schrijver et al., 2015). During the so-called Halloween event 2003, disturbances in the electrical power grids were detected and caused blackouts. In addition, satellites were damaged and routes of airplanes over polar regions were changed to prevent interference in their radio communications.

Other irregularities, which have not yet been studied in detail, can also be caused by natural hazards such as earthquakes or tsunamis. In the ionosphere, for example, the propagation of gravity waves to tsunamis could be detected (Astafyeva et al., 2013; Liu et al., 2004; Zhu et al., 2013; Rolland et al., 2011).

### 2.2.3 Ionospheric Key-Quantities

The middle part of Fig. 2.1 shows several space geodetic observation techniques. In general, all of the missions shown are equipped with transmitters or receivers which are meant to transmit or receive signals transported using radio waves. The propagation of electromagnetic signals through the ionosphere is disturbed by the free electrons. The so-called ionospheric delay

$$d_{ion} = \pm \frac{40.3}{f^2} \int_{\mathbf{x}^T}^{\mathbf{x}_R} N_e(\mathbf{x}) ds, \quad (2.1)$$

describes in S.I. units the first order ionospheric effects on the propagation of radio waves, which can be derived from dual-frequency observations (cf. Section 4.5.2 and Eqs. (4.27) and (4.29)). Higher-order ionospheric effects strongly depend on the magnetic field, the signal frequency and the distance through the ionosphere and can reach up to 0.2 cm in the zenith for GNSS signals (Bassiri and Hajj, 1993). The ionospheric delay (2.1) includes the change of the distance (bending) and change on the travel time (delay) through the atmosphere and depends on the electron density  $N_e(\mathbf{x})$  along the signal path  $s$  between the positions  $\mathbf{x}^T$  and  $\mathbf{x}_R$  of the transmitter T and the receiver R, respectively, with position vector

$$\mathbf{x} = r [\cos \varphi \cos \lambda, \cos \varphi \sin \lambda, \sin \varphi]^T. \quad (2.2)$$

The coordinate tuple  $(\varphi, \lambda, r)$  comprises here the latitude  $\varphi$ , longitude  $\lambda$  and the radial distance in a geocentric coordinate system  $\Sigma_E$ . The ionosphere is a dispersive medium for electromagnetic waves, hence the ionospheric delay is also dependent on the emitted frequency. While low-frequency radio waves up to 30 MHz are reflected by the electrons in the ionosphere, high-frequency waves can penetrate them, but suffer from the ionospheric delay (2.1). In addition, the propagation of individual waves (unmodulated) and wave groups differ in dispersive media and the sign changes from ‘-’ to ‘+’, respectively (Langley, 1998). Figure 2.1 shows the schematic observation architecture for terrestrial GNSS with the red-coloured connecting line between a GNSS satellite at the altitude of about 20000 km and the receiver on the ground, marked by the red triangle. GNSS observations are disturbed by the electrons along the signal path and allow determining the

$$STEC(\mathbf{x}^T, \mathbf{x}_R, t) = \int_{\mathbf{x}^T}^{\mathbf{x}_R} N_e(\mathbf{x}) ds \quad (2.3)$$

as the integral of the free electrons along the signal path between the transmitter T and the receiver R. Further observation techniques providing STEC information, such as the DORIS system (Doppler Orbitography and Radiopositioning Integrated by Satellite) – shown as the yellow-coloured connection of a transmitter on the Earth’s surface and the Low Earth Orbiting (LEO) satellite –, as well as the orange-coloured connection line between a GNSS and a LEO satellite performing Ionosphere Radio Occultation (IRO). The COSMIC-2 satellites and the Gravity Recovery and Climate Experiment-Follow-On Mission (GRACE-FO) are equipped with an IRO antenna and shown in Fig. 2.1. More detailed description about the different observation techniques can be found in Dettmering et al. (2011, 2014); Limberger (2015); Liang et al. (2016). As shown in Fig. 2.2, the STEC varies depending on the elevation angle of the satellite and consequently on the length of the signal path through the atmosphere. STEC therefore provides only a snapshot of the ionosphere between the satellite and the receiver and is only valid between the two points at that specific moment in time. A more general description of TEC is given by VTEC. Using a suitable conversion factor, VTEC can be derived from the STEC observation. Based on the widely accepted Single Layer Model (SLM), the conversion can be performed by the Modified Single Layer Mapping (MSLM) (Dach et al., 2015). Within the SLM, it is assumed that all electrons are concentrated on an infinitesimal thin layer, i.e. a sphere  $\Omega_H$  with radius

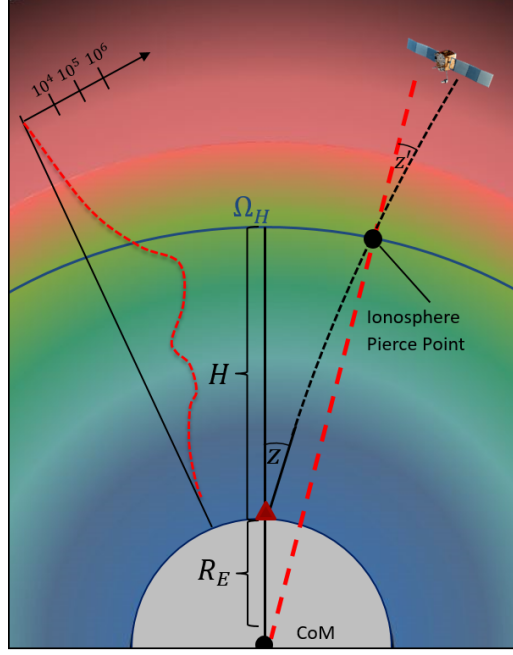


Figure 2.2: Scheme of the SLM mapping.

$R_H = R_E + H$ . The sphere is shown in Fig. 2.2 as a blue-coloured circle at height  $H$  above the surface of the spherical Earth with a radius  $R_e = 6371\text{km}$ , which usually coincides with the altitudes of the  $F_2$ -layer. The MSLM function is in good agreement with the (JPL) Extended Slab Model (ESM) and defined as

$$M(z) = \frac{1}{\cos z'} = \frac{1}{\sqrt{1 - \sin^2 z'}} = \left(1 - \left(\frac{R_e}{R_e + H} \sin \alpha z\right)^2\right)^{-1/2} \quad (2.4)$$

with  $\alpha = 0.9782$  and  $H = 506.7 \text{ km}$  (Dach et al., 2015). It provides the ratio

$$VTEC(\mathbf{x}_{IPP}, t) = \frac{STEC(\mathbf{x}^T, \mathbf{x}_R, t)}{M(z)}. \quad (2.5)$$

The ‘mapped’ VTEC is related to the position  $\mathbf{x}_{IPP}$  of the so-called Ionospheric Pierce Point (IPP) and is shown in Fig. 2.2 as the intersection point of the ray path and the shell  $\Omega_H$ . The dashed vertical line connects the IPP with the origin of  $\Sigma_E$ .

By substituting the Eqs. (2.3) and (2.5) in (2.1) the relation between VTEC and the ionospheric delay

$$d_{ion}(\mathbf{x}^T, \mathbf{x}_R, t) = -\frac{40.3}{f^2} \cdot M(z) \cdot VTEC(\mathbf{x}_{IPP}, t), \quad (2.6)$$

is determined. This formula can be used in two different ways:

1. With a given VTEC from ionospheric models, the ionospheric delay  $d_{ion}(\mathbf{x}^T, \mathbf{x}_R, t)$  can be calculated and used for correction of GNSS observations for precise navigation and positioning.
2. Deriving the ionospheric delay from dual- or multi-frequency GNSS observations allows for developing or improving an ionosphere model.





## 3 Global Navigation Satellite Systems

There are several geodetic observation systems, missions, applications and products, which suffer from the influence of the electron density in the atmosphere. Considering that the goal of this work is to develop methods for generating high-resolution VTEC maps, these perturbations serve as observation for estimating the VTEC model coefficients. Observations from various geodetic satellite missions and systems can be used for this purpose. Although terrestrial GNSS observations mainly cover the continents and their data distribution shows gaps over the oceans, they serve as the basis for most modelling approaches for VTEC due to the amount of data as well as their integrity. Therefore, the methods developed in this thesis are based on GNSS observations.

GNSS consist of three segments, the *space segment*, the *ground segment* and the *user segment*. The space segment comprises a constellation of several satellites in different orbital planes, see for instance Fig. 3.1. The satellites transmit the so-called navigation message providing information about the satellite orbits, i.e. the position of each satellite as well as the information about the satellite clocks, which are both necessary for users performing positioning and navigation. The ground segment monitors the satellites and tracks their signals, calculates and corrects the orbit information and controls the integrity of the system. The user segment operates independently from the space and the ground segment, i.e. the user only receives the signals from the satellites and processes them. This does not require any registration, so neither the space nor the ground segment will know how many users are receiving signals and for what purpose.

GNSS is a collective term for various satellite systems, which allow determining the 3-D position, the velocity and the time with high precision, in the case that the user is on the Earth's surface or in the near-Earth space. There are currently different GNSS, which will be introduced in the following Sections.

### 3.1 Global Positioning System

The NAVigational Satellite Timing And Ranging - Global Positioning System NAVSTAR-GPS or in short, GPS constellation, was developed and is operated by the U.S. Armed Forces for military purposes. As the use of GPS for civil purposes became increasingly important the artificially inserted interfering signals were enabled. Since then, GPS can be used in surveying and navigation without any interferences. In the development phase, the so-called Block-I-satellites were put into orbit beginning in 1978. GPS finally reached its operational status in 1993 with a total number of 24 satellites. These are placed along 6 orbital planes with a mean radius of 20,200 km and an inclination of  $55^\circ$  and  $60^\circ$  difference in the ascending nodes. The satellites have been regularly replaced and renewed since then. A schematic representation of the GPS satellite constellation is shown in Fig. 3.1.

There are (Status in Feb. 2020) 31 operational satellites in orbit, with 11 satellites of type Block IIR, 7 satellites of type Block IIR-M, 12 satellites of type Block IIF and one of the newest type Block II/IIIF<sup>1</sup>. The surplus satellites are called spares, which take their place after the elimination of broken satellites. The satellites transmit the signals on the carriers

---

<sup>1</sup>Information taken from <https://www.gps.gov/systems/gps/>

$$L_1: \quad f_1 = 154 \cdot f_0 = 1575.42 \text{ MHz}; \quad \lambda_1 = c/f_1 = 0.190 \text{ m},$$

$$L_2: \quad f_2 = 120 \cdot f_0 = 1227.60 \text{ MHz}; \quad \lambda_2 = c/f_2 = 0.244 \text{ m}$$

on the frequencies with the wavelengths  $\lambda_1$  and  $\lambda_2$  in L-band and based on the basis frequency  $f_0 = 10.23 \text{ MHz}$ , with  $c$  the speed of light with  $299792458 \text{ m/s}$  in SI units.

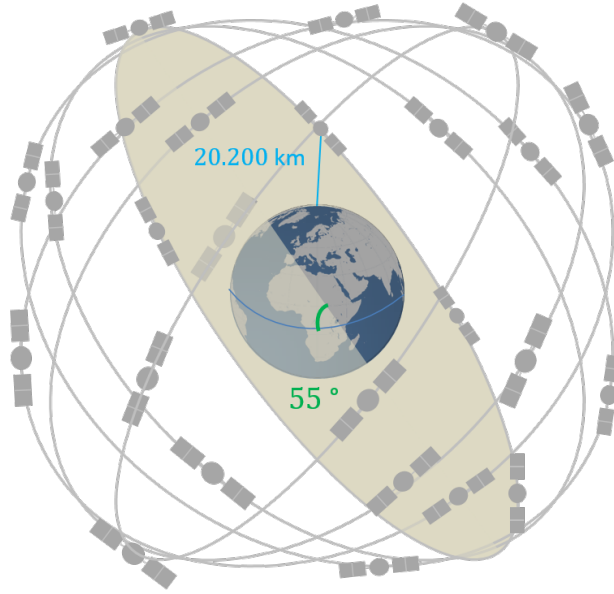


Figure 3.1: Schematic representation of the GPS constellation with six orbital planes of  $55^\circ$  inclination. The satellites are placed along the orbital plane with an altitude of  $20,200 \text{ km}$ .<sup>2</sup>

In order to transmit the navigation message, including the orbit as well as satellite clock information and to overcome ambiguities in the measurement of the signal path between satellite and receiver, the GPS signals are phase modulated by Pseudo Random Noise (PRN) codes. In the following, two codes, the so-called Coarse/Acquisition (C/A) code and the precision P(Y) code, are taken into account for determining the ionospheric observable. All available satellites transmit the C/A code modulated on the  $L_1$  carrier frequency as the ranging signal, which is available for civilian and scientific use. Furthermore, the precision P(Y) code ranging signal is modulated on the  $L_1$  carrier signal and includes the navigation message. The satellites also transmit the second P(Y) code ranging signal modulated on the  $L_2$  carrier signal. Newer satellites such as the Block-IIR-M satellite transmit the second civilian signal L2C in the  $L_2$  band, which was designed for commercial needs<sup>3</sup>. The third civilian signal  $L_5$  with carrier frequency  $f_5 = 115 \cdot f_0 = 1176.45 \text{ MHz}$  was designed exclusively for the Safety of Life (SoL) application with a larger bandwidth. It was first transmitted from Block IIF satellites and is characterised by higher signal strength. Thus, it is more robust against interference and used for higher performance applications (SoL). In the following  $L_5$  will not be used. A fourth civilian signal, L1C modulated on  $L_1$  carrier frequency, allows the interoperability between GPS and other satellite navigation systems such as the European Galileo system. However, only latest generation of spacecrafts, the Block-II/IIIF satellites, transmit the L1C signals. Table 3.1 shows the final codes which are used in Section 4.5.2 for the determination of the ionospheric observable from the raw GPS observations.

<sup>2</sup>The schematic representation of the GPS constellation was inspired by

<https://www.gps.gov/multimedia/images/constellation.jpg>

<sup>3</sup>Information about different codes taken from

<https://www.gps.gov/systems/gps/> and [https://www.unoosa.org/pdf/publications/icg\\_ebook.pdf](https://www.unoosa.org/pdf/publications/icg_ebook.pdf).

Table 3.1: GPS observation codes for determining the ionospheric observable.

Freq. Band	Code	Pseudorange	Carrier Phase	Description
$L_1$			$\Phi_1$	Carrier phase observation on $f_1 = 1575.42$ MHz
	C/A	$C_1$		Pseudorange observation of C/A code modulated on $L_1$
	P(Y)	$P_1$		Pseudorange observation of P(Y) code modulated on $L_1$
$L_2$			$\Phi_2$	Carrier phase observation on $f_2 = 1227.60$ MHz
	L2C	$C_2$		Pseudorange observation of L2C code modulated on $L_2$
	P(Y)	$P_2$		Pseudorange observation of P(Y) code modulated on $L_2$

## 3.2 GLONASS

The GLObalnaja NAWigazionnaja Sputnikowaja Sistema (GLONASS) is the GNSS of the Russian Federation and operated by the military since 1993. The constellation is set up with three orbital planes of  $120^\circ$  distance in the ascending nodes and  $64.8^\circ$  inclination. A total number of 24 satellites orbiting the Earth in an altitude of 19,100 km, with 8 satellites placed at slots of  $45^\circ$  shift along the orbital plane. As with GPS, older satellites of types Block-I and Block-II have

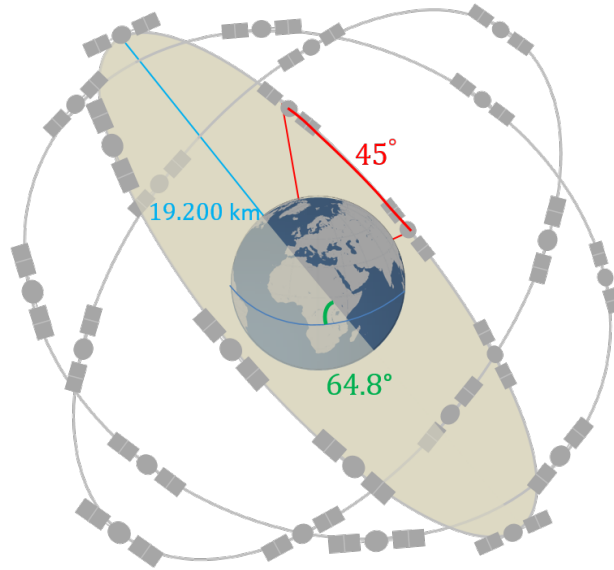


Figure 3.2: Schematic representation of the GLONASS constellation with three orbital planes of  $64.8^\circ$  inclination. Eight satellites are placed with an angular distance of  $45^\circ$  along the orbital plane with an altitude of 19,100 km.

been replaced by newer spacecrafts over the time. The newer satellites are of type GLONASS-K and GLONASS-M and transmit signals on the frequencies,

$$L_1: f_{1,k} = f_{0,L_1} + k \cdot 562.5 \text{ kHz} = 1602 \text{ MHz} + k \cdot 562.5 \text{ kHz},$$

$$L_2: f_{1,k} = f_{0,L_2} + k \cdot 437.5 \text{ kHz} = 1246 \text{ MHz} + k \cdot 437.5 \text{ kHz}$$

with  $f_{0,L_1} = 1602$  MHz and  $f_{0,L_2} = 1246$  MHz as the basis frequencies of the  $L_1$  and the  $L_2$  band, respectively. The parameter  $k = -7, \dots, 6$  refers to the frequency channel which leads to different carrier frequencies within the L-band for individual satellites. A list of the different values for  $k$  with the corresponding orbital plane and orbital slot is given in Tab. 3.2. The channel numbers

Table 3.2: Currently operational GLONASS satellites and the related channel numbers taken from <https://www.glonass-iac.ru/en/guide/navfaq.php>.

Plane 1		Plane 2		Plane 3	
Orbit Slot	Channel	Orbit Slot	Channel	Orbit Slot	Channel
01	01	09	-2	17	04
02	-4	10	-7	18	-3
03	05	11	00	19	03
04	06	12	-1	20	02
05	01	13	-2	21	04
06	-4	14	-7	22	-3
07	05	15	00	23	03
08	06	16	-1	24	02

show a systematic pattern with a repeating sequence for each orbital plane. Furthermore, the channel numbers are not repeated between different planes, and thus are reduced to a total number of 12 channels. The repeat sequence within a single plane and the shift of the satellite slots along the plane ensures that a user never receives a signal with the same frequency, e.g. the slots 01 and 05 are placed on opposite sides of the plane.

The standard positioning signal is available to all users and is submitted from the generation of GLONASS-M and GLONASS-K spacecrafts. Therefore the C/A code and the P(Y) code are similarly modulated to both the  $L_1$  and  $L_2$  frequencies as in the GPS case. Finally, the pseudorange observations given in Tab. 3.1 are available from GLONASS as well as for the frequency  $f_{1,k}$  with  $C_1$   $P_1$  and for the  $f_{2,k}$  with  $C_2$  and  $P_2$ . Furthermore, the carrier phase observations  $\Phi_1$  and  $\Phi_2$  can be determined from GLONASS as well.

### 3.3 Other GNSS Systems

For the sake of consistency, it is worth mentioning that there are other GNSS, although their observations are not used for ionosphere modelling within this thesis. Furthermore, there are the Regional Navigation Satellite Systems (RNSS) such as the Quasi Zenith Satellite System (QZSS) and the Indian Regional Navigation Satellite System (IRNSS) which are typically equipped with satellites in geosynchronous or geostationary orbits.

The GNSS *Galileo*<sup>4</sup> is the European global satellite navigation and timing system operated by the European Space Agency (ESA), which enables global navigation and positioning, and services such as the SoL by means of various modelled codes. Galileo has been in an initial operating mode since 2016. The constellation comprises a total number of 27 satellites equally distributed in altitudes of 23,222 km along three orbital planes inclined at  $56^\circ$  relative to the equator. A schematic presentation about the constellation is given in Fig. 3.3 in panel a). *BeiDou*, the Chinese satellite system comprises a global constellation with regional focus on the Asian region. To be more specific, the core of the system is similar to the other GNSS with three orbital planes with an inclination of  $55^\circ$  and eight satellites at altitudes of 21,500 km each. In addition, the system is equipped with two geosynchronous satellites and three satellites in a geostationary orbit

---

<sup>4</sup>Galileo Status: [http://esamultimedia.esa.int/docs/galileo/Galileo\\_factsheet\\_2018.pdf](http://esamultimedia.esa.int/docs/galileo/Galileo_factsheet_2018.pdf)

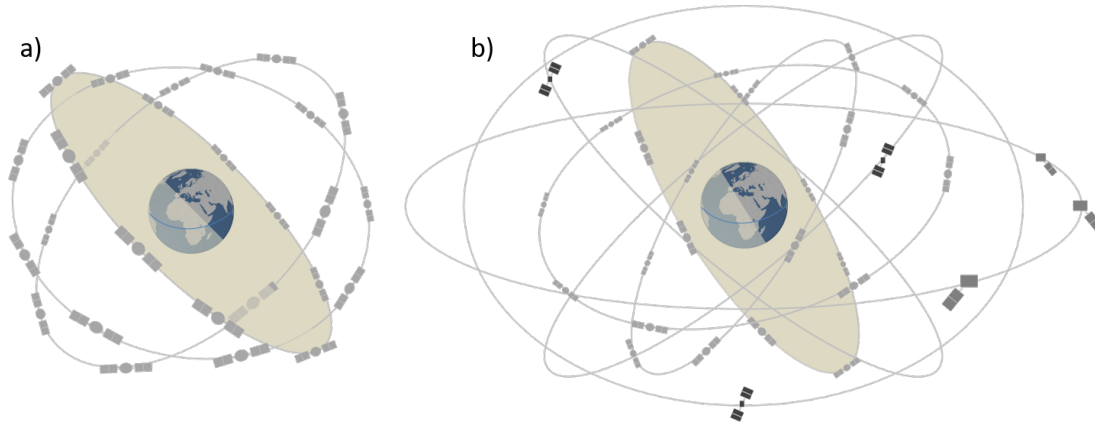


Figure 3.3: Schematic representation of the satellite constellation of Galileo in panel a) and of BeiDou in panel b)

at an altitude of 35,768 km. This constellation makes it possible for six satellites, to be always visible in the Asian region. The whole constellation is represented in a schematic way in panel b) of Fig. 3.3. Note, in the framework of this thesis, observations solely from GPS and GLONASS are considered.

### 3.4 Global and Regional GNSS Networks

GNSS networks are understood as a combination of different stations for specific regions or applications, which track the signals of different GNSS and provide these observation under the umbrella of the network for scientific and engineering purposes. GNSS networks are understood as an interconnection of terrestrial GNSS stations that receive and record the satellite signals of different GNSS. A network of stations can be related to specific regions or to a specific purpose for which the observations are made. The observations are then provided for scientific or engineering purposes under the umbrella of the network. Thereby, it is possible that individual stations provide their observations on different platforms and among different networks. This can lead to overlaps between different networks. Figure 3.4 shows the distribution of stations from different networks. The best-known global network is operated by the IGS and includes a collection of stations with a global distribution, as shown by the red dots in Fig. 3.4. The Asia Pacific Reference Frame (APREF)<sup>5</sup> is focused on Asia and the Pacific region, but also comprises stations located in other regions. Due to overlaps between the IGS and the APREF networks, it can be seen from Fig. 3.4, that individual station positions are marked with a red dot (partly behind blue or green stars) and a yellow triangle. Other networks focus on specific regions, such as EUREF<sup>6</sup>, which comprises stations distributed solely in Europe, or the Brazilian Network for Continuous Monitoring of GNSS Systems in real time (RBMC)<sup>7</sup>. UNAVCO<sup>8</sup> is a university-led consortium for geoscientific research and collects stations in a network of the same name. The focus of the UNAVCO network is on North America, but it has also stations that are available far away from the region, e.g. in Greenland. In Fig. 3.4, the regional networks are marked by different coloured stars. The positions of the stations from the EUREF network are plotted in blue, those from RBMC in grey and those from UNAVCO in green. The around 3700 stations

<sup>5</sup>APREF network: <http://www.ga.gov.au/scientific-topics/positioning-navigation/geodesy/asia-pacific-reference-frame>

<sup>6</sup>EUREF network: <http://www.epncb.oma.be/>

<sup>7</sup>RBMC Network: <https://www.ibge.gov.br/en/home-eng.html>

<sup>8</sup>UNAVCO organization: <https://www.unavco.org/>

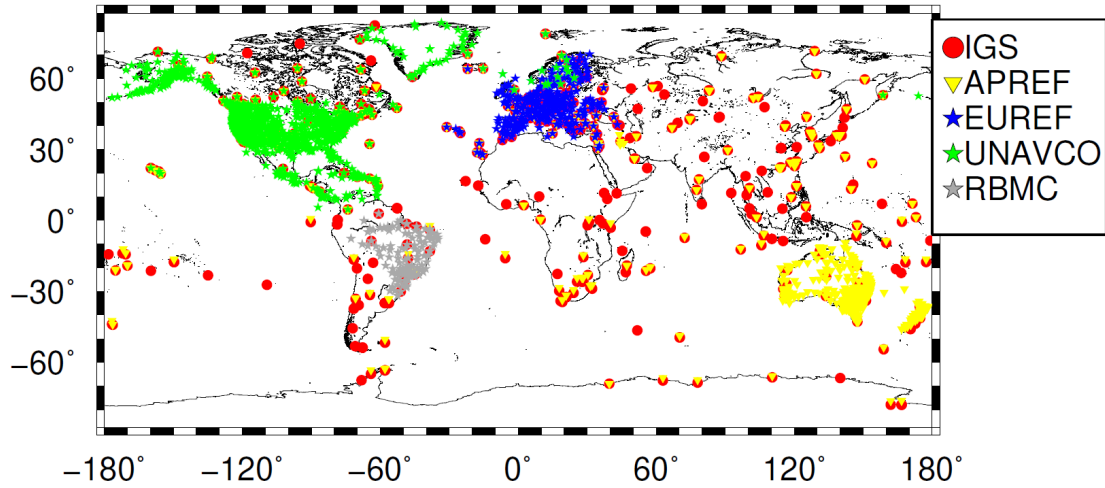


Figure 3.4: Distribution of GNSS stations that make their data available under the umbrella of various global and regional networks.

shown are all stations which are assigned to the different networks, including overlaps and stations which are currently not in operation. It needs to be noted that the represented networks are a selection of networks among several others.

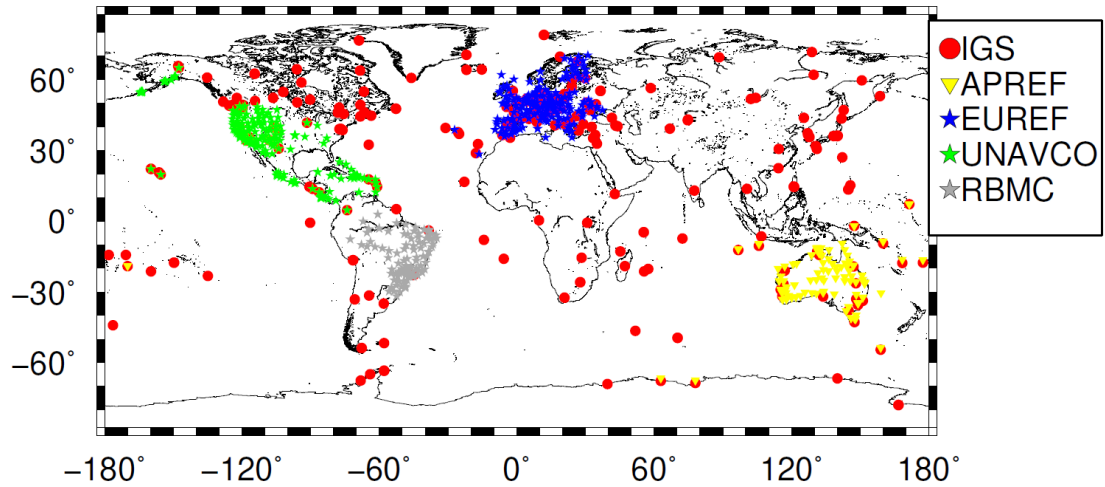


Figure 3.5: Distribution of stations that deliver data to the different networks in hourly intervals.

All these networks can be divided into different sub-networks, e.g. a sub-network for RT applications with stations providing observations via a streaming caster, or a sub-network providing data in hourly or daily data blocks via FTP servers. Within this thesis, observations provided with a latency of 1–2 hours and collected in hourly blocks by means of Receiver Independent Exchange Format (RINEX) files are used. The stations providing hourly data blocks to the previously mentioned networks are represented in Fig. 3.5. These stations are a sub-set of the stations shown in Fig. 3.4 and comprise a total number of 830<sup>9</sup>. As can be seen from Fig. 3.5 there is also less overlap, since not every station which is providing hourly blocks distributes these data via all designated networks. More specifically, stations that are shown as overlapping stations in Fig. 3.4 may only be assigned to one of the networks in the hourly data sub-networks.

<sup>9</sup>Number of stations taken on 15.05.2020

## 4 VTEC Modelling by Means of GNSS Observations

Since the development of satellite-based observation methods, modelling of the ionosphere has played a major role in geodesy. Ionosphere models are not only important for correcting the influence of electrons on signal propagation, but they are also of great scientific interest. In general, a distinction must be made between different types of models for the ionosphere.

Physical models are based on several physical equations, such as the Maxwell equation, the continuity, momentum, or transport equations, which describe the physical processes of the ionosphere and are usually solved using numerical methods Heise (2002). Although physical models provide a comprehensive solution, they require such high computing power – combined with the uncertainties associated to the number of physical parameters and approximations performed – that they are unsuitable for widespread use and are mostly applied in sciences. However, in order to use the extensive information obtained from physical models, e.g. for positioning, analytical or parameterised models are applied. In this case, the physical models are adapted by analytical functions, which enables a faster evaluation (Heise, 2002; Limberger, 2015).

Empirical models, on the other hand, are fundamentally different from physical models, as they are by definition based on observations. The ionosphere is described by underlying and simple analytical functions, whose coefficients are determined by means of observations. This requires an extensive and mostly historical database with observations from a large number of observation systems. Due to averaging processes, empirical models cannot reflect the actual state of the ionosphere, but describe its climatological variations (Heise, 2002; Schmidt et al., 2015a).

Currently, many observations of geodetic space methods are available. Using these observations, it is possible to generate a highly accurate instantaneous representation of the ionosphere in the form of GIMs and RIMs and by means of empirical models. According to Schmidt et al. (2015a), these models can also be called geodetic models. By means of a continuous collection of observations, GIMs and RIMs can be generated in RT to be provided to GNSS users (Li et al., 2020). In this chapter, a method is presented that makes it possible to create high-resolution GIMs and RIMs that can be of great importance both for the science and research and for use in precise GNSS applications.

### 4.1 Sun-Fixed Coordinate System

Before selecting suitable basis functions for the modelling of VTEC, it is necessary to choose an appropriate coordinate system in which the calculations are carried out. Considering VTEC in a geographical coordinate system  $\Sigma_E$  that rotates with the Earth – with the x-axis directed to the Greenwich meridian and the z-axis to the geographic North Pole – there are two factors that cause the greatest variations, namely ...

1. the geomagnetic latitude, as the electrons orient themselves around the geomagnetic equator through transport processes in the ionosphere and
2. the time, which is closely related to the geographical longitude.

The transformation from geographic latitude  $\varphi$  and longitude  $\lambda$  to geomagnetic latitude  $\varphi_m$  and longitude  $\lambda_m$  is straightforward (Hapgood, 1992). The transformation is merely a tilting of the z-axis of  $\Sigma_E$  by approximately  $11^\circ$  onto the polar axis of the dipolar core field of the Earth's magnetic field. The temporal variation of VTEC is largely influenced by solar radiation. However, if the ionosphere is viewed from the Sun, it would vary slowly in time, whereas the Earth rotates beneath it. Using a geocentric Sun-fixed coordinate system  $\Sigma_{sf}$ , where the x-axis is oriented to the Sun, only small temporal variations occur, which can be assumed as constant for short temporal intervals. According to Schmidt et al. (2015a), the Sun-fixed geographic latitude  $\varphi_{sf}$  and longitude  $\lambda_{sf}$  are calculated from the Earth-fixed geographic latitude  $\varphi$  and longitude  $\lambda$  by

$$\begin{aligned}\lambda_{sf} &= \lambda + UT[\text{rad}] + \pi \quad \text{and} \\ \varphi_{sf} &= \varphi,\end{aligned}\tag{4.1}$$

where  $UT[\text{rad}] =: \Theta$  is the hour angle given in Universal Time (UT). The y-axis is perpendicular to the rotation axis and the Earth-Sun line. The transformation (4.1) can be applied to the geomagnetic coordinates  $\varphi_m$  and  $\lambda_m$  in a similar way. A schematic representation of the transformation is given in Fig. 4.1, with the coordinate system  $\Sigma_{sf}$  in black. The coordinates  $\varphi_m$  and  $\lambda_{sf}$  for a point  $P(\varphi_{sf}, \lambda_{sf})$  in the Sun-fixed coordinate system are shown.

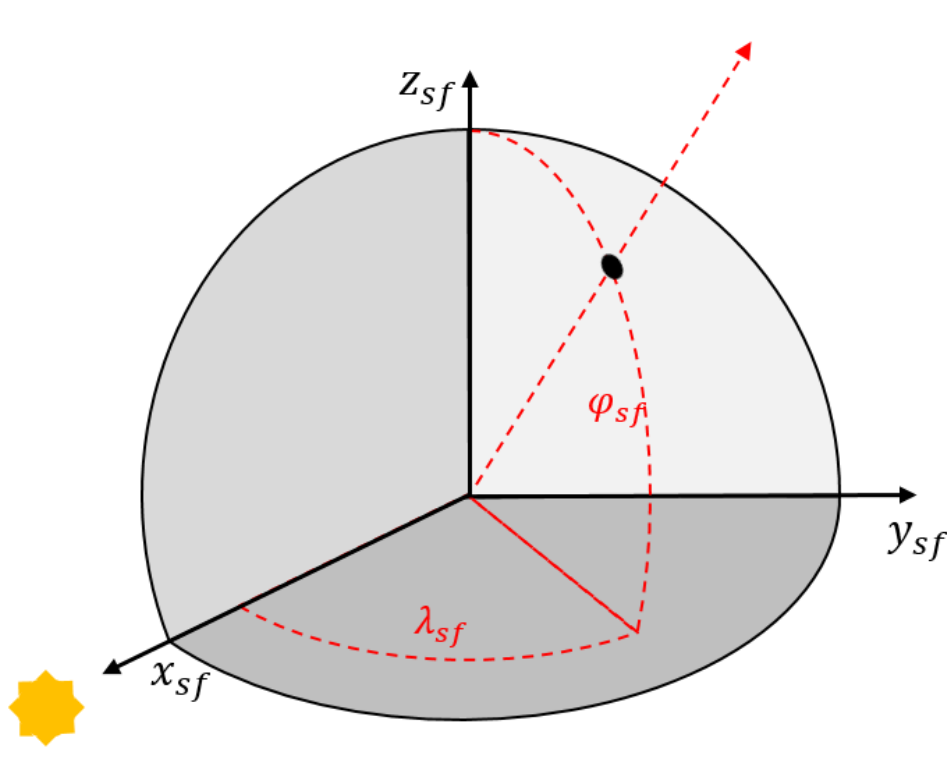


Figure 4.1: The schematic representation of the GSM coordinate system.

A suitable coordinate system that corresponds to the previous descriptions is the Geocentric Solar Magnetic (GSM) coordinate system (Laundal and Richmond, 2017; Hapgood, 1992). The following derivation of the modelling approach is carried out in the Sun-fixed geomagnetic coordinate system. The coordinates are not provided with the indices ‘ $sf$ ’ and ‘ $m$ ’ and the coordinates  $\varphi$  and  $\lambda$ , as well as the position vector  $\mathbf{x}$  from Eq. (2.2) are to be seen as in the Sun-fixed geomagnetic coordinate system.



## 4.2 Parameterisation

The electrons located on the layer  $\Omega_H$  under the assumption of SLM describe a 3-D function  $f(\mathbf{x}, t) = VTEC(\varphi, \lambda, t)$  as derived in Eqs. (2.3) to (2.5). The aim of the parameterisation is to generate a representation of that function by means of a series expansion in terms of suitable basis functions. A general representation is given by

$$f(\mathbf{x}, t) = \sum_{k=0}^{\infty} c_k(t) \phi_k(\mathbf{x}), \quad (4.2)$$

with the given space-dependent basis functions  $\phi_k(\mathbf{x})$  and the unknown time-dependent series coefficients  $c_k(t)$ . Assuming  $i_s = 1, 2, \dots, I_s$  observations  $y(\mathbf{x}_{i_s}, t_s) = VTEC(\mathbf{x}_{i_s}, t_s)$  are given at discrete moments in time  $t_s = t_0 + s \cdot \Delta t$  with  $s \in \mathbb{N}_0$  and with temporal sampling intervals  $\Delta t$ . The observations relate spatially to position  $P_{i_s} \in \Omega_H$  of the IPP with position vector  $\mathbf{x}_{i_s}$  in a geocentric coordinate system  $\Sigma_{sf}$ . Considering the measurement errors  $e(\mathbf{x}_{i_s}, t_s)$ , Eq. (4.2) can be rewritten and reads

$$y(\mathbf{x}_{i_s}, t_s) + e(\mathbf{x}_{i_s}, t_s) = f_N(\mathbf{x}_{i_s}, t_s) = \sum_{k=0}^N c_k(t_s) \phi_k(\mathbf{x}_{i_s}), \quad (4.3)$$

as a representation up to a certain degree  $N$ . In the sense of the 1-D Fourier theory, the degree  $N$  represents the number of oscillations that a signal performs within a certain interval, e.g.  $x \in [0, 2\pi]$ . The number of oscillations in the interval defines the wavelength  $L = \frac{2\pi}{N}$  of each individual oscillation. To be able to represent these oscillations unambiguously, discrete sampling points are required which, according to Nyquist's sampling theorem, must be given by mean sampling intervals of

$$\Delta x < L/2. \quad (4.4)$$

Thus, the degree  $N$  of the series expansion results from the mean sampling intervals  $\Delta x$  of the observations. The series expansion (4.3) is therefore band-limited with a cutoff frequency  $N$ . The remaining signal, which is not represented by the series expansion (4.3), is called truncation error

$$r_N(\mathbf{x}_{i_s}, t_s) = \sum_{k=N+1}^{\infty} c_k(t_s) \phi_k(\mathbf{x}_{i_s}), \quad (4.5)$$

and can be represented in the case that the actual sampling interval  $\Delta x$  allows a higher degree value  $N$ .

## 4.3 Spherical Harmonic Expansion

Among all the basis functions  $\phi_k$  in Eq. (4.2), the SHs are probably the most prominent functions for the representation of data on a sphere and thus are frequently used to generate GIMs. The usage of SHs for VTEC modelling was first introduced by Schaer (1999). In terms of SHs, the observation equation (4.3) has to be rewritten as

$$y(\mathbf{x}_{i_s}, t_s) + e(\mathbf{x}_{i_s}, t_s) = VTEC(\mathbf{x}, t_s) = \sum_{n=0}^{n_{max}} \sum_{m=-n}^n c_{n,m}(t_s) Y_{n,m}(\mathbf{x}_{i_s}), \quad (4.6)$$

where the functions  $Y_{n,m}(\mathbf{x})$ , i.e. the SHs of degree  $n = 0, \dots, n_{max}$  and order  $m = -n, \dots, n$ , are defined as

$$Y_{n,m}(\mathbf{x}) = P_{n,|m|}(\sin \varphi) \cdot \begin{cases} \cos m\lambda & \text{if } m \geq 0 \\ \sin |m|\lambda & \text{if } m < 0 \end{cases}. \quad (4.7)$$

Therein,  $P_{n,|m|}$  are the normalized associated Legendre functions of degree  $n$  and order  $m$ . The quantities  $c_{n,m}(t)$  in Eq. (4.6) are the initially unknown SH coefficients, which have to be determined for each discrete time moment  $t_s$  by an appropriate estimation procedure. The total number

$$N = (n_{max} + 1)^2 \quad (4.8)$$

of model unknowns depend on the maximum degree  $n_{max}$ . According to Nyquists sampling theorem (4.4) applied to the sphere,  $n_{max}$  is calculated in dependence on the observation sampling intervals  $\Delta\varphi$  in latitude direction and  $\Delta\lambda$  in longitude direction as

$$n_{max} \leq \frac{180^\circ}{\Delta\varphi} \quad \text{and} \quad n_{max} \leq \frac{180^\circ}{\Delta\lambda} . \quad (4.9)$$

The SHs are globally defined basis functions, which means that they are different from zero almost everywhere on the sphere, as can be seen from Eq. (4.7). In fact, SHs can easily be applied to model VTEC on the sphere  $\Omega_H$ , but they require homogeneously distributed data on  $\Omega_H$ , i.e. the IPPs  $P_{i_s}$ . To be more specific, the acquisition of an observation in (4.6) affects the representation globally (Schmidt et al., 2011). Thus, each coefficient  $c_{n,m}$  has to be recomputed by considering one additional observation.

As described at the beginning of this chapter, observations of GNSS stations usually provide the basis for the generation of GIMs with low latency, since their data can continuously be acquired. However, the distribution of IPPs is characterised by large data gaps over the oceans and dense observation clusters over the continents, and thus hits the weak point of SHs. Consequently, the modelling of VTEC by means of SHs is limited in terms of the spectral resolution (Schmidt et al., 2011).

## 4.4 B-spline Series Expansion

A more suitable approach for modelling the ionosphere is based on B-spline functions. In contrast to the SHs with globally defined basis functions, B-splines have a compact support, i.e. they only differ from zero in a limited area. This allows heterogeneously distributed data with data gaps to be handled more appropriately. However, the B-splines originate from wavelet theory and computer graphics (Stollnitz et al., 1995a) (Stollnitz et al., 1995b) and are typically defined as 1-D basis functions. The use of B-splines to model 2-D functions on a sphere originated from Lyche and Schumaker (2001) and is further described in Schumaker and Traas (1991); Jekeli (2005). The modelling of the ionospheric parameters by means of B-splines was applied by Schmidt (2007) and Schmidt et al. (2008), who also pointed out its advantage compared to SHs (Schmidt et al., 2011). In this regard two different types of B-splines are considered.

### 4.4.1 1-D Polynomial B-splines Expansion

The polynomial quadratic B-splines are denoted as

$$\phi_{k_\phi}^{J_\phi}(x) := N_{J_\phi, k_\phi}^2(x) \quad (4.10)$$

and used for representing signals in bounded intervals  $\mathbb{I}_x = [x_{min}, x_{max}]$ . The resolution level  $J_\phi \in \mathbb{N}_0$  defines the total number  $K_{J_\phi} = 2^{J_\phi} + 2$  of polynomial B-spline functions which are distributed along the interval  $\mathbb{I}_x$  with shift  $k_\phi = 0, \dots, K_{J_\phi} - 1$ . For the construction of the  $K_{J_\phi}$  polynomial quadratic B-spline along the interval, the sequence

$$x_{min} = \nu_0^{J_\phi} = \nu_1^{J_\phi} = \nu_2^{J_\phi} < \nu_3^{J_\phi} < \dots < \nu_{K_{J_\phi}}^{J_\phi} = \nu_{K_{J_\phi}+1}^{J_\phi} = \nu_{K_{J_\phi}+2}^{J_\phi} = x_{max} \quad (4.11)$$

of knot points  $\nu_{k_\phi}^{J_\phi}$  is established, considering multiple knot points at the boundaries. This is called the ‘endpoint-interpolating’ feature, which ensures the closing of the modelling interval. The distance between two successive knots  $\nu_{k_\phi+1}^{J_\phi}$  of shift  $k_\phi = 2, \dots, K_{J_\phi}$  is defined by  $\bar{x}/2^{J_\phi}$ , with  $\bar{x}$  as the length of the interval  $\mathbb{I}_x$ . Following Schumaker and Traas (1991) and Stollnitz et al. (1995a,b), the polynomial B-splines are calculated recursively by

$$N_{J_\phi, k_\phi}^n(x) = \frac{x - \nu_{k_\phi}^{J_\phi}}{\nu_{k_\phi+n}^{J_\phi} - \nu_{k_\phi}^{J_\phi}} N_{J_\phi, k_\phi}^{n-1}(x) + \frac{\nu_{k_\phi+n+1}^{J_\phi} - x}{\nu_{k_\phi+n+1}^{J_\phi} - \nu_{k_\phi+1}^{J_\phi}} N_{J_\phi, k_\phi+1}^{n-1}(x), \quad (4.12)$$

with  $n = 1, 2$  from the initial values

$$N_{J_\phi, k_\phi}^0(x) = \begin{cases} 1 & \text{if } \nu_{k_\phi}^{J_\phi} \leq x < \nu_{k_\phi+1}^{J_\phi} \text{ and } \nu_{k_\phi}^{J_\phi} < \nu_{k_\phi+1}^{J_\phi} \\ 0 & \text{otherwise} \end{cases}.$$

Note, in Eq. (4.12) a factor is set to zero if the denominator is equal to zero. As can be seen from

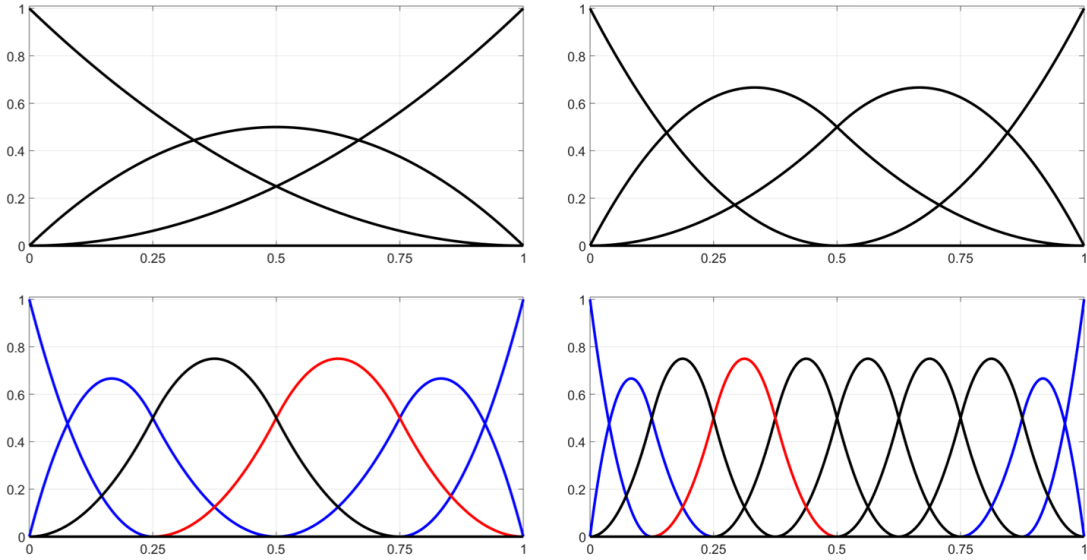


Figure 4.2: Polynomial B-splines of different levels  $J_\phi = 0, 1, 2, 3$  with the corresponding total numbers  $K_{J_\phi} = 3, 4, 6, 10$  of B-splines along the unit interval  $[0, 1]$  from the top left to the bottom right. The red-coloured spline functions  $N_{2,3}^2(x)$  (left) and  $N_{3,3}^3(x)$  (right) in the bottom panels correspond to the shift value  $k_\phi = 3$ . The blue-coloured spline functions in the bottom panels ensure the closure of the modelling interval at the boundaries.

Fig. 4.2, the total number  $K_{J_\phi}$  of B-splines along the interval increases with the level  $J_\phi$ . The higher the number of spline functions, the finer the structures that can be modelled. As can be seen from the red-coloured B-spline functions of shift  $k_\phi = 3$  in the bottom panels, the B-splines are different from zero only within a small sub-interval of a length  $\Delta_{J_\phi} \approx 3 \cdot h_{J_\phi}$  with

$$h_{J_\phi} = \frac{\bar{x}}{2^{J_\phi} + 1}. \quad (4.13)$$

Consequently, a input data sampling interval of

$$\Delta x < h_{J_\phi}, \quad (4.14)$$

is required, see Schmidt et al. (2011) and **P-I**. Solving Eq. (4.14) under the consideration of Eq. (4.13) for the level value  $J_\phi$ , the inequality

$$J_\phi \leq \log_2 \left( \frac{\bar{x}}{\Delta x} - 1 \right) \quad (4.15)$$

results.

#### 4.4.2 1-D Trigonometric B-splines Expansion

The second type of B-spline functions are trigonometric B-splines  $T_{J_T, k_T}^3(\lambda)$  of order 3 and level  $J_T \in \mathbb{N}_0$ , which are used for the signal representation in longitude direction. There are two different methods for defining the trigonometric B-spline: the first follows an approach according to Schumaker and Traas (1991), Jekeli (2005) and Limberger (2015), in which the trigonometric B-splines are calculated using a recurrence formula similar to Eq. (4.12), but the coefficients are subject to constraints to ensure a continuous representation along the circle of the equator. The second method was introduced by Lyche and Schumaker (2001) and used by Schmidt et al. (2011). The second method is used in **P-I**, and is described below.

The  $K_{J_T} = 3 \cdot 2^{J_T}$  trigonometric B-splines are located along the interval  $\lambda \in [0^\circ, 360^\circ)$  for the longitudes  $\lambda$ . Thereby, the position of each spline function is defined by the shift  $k_T = 0, 1, \dots, K_{J_T} - 1$ . The sequence of non-decreasing equally spaced knot points can be established as

$$0^\circ = \lambda_0^{J_T} < \lambda_1^{J_T} < \dots < \lambda_{k_T}^{J_T} < \dots < \lambda_{K_{J_T}-1}^{J_T} < 360^\circ. \quad (4.16)$$

Additional knots

$$\lambda_{K_{J_T}+i}^{J_T} = \lambda_i^{J_T} + 360^\circ \quad \text{for } i = 0, 1, 2 \quad (4.17)$$

are introduced to consider the periodicity along the circle along the interval  $[0^\circ, 360^\circ)$ . The distance

$$h_{J_T} = \frac{360^\circ}{K_{J_T}} = \frac{120^\circ}{2^{J_T}} \quad (4.18)$$

between two consecutive knots  $\lambda_{k_T}^{J_T}$  and  $\lambda_{k_T+1}^{J_T}$  for  $k_T = 0, 1, \dots, K_{J_T} - 1$  determines the length  $\Delta_{J_T} = 3 \cdot h_{J_T} = 360^\circ / 2^{J_T}$  of the non-zero sub-interval of a trigonometric B-spline function  $T_{J_T, k_T}^3(\lambda)$ . Following Lyche and Schumaker (2001), the functions

$$M_{J_T, k_T}(\lambda) = T_{J_T, k_T}^3(\lambda) = T_h^3(\Theta) \quad (4.19)$$

with  $h_{J_T} =: h$  and  $\lambda - \lambda_{k_T}^{J_T} =: \Theta$  for simplification can be calculated via

$$T_h^3(\Theta) = \begin{cases} \frac{\sin^2(\Theta/2)}{\sin(h/2) \sin(h)} & \text{for } 0 \leq \Theta < h \\ \frac{1}{\cos(h/2)} \frac{\sin^2((\Theta-h)/2) + \sin^2((2h-\Theta)/2)}{\sin(h/2) \sin(h)}, & \text{for } h \leq \Theta < 2h \\ \frac{\sin^2((3h-\Theta)/2)}{\sin(h/2) \sin(h)}, & \text{for } 2h \leq \Theta < 3h \\ 0, & \text{otherwise.} \end{cases} \quad (4.20)$$

The trigonometric B-spline basis functions are finally defined as

$$\tilde{\phi}_{k_T}^{J_T}(\lambda) = \begin{cases} M_{J_T, k_T}(\lambda), & \text{for } k_T = 0, \dots, K_{J_T} - 3 \\ M_{J_T, k_T}(\lambda) + M_{J_T, k_T}(\lambda - 360^\circ), & \text{for } k_T = K_{J_T} - 2, K_{J_T} - 1 \end{cases}. \quad (4.21)$$

Figure 4.3 shows trigonometric B-splines of different levels  $J_T$  with an increasing number of trigonometric B-spline functions distributed along the circle  $[0^\circ, 360^\circ)$ . As can be seen, the

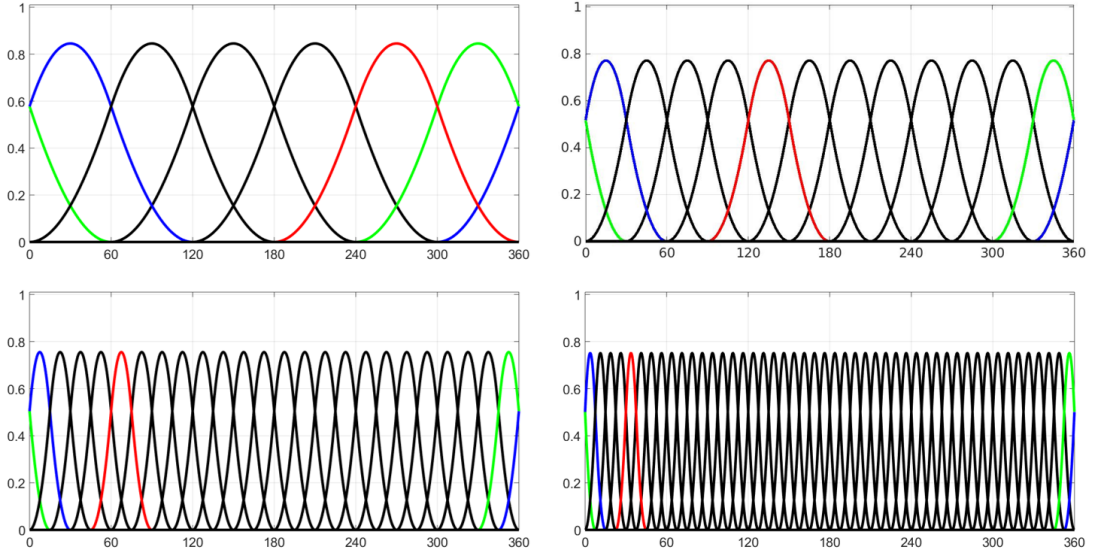


Figure 4.3: Trigonometric B-splines  $\tilde{\phi}_{k_T}^{J_T}(\lambda)$  of different level  $J_T = 1, 2, 3, 4$  from the top left panel to the bottom right with increasing total number of B-splines distributed on the circle  $[0^\circ, 360^\circ)$ . The red-coloured spline function  $\tilde{\phi}_3^{J_T}(\lambda)$  with shift value  $k_T = 3$  in each panel is different from zero only in the sub-interval of length  $\Delta_{J_T} = 360^\circ/2^{J_T}$ . The green- and blue-coloured B-spline functions  $\tilde{\phi}_{K_{J_T}}^{J_T}(\lambda)$  show the effect of the continuous modelling around the equator.

higher the level  $J_T$ , the more B-spline functions are distributed along the longitude  $[0^\circ, 360^\circ)$  and consequently, the finer are the structures which can be represented by the series expansion. Analogous to polynomial B-spline functions, the choice of the level value  $J_T$  depends on the input data sampling interval and thus, the inequality

$$\Delta\lambda < h_{J_T} \quad (4.22)$$

has to be fulfilled. Therein,  $\Delta\lambda$  denotes the average value of the data sampling interval along the longitude  $[0^\circ, 360^\circ)$ . Finally, under consideration of Eq. (4.18) the inequality

$$J_T \leq \log_2 \left( \frac{120^\circ}{\Delta\lambda} \right) \quad (4.23)$$

for determining the level value  $J_T$  is obtained.

## 4.5 GNSS Data Acquisition and Processing

The GNSS satellites continuously transmit their individual codes, the current time  $t_S$ , and their individual orbit data, which the user receives for positioning. Depending on the type of receiver, four code measurements (C/A and P(Y) on  $L_1$  and  $L_2$  each) are made per satellite and receiver connection. The position is determined by measuring the approximate distance between the receiver R and the respective visible GNSS satellites S. The pseudorange

$$P_{R,f}^S = c(t_S - t_R), \quad (4.24)$$

is determined by measuring the ‘propagation’ time as the difference between the satellite transmitting time  $t_S$  and the reception time  $t_R$  at the receiver at which the signal is received, and

multiplying the difference with the speed of light  $c$ . The pseudorange  $P_{R,f}^S$  can be observed on both frequencies  $f \in [f_1, f_2]$ . To determine the position, at least four visible satellites are necessary. They are used to determine the position and the receiver clock errors. The pseudorange contains besides, the true geometric distance between the GNSS satellite and the receiver, a number of error terms, which can either be determined by the user or be provided by external models, e.g. atmosphere models. In Tab. 4.1 the error sources are listed and sorted by the

Table 4.1: Errors in [m] in the pseudorange related to different error sources.

Error Source	Error in [m]
Receiver noise	$\pm 0.3$ m
Troposphere	$\pm 0.5$ m
Multipath Effect	$\pm 1.0$ m
Satellite Clocks	$\pm 2.0$ m
Orbit	$\pm 2.5$ m
Ionosphere	$\pm 5.0$ m

magnitude of disturbance on the pseudorange observation, when using broadcast corrections <sup>1</sup>. The error caused by the ionosphere is by far the largest (Klobuchar, 2013). In positioning it can even reach an error of 10 meters (Petit and Luzum, 2010), depending on the ionospheric state.

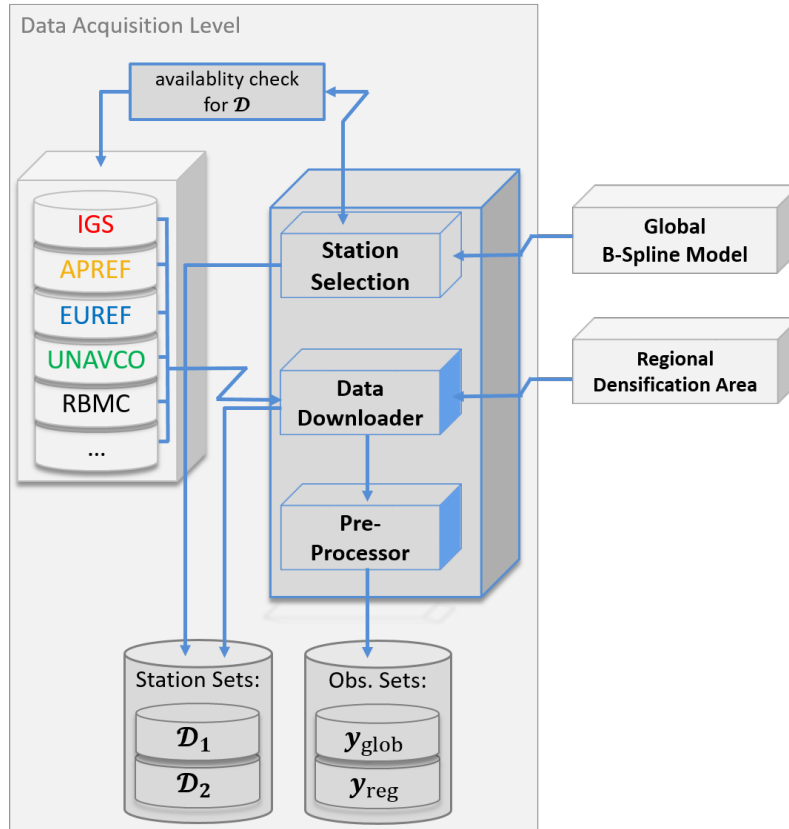


Figure 4.4: *Processing chain*: Flowchart of the processing chain, including the steps to be followed within the data acquisition level.

Figure 4.4 shows the first step of the entire processing chain for ionosphere products. The

<sup>1</sup>Numbers taken from: <https://novatel.com/an-introduction-to-gnss/chapter-4-gnsserror-sources>

description of the first step requires knowledge about the B-splines basis functions, which are derived in Sections 4.4.1 and 4.4.2 for the polynomial and trigonometric B-splines, respectively. The focus of this sub-section lies on the data acquisition comprising the station selection, the data download and the data pre-processing, as marked in blue in Fig. 4.4.

These steps are repeated at each time a new ionospheric information in terms of a GIM is to be generated. It needs to be noted at this point that the processing steps described in this section are based on the processing of hourly data blocks.

### 4.5.1 GNSS Data Selection Step

Compared to the total number of global distributed stations (cf. Fig. 3.4), the number of about 830 stations (cf. Fig. 3.5) providing hourly data seems to be small. However, due to improvements in the infrastructure in distant areas and further developments in network expansion, new stations are constantly being added to station networks providing hourly data. The demand for the provision of high-quality ionospheric corrections increases with the requirements in terms of positioning accuracy for modern applications. In fact, the quality of ionospheric corrections is related to the quality and the distribution of the input observations of GNSS. Thus, high resolution can only be generated where sufficient observations are provided by global or regional station networks. In order to simultaneously meet the requirements for the latency for the provision of ionospheric corrections, it is necessary to avoid long process sequences along the processing chain. A limitation of the stations to be used results in a reduction of the processing time but the selected observations need to fulfill the requirements for the generation of high-resolution ionosphere products. A suitable selection algorithm for stations is described below and addresses the research questions **Q-1**:

#### **Q-1** Selection of input data for global and regional high-resolution VTEC modelling

The map in Fig. 3.4 shows all stations from the networks IGS, EUREF, APREF, UNAVCO and RBMC, which provide hourly data blocks, whereby an inhomogeneous station distribution is given. Continental regions are mostly characterised by a dense station coverage, while there are large gaps over the oceans. For a global representation of the VTEC as will be described in particular in Section 4.6 and Eq. (4.38), the following situation prevails:

1. The large gaps over the oceans limit the modelling in the spatial and spectral resolution. This means that the modelling approach has to be adapted to the given circumstances. Consequently, the model resolutions of the global models are mostly of a lower spectral degree.
2. There is a high degree of redundancy, especially in those regions that have a regional network. This means that a particularly dense station coverage and thus more observations are available than it is necessary for estimating a global model with a low spectral degree.

Consequently, a number of the stations can be removed from the database for the global model. Within the framework of the model approach (4.37), which will be presented in Section 4.6, the eliminated stations can be added for a further densification case in certain regions.

In the literature, there are different approaches for the selection of GNSS stations. For example, by means of a Voroni diagram. Thereby, the Earth's surface is divided into regions assigned to each station (Kim et al., 2013; Lee and Kim, 2017). The stations which are assigned to regions of a size smaller than a predefined threshold are eliminated. This procedure yields a more homogeneous distribution of stations over the globe, but is time consuming and therefore not suitable (Mason, 2017). Besides the geographical location, quality characteristics such as the number of cycle slips, or the number and length in time for which individual stations do

not provide data can be defined in order to perform an appropriate station selection. Different approaches can be found in Rebischung et al. (2012); Grejner-Brzezinska et al. (2005); Kim et al. (2014); Lee and Kim (2017).

### B-spline Adaptive Station Selection

In this thesis a station selection procedure is presented, which is adapted to the global B-spline model, which represents VTEC as a continuous function on a sphere in terms of the SLM (cf. Section 2.2.3) with tensor products of polynomial and trigonometric B-splines. The B-splines are localising basis functions, thus the tensor products cover only a limited area of the entire sphere. The corresponding series coefficients are estimated from GNSS observations. In order to avoid rank deficiencies in the normal equations, each tensor product must be supported by observations. Consequently, for station selection this requirement has to be taken into account. The distribution of the B-spline knot points from Eqs. (4.11) and (4.16) define the position of the tensor products on the sphere. They are typically distributed with constant spacing along the latitudes and longitudes and form the basis for the station selection. The spacing depends on the selected B-spline levels  $J_\phi$  and  $J_T$ , see Eqs. (4.15) and (4.23).

The station selection block represented in the top part of the data acquisition block in Fig. 4.4 comprises the following sub-steps:

1. The first sub-step is to access the FTP servers of the networks to create a set  $\mathcal{D}$  containing the names of all stations that are currently providing hourly data blocks. These are then separated into two groups according to their position.
2. Information about the global B-spline model, in particular the information about the levels  $J_\phi$  and  $J_T$  of the polynomial and trigonometric B-spline expansion, is needed. Therefore, the information of the global B-spline model is provided to the station selection block in Fig. 4.4. Based on this information, a grid is created using the knot sequences (4.11) and (4.16). However, only the knots with shift  $k_\phi = 2, \dots, K_{J_\phi}$  for polynomial and the knots with shift  $k_T = 0, \dots, K_{J_T} - 1$  for trigonometric B-splines are used. Figure 4.5 shows in panel a) the global map with the stations from  $\mathcal{D}$ , and the grid generated by means of the knots of a B-spline expansion with levels  $J_\phi = 4$  and  $J_T = 3$ .
3. In the third sub-step, stations are selected in such a way that a globally more homogeneous distribution is created. From each grid point, the closest station is selected which lies within the surrounding four grid cells. It is assumed that the selected station provides a sufficient number of observations to avoid rank deficiencies for estimating the coefficients. The selected stations are to be further assigned to the station set  $\mathcal{D}_1 \in \mathcal{D}$ . All non-selected stations are consequently assigned to the station set  $\mathcal{D}_2 \in \mathcal{D}$ . The two station sets  $\mathcal{D}_1$  and  $\mathcal{D}_2$  are finally saved in the repository (cf. Fig. 4.4) in order to be accessible for the further process.

Figure 4.5 shows in panels b) and c) two cases to be distinguished when performing the third step of the previous enumeration.

- b) Problems arise if in regions, such as oceans, there are not enough stations to satisfy each of the grid points – here marked with yellow circles. The two stations marked in blue can be assigned to two of the marked grid points marked with yellow circles and added to the set  $\mathcal{D}_1$ . For the third grid point marked with an orange-coloured circle, however, there is no station left within the surrounding four grid cells, since these are already assigned to the other grid points. In this case no station can be selected, i.e. the grid point is neglected. This handling is permissible, since it is assumed that the selected stations perform a sufficient number of



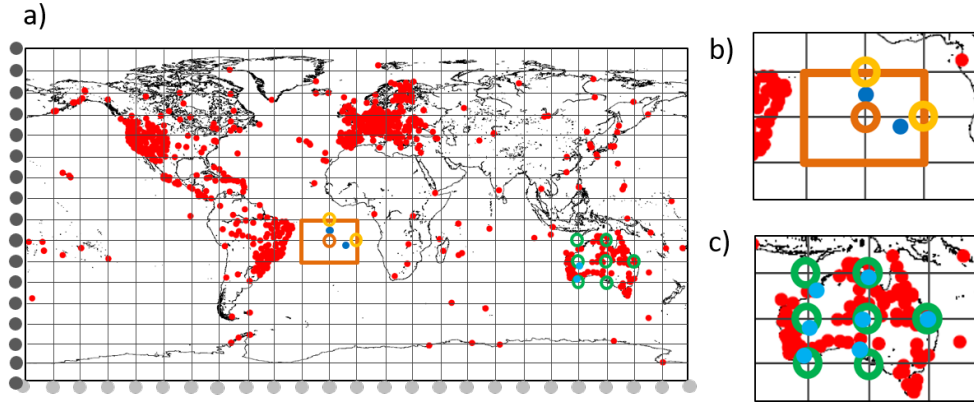


Figure 4.5: Schematic representation of the B-spline adapted station selection with the distribution of knot points  $\nu_{k_\phi}^{J_\phi}$  along the latitudes and knot points  $\lambda_{k_T}^{J_T}$  for B-spline expansions of level  $J_\phi = 4$  and  $J_T = 3$ . The left panel a) shows the global map with the grid and the stations, and panels b) and c) consider two specific cases which need to be taken into account within the third step of the selection procedure.

observations within the entire area. In regions where no station can be assigned to several successive grid points, the estimation procedure is adapted accordingly, see Sections 4.1 and 4.7.

- c) If there is a high station density in certain regions so that there are more stations than grid points, the closest stations (marked with cyan dots) are assigned to the grid points and included in the station set  $\mathcal{D}_1$ . All other stations that are not selected in this way are assigned to the station set  $\mathcal{D}_2$ .

The two maps in Fig. 4.6 represent the stations of the station set  $\mathcal{D}_1$  in panel a) and the stations of the station set  $\mathcal{D}_2$  in panel b). The station set  $\mathcal{D}_1$  provides a more homogeneous global distribution than the stations shown in Fig. 3.4. However, larger gaps in the station distribution can still be found over the oceans. Choosing lower level values  $J_\phi < 4$  and  $J_T < 3$  lead to a grid with larger cells and less stations assigned to the  $\mathcal{D}_1$ .

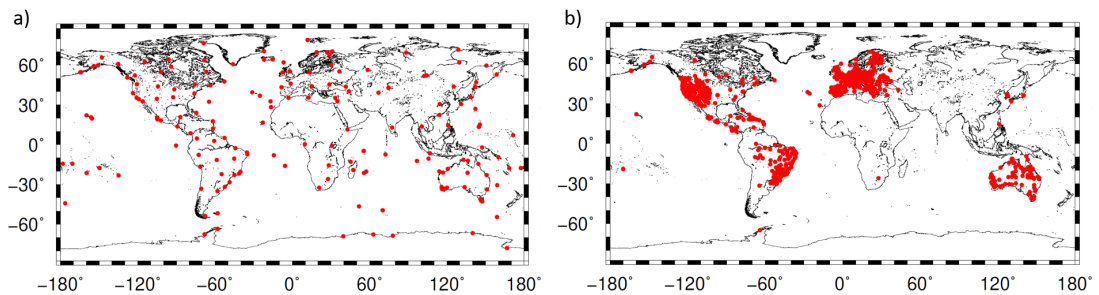


Figure 4.6: The stations assigned to the global station set  $\mathcal{D}_1$  in panel a), as well as the station assigned to the station set  $\mathcal{D}_2$  in panel b), based on the total number of stations providing hourly data, which are shown in 3.4.

### GNSS Download Step

In order to satisfy the needs for a fast process generating ionospheric corrections, the data selection procedure needs to be applied before downloading the GNSS data. From all stations providing

hourly data sets via the FTP servers of the networks, only observations of those added to the set  $\mathcal{D}_1$  are downloaded. The observations from stations which are assigned to the set  $\mathcal{D}_2$  can additionally be downloaded for potential regional densifications. For the download the following strategies are considered:

1. If no densification in certain regions should be performed, only observations from stations assigned to  $\mathcal{D}_1$  are downloaded.
2. If a densification in one region A should be performed, the stations of set  $\mathcal{D}_2$ , which are located within the region are assigned to the sub-set  $\mathcal{D}_{2A}$ . Their observations are downloaded additionally to the observations from  $\mathcal{D}_1$ .
3. If multiple regions A, B, ... are selected for a densification, the stations of set  $\mathcal{D}_2$ , which are located in regions A and B are assigned to the sets  $\mathcal{D}_{2A}$ ,  $\mathcal{D}_{2B}$ , .... Their observations are downloaded in addition to the observations of  $\mathcal{D}_1$ .

Typically, RINEX files are downloaded. These files are directly used by the pre-processor, as shown in Fig. 4.4.

#### 4.5.2 GNSS Pre-Processing Step

By means of the RINEX files, the observations on the codes C/A and P(Y) on different frequency bands  $L_1$  and  $L_2$  are provided and allow for establishing the observation equation (4.24). Considering the error quantities listed in Tab. 4.1, Eq. (4.24) can be rewritten as

$$P_{R,f}^S = \rho_R^S + c (\Delta t_S - \Delta t_R) + d_{trop} + [d_{ion} + c (b_R + b^S) + \epsilon_P]_f, \quad (4.25)$$

where  $\rho_R^S$  is the geometrical distance,  $d_{trop}$  the tropospheric propagation error and  $d_{ion}$  the ionospheric delay from Eq. (2.1) (Heise, 2002; Erdogan et al., 2017).  $\Delta t_S$  and  $\Delta t_R$  are the clock offsets and  $b_R$  and  $b^S$  the code biases of the receiver and satellite due to hardware delays. The quantity  $\epsilon_P$  consists of the remaining error parts of the code observation on the P-Code, such as multipath and receiver noise.

Using the phase observation  $\Phi_{R,f}^S$  in meter, the distance between the satellite S and the receiver reads

$$\Phi_{R,f}^S = \rho_R^S + c (\Delta t_S - \Delta t_R) + d_{trop} + [-d_{ion} + \lambda N + c (B_R + B^S) + \epsilon_\Phi]_f, \quad (4.26)$$

see Heise (2002); Limberger (2015); Erdogan et al. (2017, 2020). The ionospheric delay acts on carrier and code phase measurements with opposite signs as described in 2.2.3 by Eq. (2.1). The carrier phase observation equation (4.26) contains the interfrequency biases  $B_R$  and  $B^S$  of the receiver and the satellite, respectively, and an additional term including the phase ambiguities  $\lambda N$ , which means an unknown number  $N$  of phase transitions multiplied with the wavelength  $\lambda$  of the carrier signal.

The ionospheric delay  $d_{ion}$ , the biases  $b_R$ ,  $b_R$ ,  $B_R$  and  $B^S$  as well as the phase ambiguities  $\lambda N$  are frequency dependent and therefore put into parentheses in Eqs. (4.25) and (4.26).

By means of the geometry-free linear combination (Ciraolo et al., 2007) ionospheric information can be extracted from GNSS dual-frequency measurements, using the code pseudoranges  $P_{R,f_1}^S$  and  $P_{R,f_2}^S$  and the carrier phase observations  $\Phi_{R,f_1}^S$  and  $\Phi_{R,f_2}^S$  on the two carrier frequencies  $f_1$  and  $f_2$ . The geometry-free linear combination, as the differences on both frequencies for the pseudorange observation reads

$$P_{R,f_2}^S - P_{R,f_1}^S = d_{ion,f_2} - d_{ion,f_1} + c (b_{R,f_2} + b_{f_2}^S - b_{R,f_1} - b_{f_1}^S) + (\epsilon_{P,f_2} - \epsilon_{P,f_1}), \quad (4.27)$$

see Erdogan et al. (2017). Substituting Eq. (2.6) for  $d_{ion,f_1}$  and  $d_{ion,f_2}$ , combining the differences  $b_R = b_{R,f_2} - b_{R,f_1}$  and  $b^S = b_{f_2}^S - b_{f_1}^S$  in the biases to one so-called Differential Code Bias (DCB)  $DCB_R^S = b_R + b^S$  and after some reformulations the ionosphere observable reads

$$P_{R,I}^S = \alpha \cdot \text{STEC} + DCB_R^S + \epsilon_{P,I} . \quad (4.28)$$

The linear combination of the carrier phase observations reads

$$\Phi_{R,f_1}^S - \Phi_{R,f_2}^S = -d_{ion,f_1} + d_{ion,f_2} + c (B_{R,f_1} + B_{f_1}^S - B_{R,f_2} - B_{f_2}^S) + (\lambda_{f_1} N_{f_1} - \lambda_{f_2} N_{f_2}) + (\epsilon_{\Phi,f_1} - \epsilon_{\Phi,f_2}), \quad (4.29)$$

which consists of the so-called Carrier Phase Bias (CPB)

$$CPB_R^S = c(B_{R,f_1} + B_{f_1}^S - B_{R,f_2} - B_{f_2}^S) + \lambda_{f_1} N_{f_1} - \lambda_{f_2} N_{f_2} \quad (4.30)$$

as a combination of the differenced  $B_R$  and  $B_S$  as well as the ambiguity term  $\lambda_{f_1} N_{f_1} - \lambda_{f_2} N_{f_2}$  which are constant for continuous arcs. For an unbroken connection between the satellite and the receiver, the ionosphere observable reads

$$L_{R,I}^S = \alpha \cdot \text{STEC} + CPB_R^S + \epsilon_{L,I} . \quad (4.31)$$

The constant  $\alpha$  defined as

$$\alpha = 40.3 \frac{f_1^2 - f_2^2}{f_1^2 f_2^2} \quad (4.32)$$

is a scaling factor between the two frequencies and relates the linear combination (4.28) in meter unit to the STEC in TECU. The index  $I$  identifies the target quantity, the ionosphere, and corresponds to the common standard. The parameter  $\epsilon_{P,I} = \epsilon_{P,f_1} - \epsilon_{P,f_2}$  as well as  $\epsilon_{L,I} = \epsilon_{\Phi,f_1} - \epsilon_{\Phi,f_2}$  contain remaining uncertainties.

### Carrier Phase Leveling

The observable  $P_{R,I}^S$  of the pseudorange observations is rather noisy but unambiguous, while the observable  $\Phi_{R,I}^S$  of the carrier phase observations is two orders of magnitude more precise but ambiguous (Ciraolo et al., 2007; Rovira-Garcia et al., 2015). In order to exploit the precision of phase observations, the ambiguity bias – the unknown number  $N$  of whole cycles of the signal between satellite and receiver – needs to be determined. Since the ambiguity term and the satellite and receiver biases are assumed to be constant for continuous arcs (Ciraolo et al., 2007; Mannucci et al., 1998, 1993), the  $CPB_R^S$  can be determined by averaging the differences of  $P_{R,I}^S$  and  $L_{R,I}^S$  as

$$CPB_R^S \approx \frac{1}{L} \sum_{l=1}^L (L_{R,I}^S - P_{R,I}^S)_l, \quad (4.33)$$

with  $L$  for the number of observations along a continuous arc (Ciraolo et al., 2007; Erdogan et al., 2020). Substituting Eq. (4.33) in (4.31), the levelled geometry-free phase observation  $\widetilde{L}_{R,I}^S$  for a continuous arc reads

$$\widetilde{L}_{R,I}^S = L_{R,I}^S - CPB_R^S = \alpha \cdot \text{STEC} + DCB_R^S - \widetilde{e}_{L_I}, \quad (4.34)$$

with  $\widetilde{e}_{L_I}$  as the error of the phase-levelled carrier phase observation. Finally, the phase-levelled carrier phase observation can be rewritten as

$$y_{\text{glob}} + \widetilde{e}_{L_I} = \alpha \cdot \text{STEC} + DCB_R^S, \quad (4.35)$$

for observations determined from stations assigned to the station set  $\mathcal{D}_1$  and as

$$y_{\text{reg}} + \widetilde{e}_{L_I} = \alpha \cdot \text{STEC} + DCB_R^S, \quad (4.36)$$

for all observations determined from stations assigned to  $\mathcal{D}_2$ .

## 4.6 Multi-Scale Modelling of the Ionosphere

The B-spline functions as introduced above allow for the generation of a MSR. The MSR is interpreted as viewing on a signal under different resolutions like a microscope does. This means that the target function can be displayed on different scales as a low-pass, band-pass or high-pass filtered signal.

The MSR is subject to the publications **P-I** and **P-II**. The contents of both publications are repeated in this work for reasons of consistency. Some parts are taken directly from the publications. The equations, figures and section numbers are adapted to the framework of this thesis. These text passages are indicated and written as indented.

### Two-Step Model

In order to carry out a parameterisation as described above, observations are required. The higher the observation density, the finer are the structures that can be modelled. As shown in Chapter 3, the data basis for ionosphere modelling based on GNSS observations consists of a heterogeneous distribution. While the densely distributed observations over the continents allow for modelling of finer structures in VTEC, the large data gaps over the oceans restrict the VTEC representation on a global scale. Finer structures in VTEC, which can be observed by GNSS due to the high data density, especially over continental regions, therefore remain in the truncation error.

Within this thesis, a multi-scale model is developed, which contains a global representation as well as a regional representation of VTEC, considering the large data gaps on a global scale and dense observation clusters on a regional scale.

The basic equation of the so-called Two-Step Model (TSM) for VTEC reads

$$VTEC_{\text{reg}}(\varphi, \lambda, t) = VTEC_{\text{glob}}(\varphi, \lambda, t) + \Delta VTEC_{\text{reg}}(\varphi, \lambda, t), \quad (4.37)$$

with the global  $VTEC_{\text{glob}}(\varphi, \lambda, t)$  (first step) representing the low-frequency signal part in VTEC and the regional  $\Delta VTEC_{\text{reg}}(\varphi, \lambda, t)$  (second step) representing the finer structures for regions with dense data coverage **P-II**.

Both model parts are estimated separately from each other using the independent GNSS datasets, as defined in the previous section. At first, it does not seem necessary to make this separation, as all observations can contribute to support both parts of the model. Consequently, based on the estimation theory, a strict separation is not permissible. In fact both models must be estimated together, since the parameters of the two model parts in Eq. (4.37) are correlated. In this thesis, however, separation is preferred for the following reasons:

- The regional model is limited to a defined region with a certain extent in latitude and longitude. Since the regional model represents the  $\Delta VTEC$  with the main trend of the signal coming from the global modelling part, the regional model is set up in the Earth-fixed coordinate system. The global model on the other hand is defined within a Sun-fixed geomagnetic coordinate system (cf. Eq. (4.1)). A combined estimation would need a consideration of the coordinate transformation.
- Both model parts are based on different basis functions. The global model considers a series expansion (4.38) in terms of polynomial and trigonometric B-splines for latitude and longitude, respectively. Whereas for the regional model a series expansion of polynomial B-splines (4.52) is used, since the endpoint interpolating feature is needed to close the region at the boundaries.

The use of a separated approach allows both parts of the model to be provided separately. A combined estimation of the unknown model parameters of both model steps would lead to correlations between both model parts. Consequently, both parts have to be disseminated as a combined model, since the global model would not be usable within the densification region without the second step of the TSM approach. Another advantage of the separated approach is that it can be extended to different densification regions, even in post-processing. As long as the global model is already available and the observations in the desired region permit a densification, this can be carried out for any region.

In this context, the flowchart from Fig. 4.4 is extended by two modules included in the modelling level. The module for the global model is represented with a red frame and the module for the regional model is represented with a green frame in Fig. 4.7. Within this section, the TSM

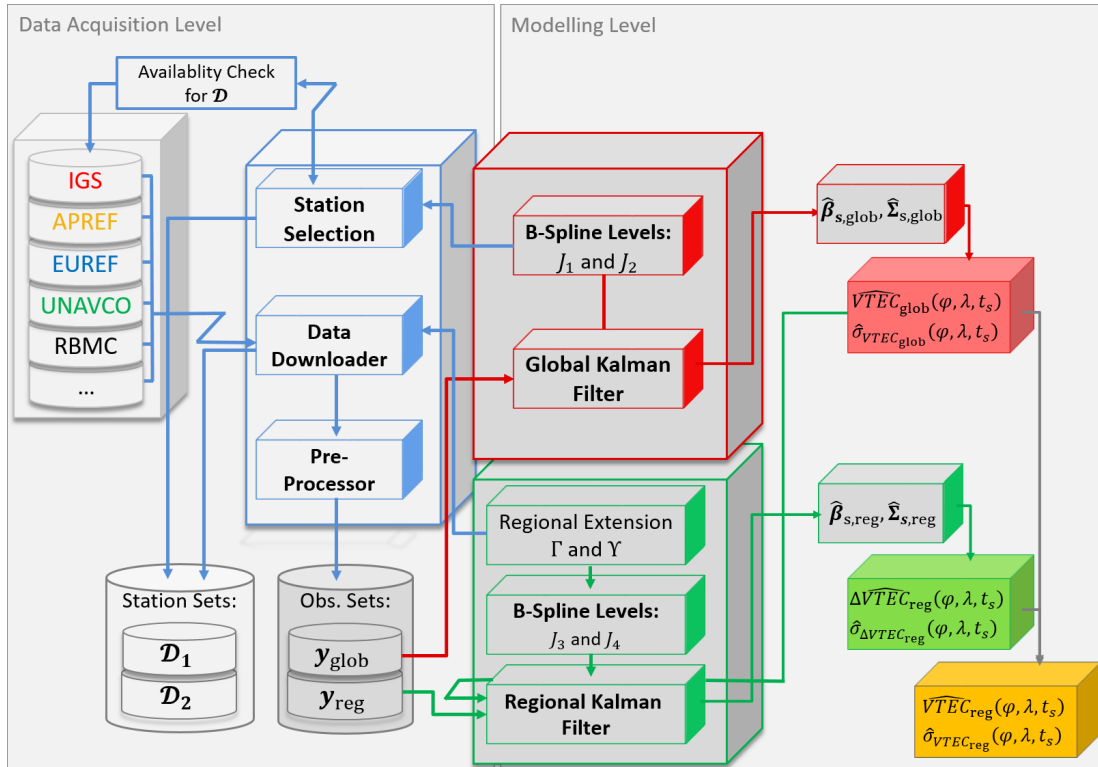


Figure 4.7: *Processing chain*: Flowchart of the processing chain, including the data acquisition level (cf. Section 4.5) and the modelling level with the TSM comprising the global and the regional modelling modules.

is described in more detail based on the publications **P-I** and **P-II**. The Kalman filter (KF) estimation as shown in Fig. 4.7 is described in Section 4.7, and the resulting products in Section 5.

### 4.6.1 Global B-spline VTEC Model

The present chapter deals with the global modelling of the function  $f(\mathbf{x}_{i_s}, t_s) = VTEC(\mathbf{x}_{i_s}, t_s)$  and addresses the research questions **Q-2**:

**Q-2** Global high-resolution modelling of the Vertical Total Electron Content

Using the observations  $y_{\text{glob}}(\mathbf{x}_{i_s}, t_s)$  observed by the stations which are assigned to the set  $\mathcal{D}_1$  and the corresponding observation errors  $e_{\text{glob}}(\mathbf{x}_{i_s}, t_s)$ , the observation equation (4.3) can be written in terms of B-splines as

$$y_{\text{glob}}(\mathbf{x}_{i_s}, t_s) + e_{\text{glob}}(\mathbf{x}_{i_s}, t_s) = VTEC_{\text{glob}}(\mathbf{x}_{i_s}, t_s) = \sum_{k_1=0}^{K_{J_1}-1} \sum_{k_2=0}^{K_{J_2}-1} d_{k_1, k_2}^{J_1, J_2}(t_s) \phi_{k_1, k_2}^{J_1, J_2}(\mathbf{x}_{i_s}), \quad (4.38)$$

with the 2-D tensor product basis functions

$$\phi_{k_1, k_2}^{J_1, J_2}(\varphi, \lambda, t_s) = \phi_{k_1}^{J_1}(\varphi) \tilde{\phi}_{k_2}^{J_2}(\lambda). \quad (4.39)$$

The tensor products are formed by polynomial B-splines  $\phi_{k_1}^{J_1}(\varphi)$  from Eq. (4.10) of level  $J_\phi = J_1$  and by trigonometric B-splines  $\tilde{\phi}_{k_2}^{J_2}(\lambda)$  from Eq. (4.21) of level  $J_T = J_2$ . Polynomial B-splines are applied in latitude direction with the boundaries at the latitude values  $\varphi = -90^\circ$  and  $\varphi = 90^\circ$  for the South and the North pole, respectively. The trigonometric B-splines consider a continuous representation along the longitudes  $\lambda \in [0^\circ, 360^\circ)$  **P-I**.

### Spectral Resolution of the Global VTEC Model

The large data gaps do not allow for an arbitrary choice of the B-spline level values  $J_1$  and  $J_2$ , thus, the inequalities (4.15) and (4.23) have to be considered. For determining appropriate levels, the following strategies can be applied.

This entire section is taken from **P-I**<sup>2</sup>:

In the Section 4.3, we derived the relations between the maximum degree  $n_{\text{max}}$  of a SH expansion and the sampling intervals  $\Delta\varphi$  and  $\Delta\lambda$  of the input data. In the previous Section 4.4, the corresponding relations between the level values  $J_\phi = J_1$  and  $J_T = J_2$  of a B-spline expansion and the data sampling intervals have been deduced. The substitution of the expression  $180^\circ/n_{\text{max}}$  from the inequalities (4.9) into the Eqs. (4.15) and (4.23) yields the altogether six inequalities

$$\begin{aligned} J_1 &\leq \log_2 \left( \frac{180^\circ}{\Delta\varphi} - 1 \right) \leq \log_2 (n_{\text{max}} - 1), \\ J_2 &\leq \log_2 \left( \frac{120^\circ}{\Delta\lambda} \right) \leq \log_2 \left( \frac{2 \cdot n_{\text{max}}}{3} \right). \end{aligned} \quad (4.40)$$

Given the numerical values 1 to 6 for the B-spline levels  $J_1$  and  $J_2$  Table 4.2 presents the corresponding largest numerical values for each, the SH degree  $n_{\text{max}}$  as well as the sampling intervals  $\Delta\varphi$  and  $\Delta\lambda$  by evaluating the inequalities (4.40).

From the spectral point of view the six inequalities (4.40) comprise the following three scenarios:

1. If the global sampling intervals  $\Delta\varphi$  and  $\Delta\lambda$  are known, the mid parts of the inequalities (4.40) are given. The maximum degree  $n_{\text{max}}$  is calculable from the right-hand side inequalities and may be inserted into the SH expansion (4.6). The left-hand side inequalities yield the two level values  $J_1$  and  $J_2$ , which can be inserted into the B-spline expansion (4.38).

---

<sup>2</sup>The numbering of equations, figures and tables does not coincide with the numbering in the publication **P-I** Goss et al. (2019) but are adapted to this thesis. Spelling and punctuation are corrected in the indented section.

Table 4.2: Numerical values for the B-spline levels  $J_1$  and  $J_2$ , the maximum SH degree  $n_{max}$  and the input data sampling intervals  $\Delta\varphi$  and  $\Delta\lambda$  by evaluating the inequalities (4.40); the left part of the table presents the numbers along a meridian (upper inequalities in Eq. (4.40)), the right part the corresponding numbers along the equator and its parallels according to the lower inequalities in Eq. (4.40).

Latitude							Longitude						
$J_1$	1	2	3	4	5	6	$J_2$	1	2	3	4	5	6
$n_{max}$	3	5	9	17	33	63	$n_{max}$	3	6	12	24	48	96
$\Delta\varphi$	60°	36°	20°	10.5°	5.45°	2.85°	$\Delta\lambda$	60°	30°	15°	7.5°	3.75°	1.875°

2. With a specified numerical value for  $n_{max}$ , the right-hand parts of the inequalities (4.40) are given. The data input sampling intervals  $\Delta\varphi$  and  $\Delta\lambda$  can be determined from the mid parts of the inequalities. Next, the two numerical values for level values  $J_1$  and  $J_2$  are calculable from the left-hand side inequalities and can be inserted into the B-spline expansion (4.38).
3. If the processing time of VTEC maps has to be considered, the level values  $J_1$  and  $J_2$  are subject to certain restrictions, since as a matter of fact the number of numerical operations increases exponentially with the chosen numerical values for the levels. In this case, from the given left-hand side inequalities the data sampling intervals  $\Delta\varphi$  and  $\Delta\lambda$  can be determined from the mid parts. Finally, the right-hand side inequalities yield numerical values for the maximum SH degree  $n_{max}$ .

### Multi-Scale Analysis

The B-spline functions as introduced in the Sections 4.4.1 and 4.4.2 allow for the generation of a Multi-Scale Analysis (MSA) in terms of wavelet decomposition. When choosing the highest possible B-spline levels based on the strategies derived above, lower resolution levels can be derived by applying the pyramid algorithm, see e.g. Schumaker and Traas (1991); Lyche and Schumaker (2001); Schmidt (2012); Schmidt et al. (2015a,b); Liang (2017). In the first-author publication **P-I**, the 2-D pyramid algorithm for the regional B-spline approach published in the above-mentioned publications is applied to the global B-spline approach for VTEC representation.

The following indented part is taken from **P-I**<sup>3</sup>:

To decompose VTEC into its spectral components the Eqs. (4.38) and (4.39) need to be rewritten in vector and matrix notation. For this purpose we introduce the  $K_{J_1} \times 1$  vector

$$\phi_{J_1}(\varphi) = [\phi_0^{J_1}(\varphi), \phi_1^{J_1}(\varphi), \dots, \phi_{K_{J_1}-1}^{J_1}(\varphi)]^T, \quad (4.41)$$

the  $K_{J_2} \times 1$  vector

$$\tilde{\phi}_{J_2}(\lambda) = [\tilde{\phi}_0^{J_2}(\lambda), \tilde{\phi}_1^{J_2}(\lambda), \dots, \tilde{\phi}_{K_{J_2}-1}^{J_2}(\lambda)]^T \quad (4.42)$$

as well as the  $K_{J_1} \times K_{J_2}$  coefficient matrix

$$\mathbf{D}_{J_1, J_2} = \begin{bmatrix} d_{0,0}^{J_1, J_2} & d_{0,1}^{J_1, J_2} & \cdots & d_{0, K_{J_2}-1}^{J_1, J_2} \\ d_{1,0}^{J_1, J_2} & d_{1,1}^{J_1, J_2} & \cdots & d_{1, K_{J_2}-1}^{J_1, J_2} \\ \vdots & \ddots & \ddots & \vdots \\ d_{K_{J_1}-1,0}^{J_1, J_2} & d_{K_{J_1}-1,1}^{J_1, J_2} & \cdots & d_{K_{J_1}-1, K_{J_2}-1}^{J_1, J_2} \end{bmatrix}. \quad (4.43)$$

<sup>3</sup>The numbering of equations, figures and tables does not coincide with the numbering in the publication **P-I** Goss et al. (2019) but are adapted to this thesis. Spelling and punctuation are corrected in the indented section.

Considering the computation rules for the Kronecker product ‘ $\otimes$ ’ (cf. (Koch, 1999)), Eq. (4.38) can be written as

$$\begin{aligned} f(\varphi, \lambda, t) &= (\tilde{\phi}_{J_2}(\lambda) \otimes \phi_{J_1}(\varphi))^T \text{vec} \mathbf{D}_{J_1, J_2}(t) \\ &= \phi_{J_1}^T(\varphi) \mathbf{D}_{J_1, J_2}(t) \tilde{\phi}_{J_2}(\lambda) \end{aligned} \quad (4.44)$$

wherein ‘vec’ refers to the vec-operator.

Neglecting the time dependency the B-spline approach (4.44) reads

$$f_{J_1, J_2}(\varphi, \lambda) = \phi_{J_1}^T(\varphi) \mathbf{D}_{J_1, J_2} \tilde{\phi}_{J_2}(\lambda). \quad (4.45)$$

In the context of the MSR, the vectors  $\phi_{J_1}(\varphi)$  and  $\tilde{\phi}_{J_2}(\lambda)$  are called scaling vectors, the elements  $d_{k_1, k_2}^{J_1, J_2}$  of the matrix  $\mathbf{D}_{J_1, J_2}$  are denoted as scaling coefficients.

With  $J'_1 = J_1 - J$ ,  $J'_2 = J_2 - J$  and  $0 < J \leq \min(J_1, J_2)$ , we obtain the 2-D MSR of the target function  $f(\mathbf{x})$  introduced in Eq. (4.2) as

$$f_{J_1, J_2}(\varphi, \lambda) = f_{J'_1, J'_2}(\varphi, \lambda) + \sum_{j=1}^J \sum_{\vartheta=1}^3 g_{J_1-j, J_2-j}^{\vartheta}(\varphi, \lambda). \quad (4.46)$$

Following the argumentation of Schmidt et al. (2015b) but considering the polynomial and the trigonometric B-spline functions, the low-passed filtered level- $(J'_1, J'_2)$  signal  $f_{J'_1, J'_2}(\varphi, \lambda)$  and the band-pass filtered level- $(J_1 - j, J_2 - j)$  detail signals  $g_{J_1-j, J_2-j}^{\vartheta}(\varphi, \lambda)$  are computable via the relations

$$\begin{aligned} f_{J'_1, J'_2}(\varphi, \lambda) &= \phi_{J'_1}^T(\varphi) \mathbf{D}_{J'_1, J'_2} \tilde{\phi}_{J'_2}(\lambda), \\ g_{j_1-1, j_2-1}^1(\varphi, \lambda) &= \phi_{j_1-1}^T(\varphi) \mathbf{C}_{j_1-1, j_2-1}^1 \tilde{\psi}_{j_2-1}(\lambda), \\ g_{j_1-1, j_2-1}^2(\varphi, \lambda) &= \psi_{j_1-1}^T(\varphi) \mathbf{C}_{j_1-1, j_2-1}^2 \tilde{\phi}_{j_2-1}(\lambda), \\ g_{j_1-1, j_2-1}^3(\varphi, \lambda) &= \psi_{j_1-1}^T(\varphi) \mathbf{C}_{j_1-1, j_2-1}^3 \tilde{\psi}_{j_2-1}(\lambda), \end{aligned} \quad (4.47)$$

where we introduced the definitions  $j_1 = J_1 - j + 1$  and  $j_2 = J_2 - j + 1$  for  $j = 1, \dots, J$ . Herein, the  $K_{j_1-1} \times 1$  and  $K_{j_2-1} \times 1$  scaling vectors  $\phi_{j_1-1}(\varphi)$  and  $\tilde{\phi}_{j_2-1}(\lambda)$  as well as the  $L_{j_1-1} \times 1$  and  $L_{j_2-1} \times 1$  wavelet vectors  $\psi_{j_1-1}(\varphi)$  and  $\tilde{\psi}_{j_2-1}(\lambda)$  can be calculated by means of the two-scale relations

$$\begin{aligned} \phi_{j_1-1}^T(\varphi) &= \phi_{j_1}^T(\varphi) \mathbf{P}_{j_1}, \\ \tilde{\phi}_{j_2-1}^T(\lambda) &= \tilde{\phi}_{j_2}^T(\lambda) \tilde{\mathbf{P}}_{j_2}, \\ \psi_{j_1-1}^T(\varphi) &= \phi_{j_1}^T(\varphi) \mathbf{Q}_{j_1}, \\ \tilde{\psi}_{j_2-1}^T(\lambda) &= \tilde{\phi}_{j_2}^T(\lambda) \tilde{\mathbf{Q}}_{j_2}, \end{aligned} \quad (4.48)$$

with  $L_{j_1-1} = K_{j_1} - K_{j_1-1}$  and  $L_{j_2} = K_{j_2} - K_{j_2-1}$ .

The numerical entries of the  $K_{j_1} \times K_{j_1-1}$  matrix  $\mathbf{P}_{j_1}$  and the  $K_{j_1} \times L_{j_1-1}$  matrix  $\mathbf{Q}_{j_1}$  can be taken from Stollnitz et al. (1995b) or Zeilhofer (2008); the corresponding entries of the  $K_{j_2} \times K_{j_2-1}$  matrix  $\tilde{\mathbf{P}}_{j_2}$  and the  $K_{j_2} \times L_{j_2-1}$  matrix  $\tilde{\mathbf{Q}}_{j_2}$  are provided by Lyche and Schumaker (2001).

In the Eqs. (4.47) we introduced the  $K_{j_1-1} \times K_{j_2-1}$  matrix  $\mathbf{D}_{j_1-1, j_2-1}$  of scaling coefficients  $d_{k_1, k_2}^{j_1-1, j_2-1}$  as well as the  $K_{j_1-1} \times L_{j_2-1}$  matrix  $\mathbf{C}_{j_1-1, j_2-1}^1$ , the  $L_{j_1-1} \times K_{j_2-1}$  matrix  $\mathbf{C}_{j_1-1, j_2-1}^2$



and the  $L_{j_1-1} \times L_{j_2-1}$  matrix  $C_{j_1-1,j_2-1}^3$  of wavelet coefficients. These four matrices are calculable via the 2-D downsampling equation

$$\begin{bmatrix} D_{j_1-1,j_2-1} & C_{j_1-1,j_2-1}^1 \\ C_{j_1-1,j_2-1}^2 & C_{j_1-1,j_2-1}^3 \end{bmatrix} = \begin{bmatrix} \bar{P}_{j_1} \\ \bar{Q}_{j_1} \end{bmatrix} D_{j_1,j_2} \begin{bmatrix} \tilde{P}_{j_2}^T & \tilde{Q}_{j_2}^T \end{bmatrix} \quad (4.49)$$

also known as the 2-D pyramid algorithm. The  $K_{j_1-1} \times K_{j_1}$  matrix  $\bar{P}_{j_1}$ , the  $K_{j_2-1} \times K_{j_2}$  matrix  $\tilde{P}_{j_2}$ , the  $L_{j_1-1} \times K_{j_1}$  matrix  $\bar{Q}_{j_1}$  and the  $L_{j_2-1} \times K_{j_2}$  matrix  $\tilde{Q}_{j_2}$  are computable via the identities

$$\begin{bmatrix} \bar{P}_{j_1} \\ \bar{Q}_{j_1} \end{bmatrix} = \begin{bmatrix} P_{j_1} & Q_{j_1} \end{bmatrix}^{-1}, \quad (4.50)$$

$$\begin{bmatrix} \tilde{P}_{j_2} \\ \tilde{Q}_{j_2} \end{bmatrix} = \begin{bmatrix} \tilde{P}_{j_2} & \tilde{Q}_{j_2} \end{bmatrix}^{-1}; \quad (4.51)$$

see e.g. Schmidt (2007). The 2-D pyramid algorithm based on the decomposition (4.46) is visualised in Fig. 4.8. The '0<sup>th</sup>' step transforms according to the Eqs. (4.38) and (4.44) the observations  $y(\mathbf{x}_{i_j}, t_j)$  into the elements of the scaling matrix  $D_{J_1,J_2}(t_j)$  as introduced in Eq. (4.43). The applied procedure will be explained in Section 4.7.

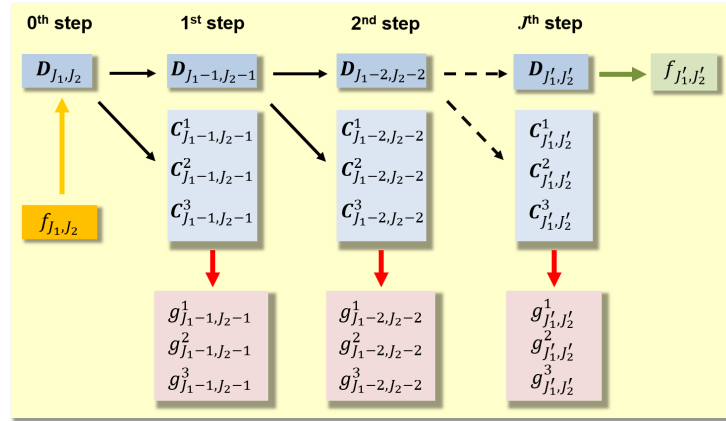


Figure 4.8: 2-D MSR of the signal  $f_{J_1,J_2}(\varphi, \lambda)$ .

### 4.6.2 Regional B-spline VTEC Model

In this section, the regional modelling part of the TSM is described and addresses the research questions **Q-3**:

#### **Q-3** Regional high-resolution modelling of the Vertical Total Electron Content

For the regional representation of the function  $f(\mathbf{x}_{i_s}, t) = \Delta VTEC(\mathbf{x}_{i_s}, t)$  in Eq. (4.37), the global model from Section 4.6.1 serves as the background model. This is indicated in the flowchart in Fig. 4.7 with the values  $VTEC_{\text{glob}}(\varphi, \lambda, t)$  as input to the estimation procedure of the regional model using a KF. The observation equation (4.3) is rewritten as

$$y_{\text{reg}}(\mathbf{x}_{i_s}, t_s) + e_{\text{reg}}(\mathbf{x}_{i_s}, t_s) - VTEC_{\text{glob}}(\mathbf{x}_{i_s}, t_s) = \sum_{k_3=0}^{K_{J_3}-1} \sum_{k_4=0}^{K_{J_4}-1} d_{k_3,k_4}^{J_3,J_4}(t_s) \phi_{k_3,k_4}^{J_3,J_4}(\mathbf{x}_{i_s}), \quad (4.52)$$

with the observations  $y_{\text{reg}}(\mathbf{x}_{i_s}, t_s)$  and corresponding observation errors  $e_{\text{reg}}(\mathbf{x}_{i_s}, t_s)$  from the stations which are listed in the station list  $\mathcal{D}_2$ . The 2-D tensor products

$$\phi_{k_3, k_4}^{J_3, J_4}(\varphi, \lambda, t_s) = \phi_{k_3}^{J_3}(\varphi) \phi_{k_4}^{J_4}(\lambda) \quad (4.53)$$

consist of polynomial B-splines in both directions, since  $VTEC_{\text{reg}}(\mathbf{x}_{i_s}, t_s)$  is fixed to a bounded area and the modelling area has to be closed at the boundaries. Hence, polynomial B-spline functions (4.10) of level  $J_\phi = J_3$  are applied in latitude direction within the interval  $\varphi \in [\varphi_{\min}, \varphi_{\max}]$  and of level  $J_\phi = J_4$  in longitude direction within the interval  $\lambda \in [\lambda_{\min}, \lambda_{\max}]$ , see **P-II**.

### Spectral Resolution of the Regional VTEC Model

Since Eq. (4.52) is applied for rectangular areas  $\Delta\Omega \in \Omega_H$  of size  $\Upsilon \times \Gamma$ , the levels  $J_3$  and  $J_4$  are to be chosen in dependence of the extension  $\Upsilon$  of the region in latitude direction and  $\Gamma$  in longitude direction.. To avoid possible spectral gaps in the representation of the TSM (4.37), the extension of the region is subject to restrictions. The inequalities

$$\Upsilon \geq L_\varphi \quad \text{and} \quad \Gamma \geq L_\lambda, \quad (4.54)$$

with the minimum wavelength  $L_\varphi = 2 \cdot \Delta\varphi$  represented by the global model (4.38) in latitude direction and the minimum wavelength  $L_\lambda = 2 \cdot \Delta\lambda$  in longitude direction have to be considered. In this way, it is guaranteed that the minimum wavelengths which are represented in both directions by the global model fit into the region and no spectral gap is generated. The inequality relation (4.15) for determining the polynomial B-spline level has to be adapted and reads

$$\begin{aligned} J_3 &\leq \log_2 \left( \frac{\Upsilon}{\Delta\varphi} - 1 \right) \leq \log_2 \left( \frac{\Upsilon \cdot n_{\max}}{180^\circ} \right) \\ J_4 &\leq \log_2 \left( \frac{\Gamma}{\Delta\lambda} - 1 \right) \leq \log_2 \left( \frac{\Gamma \cdot n_{\max}}{180^\circ} \right) \end{aligned} \quad (4.55)$$

$J_3$  and  $J_4$  can be derived in dependence of the average sampling intervals  $\Delta\varphi$  and  $\Delta\lambda$  of the observations within the region  $\Delta\Omega$ . Numerical values from the inequality chains (4.55) can be found in the look-up table in Fig. 4.9

The look-up table is flexibly designed in a way that the global background model can be given with any combination of levels  $J_1$  and  $J_2$  and vary according to the MSA derived in Section 4.6.1. The look-up table allows for determining the region size  $\Upsilon \times \Gamma$  in dependence of the global model as well as levels  $J_3$  and  $J_4$  in dependence of the given data distribution.

The table in the upper left panel of Fig. 4.9 shows the spectral resolution in terms of  $n_{\max}$  according to Tab. 4.2 with  $n_{\max}$  depending on  $J_1$  depicted in the dark grey triangles and  $n_{\max}$  depending on  $J_2$  depicted in light grey triangles. The inclined red arrow shows the spectral decomposition according to Section 4.6.1 in both dimensions. On the right and below this table, the global mean sampling intervals  $\Delta\varphi$  and  $\Delta\lambda$  derived from Eqs. (4.15) and (4.23), the minimum wavelength  $L_\varphi$  and  $L_\lambda$ , as well as the resulting minimum region size  $\Upsilon$  and  $\Gamma$  according to the inequalities (4.54) are shown for the respective level  $J_1$  and  $J_2$ . The table in the lower right panel shows the spectral resolution  $n_{\max}$  in dependence of  $J_3$  in latitude direction depicted in dark grey triangles and in dependence of  $J_4$  in longitude direction in light grey triangles. The values for  $n_{\max}$  are calculated for the different region sizes  $\Upsilon$  and  $\Gamma$  according to (4.55). The respective minimal sampling intervals are depicted for  $\Delta\varphi$  in the upper right panel and for  $\Delta\lambda$  in the lower left panel of the look-up table.

To explain how the look-up table works, two cases are marked in different colour.

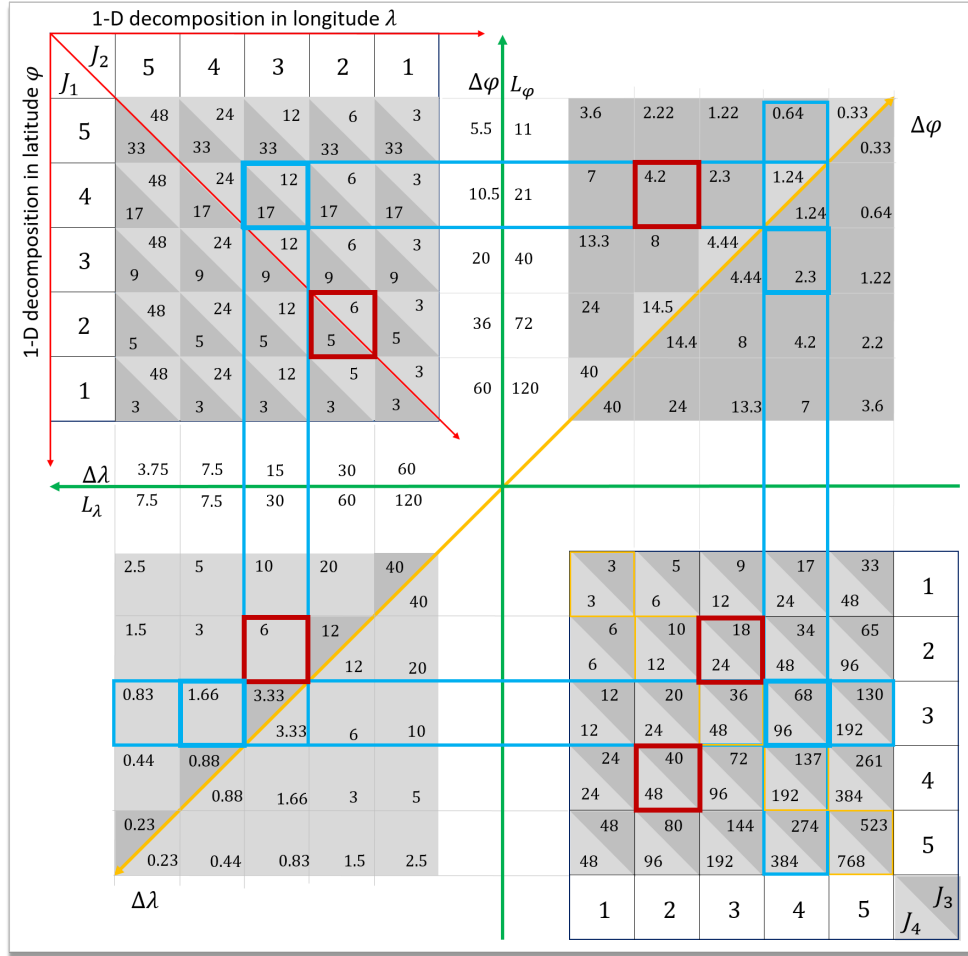


Figure 4.9: Look-up table to determine regional B-spline levels  $J_3$  and  $J_4$  and the corresponding spektral resolution.

- Case 1:

Starting from a global model generated with levels  $J_1 = 4$  and  $J_2 = 3$ , a densification in a region with the minimum extension of  $21^\circ \times 30^\circ$  can be implemented. Where  $\Upsilon = 21^\circ$  is obtained by projecting horizontally along the line of  $J_1$  within the blue frame to the right side of the table and  $\Gamma = 30^\circ$  is obtained by vertically projecting the values for  $\Gamma$  within the blue frame of the column of level  $J_2$ . Within the upper right panel, the blue frame encloses the minimum sampling intervals necessary for different  $J_3$  within the region of extend  $\Upsilon = 21^\circ$ . Different sampling intervals are given, mirrored on the yellow diagonal. For the selection of a suitable level  $J_3$ , only the vertically arranged sampling intervals inside the blue box have to be taken into account. In the present case, it is assumed that a sampling of  $\Delta\varphi = 2.3^\circ$  is given. The number is marked with a blue box. By flipping down the upper right panel via the horizontal green axis, a level value of  $J_3 = 3$  is obtained from the present sampling. Consequently, a signal representation with a cutoff frequency of  $n_{max} = 68$  in latitude direction can be modelled within the region. To choose level  $J_4$ , the same procedure is followed via the lower left panel and with a region size of  $\Gamma = 30^\circ$ . It is assumed that there is an average sampling of  $\Delta\lambda = 1.66^\circ$ , marked with a thick blue box. By flipping via the vertical green axis onto the lower right panel, a level of  $J_4 = 4$  can be chosen and a signal representation with a cutoff frequency of  $n_{max} = 96$  in latitude direction can be generated.

- Case 2:

The specific values in the look-up table for the second case are highlighted in dark red. Assuming a global background model generated with the level values  $J_1 = 2$  and  $J_2 = 2$  the minimum region size must be chosen with an extension of  $\Upsilon = 72^\circ$  and  $\Gamma = 60^\circ$  in latitude and longitude, respectively. The values can be found next to and below the table in the upper left panel, along the green axis. With assumed sampling interval  $\Delta\varphi = 4.2^\circ$  and  $\Delta\lambda = 6^\circ$  within the region – both marked with red-coloured boxes in the upper right and lower left panel – the level values  $J_3 = 4$  and  $J_2 = 2$  can be obtained by flipping of the red boxes onto the right lower panel. With these levels, a regional representation of VTEC with a cutoff frequency of  $n_{max} = 40$  in latitude and  $n_{max} = 24$  in longitude direction can be generated.

The look-up table as well as the discussed cases contain only extreme conditions. This means that the spectral resolutions in the lower right panel are calculated only on the basis of the minimum region sizes and the minimum sampling intervals present therein. According to the inequalities (4.54), the densification region can be chosen larger. In the look-up table the region size is given with discrete values for  $\Upsilon$  and  $\Gamma$ . If level values  $J_3$  and  $J_4$  are selected for densification in regions of arbitrary extend with arbitrary sampling, the look-up table is to be used for rough estimation of the necessary values  $\Upsilon$ ,  $\Gamma$ ,  $J_3$  and  $J_4$ .

### Multi-Scale Analysis

With MSA it is also possible to decompose the regional model into smoothed versions and detail signals. In this way, the connection of the different level values in the lower right panel of the look-up table 4.9 can be found for fixed region sizes. Similar to the global model with Eq. (4.45) and by neglecting the time dependency, the regional model (4.52) can be rewritten as

$$f_{J_3, J_4}(\varphi, \lambda) = \phi_{J_3}^T(\varphi) \mathbf{D}_{J_3, J_4} \phi_{J_4}(\lambda), \quad (4.56)$$

with the  $K_{J_3} \times 1$  vector  $\phi_{J_3}(\varphi)$  and the  $K_{J_4} \times 1$  vector  $\phi_{J_4}(\lambda)$  of polynomial B-splines in latitude and longitude direction, respectively, as well as the  $K_{J_3} \times K_{J_4}$  coefficient matrix  $\mathbf{D}_{J_3, J_4}$ .

The 2-D MSR for the regional model (4.52) is given as

$$f_{J_3, J_4}(\varphi, \lambda) = f_{J'_3, J'_4}(\varphi, \lambda) + \sum_{j=1}^J \sum_{\vartheta=1}^3 g_{J_3-j, J_4-j}^{\vartheta}(\varphi, \lambda), \quad (4.57)$$

with  $J'_3 = J_3 - J$ ,  $J'_4 = J_4 - J$  and  $0 < J \leq \min(J_3, J_4)$  (Lyche and Schumaker, 2001; Zeilhofer, 2008). According to Schmidt (2012) and Schmidt et al. (2015a), the low-pass filtered version  $f_{J'_3, J'_4}(\varphi, \lambda)$ , as well as the band-pass filtered detail signals  $g_{J_3-j, J_4-j}^{\vartheta}(\varphi, \lambda)$  are obtained by the relations

$$\begin{aligned} f_{J'_3, J'_4}(\varphi, \lambda) &= \phi_{J'_3}^T(\varphi) \mathbf{D}_{J'_3, J'_4} \phi_{J'_4}(\lambda), \\ g_{j_3-1, j_4-1}^1(\varphi, \lambda) &= \phi_{j_3-1}^T(\varphi) \mathbf{C}_{j_3-1, j_4-1}^1 \psi_{j_4-1}(\lambda), \\ g_{j_3-1, j_4-1}^2(\varphi, \lambda) &= \psi_{j_3-1}^T(\varphi) \mathbf{C}_{j_3-1, j_4-1}^2 \phi_{j_4-1}(\lambda), \\ g_{j_3-1, j_4-1}^3(\varphi, \lambda) &= \psi_{j_3-1}^T(\varphi) \mathbf{C}_{j_3-1, j_4-1}^3 \psi_{j_4-1}(\lambda), \end{aligned} \quad (4.58)$$

wherein  $j_3 = J_3 - j + 1$  and  $j_4 = J_4 - j + 1$  for  $j = 1, \dots, J$ . By means of the two-scale relations

$$\begin{aligned} \phi_{j_3-1}^T(\varphi) &= \phi_{j_3}^T(\varphi) \mathbf{P}_{j_3}, \\ \phi_{j_4-1}^T(\lambda) &= \phi_{j_4}^T(\lambda) \mathbf{P}_{j_4}, \\ \psi_{j_3-1}^T(\varphi) &= \phi_{j_3}^T(\varphi) \mathbf{Q}_{j_3}, \\ \psi_{j_4-1}^T(\lambda) &= \phi_{j_4}^T(\lambda) \mathbf{Q}_{j_4}, \end{aligned} \quad (4.59)$$

the  $K_{j_3-1} \times 1$  and  $K_{j_4-1} \times 1$  scaling vectors  $\phi_{j_3-1}(\varphi)$  and  $\phi_{j_4-1}(\lambda)$  as well as the  $L_{j_3-1} \times 1$  and  $L_{j_4-1} \times 1$  wavelet vectors  $\psi_{j_3-1}(\varphi)$  and  $\psi_{j_4-1}(\lambda)$  can be calculated. The numerical entries of the  $K_{j_3} \times K_{j_3-1}$  and  $K_{j_4} \times K_{j_4-1}$  matrices  $\mathbf{P}_{j_3}$  and  $\mathbf{P}_{j_4}$  as well as for the  $K_{j_3} \times L_{j_3-1}$  and  $K_{j_4} \times L_{j_4-1}$  matrices  $\mathbf{Q}_{j_3}$  and  $\mathbf{Q}_{j_4}$  can be found in Stollnitz et al. (1995b), Lyche and Schumaker (2001) and Zeilhofer (2008). The  $K_{j_3-1} \times K_{j_4-1}$  matrix  $\mathbf{D}_{J_3-1, J_4-1}$  of scaling coefficients as well as the  $K_{j_3-1} \times L_{j_4-1}$  matrix  $\mathbf{C}_{j_3-1, j_4-1}^1$ , the  $L_{j_3-1} \times K_{j_4-1}$  matrix  $\mathbf{C}_{j_3-1, j_4-1}^2$  and the  $L_{j_3-1} \times L_{j_4-1}$  matrix  $\mathbf{C}_{j_3-1, j_4-1}^3$  of wavelet coefficients are calculable via the 2-D downsampling equation

$$\begin{bmatrix} \mathbf{D}_{j_3-1, j_4-1} & \mathbf{C}_{j_3-1, j_4-1}^1 \\ \mathbf{C}_{j_3-1, j_4-1}^2 & \mathbf{C}_{j_3-1, j_4-1}^3 \end{bmatrix} = \begin{bmatrix} \bar{\mathbf{P}}_{j_3} \\ \bar{\mathbf{Q}}_{j_3} \end{bmatrix} \mathbf{D}_{j_3, j_4} \begin{bmatrix} \bar{\mathbf{P}}_{j_4}^T & \bar{\mathbf{Q}}_{j_4}^T \end{bmatrix}. \quad (4.60)$$

The  $K_{j_3-1} \times K_{j_3}$  matrix  $\bar{\mathbf{P}}_{j_3}$  and the  $L_{j_4-1} \times K_{j_4}$  matrix  $\bar{\mathbf{Q}}_{j_3}$  can be similarly calculated as for the global model by (4.50), see Schmidt (2012).

## 4.7 Estimation of Model Parameters

The unknown parameter, i.e. the coefficients  $d_{k_1, k_2}^{J_1, J_2}(t)$  of the global B-spline expansion (4.38), the coefficients  $d_{k_3, k_4}^{J_3, J_4}(t)$  of the regional B-spline expansion (4.52) and additional bias parameters, e.g. the DCBs, which have been derived in Section 4.5.2 can be estimated using an appropriate estimation procedure. In the following a recursive estimator, namely a (KF) is used. Erdogan et al. (2017) proposed the usage of a KF for the estimation of B-spline coefficients for global VTEC modelling. Thereby, the KF allows for the calculation of the coefficients recursively by processing the incoming observations immediately after their acquisition. The procedure is applied to the estimation problems within the first-author publications **P-I** and **P-II**.

The following indented part is taken from **P-II** and is based on Erdogan et al. (2017)<sup>4</sup>:

The Kalman filter (KF, Kalman, 1960) is a sequential estimator which yields the ionospheric parameters for both modelling steps (global and regional). In the KF the input data from the past have not to be stored and the current state is updated as soon as new observations are available (Gelb, 1974). It is an optimal recursive estimator in terms of minimum variance estimation including a time update (prediction step) and a measurement update (correction step); see e.g. Grewal and Andrews (2008), Simon (2006) and Gelb (1974). The approach consists of a linear formulation of the state equations

$$\boldsymbol{\beta}_s = \mathbf{F}_s \boldsymbol{\beta}_{s-1} + \mathbf{w}_{s-1} \quad (4.61)$$

and of the observation equations

$$\mathbf{y}_s + \mathbf{e}_s = \mathbf{A}_s \boldsymbol{\beta}_s. \quad (4.62)$$

In Eq. (4.61),  $\boldsymbol{\beta}_s$  is the  $u \times 1$  vector of unknown series coefficients at time  $t_s$  predicted from the state vector  $\boldsymbol{\beta}_{s-1}$  of the previous time step  $t_{s-1}$  by means of the  $u \times u$  transition matrix  $\mathbf{F}_s$  and the  $u \times 1$  vector  $\mathbf{w}_{s-1}$  of the process noise with  $u$  as the number of unknown series coefficients. Equation (4.62) consists of the  $I_s \times 1$  vector  $\mathbf{y}_s = (y(\mathbf{x}_{i_s}, t_s))$  of observations, the vector  $\mathbf{e}_s = (e(\mathbf{x}_{i_s}, t_s))$  of corresponding measurement errors and  $\mathbf{A}_s$  the corresponding  $I_s \times u$  design matrix. The vectors  $\mathbf{e}_s$  and  $\mathbf{w}_s$  are characterised by the expectation vectors  $E(\mathbf{e}_s) = \mathbf{0}$  and  $E(\mathbf{w}_s) = \mathbf{0}$ , as well as the covariance matrices

$$E(\mathbf{w}_s \mathbf{w}_l^T) = \boldsymbol{\Sigma}_w \delta_{s,l}, \quad E(\mathbf{e}_s \mathbf{e}_l^T) = \boldsymbol{\Sigma}_y \delta_{s,l}, \quad E(\mathbf{w}_s \mathbf{e}_l^T) = \mathbf{0}, \quad (4.63)$$

<sup>4</sup>The numbering of equations, figures and tables does not coincide with the numbering in the publication **P-II** Goss et al. (2020b) but are adapted to this thesis. Spelling and punctuation are corrected in the indented section.

where  $\delta_{s,l}$  is the delta symbol which equals to 1 for  $s = l$  and to 0 for  $s \neq l$ ; see Erdogan et al. (2017) and Goss et al. (2019).

#### 4.7.1 Global Measurement Model of the Kalman Filter

Following Erdogan et al. (2017), the observation equation (4.35) can be rewritten for the systems GPS and GLONASS separately as

$$\begin{aligned} y_{s,\text{glob}}^{GPS}(\mathbf{x}_i, t_s) + \epsilon_{s,L_I}^{GPS} &= \alpha M(z) \cdot VTEC_{\text{glob}}(\mathbf{x}_i, t_s) + b_R^{GPS} + b^{S,GPS} \quad \text{and} \\ y_{s,\text{glob}}^{GLO}(\mathbf{x}_i, t_s) + \epsilon_{s,L_I}^{GLO} &= \alpha M(z) \cdot VTEC_{\text{glob}}(\mathbf{x}_i, t_s) + b_R^{GLO} + b^{S,GLO}, \end{aligned} \quad (4.64)$$

with the frequency dependent factor  $\alpha$  from Eq. (4.32), the zenith angle depending mapping function  $M(z)$  from Eq. (2.4) and the DCBs  $b_R^{GPS}$ ,  $b^{S,GPS}$ ,  $b_R^{GLO}$  and  $b^{S,GLO}$  from Eq. (4.27). Substituting Eq. (4.38) for  $VTEC_{\text{glob}}(\mathbf{x}_i, t_s)$  and rewriting Eq. (4.64) for the  $I_s$  observations given at the time moment  $t_s$ , the system of equations

$$\mathbf{y}_{s,\text{glob}} + \mathbf{e}_{s,\text{glob}} = \mathbf{A}_{s,\text{glob}} \boldsymbol{\beta}_{s,\text{glob}}, \quad (4.65)$$

can be established (Erdogan et al., 2017). The  $I_s \times 1$  observation vector

$$\mathbf{y}_{s,\text{glob}} = \begin{bmatrix} \mathbf{y}_{s,\text{glob}}^{GPS} \\ \mathbf{y}_{s,\text{glob}}^{GLO} \end{bmatrix} \quad (4.66)$$

consists of the sub-vectors  $\mathbf{y}_{s,\text{glob}}^{GPS}$  and  $\mathbf{y}_{s,\text{glob}}^{GLO}$  for the observations from GPS and GLONASS, respectively. The corresponding error vector

$$\mathbf{e}_{s,\text{glob}} = \begin{bmatrix} \mathbf{e}_{s,\text{glob}}^{GPS} \\ \mathbf{e}_{s,\text{glob}}^{GLO} \end{bmatrix} \quad (4.67)$$

is of same size and consists of the respective measurement error vectors  $\mathbf{e}_{s,\text{glob}}^{GPS}$  and  $\mathbf{e}_{s,\text{glob}}^{GLO}$  for GPS and GLONASS, respectively. On the right side of the equal sign in Eq. (4.65) is the design matrix  $\mathbf{A}_{s,\text{glob}}$  and the state vector

$$\boldsymbol{\beta}_{s,\text{glob}} = \begin{bmatrix} \mathbf{d}_s \\ \mathbf{b}_{s,R}^{GPS} \\ \mathbf{b}_s^{S,GPS} \\ \mathbf{b}_{s,R}^{GLO} \\ \mathbf{b}_s^{S,GLO} \end{bmatrix} \quad (4.68)$$

of the unknown model parameters, with the sub-vectors  $\mathbf{d}_s = (d_{k_1, k_2}^{J_1, J_2}(t_s))$  for the model coefficients, as well as the sub-vectors  $\mathbf{b}_{s,R}^{GPS}$ ,  $\mathbf{b}_s^{S,GPS}$ ,  $\mathbf{b}_{s,R}^{GLO}$  and  $\mathbf{b}_s^{S,GLO}$  of the satellites and the receivers DCBs for both GNSS, see Erdogan et al. (2017). Consequently, the design matrix is given as

$$\mathbf{A}_{s,\text{glob}} = \begin{bmatrix} \mathbf{A}_{s,d_{GPS}} & \mathbf{A}_{s,b_R^{GPS}} & \mathbf{A}_{s,b^{S,GPS}} & 0 & 0 \\ \mathbf{A}_{s,d_{GLO}} & 0 & 0 & \mathbf{A}_{s,b_R^{GLO}} & \mathbf{A}_{s,b^{S,GLO}} \end{bmatrix}, \quad (4.69)$$

with the design sub-matrices  $\mathbf{A}_{s,d_{GPS}}$  and  $\mathbf{A}_{s,d_{GLO}}$  in connection to the vector  $\mathbf{d}_s$  and the design sub-matrices  $\mathbf{A}_{s,b^{S,GPS}}$  and  $\mathbf{A}_{s,b_R^{GPS}}$  in connection to the satellite and the receiver DCBs of the GPS system, as well as the  $\mathbf{A}_{s,b^{S,GLO}}$  and  $\mathbf{A}_{s,b_R^{GLO}}$  in connection to the satellite and the receiver DCBs of the GLONASS system.

Since the observations in the sub-vectors  $\mathbf{y}_{s,\text{glob}}^{GPS}$  and  $\mathbf{y}_{s,\text{glob}}^{GLO}$  of Eq. (4.64) are derived from different GNSS, different accuracies for the observations but no correlation between the two systems are

assumed within the parameter estimation. In this regard, individual variance factors  $\sigma_{s,y_{\text{glob}}}^2$  and  $\sigma_{s,y_{\text{glob}}}^2$  are introduced and the covariance matrix of the observations reads

$$\Sigma_{y_{\text{glob}},s} = \begin{bmatrix} \sigma_{s,y_{\text{glob}}}^2 \mathbf{P}_{s,y_{\text{glob}}}^{-1} & 0 \\ 0 & \sigma_{s,y_{\text{glob}}}^2 \mathbf{P}_{s,y_{\text{glob}}}^{-1} \end{bmatrix}, \quad (4.70)$$

with the given positive definite weight matrices  $\mathbf{P}_{s,y_{\text{glob}}}^{GPS}$  and  $\mathbf{P}_{s,y_{\text{glob}}}^{GLO}$ . The weighting allows the estimation of the unknown to be more sensitive to observations of higher quality, such as observations with a higher elevation angle; see for example Wang et al. (2016b) and Erdogan et al. (2017).

### 4.7.2 Regional Measurement Model of the Kalman Filter

The measurement model for the regional modelling step is structured similar to the global measurement model, thus, Eq. (4.36) can be rewritten for GPS and GLONASS as

$$\begin{aligned} y_{s,\text{reg}}^{GPS}(\mathbf{x}_i, t_s) + \epsilon_{s,L_I}^{GPS} &= \alpha M(z) \cdot VTEC_{\text{reg}}(\mathbf{x}_i, t_s) + b_R^{GPS} + b^{S,GPS} \quad \text{and} \\ y_{s,\text{reg}}^{GLO}(\mathbf{x}_i, t_s) + \epsilon_{s,L_I}^{GLO} &= \alpha M(z) \cdot VTEC_{\text{reg}}(\mathbf{x}_i, t_s) + b_R^{GLO} + b^{S,GLO}. \end{aligned} \quad (4.71)$$

Substituting Eq. (4.52) for  $VTEC_{\text{reg}}(\mathbf{x}_i, t_s)$  and rewriting Eq. (4.71) for a total number  $I_s$  of observations provided by the stations of the station list  $\mathcal{D}_2$  the equation system

$$\mathbf{y}_{s,\text{reg}} + \mathbf{e}_{s,\text{reg}} = \mathbf{A}_{s,\text{reg}} \boldsymbol{\beta}_{s,\text{reg}}, \quad (4.72)$$

for the regional model can be established (adapted from Erdogan et al. (2017)). Therein, the  $I_s \times 1$  observation vector

$$\mathbf{y}_{s,\text{reg}} = \begin{bmatrix} y_{\text{reg}}^{GPS}(\mathbf{x}_1, t_s) - VTEC_{\text{glob}}(\mathbf{x}_1, t_s) - b^{S,GPS} \\ y_{\text{reg}}^{GPS}(\mathbf{x}_2, t_s) - VTEC_{\text{glob}}(\mathbf{x}_2, t_s) - b^{S,GPS} \\ \vdots \\ y_{\text{reg}}^{GLO}(\mathbf{x}_{I_s}, t_s) - VTEC_{\text{glob}}(\mathbf{x}_{I_s}, t_s) - b^{S,GLO} \end{bmatrix} \quad (4.73)$$

consists of the differences between the observations and the global model  $VTEC_{\text{glob}}(\mathbf{x}_{i_s}, t_s)$  at the position  $\mathbf{x}_{i_s}$  given at the time  $t_s$ . In the sense of the TSM, the global background model is generated in the first step, as shown in Fig. 4.7. The vector  $\mathbf{e}_{s,\text{reg}}$  is defined as the vector  $\mathbf{e}_{s,\text{glob}}$  from Eq. (4.67). The state vector

$$\boldsymbol{\beta}_{s,\text{reg}} = \begin{bmatrix} \mathbf{d}_s \\ \mathbf{b}_{s,R}^{GPS} \\ \mathbf{b}_{s,R}^{GLO} \end{bmatrix}. \quad (4.74)$$

consists of the sub-vector  $\mathbf{d}_s = (d_{k_3,k_4}^{J_3,J_4}(t_s))$  of B-spline coefficients, as well as the sub-vectors  $\mathbf{b}_{s,R}^{GPS}$  and  $\mathbf{b}_{s,R}^{GLO}$  of the receiver DCBs for those receiver stations which are assigned to  $\mathcal{D}_2$ . The satellites DCBs are considered in (4.73), as they are already estimated with the global model and thus are given. Consequently, the design matrix  $\mathbf{A}_{s,\text{reg}}$  is constructed with the sub-matrices  $\mathbf{A}_{s,d_{GPS}}$  and  $\mathbf{A}_{s,d_{GLO}}$  in connection to the vector  $\mathbf{d}_s$  and the sub-matrices  $\mathbf{A}_{s,b_R^{GPS}}$  and  $\mathbf{A}_{s,b_R^{GLO}}$  in connection to the receiver DCB and reads

$$\mathbf{A}_{s,\text{reg}} = \begin{bmatrix} \mathbf{A}_{s,d_{GPS}} & \mathbf{A}_{s,b_R^{GPS}} & 0 \\ \mathbf{A}_{s,d_{GLO}} & 0 & \mathbf{A}_{s,b_R^{GLO}} \end{bmatrix}. \quad (4.75)$$

The measurement co-variance matrix  $\Sigma_{y_{\text{reg}},s}$  for the observations of the stations assigned to the data set  $\mathcal{D}_2$  is set up similarly as the measurement co-variance matrix  $\Sigma_{y_{\text{glob}},s}$  for the global model with individual variance factors and weighting depending on the elevation of separate observations. It reads

$$\Sigma_{y_{\text{reg}},s} = \begin{bmatrix} \sigma_{s,y_{\text{reg}}}^{GPS} \mathbf{P}_{s,y_{\text{reg}}}^{-1} & 0 \\ 0 & \sigma_{s,y_{\text{reg}}}^{GLO} \mathbf{P}_{s,y_{\text{reg}}}^{-1} \end{bmatrix}. \quad (4.76)$$

A more sophisticated weighting of the observations can be achieved by considering the arc length of the satellite receiver connection (Erdogan et al., 2020), or by considering the modelled accuracies of the global background model.

### 4.7.3 Kalman Filter

The application of the KF to the observation equations (4.65) and (4.72) with a random walk originates from Erdogan et al. (2017). The KF is applied within the first-author publications **P-I** and **P-II** to calculate the unknown model coefficients.

The following indented versions are taken from the publication **P-II** and based on Erdogan et al. (2017).<sup>5</sup>

The solution of the estimation problem as defined by the Eqs. (4.61) and (4.62) can be found by sequential application of the prediction step and the correction step. Hence, the state equation (4.61) is used to obtain the predicted ionospheric target parameter vector  $\beta_s^-$  and its covariance matrix  $\Sigma_{\beta,s}$  as

$$\beta_s^- = \mathbf{F}_s \hat{\beta}_{s-1} \text{ and} \quad (4.77)$$

$$\Sigma_{\beta,s}^- = \mathbf{F}_s \hat{\Sigma}_{\beta,s-1} \mathbf{F}_s^T + \Sigma_w, \quad (4.78)$$

for details see Erdogan et al. (2017). Once the prediction of the state vector from time  $t_{s-1}$  to time  $t_s$  is given, the predicted state vector and its covariance matrix are updated with the new allocated measurements at time  $t_s$  by

$$\hat{\beta}_s = \beta_s^- + \mathbf{K}_s (\mathbf{y}_s - \mathbf{A}_s \beta_s^-) \quad (4.79)$$

and

$$\hat{\Sigma}_{\beta,s} = (\mathbf{I} - \mathbf{K}_s \mathbf{A}_s) \Sigma_{\beta,s}^-, \quad (4.80)$$

where  $\hat{\beta}_s$  and  $\hat{\Sigma}_{\beta,s}$  are the updated state vector and its covariance matrix. Thereby, the so-called Kalman gain matrix

$$\mathbf{K}_s = \Sigma_{\beta,s}^- \mathbf{A}_s^T (\mathbf{A}_s \Sigma_{\beta,s}^- \mathbf{A}_s^T + \Sigma_y)^{-1} \quad (4.81)$$

behaves like a weighting matrix between the new measurements and the predicted state vector.

### 4.7.4 Global and Regional Prediction Model

VTEC contains temporally and spatially variable structures and thus requires an appropriate model for representing the temporal propagation between consecutive time steps  $t_{s-1}$  and  $t_s$  in Eq. (4.61). The strongest spatio-temporal variations originate from the Earth's rotation and follow the geomagnetic equator. The B-spline coefficients, due to their localising feature, can be assigned to a specific region, which results in an imitation of the VTEC structure (Erdogan et al., 2020).

---

<sup>5</sup>The numbering of equations, figures and tables does not coincide with the numbering in the publication **P-II** but are adapted to this thesis. Spelling and punctuation are corrected in the indented section.



Hence, they reflect the energy of the signal and allow for a physical interpretation. Furthermore, the global model (4.38) is set up according to Section 4.1 in the Sun-fixed geomagnetic coordinate system, which results in much slower variations of the B-spline coefficients in time. Moreover, the satellite and receiver DCBs vary very slowly between the two discrete time steps  $t_s$  and  $t_{s+1}$ , and thus a *random walk* procedure with the transition matrix  $\mathbf{F}_s = \mathbf{I}$  is chosen for the prediction model according to Erdogan et al. (2017, 2020).

The regional model (4.52) is set up in the Earth-fixed geographical coordinate system. Although VTEC varies significantly faster in this coordinate system, the main part of the VTEC trend is represented by the background model. The estimated differences of  $\Delta VTEC_{\text{reg}}$  exhibit much slower time variations compared to the background values  $VTEC_{\text{glob}}$ . Additionally, the phase biases in the unknown state vector are constant during phase-continuous arcs. Consequently, the random walk approach can also be considered as the prediction model for the unknown target parameters of the regional model.

The definition of the prediction model, including an adapted process noise depending on the signal energy which is different between the global and the regional modelling steps of the TSM, the number of observations supporting each coefficient, i.e. tensor product, as well as a consideration of the spatial variations of surrounding coefficients, is considered in the KF within this thesis. This adaptation was developed by Erdogan et al. (2020) and can be found therein.

#### 4.7.5 Two-Step Model Outputs

Applying the KF from Eqs. (4.77) to (4.80) to the observation equation (4.65) with observations of the global station set  $\mathcal{D}_1$  yields the estimations  $\hat{\beta}_{s,\text{glob}}$  and  $\hat{\Sigma}_{\beta,s,\text{glob}}$  for the global model. In Fig. 4.7, the estimates are shown in the red-framed box as output of the KF of the global model. These estimates allow for the evaluation of the  $V \times 1$  vector

$$\hat{\mathbf{f}}_{s,\text{glob}} = \bar{\mathbf{A}}_{s,\text{glob}} \hat{\beta}_{s,\text{glob}} \quad (4.82)$$

and the  $V \times V$  matrix

$$\hat{\Sigma}_{s,\text{glob}} = \bar{\mathbf{A}}_{s,\text{glob}} \hat{\Sigma}_{\beta,s,\text{glob}} \bar{\mathbf{A}}_{s,\text{glob}}^T. \quad (4.83)$$

The vector  $\hat{\mathbf{f}}_{s,\text{glob}}$  consists of the estimated values  $\widehat{VTEC}_{\text{glob}}(\varphi_v, \lambda_v, t_s)$  at  $v = 1, \dots, V$  arbitrary points  $P(\varphi_v, \lambda_v)$ . The corresponding standard deviations are determined by

$$\hat{\sigma}_{VTEC,\text{glob}}(\varphi_v, \lambda_v, t_s) = \sqrt{\hat{\sigma}_{s,\text{glob}}^2(\varphi_v, \lambda_v)}, \quad (4.84)$$

where the values  $\hat{\sigma}_{s,\text{glob}}^2(\varphi_v, \lambda_v)$  are given as the diagonal elements of the estimated covariance matrix  $\hat{\Sigma}_{s,\text{glob}}$ . The matrix  $\bar{\mathbf{A}}_{s,\text{glob}}$  in Eqs. (4.82) and (4.83) is set up in a similar way as the sub-matrix  $\mathbf{A}_{s,dGPS}$  or  $\mathbf{A}_{s,dGLO}$  in Eq. (4.69). The model results from Eqs. (4.82) to (4.84) are shown in the flowchart in Fig. 4.7 in the red box and are the final result of the global model.

By applying the KF to the regional observation equation (4.72) with observations from stations of the set  $\mathcal{D}_2$ , the estimations  $\hat{\beta}_{s,\text{reg}}$  and  $\hat{\Sigma}_{\beta,s,\text{reg}}$  are established. These are represented in the flowchart in Fig. 4.7 in the green-framed box as output of the KF for the regional densification model. The  $w = 1, \dots, W$  values  $\Delta VTEC_{\text{reg}}(\varphi_w, \lambda_w, t_s)$  at the points  $P(\varphi_w, \lambda_w)$  within the region  $\Delta\Omega$  are evaluated by

$$\hat{\mathbf{f}}_{s,\text{reg}} = \bar{\mathbf{A}}_{s,\text{reg}} \hat{\beta}_{s,\text{reg}}. \quad (4.85)$$

Therein, the  $W \times 1$  vector  $\hat{\mathbf{f}}_{s,\text{reg}}$  consists of the regional estimates  $\Delta VTEC_{\text{reg}}(\varphi_w, \lambda_w, t_s)$ . The corresponding  $W \times W$  covariance matrix reads

$$\hat{\Sigma}_{s,\text{reg}} = \bar{\mathbf{A}}_{s,\text{reg}} \hat{\Sigma}_{\beta,s,\text{reg}} \bar{\mathbf{A}}_{s,\text{reg}}^T \quad (4.86)$$

and allows for determining the corresponding standard deviation as

$$\hat{\sigma}_{\Delta VTEC, \text{reg}}(\varphi_w, \lambda_w, t_s) = \sqrt{\hat{\sigma}_{s, \text{reg}}^2(\varphi_w, \lambda_w)} , \quad (4.87)$$

with  $\hat{\sigma}_{s, \text{reg}}^2(\varphi_w, \lambda_w)$  given by the diagonal elements of  $\hat{\Sigma}_{s, \text{reg}}$ . The matrix  $\bar{\mathbf{A}}_{s, \text{reg}}$  is set up similar to  $\bar{\mathbf{A}}_{s, d_{GPS}}$  or  $\bar{\mathbf{A}}_{s, d_{GLO}}$  from Eq. (4.75). The evaluated model results from the Eqs. (4.85) to (4.87) are the intermediate result of the TSM. These are represented in the green box in Fig. 4.7 as output of the regional model.

Assuming that the model parts of the TSM in Eq. (4.37) are uncorrelated and that the coordinates coincide, i.e. for latitude  $\varphi = \varphi_v = \varphi_w$  and for longitude  $\lambda = \lambda_v = \lambda_w$ , the total VTEC within the region  $\Delta\Omega$  can be calculated as

$$\widehat{VTEC}_{\text{reg}}(\varphi, \lambda, t_s) = \widehat{VTEC}_{\text{glob}}(\varphi, \lambda, t_s) + \Delta\widehat{VTEC}_{\text{reg}}(\varphi, \lambda, t_s) . \quad (4.88)$$

Similarly, the standard deviation is established as

$$\hat{\sigma}_{VTEC, \text{reg}}(\varphi, \lambda, t_s) = \sqrt{\hat{\sigma}_{s, \text{reg}}^2(\varphi, \lambda) + \hat{\sigma}_{s, \text{glob}}^2(\varphi, \lambda)} . \quad (4.89)$$

The final result of the TSM is shown in Fig. 4.7 on the right in the yellow box as the combination of the results of the KF for the global and the regional model.

## 5 Ionosphere Products and Validation

The parameterisation approaches based on B-splines, which have been described in Chapter 4 and in particular in the Section 4.6 allow the generation of global and regional VTEC products. For the dissemination of these VTEC products, which are to be used for positioning and navigation, the estimates must be provided by means of suitable data formats. Therefore, the products are divided into different product types as described below, which can be provided using different data formats. Which of the data formats are suitable for a particular product type is described below on the basis of the VTEC products generated in the publications **P-I**, **P-II** and **P-III**.

### 5.1 Data Types and Products

The estimated coefficients from Section 4.7.3 as well as VTEC values evaluated by means of Eqs. (4.82) to (4.89) in Section 4.7.5, determine the two different product types:

#### *Product Type 1:*

Estimated series coefficients, i.e. the vector  $\hat{\beta}_{s,\text{glob}}$  comprising the coefficients  $\hat{\mathbf{d}}_s = (d_{k_1,k_2}^{J_1,J_2}(t_s))$  of the global B-spline series expansion estimated by the KF, in Section 4.7.3 as well as the corresponding estimated covariance information in  $\hat{\Sigma}_{\beta,s,\text{glob}}$ . With given coefficients, users can evaluate the VTEC information for any arbitrary positions using a suitable converter.

#### *Product Type 2:*

Evaluated values  $\widehat{VTEC}(\varphi, \lambda, t_s)$ , as well as their corresponding standard deviations  $\hat{\sigma}_{VTEC}(\varphi, \lambda, t_s)$  on regular grids with output sampling  $\Delta\Phi$  in latitude direction and  $\Delta\Lambda$  in longitude direction.

The different product types are described with examples in the following sections. The examples have been calculated in the frame of the publications **P-I** and **P-II** for a time period in March 2015. As input data serve the observations of GPS and GLONASS, which are provided by the GNSS stations of the station lists  $\mathcal{D}_1$  and  $\mathcal{D}_2$ . In the context of the TSM, the regional model is used for the densification of the global model over Europe. The specific region is indicated with the blue box in 5.1 b).

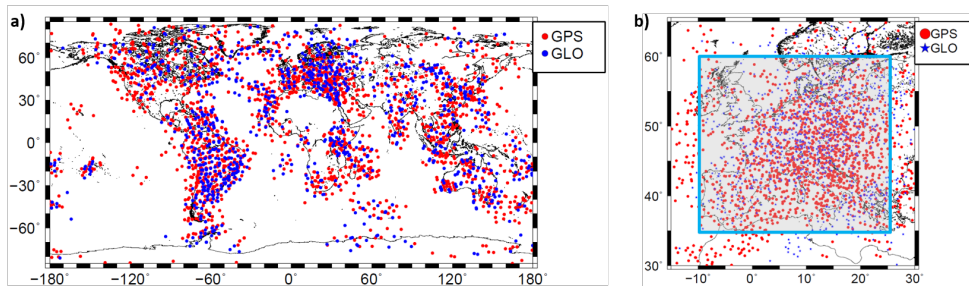


Figure 5.1: Distribution of observations provided by the stations of set  $\mathcal{D}_1$  in a) and provided by the stations of set  $\mathcal{D}_2$  in b) for 17 March 2015 at 12:00 UT.

### 5.1.1 Ionosphere Products Type 1

In the context of the TSM, the *Product Type 1* comprises the estimated coefficients of the global and the regional B-spline series expansion. These products are represented in the processing chain in Fig. 4.7 with the boxes, which are framed in red and green for the global and the regional model, respectively. To distinguish the *Product Type 1* for both model steps of the TSM, *Product Types 1a* and *1b* are defined.

#### Global Ionosphere Products Type 1a:

The *Product Type 1a* comprises the set of estimated coefficients

$$\hat{d}_{k_1, k_2}^{J_1, J_2}(t_s) \big|_{k_1=0, \dots, K_{J_1}-1, k_2=0, \dots, K_{J_2}-1} \quad (5.1)$$

given as elements of the vector  $\hat{\beta}_{s, \text{glob}}$  from Eq. (4.79), for the time  $t_s$  and for the chosen level values  $J_1$  and  $J_2$ . The corresponding standard deviations

$$\hat{\sigma}_{d; k_1, k_2}^{J_1, J_2}(t_s) \big|_{k_1=0, \dots, K_{J_1}-1, k_2=0, \dots, K_{J_2}-1} \quad (5.2)$$

of the coefficients are given as diagonal elements of the matrix  $\hat{\Sigma}_{\beta, s, \text{glob}}$  from Eq. (4.80). Since the B-splines are localising basis functions, the estimated coefficients (5.1) and the corresponding estimated standard deviations (5.2) can be assigned to spatial positions using the shift parameters  $k_1$  and  $k_2$ . Taking into account the different opportunities for the definition of appropriate level values  $J_1$  and  $J_2$  from Section 4.6.1, lower levels can be generated by applying the pyramid algorithm as defined in Eq. (4.49). A given model of level  $J_1$  and  $J_2$  with estimated coefficients (5.1) as well as their standard deviations (5.2) can be decomposed to a model of lower levels. Consequently, further sub-products of *Product Type 1a* with levels  $J'_1 \leq J_1$  and  $J'_2 \leq J_2$  as

$$\hat{d}_{k_1, k_2}^{J'_1, J'_2}(t_s) \big|_{k_1=0, \dots, K_{J'_1}-1, k_2=0, \dots, K_{J'_2}-1} \quad (5.3)$$

and

$$\hat{\sigma}_{d; k_1, k_2}^{J'_1, J'_2}(t_s) \big|_{k_1=0, \dots, K_{J'_1}-1, k_2=0, \dots, K_{J'_2}-1} \quad (5.4)$$

can be defined. The global modelling procedure and the MSA are subject to the publication **P-I**. Figure 5.2 shows the coefficients of  $\hat{d}_{k_1, k_2}^{J_1, J_2}(t_s)$  and standard deviations  $\hat{\sigma}_{d; k_1, k_2}^{J_1, J_2}(t_s)$  as well as the coefficients  $\hat{d}_{k_1, k_2}^{J'_1, J'_2}(t_s)$  and standard deviations  $\hat{\sigma}_{d; k_1, k_2}^{J'_1, J'_2}(t_s)$  at their geographical position, which have been estimated in **P-I**. The initial model is calculated with levels  $J_1 = 5$  and  $J_2 = 3$  and its coefficients and standard deviations are represented in Fig. 5.2 a) and b), whereas the smoothed versions are of level  $J'_1 = 4$  and  $J'_2 = 3$  and represented in c) and d). The initial product based on the level values  $J_1 = 5$  and  $J_2 = 3$  can be referred to as high-resolution product since finer structures can be represented by smaller areas which are covered by the coefficients, see Fig. 5.2 a). Since the two products differ only in the level  $J_1$  for the latitude direction, the number of pixels in latitude direction is different. In the upper panels, there are  $K_{J_1} = 34$  pixels distributed along the meridians and  $K_{J_2} = 24$  pixels distributed along the longitude. In panels c) and d), the number of latitude dependent pixels is decreased to  $K_{J'_1} = 18$ . Consequently, the width of the pixels in latitude direction is narrower in panels a) and b) than in c) and d), which means that finer structures can be represented. Hence, a difference in the spectral resolution is generated by applying the MSA and the cutoff frequency is decreased from  $n_{\text{max}} = 33$  for  $J_1 = 5$  to  $n_{\text{max}} = 17$  for  $J'_1 = 4$ , cf. Tab. 4.2. Since the represented coefficients – due to their localising feature – reflect the energy of the signal and thus imitate the structure of the VTEC as described in Section 4.7.4, the difference in spectral resolution in latitude direction can be seen.

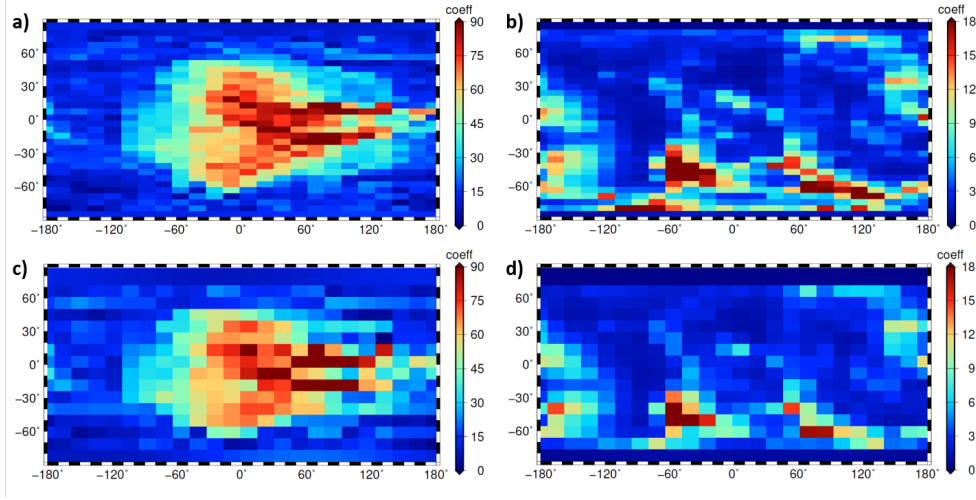


Figure 5.2: *Product Type 1a*: Estimated coefficients and standard deviations of the B-spline series expansion for 17 March 2015 at 12:00 UT. Panels a) and b) show the high-resolution product generated with level values  $J_1 = 5$  and  $J_2 = 3$  and panels c) and d) show its smoothed version of levels  $J'_1 = 4$  and  $J_2 = 3$ .

### Regional Ionosphere Products Type 1b

The *Product Type 1b* contains the estimates of the regional densification model. The set of estimated coefficients

$$\hat{d}_{k_3, k_4}^{J_3, J_4}(t_s) \big|_{k_3=0, \dots, K_{J_3}-1, k_4=0, \dots, K_{J_4}-1} \quad (5.5)$$

in the vector  $\hat{\beta}_{s, \text{reg}}$ , as well as the corresponding standard deviations

$$\hat{\sigma}_{d; k_3, k_4}^{J_3, J_4}(t_s) \big|_{k_3=0, \dots, K_{J_3}-1, k_4=0, \dots, K_{J_4}-1} \quad (5.6)$$

derivable from the diagonal of the estimated covariance matrix  $\hat{\Sigma}_{\beta, s, \text{reg}}$  in Eq. (5.6) define the *Product Type 1b*. Using the pyramid algorithm (4.60), it is possible to create further sub-products from the regional model with levels  $J'_3 \leq J_3$  and  $J'_4 \leq J_4$ , as well as the corresponding detail signals. The sub-products of *Product Type 1b* consist of the coefficients

$$\hat{d}_{k_3, k_4}^{J'_3, J'_4}(t_s) \big|_{k_3=0, \dots, K_{J'_3}-1, k_4=0, \dots, K_{J'_4}-1} \quad (5.7)$$

as well as the corresponding standard deviations

$$\hat{\sigma}_{d; k_3, k_4}^{J'_3, J'_4}(t_s) \big|_{k_3=0, \dots, K_{J'_3}-1, k_4=0, \dots, K_{J'_4}-1} . \quad (5.8)$$

Since the *Product Type 1b* is the result of the second step of the TSM, which is applied to the modelling of the differences between the global model and the observations provided by the stations assigned to station list  $D_2$ , the *Product Type 1a* is additionally required to determine the absolute VTEC information within the region. The generation of the *Product Type 1b* is subject to the publication **P-II**. Figure 5.3 shows the coefficients  $\hat{d}_{k_3, k_4}^{J_3, J_4}(t_s)$  as well as the coefficients  $\hat{d}_{k_3, k_4}^{J'_3, J'_4}(t_s)$  for  $\Delta VTEC$  in panels a) and c), respectively. The corresponding standard deviations  $\hat{\sigma}_{d; k_3, k_4}^{J_3, J_4}(t_s)$  and  $\hat{\sigma}_{d; k_3, k_4}^{J'_3, J'_4}(t_s)$  are shown in panels b) and c). The coefficients and their standard deviations have been estimated as the second step of the TSM for 17 March 2015 at 12:00 UT.

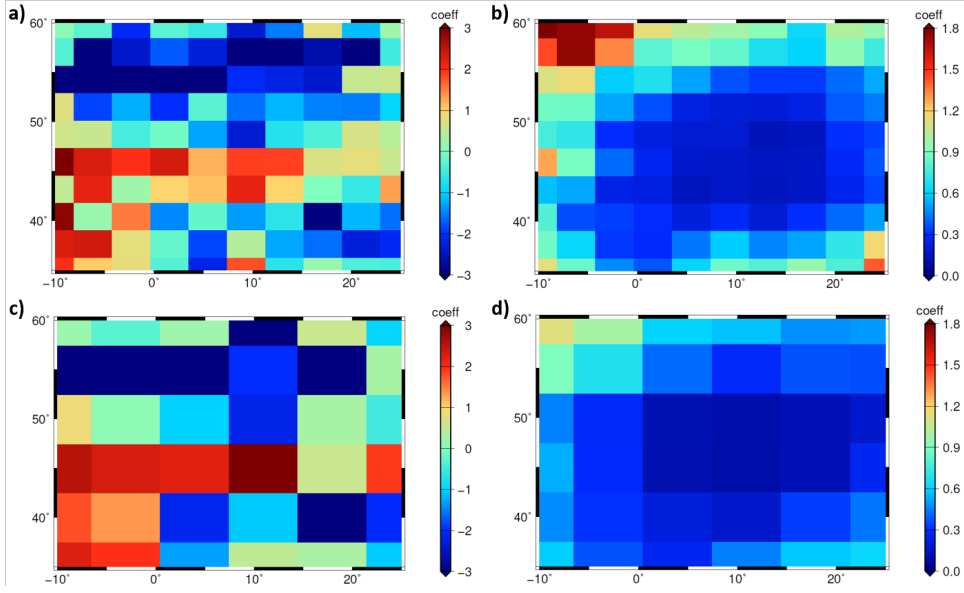


Figure 5.3: *Product Type 1b*: Estimated coefficients of the regional B-spline series expansion for  $\Delta VTEC$  for 17 March 2015 at 12:00 UT. In a) the B-spline coefficients and in b) the corresponding standard deviations for a B-spline expansion of level  $J_3 = 3$  and  $J_4 = 3$  are shown. c) and d) show the smoothed version of level  $J'_3 = 2$  and  $J'_4 = 2$ .

For this particular example, the global background values for VTEC are obtained from a global B-spline expansion with the values  $J_1 = 4$  and  $J_2 = 3$ , which allows a densification into regions with a minimum expansion of  $\Upsilon = 21^\circ$  in latitude and  $\Gamma = 30^\circ$  in longitude direction in order to satisfy the inequalities (4.54). Given the mean sampling intervals  $\Delta\varphi = 2.5^\circ$  and  $\Delta\lambda = 2.5^\circ$  of the observations within the blue box of size  $\Upsilon = 25^\circ$  and  $\Gamma = 35^\circ$  (cf. Fig. 5.1b)) and which are provided by the stations assigned to set  $\mathcal{D}_2$ , the level values  $J_3 = 3$  and  $J_4 = 3$  can be obtained from the look-up table in Fig. 4.9. The corresponding regional coefficients estimated by means of a regional B-spline series expansion are shown in the top panels of Fig. 5.3. By substituting the values for  $\Upsilon$  and  $\Gamma$  and the B-spline levels  $J_3 = 3$  and  $J_4 = 3$  into the inequalities (4.55), the cutoff frequencies for the regional model in TSM are calculated to  $n_{max} = 64$  in latitude and  $n_{max} = 47$  in longitude direction. By applying the pyramid algorithm Eq. (4.60) to the coefficients in the top panels of Fig. 5.3, their smoothed versions with level values  $J'_3 = 2$  and  $J'_4 = 2$  are generated and represented in the bottom panels. By means of the inequalities (4.55) the cutoff frequencies for the smoothed version are calculable with  $n_{max} = 36$  in latitude and  $n_{max} = 25$  in longitude.

### 5.1.2 Ionosphere Products Type 2

The *Product Type 2* comprises products which are given as evaluated VTEC values at points  $P(\varphi_l, \lambda_r)$  of a regular grid with  $l = 1, \dots, L$  and  $r = 1, \dots, R$ . Three sub-types of *Product Type 2* are generated within the TSM, as described in Section 4.7.5. The three products are represented with boxes in different colours in the processing chain in Fig. 4.7 and will be described in the following section.

#### Global Ionosphere Products Type 2a

The *Product Type 2a* comprises the estimated values  $\widehat{VTEC}_{\text{glob}}(\varphi_l, \lambda_r, t_s)$ , as well as the corresponding estimated standard deviations  $\widehat{\sigma}_{VTEC_{\text{glob}}}(\varphi_l, \lambda_r, t_s)$ , which are evaluated by means of

Eqs. (4.82) and (4.84), respectively. The output sampling intervals  $\Delta\Phi$  of the grid points in the direction of the latitude and  $\Delta\Lambda$  in the direction of the longitude can be selected arbitrarily. The coordinates of the grid points  $P(\varphi_l, \lambda_r)$  lie within the intervals  $\varphi_l \in [-90^\circ, 90^\circ]$  and  $\lambda_r \in [0^\circ, 360^\circ)$  and are calculated by  $\varphi_l = -90^\circ + (l-1) \cdot \Delta\Phi$  and  $\lambda_r = 0^\circ + (r-1) \cdot \Delta\Lambda$ . Since the *Product Type 2a* is determined from *Product Type 1a* and its sub-products (cf. Fig. 5.2), one high-resolution version and several smoothed versions of *Product Type 2a* according to the MSA from Section 4.6.1 can be evaluated. The products 2a represented in Fig. 5.4 show the VTEC maps, as well

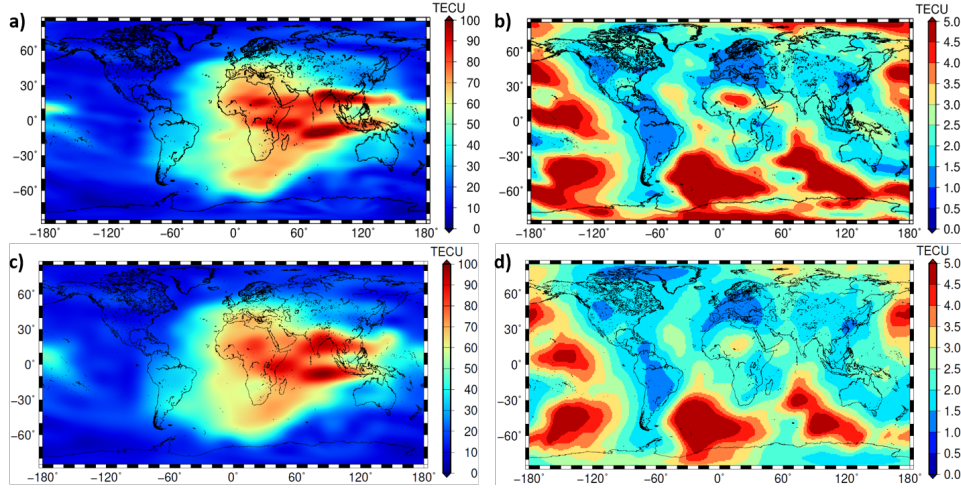


Figure 5.4: *Product Type 2a*: Estimated values of  $\widehat{VTEC}_{\text{glob}}(\varphi_l, \lambda_r, t_s)$  in panels a) and c) and  $\widehat{\sigma}_{VTEC_{\text{glob}}}(\varphi_l, \lambda_r, t_s)$  in b) and d), for 17 March 2015 at 12:00 UT. The values are given on a grid with sampling intervals of  $\Delta\Phi = 2.5^\circ$  and  $\Delta\Lambda = 5^\circ$ .

as the corresponding standard deviation maps for 17 March 2015 at 12:00 UT. Panels a) and b) show the VTEC map and the corresponding standard deviation, respectively, which are evaluated from a B-spline model with level values  $J_1 = 5$  and  $J_2 = 3$ . In panels c) and d) their smoothed versions are represented, which corresponds to level values  $J'_1 = 4$  and  $J'_2 = J_2 = 3$ . Similar to Fig. 5.2, the differences of the spectral resolution in latitude direction between the panels a) and c) can be seen. The high-resolution map of VTEC in panel a) shows finer structures and can represent the dual peak around the equator more distinctly than the VTEC map in c). The map in a) is modelled with a cutoff frequency of  $n_{\text{max}} = 33$  in latitude direction, whereas the map in c) can be referred to a cutoff frequency of  $n_{\text{max}} = 17$ . Panels b) and d) represent the standard deviations, which are generally larger, where no or only a few observations from the stations in set  $\mathcal{D}_1$  are provided. As can be seen within the oceanic regions, the standard deviations reach values of 4-5 TECU, whereas over the continents smaller values of 1-2 TECU are provided, since the observations are denser (cf. Fig. 5.1 a)).

### Regional Ionosphere Products Type 2b

The *Product Type 2b* is determined from *Product Type 1b* by evaluating the Eqs. (4.85) and (4.87). The estimated values  $\widehat{\Delta VTEC}_{\text{reg}}(\varphi_l, \lambda_r, t_s)$  as well as the corresponding standard deviations  $\widehat{\sigma}_{\Delta VTEC_{\text{reg}}}(\varphi_l, \lambda_r, t_s)$  are evaluated at the grid points  $\varphi_l = \varphi_{\text{min}} + (l-1) \cdot \Delta\Phi$  for latitude and  $\lambda_r = \lambda_{\text{min}} + (l-1) \cdot \Delta\Lambda$  for longitude, where  $\varphi_{\text{min}}$  is the southern boundary value of latitude in the interval  $\varphi_l \in [\varphi_{\text{min}}, \varphi_{\text{max}}]$  of length  $\Upsilon$  and  $\lambda_{\text{min}}$  is the western boundary of the interval  $\lambda_r \in [\lambda_{\text{min}}, \lambda_{\text{max}}]$  of the length of  $\Gamma$ . The maps of *Product Type 2b* are shown in Fig. 5.5. Panels a) and b) show the evaluated values of  $\Delta VTEC$ , as the differences between the global model and the observations from the station list  $\mathcal{D}_2$  as well as the corresponding standard deviations. Panels c)



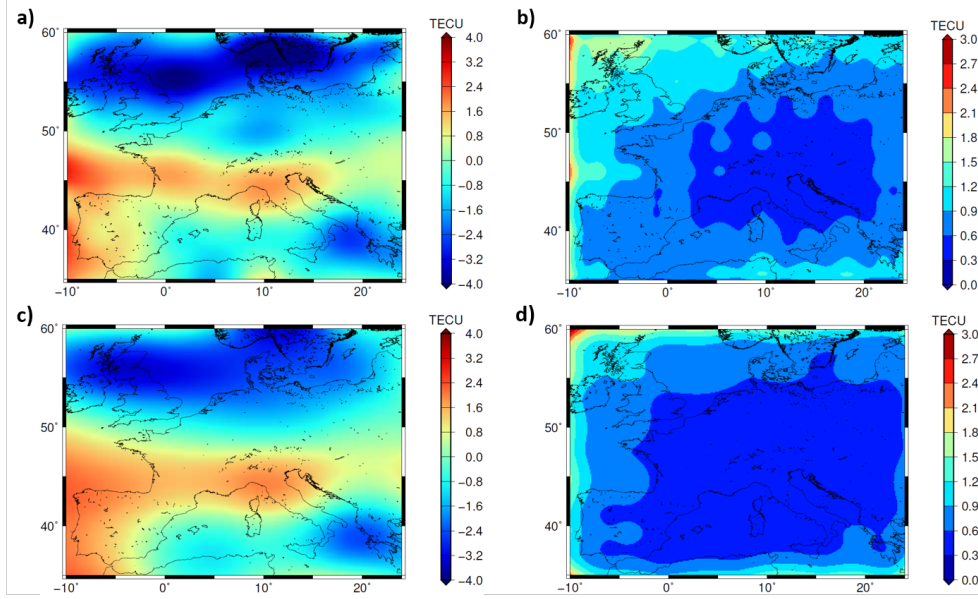


Figure 5.5: *Product Type 2b*: Values of  $\widehat{\Delta VTEC}_{\text{reg}}$  in a) and c) and the corresponding standard deviation  $\widehat{\sigma}_{\Delta VTEC_{\text{reg}}}$  in b) and d).

and d) show the corresponding smoothed versions, generated by the pyramid algorithm (4.60). For a continuous representation of the signal, a bi-linear interpolation as described in Section 5.2.1 is applied. The represented  $\Delta VTEC$  is the intermediate result of the TSM. It was generated in the context of the publication **P-II** with the B-spline levels  $J_3 = 3$  and  $J_4 = 3$ , for 17 March 2015 at 12:00 UT and can be seen as a complementary part to *Product Type 2a* and Fig. 5.4 c) for the region over Europe with  $\Upsilon \times \Gamma$  and  $[35^\circ, 60^\circ] \times [-10^\circ, 25^\circ]$ .

### Regional Ionosphere Products Type 2c

The final product of the TSM is the *Product Type 2c* as the combination of the *Product Type 2a* and the *Product Type 2b* by means of Eqs. (4.88) and (4.89). The maps represented in Fig. 5.6

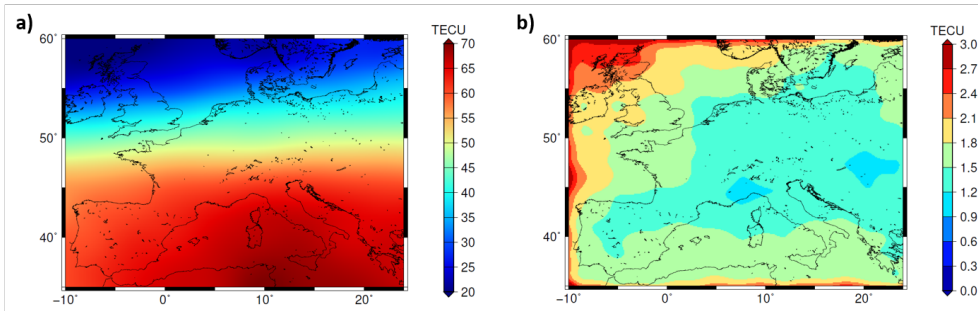


Figure 5.6: *Product Type 2c*: Evaluated values  $\widehat{VTEC}_{\text{reg}}(\varphi_l, \lambda_r, t_s)$  in a) and the corresponding standard deviations  $\widehat{\sigma}_{VTEC_{\text{reg}}}(\varphi_l, \lambda_r, t_s)$  in panel b), as the final map of the TSM.

show the final values  $\widehat{VTEC}_{\text{reg}}(\varphi_l, \lambda_r, t_s)$  in panel a) and the corresponding standard deviations  $\widehat{\sigma}_{VTEC_{\text{reg}}}(\varphi_l, \lambda_r, t_s)$  in panel b). These maps are the final results of the TSM (4.88), which are subject to the publication **P-II** and have been created for 17 March 2015 at 12:00 UT. Due to the absolute magnitude of about 100 TECU globally at that time and with background values  $\widehat{VTEC}_{\text{glob}}(\varphi_l, \lambda_r, t_s)$  of up to 70 TECU within the densification region (cf. Fig. 5.4 panel a)



and panel c)), the small values of  $\pm 4$  TECU which are generated by the second step of the TSM cannot be visualised in Fig 5.6 a).

## 5.2 Data Formats

In view of the different products and product types, suitable data formats must be used to disseminate them to potential users. In this context, it is necessary to consider in which way the products are to be used; a distinction is made between 1) RT applications and 2) post-processing applications. In this regard, the product types defined in Sections 5.1.1 and 5.1.2 can further be separated into the following latency types:

- final GIM and final RIM
- rapid GIM and rapid RIM
- ultra-rapid GIM and ultra-rapid RIM (UR-GIM, UR-RIM)
- near real-time GIM and near real-time RIM (NRT-GIM, NRT-RIM)
- real-time GIM and real-time RIM (RT-GIM, RT-RIM)

The exact distinction is typically based on the type of input data, which is described in the introduction. The usage determines the latency type, thus for post-processing applications final

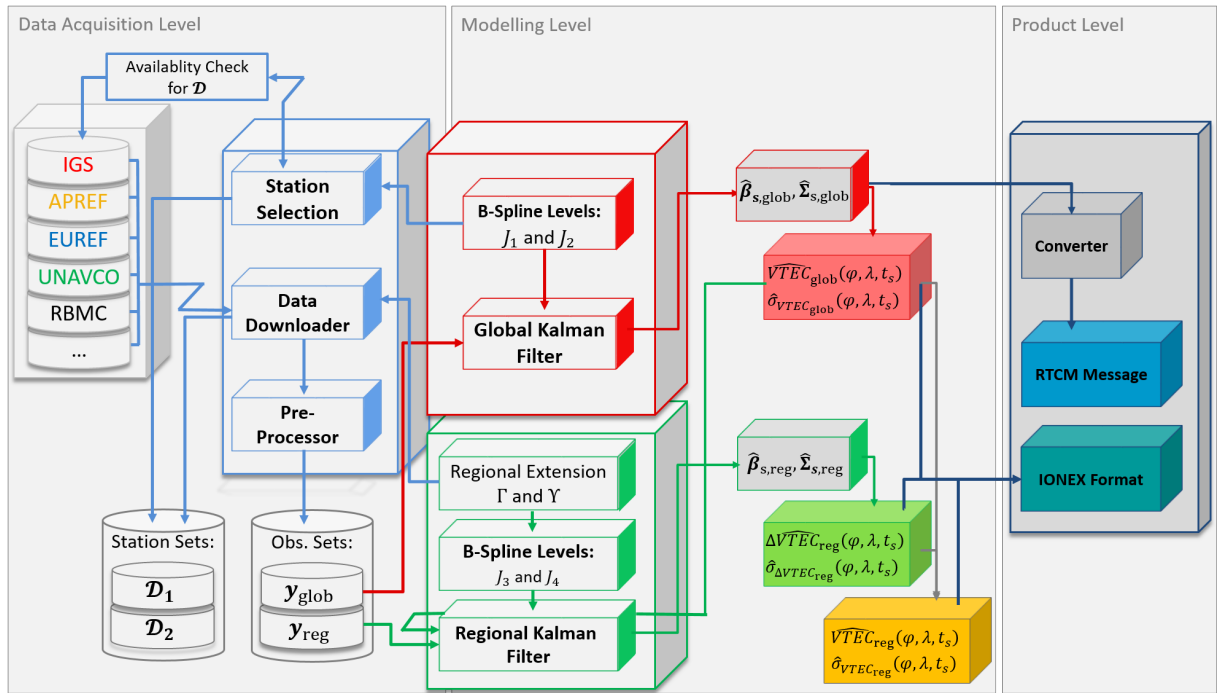


Figure 5.7: *Processing chain*: Flowchart of the processing chain including the data acquisition level (cf. Section 4.5), the modelling level with the TSM (cf. Section 4.6) and the product level comprising different format types to be used for data dissemination of ionosphere products.

products are typically chosen, whereas for RT applications the RT products have to be used. If ionospheric corrections are required for a post-processing application but no final product is available yet, the near real-time, or possibly ultra-rapid or rapid products are available. Furthermore,

the designated use also leads to the choice of the appropriate file format for the dissemination. Figure 5.7 shows the final stage of the processing chain with additional boxes representing the different file formats used for dissemination. The commonly used file formats, the IONEX format and the SSR VTEC message in the frame of the RTCM standard, are thus shown as green and blue boxes on the right hand side of Fig. 5.7. The following description of the file formats addresses the research questions **Q-4**:

#### Q-4 Strategy for the dissemination and use of high-resolution VTEC products

In this regard, the two aforementioned file formats the IONEX and the SSR VTEC message, their advantages and disadvantages and the adaptation of the B-spline model for their usage are discussed.

### 5.2.1 IONosphere EXchange Format

The IONosphere EXchange Format (IONEX) is an ASCII-based data type, which was developed and modified by Schaer et al. (1998) in order to disseminate GIMs in terms of VTEC grids. Thereby, the grid resolution, i.e. the spatial sampling  $\Delta\Phi$  in latitude and  $\Delta\Lambda$  in longitude direction can be chosen arbitrarily. In addition, a distinction is usually made between so-called epoch IONEX files and multi-epoch IONEX and in particular daily IONEX files. This means that within one IONEX file several snapshot maps for VTEC and for consecutive epochs  $t_s$  of arbitrarily selectable temporal sampling intervals  $\Delta T = t_s - t_{s-1}$  can be provided. Furthermore, IONEX can be used to distribute both GIMs and RIMs with different spatial sampling intervals. Obviously, the IONEX format is suitable for the distribution of *Product Type 2*. The file size of IONEX increases with the spatial and temporal resolution, i.e. with increasing  $\Delta\Phi$ ,  $\Delta\Lambda$  and  $\Delta T$  the size of one IONEX file increases. The IAACs of the IGS typically distribute their final, rapid and ultra-rapid products using the IONEX file format with a spatial sampling of  $\Delta\Phi = 2.5^\circ$  and  $\Delta\Lambda = 5^\circ$ . The temporal sampling is typically fixed with  $\Delta T = 2$  hours for final products, but CODE, for instance, provides their final map with  $\Delta T = 1$  hour. The rapid products are mostly provided with a temporal sampling of  $\Delta T = 15$  min. The sampling intervals given in the IONEX file play a major role in the use of the ionospheric information because usually the information is not needed at the grid points or at the time  $t_s$  of a certain snapshot map, but at arbitrary points in between. For the calculation of a value  $VTEC(\varphi, \lambda, t)$  for an arbitrary position  $P(\varphi = \varphi_l + q \cdot \Delta\Phi, \lambda = \lambda_r + p \cdot \Delta\Lambda)$  with  $0 \leq q \leq 1$  and  $0 \leq p \leq 1$  and for any arbitrary time moment  $t$ , a bi-linear spatial interpolation according to Schaer et al. (1998) and using the VTEC grad values of the four surrounding corner points  $P(\varphi_l, \lambda_r)$ ,  $P(\varphi_l, \lambda_r + \Delta\Lambda)$ ,  $P(\varphi_l + \Delta\Phi, \lambda_r)$  and  $P(\varphi_l + \Delta\Phi, \lambda_r + \Delta\Lambda)$  is performed as

$$\begin{aligned} VTEC(\varphi_l + q \cdot \Delta\Phi, \lambda_r + p \cdot \Delta\Lambda, t) &= \\ &= (1 - q) \cdot (1 - p) \cdot VTEC(\varphi_l, \lambda_r, t) + q \cdot (1 - p) \cdot VTEC(\varphi_l + \Delta\Phi, \lambda_r, t) \\ &+ p \cdot (1 - q) \cdot VTEC(\varphi_l, \lambda_r + \Delta\Lambda, t) + q \cdot p \cdot VTEC(\varphi_l + \Delta\Phi, \lambda_r + \Delta\Lambda, t) . \end{aligned} \quad (5.9)$$

Figure 5.8 provides a schematic representation of the bi-linear interpolation.

Note, by applying the interpolation formula (5.9), the quality of the calculated VTEC value decreases with increasing spatial resolution intervals  $\Delta\Phi$  and  $\Delta\Lambda$  and depends on the position within the grid cell. In order to improve the quality of the VTEC computation, two ways can be performed, namely

1. the chosen model approach, e.g. the SH or the B-spline expansion can be used directly to calculate VTEC values at any arbitrary point  $P(\varphi, \lambda)$ ,
2. the resolution intervals  $\Delta\Phi$  and  $\Delta\Lambda$  of the output grid can be set to smaller values, e.g. to  $1^\circ$  as it was proposed at the IGS workshop 2012 (Dach and Jean, 2013).

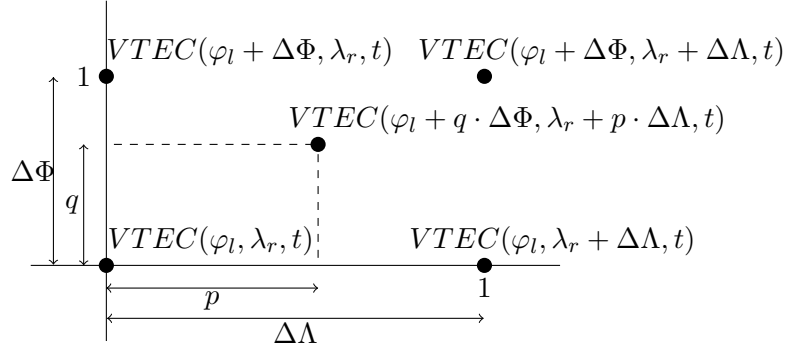


Figure 5.8: Schematic representation of the 4-point spatial interpolation to calculate the VTEC value at  $P(\varphi_l + q \cdot \Delta\Phi, \lambda_r + p \cdot \Delta\Lambda, t)$  from the four corner points of the grid cell of interest.

For the calculation of a VTEC value  $VTEC(\varphi, \lambda, t)$  at an arbitrary time moment  $t = t_s + r \cdot \Delta T$  with  $0 \leq r \leq 1$  at a given spatial location  $P(\varphi, \lambda)$ , an interpolation with respect to time can be applied. Commonly, the linear interpolation

$$VTEC(\varphi, \lambda, t) = (1 - r) \cdot VTEC(\varphi, \lambda, t_s) + r \cdot VTEC(\varphi, \lambda, t_s + \Delta T) \quad (5.10)$$

between the two consecutive maps at epochs  $t_s$  and  $t_s + \Delta T$  is performed; see Schaer et al. (1998). The interpolation methods allow for the calculation of VTEC values  $VTEC(\varphi, \lambda, t)$  at any arbitrary position  $P(\varphi, \lambda)$  and at any time moment  $t$ . According to Liu et al. (2021), the temporal sampling  $\Delta T$  of consecutive maps has a strong influence on the interpolation accuracy, especially during high solar and geomagnetic activity. There is also a discrepancy between different latitudes. At higher latitudes, temporal sampling has less influence on interpolation accuracy, while at lower latitudes and at the equator the effect is more significant Liu et al. (2021).

In the publication **P-I**, the advantage of the high temporal output resolution and its effect on the accuracy of the VTEC interpolation has been discussed on a global scale and for the solar storm time in September 2017. Thereby GIM products, given in IONEX format with a spatial resolution of  $\Delta\Phi = 2.5^\circ$  and  $\Delta\Lambda = 5^\circ$  and with different temporal resolutions  $\Delta T = 2\text{h}, 1\text{h}, 10\text{min}$ , were compared with independent GNSS observations. When comparing the estimated VTEC with independent GNSS observations, the increase in time sampling from 2h to 10 min shows an improvement of more than 20%. The investigations were based on *Product Type 2a* for an investigation period covering September 2017 including a medium intensity solar event.

Although the interpolation enables determining high accuracy VTEC values if a high spatial and temporal resolution of the snapshot grids is given, the IONEX format is not suitable for the dissemination of RT information. Both the computation times of the grids according to the evaluation formulas (4.82) to (4.89) and the spatial and temporal interpolation from (5.9) and (5.10) exceed the conditions necessary for RT application.

### 5.2.2 SSR VTEC - Message

The dissemination of RT corrections for positioning is typically based on the SSR VTEC message and the RTCM standards. The following description of this message is taken from the first-author publication **P-III** and marked here by the indentation.<sup>1</sup>

<sup>1</sup>The numbering of equations, figures and tables does not coincide with the numbering in the publication **P-III** Goss et al. (2020a) but are adapted to this thesis. Spelling and punctuation are corrected.

The currently preferred method for dissemination of ionospheric corrections for RT positioning is based on SH coefficients, follows *Product Type 1* and is based on RTCM streams. The SSR VTEC message allows the dissemination of estimated coefficients  $\hat{c}_{n,m}(t_s)$  of a SH model with additional information about degree  $n$  and order  $m$  of the underlying SH model, as well as the time moments  $t_s$  and the height  $H$  of the single layer model for which the coefficients are valid. According to the message specifications, the coefficients must be provided in Sun-fixed longitude with a phase shift of 2 h to the approximate VTEC maximum at 14:00 local time. This means that a coordinate transformation must be carried out for the values  $VTEC(\varphi_{IPP}, \lambda_{IPP}, t_s)$ , which first provides a transformation to the Sun-fixed geographic coordinate system and then a rotation around the spin-axis of the Earth by 2h. The SSR VTEC message is designed for the dissemination of SH coefficients and allows them only up to degree and order  $n = 16$ . This means that higher resolution models cannot be distributed via the SSR VTEC message. Another restriction of the message is that models not based on SHs require always a transformation to SHs.

### 5.2.3 Real-Time Dissemination of High-Resolution B-spline Products

The SSR VTEC message is currently the only file format that can be used to distribute *Product Type 1*. However, the SSR VTEC message solely allows the dissemination of coefficients of a series expansion in terms of SHs. It can be concluded that *Product Type 1a* and *1b* based on B-spline functions as described in Section 4.6 cannot be distributed by means of this format. Therefore, a transformation of the B-spline approach to the SH approach is required. A method was developed and tested in the publication **P-III** for transformation of a global B-spline model to SHs. Since the dissemination of the corrections should be performed in RT, some requirements have to be considered, which are described in the following.

The entire section is taken from the publication **P-III** and therefore indented:<sup>2</sup>

For the dissemination of a B-spline-based RT ionospheric correction to a user by means of *Product Type 1* and the currently intended data format, i.e. the SSR VTEC message, a transformation of the B-spline model into SH coefficients is required. For the transformation of the B-spline model, it must be considered that:

1. The transformation should be done with high precision, i.e., since B-splines and SHs are characterised by different features, a high degree  $n_{max}$  of the SH expansion needs to be considered.
2. The time which is needed for the transformation is limited. Hence, the processing time including the generation of pseudo-observations—the evaluation of Eq. (5.16)—and the estimation of the SH coefficients (cf. Eq. (5.18)) should be completed within seconds.

### Transformation of a B-spline Model to Spherical Harmonics

The transformation of the B-spline model to SHs requires input data generated by the B-spline model, which reflect the variations in the GIM globally, i.e. VTEC values given as pseudo-observations on a global grid. As a matter of fact, a reliable computation of SH series coefficients requires homogeneously distributed input data. Since a regular grid as described in Section 5.2.1 does not fulfil this criterion, a Reuter grid is used instead (Reuter, 1982). The Reuter grid provides equi-distributed points  $P(\varphi_l, \lambda_{l,r})$  on the sphere with spherical

---

<sup>2</sup>The numbering of equations, figures and tables does not coincide with the numbering in the publication **P-III** Goss et al. (2020a) but are adapted to this thesis. Spelling and punctuation are corrected in the indented section. Abbreviations for equation, table and figure are used.

coordinates

$$\varphi_0 = -90^\circ \quad \text{and} \quad \lambda_{0,0} = 0^\circ, \quad (5.11)$$

$$\varphi_l = -90^\circ + l \Delta\varphi_l \quad \text{and} \quad \lambda_{l,r} = r \frac{360^\circ}{\gamma_l}, \quad (5.12)$$

$$\varphi_\gamma = 90^\circ \quad \text{and} \quad \lambda_{\gamma,0} = 0^\circ \quad (5.13)$$

for  $r = 0, \dots, \gamma_l - 1$  and  $l = 1, \dots, \gamma - 1$  with  $\gamma \in \mathbb{N}$  and the sampling intervals  $\Delta\varphi_l = \frac{180^\circ}{\gamma}$  in latitude direction. Furthermore,

$$\gamma_l = \lfloor 360^\circ / \arccos((\cos \Delta\varphi_l - \sin^2 \varphi_l) / \cos^2 \varphi_l) \rfloor \quad (5.14)$$

means the total number of grid points along the circle of latitude  $\varphi_l$ . Reforming of Eq. (5.14) results in the sampling interval  $\Delta\lambda_l$  of the grid points in longitude direction. For  $\varphi_l = 0$ , it applies  $\Delta\varphi_l = \Delta\lambda_l$ . More information about the Reuter grid can be found in (Freeden et al., 1998; Eicker, 2008).

The left part of the Tab. 5.1 shows for different values of  $\gamma$  the values of the spatial sampling intervals  $\Delta\varphi_l$  along the meridian and  $\Delta\lambda_l$  at the equator, as well as the total number  $V$  of Reuter grid points. The right part of Tab. 5.1 provides, for each degree  $n_{max}$ , the necessary mean sampling intervals  $\Delta\varphi$  and  $\Delta\lambda$  from Eq. (4.9) and the corresponding total number of coefficients  $N$ .

Table 5.1: Sampling intervals  $\Delta\varphi_l$  and  $\Delta\lambda_l$  of the Reuter grid points for different values of  $\gamma$  and the corresponding number  $V$  of Reuter grid points. Required max. sampling intervals  $\Delta\varphi_{SH}$  and  $\Delta\lambda_{SH}$  and the number of unknown coefficients of SHs with different values for  $n_{max}$ .

Reuter Grid						Spherical Harmonics					
$\gamma$	16	21	25	31	35	$n_{max}$	15	20	24	30	34
$\Delta\varphi_l, \Delta\lambda_l$	11.25°	8.57°	7.2°	5.8°	5.14°	$\Delta\varphi, \Delta\lambda$	12	9	7.5	6	5.3
$V$	317	563	797	1225	1561	$N$	256	441	625	961	1224

The Reuter grid is particularly advantageous for the RT conversion of the B-spline model to SHs, because it provides a homogeneous distribution of the pseudo-observations and fulfills at the same time the conditions of the inequalities (4.9). Furthermore, a small number  $V$  of pseudo-observations allows a transformation with short processing time. The values  $\Delta\varphi_l$  and  $\Delta\lambda_l$  for Reuter grids of  $\gamma = 16, 21, 25, 31, 35$  in the left part of Tab. 5.1 fulfill the conditions (4.9) for SHs with maximum degrees  $n_{max} = 15, 20, 24, 30, 34$  in the right part.

Figure 5.9 shows the distribution of Reuter grid points for different values for  $\gamma$ . Due to the projection in the map, the Reuter grid points diverge with increasing latitude.

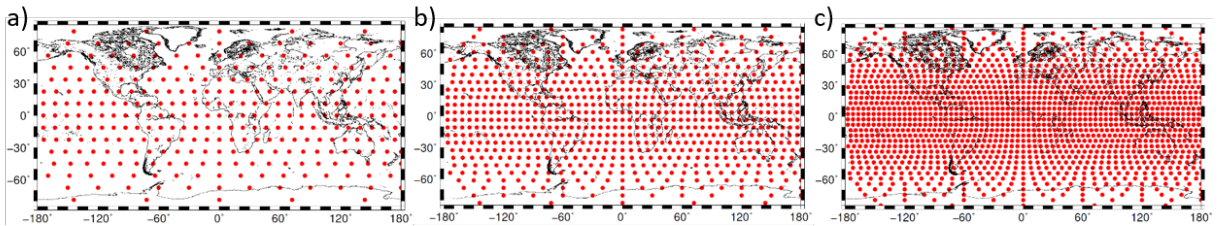


Figure 5.9: Reuter grids with values  $\gamma = 16$  in panel (a),  $\gamma = 25$  in panel (b) and  $\gamma = 35$  in panel (c).

### Pseudo-Observations from B-spline Model Output

The pseudo-observations are generated by means of the given  $u \times 1$  vector

$$\hat{\beta}_s = [\hat{d}_{0,1}^{J_1,J_2}(t_s), \hat{d}_{0,2}^{J_1,J_2}(t_s), \dots, \hat{d}_{K_{J_1}-1, K_{J_2}-1}^{J_1,J_2}(t_s)] \quad (5.15)$$

of estimated B-spline coefficient  $\hat{d}_{k_1,k_2}^{J_1,J_2}(t_s)$  of levels  $J_1$  and  $J_2$  with  $u = K_{J_1} \cdot K_{J_2}$  for the time moment  $t_s$ . We rewrite Eq. (4.82) for the B-spline case as

$$\hat{f}_s = \mathbf{A}_s \hat{\beta}_s \quad (5.16)$$

with the  $V \times u$  design matrix  $\mathbf{A}_s$  consisting B-spline tensor products according to Eq. (4.39).  $\hat{f}_s$  is a  $V \times 1$  vector comprising the values  $\widehat{VTEC}_R(\varphi_l, \lambda_r, t_s)$ , with the index  $R$  indicating the VTEC values on a Reuter grid.

### Estimation of SHs Coefficients from Reuter Grid

The series coefficients  $c_{n,m}$  are estimated by parameter estimation from  $V > N$  pseudo-observations  $\hat{f}_s$ . By rewriting the observation equation (4.6), the linear equation system

$$\hat{f}_s + \mathbf{e}_s = \mathbf{X}_s \mathbf{c}_s \quad (5.17)$$

can be established, with the  $V \times 1$  consistency vector  $\mathbf{e}_s$ , the  $(N+1) \times 1$  vector  $\mathbf{c}_s = [c_{0,0}, c_{1,0}, \dots, c_{N,N}]^T$  of series coefficients, as well as the  $V \times (N+1)$  design matrix  $\mathbf{X}_s$  comprising the functions  $Y_{n,m}(\varphi_l, \lambda_r)$  according to (4.7). In case of a matrix  $\mathbf{X}_s$  with full column rank, the problem can be solved by

$$\hat{\mathbf{c}}_s = [\mathbf{X}_s^T \mathbf{P}_s \mathbf{X}_s]^{-1} \mathbf{X}_s^T \mathbf{P}_s \hat{f}_s. \quad (5.18)$$

Substituting Eq. (5.16) for the observations vector  $\hat{f}_s$ , the transformation between the B-spline and the SH coefficients is established and reads

$$\hat{\mathbf{c}}_s = [\mathbf{X}_s^T \mathbf{P}_s \mathbf{X}_s]^{-1} \mathbf{X}_s^T \mathbf{P}_s \mathbf{A}_s \hat{\beta}_s = \mathbf{T}_s \hat{\beta}_s, \quad (5.19)$$

with the  $(N+1) \times u$  transformation matrix  $\mathbf{T}_s$ .

### Assessment of the Transformation Methodology

The developed methodology for the transformation allows representing the global B-spline model by a series expansion of SH functions. Thus, global B-spline models can also be made available to a user by means of the SSR VTEC message in RT. A distribution of regional maps by means of SSR VTEC message is not yet planned and therefore not considered within this thesis. In order to test the quality of the transformation, different cases with different values for  $\gamma$  and  $n_{max}$  were tested for the period from 2 September 2017 to 12 September 2017, including a geomagnetic storm of medium strength. For the transformation, the *Product Type 1a* with level values  $J_1 = 5$  and  $J_2 = 3$  was used, which can – according to the Tab. 4.2 – be referred to as a SH expansion with a cutoff frequency of  $n_{max} = 33$  in latitude and  $n_{max} = 12$  in longitude direction. In order to rate the applicability of the derived procedure from Section 5.2.3, the original GIM  $\widehat{VTEC}(\varphi_l, \lambda_r, t_s)$  and its transformation  $\widehat{VTEC}_{SH}(\varphi_l, \lambda_r, t_s)$  have been compared in the publication **P-III**. This part is repeated at this stage for consistency reasons within this thesis.

The following intended part is taken from this publication: <sup>3</sup>

<sup>3</sup>The numbering of equations, figures and tables does not coincide with the numbering in the publication **P-III** Goss et al. (2020a) but are adapted to this thesis. Spelling and punctuation are corrected in the indented section. Abbreviations for equation, table and figure are used.

The quality characteristics, Root Mean Square (RMS, in % and in TECU), mean value  $\delta_{mean}$ , maximum value  $\delta_{max}$  and minimum value  $\delta_{min}$  are determined based on the deviations, i.e., the differences  $\delta(\varphi_l, \lambda_r, t_s) = \widehat{VTEC}(\varphi_l, \lambda_r, t_s) - \widehat{VTEC}_{SH}(\varphi_l, \lambda_r, t_s)$  between the original GIM and the SH GIM. The applicability of the approach is executed on the basis of the necessary processing time  $\widetilde{\Delta t}$  per epoch, which is needed for the transformation. For comparison reasons, the transformations have been computed on a workstation with 64 GB RAM, and a 8-core processor of 3.2 GHz clock rate. Thereby,  $\widetilde{\Delta t}$  comprises the evaluation time for the pseudo-observations as well as the estimation of the SH coefficients. All values given in Tab. 5.2 are averages obtained from transformed version computed with a  $\Delta T = 10$  min temporal sampling within the designated time span.

Table 5.2: Numerical and statistical results to estimate the quality and feasibility for the different cases.

	1. Case	2. Case	3. Case	4. Case	5. Case
$\gamma$	16	21	25	31	35
$V$	317	563	797	1225	1561
$n_{max}$	15	20	24	30	34
$N$	256	441	625	961	1224
$\widetilde{\Delta t}$	1.43s	1.85s	3.12s	4.99s	8.23s
rel. RMS [%]	9.23	5.83	4.19	2.54	1.83
RMS [TECU]	1.31	0.83	0.60	0.36	0.26
$\delta_{max}$ [TECU]	8.22	5.91	5.23	2.22	1.79
$\delta_{min}$ [TECU]	-8.06	-6.29	-4.21	-2.23	-1.9
$\delta_{mean}$ [TECU]	0.016	0.0012	0.014	0.0033	0.003

In the following, we discuss the given cases in more detail. In the first case, with  $V = 317$  pseudo-observations given on a Reuter grid with  $\gamma = 16$ , a SH series expansion with degree  $n_{max} = 15$  and  $N = 256$  coefficients has to be estimated. The average processing time for the transformation took  $\widetilde{\Delta t} = 1.43$  s. However, the transformed version with degree  $n_{max} = 15$  produces systematic errors compared to the original GIM. The RMS value of the deviations shows with 1.31 TECU significant differences. The relative RMS value

$$rel. RMS[\%] = 100 \cdot \sqrt{\frac{\sum_{l=1}^L \sum_{r=1}^R (\delta(\varphi_l, \lambda_r, t_s))^2}{\sum_{l=1}^L \sum_{r=1}^R (\widehat{VTEC}(\varphi_l, \lambda_r, t_s))^2}} \quad (5.20)$$

provides the RMS in percentage with 9.23% for the first case. The first column in Fig. 5.10 shows the SH GIM in the top panel and the deviation map in the bottom panel. The deviation map represents mainly stripes in east–west direction, which indicate the difference in the spectral resolution for latitude direction between the original GIM corresponding to  $n_{max} = 33$  and representing the minimum wavelengths of  $L_\varphi = 10.9^\circ$  and the SH GIM of  $n_{max} = 15$ , representing the minimum of wavelengths  $L_\varphi = 24^\circ$ . Visible are deviations with maximum values of  $\delta_{max} = 8.22$  TECU and minimum  $\delta_{min} = -8.06$  TECU, whereas the average  $\delta_{mean}$  is close to 0 TECU. In the second case, both the grid resolution and the degree of the SH expansion are increased to  $\gamma = 21$  and  $n_{max} = 20$ , respectively. This causes an insignificant increase in computation time to  $\widetilde{\Delta t} = 1.85$  s, but a significant improvement in the transformation accuracy to a relative RMS of 5.83% (cf. Tab. 5.2). For the third case, the processing time doubles compared to the first case with  $\widetilde{\Delta t} = 3.12$  s, but the error of the transformation is reduced by a half and a relative RMS of 4.19% can be achieved. This improvement is also visible in the second column of Fig. 5.10. Due to the increased



degree of the SHs, finer structures in latitude direction can be represented better than in the first case. Therefore, the stripes in east–west direction in the deviation map show a smaller extension in latitude direction and occur with decreased magnitude of  $\delta_{max} = 5.23$  TECU and  $\delta_{min} = -4.21$  TECU. Further improvements can be achieved by increasing the degree

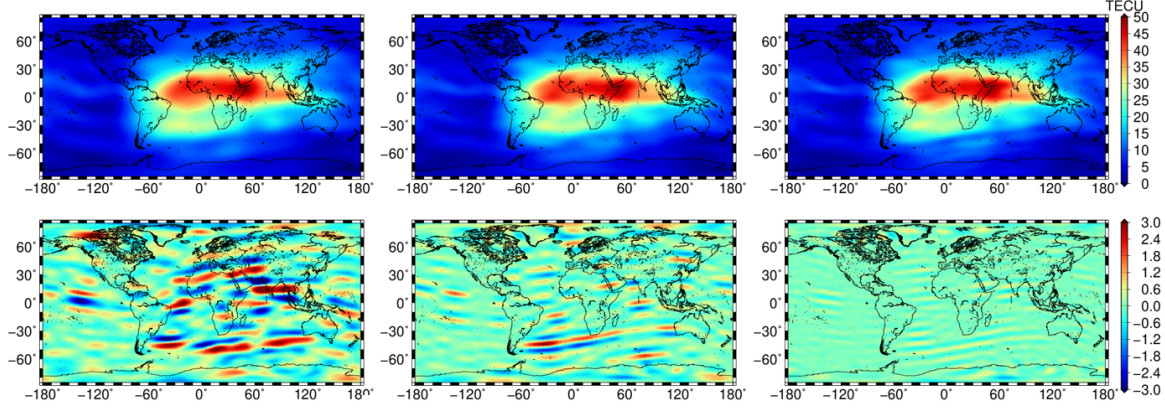


Figure 5.10: SH GIM (**top panels**) and deviation maps (**bottom panels**) of the 1. (**left column**), 3. (**middle column**) and 5. (**right column**) test case from Tab. 5.2 for September 8, at 12:00 UT.

of the SH expansion for the transformation, but with a further extension of the processing time per epoch. The transformation using  $n_{max} = 34$  needs an average transformation time of  $\Delta t = 8.23$  s per epoch. The corresponding SH GIM is shown in the top right panel in Fig. 5.10. The east–west stripes in the deviation map below are mainly visible in the area of the equatorial anomaly with maximum values of  $\delta_{max} = 1.79$  TECU and minimum values of  $\delta_{min} = -1.9$  TECU. The SH GIM describes a relative RMS of 1.83% compared to the original GIM. For these five cases, it can be concluded that the quality of the transformation improves with increasing degree  $n_{max}$  for the SH series expansion.

Accordingly, Fig. 5.11 shows on the left the relative RMS values and on the right the RMS values of the deviations for the period from 2 September 2017 and 12 September 2017 with decreasing magnitude.

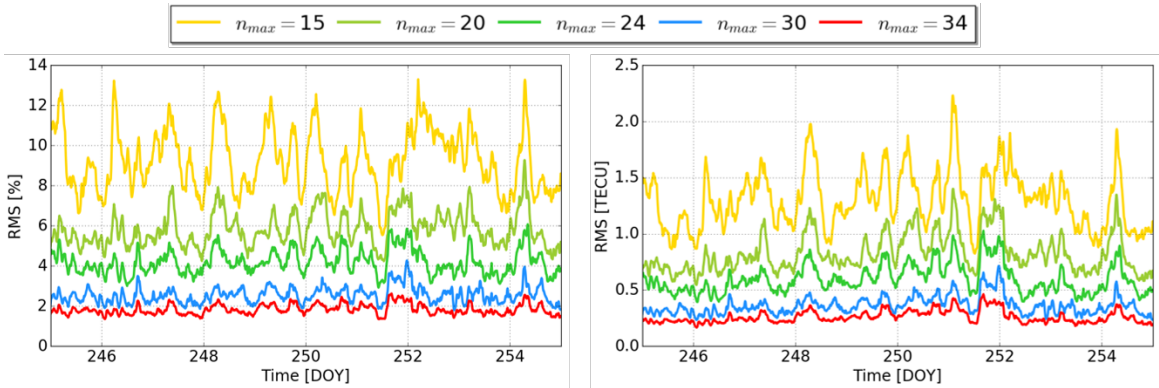


Figure 5.11: Change in relative RMS values (**left**) and RMS values (**right**), for the period from 2 September 2017 (Day Of Year 245) to 12 September 2017 (Day Of Year 255); temporal sampling intervals of 10 min.

A validation in terms of the positioning accuracy using the reconstructions as ionosphere corrections is included in the following, Section 5.3.



## 5.3 Validation and Assessment

In order to rate the quality improvements of the high-resolution products, two types of validations are applied. The first is based on a comparison with observations from independent GNSS stations and called *self-consistency validation* or *dSTEC analysis*. It allows to assessing the VTEC products given in IONEX format. In constrast, the second validation is performed in the positioning domain and allows for an assessment of VTEC products given in SSR VTEC message. Although the SSR VTEC message allows providing SH coefficients to a degree of  $n_{max} = 16$ , it is here assumed that higher degrees are possible, and thus a conclusion can be found of how high-resolution ionosphere corrections can improve the positioning for further RT applications.

### 5.3.1 Self-Consistency Validation

In order to assess the quality of the generated products, the dSTEC analysis is applied (Hernández-Pajares et al., 2017a; Orus et al., 2007; Rovira-Garcia et al., 2015; Roma-Dollase et al., 2017). Thereby, the generated VTEC values, in terms of *Product Type 2* are compared with data obtained from GNSS stations. The selection of suitable stations is based on the following three criteria:

1. The observations of the stations are used in the estimation of all products to be validated and compared.
2. None of the stations provide data for the estimation of the products. The stations are therefore independent of the products.
3. A mixed selection of stations, where the previous criteria 1) and 2) are satisfied.

For the calculation of the products of the TSM, the non-overlapping station lists  $\mathcal{D}_1$  and  $\mathcal{D}_2$  are generated by means of the station separation procedure (cf. Section 4.5.1). Since all stations are partitioned among the datasets, the first two criteria cannot be taken into account. Therefore, in the following, criterion 3) is used and the differences

$$dSTEC_{obs}(t_s) = STEC(\mathbf{x}_s^T, \mathbf{x}_{s,R}, t_s) - STEC(\mathbf{x}_{ref}^T, \mathbf{x}_{ref,R}, t_{ref}) \quad (5.21)$$

are calculated for a phase-continuous satellite arc, i.e. a receiver and satellite connection. The observations  $STEC(\mathbf{x}_s^T, \mathbf{x}_{s,R}, t_s)$  at the time moment  $t_s$  and the observations  $STEC(\mathbf{x}_{ref}^T, \mathbf{x}_{ref,R}, t_{ref})$  at a reference time  $t_{ref}$  are obtained from a mixture of stations from the station lists  $\mathcal{D}_1$  and  $\mathcal{D}_2$ . The reference observation is typically the observation with the largest elevation angle along the phase-continuous arc. The values

$$dSTEC_{map}(t_s) = M(z_s) \cdot VTEC(\mathbf{x}_{s,IPP}, t_s) - M(z_{ref}) \cdot VTEC(\mathbf{x}_{ref,IPP}, t_{ref}) \quad (5.22)$$

are calculated from  $VTEC(\mathbf{x}_{s,IPP}, t_s)$  and  $VTEC(\mathbf{x}_{ref,IPP}, t_{ref})$  interpolated by means of Eqs. (5.9) and (5.10) from the *Product Type 2a* and *Product Type 2c* to the position of the IPP and mapped in slant direction by means of the mapping function (2.5). The quality is finally assessed by studying the differences

$$dSTEC(t_s) = dSTEC_{obs}(t_s) - dSTEC_{map}(t_s) \quad (5.23)$$

with expectation value  $E(dSTEC(t_s)) = 0$ . The stations used for the dSTEC analysis are shown in Fig. 5.12. In the analysis, the different products of the TSM are compared. The products are named as defined in **P-I**, where the first digit ‘o’ is chosen in accordance with the processing

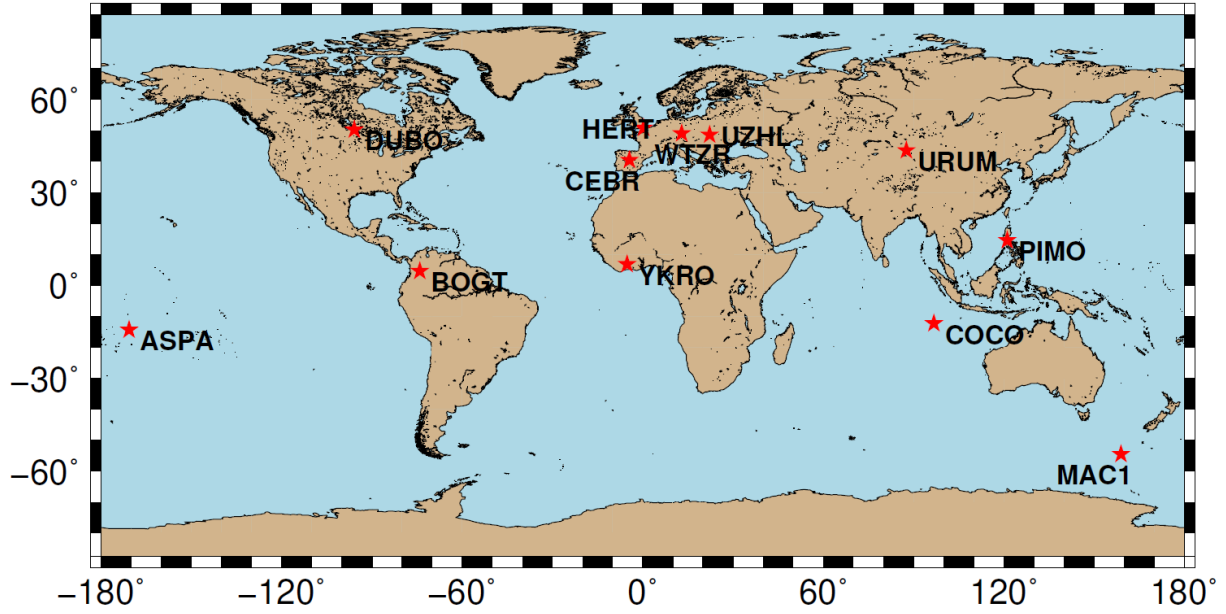


Figure 5.12: Stations used in the dSTEC analysis, selected according to criteria 3).

software OPTIMAP<sup>4</sup>. The second digit ‘t’ defines the temporal sampling of  $\Delta T = 10$  min ( $t = \text{ten}$ ) of consecutive snapshot maps. The third digit describes the spectral resolution with ‘h’ for high-resolution and ‘l’ for low-resolution and the last digit the extension of the model with ‘g’ for global and ‘r’ for regional. Thus the products ...

... ‘othg’ as the high-resolution *Product Type 2a* generated with B-spline levels  $J_1 = 5$  and  $J_2 = 3$ ,

... ‘otlg’, as the smoothed version of ‘othg’ with B-spline levels  $J'_1 = 4$  and  $J'_2 = J_2 = 3$  and

... ‘othr’, the high-resolution regional *Product Type 2c* generated in the second step of the TSM with B-spline levels  $J_3 = 3$  and  $J_2 = 3$

are defined. For comparison, two additional global products ‘codg’ and ‘uqrg’ of the IAACs are used. The product ‘codg’ is a final product and is provided by CODE with a temporal sampling of  $\Delta T = 1$  hour. The product ‘uqrg’ is a rapid solution and is provided by UPC with a latency of one day and a temporal sampling of  $\Delta T = 15$  min. For regional comparison the product ‘robr’ of ROB was added to the analysis, which is a RIM generated for Europe with a temporal resolution of  $\Delta T = 15$  min. Table 5.3 depicts the RMS values of  $d\text{STEC}(t_s)$  calculated for the six different products at the stations shown in Fig. 5.12. For the analysis, six days from March 14 to 20 in 2015 were chosen as the period of time, which includes the solar storm on St. Patrick’s Day on 17 March. Table 5.3 is divided into two parts: the upper part contains the RMS values which are calculated at all globally distributed stations for the global products. The lower part contains the RMS values which are determined for all global and regional products for the stations located within the area of the regional model. The values printed in bold are the average RMS values of all stations in the respective sub-table. It can be seen that ‘othg’ has lower RMS values at all stations than its smoothed version ‘otlg’. Hence, the high spectral resolution allows a more precise representation of VTEC. In comparison with ‘codg’, which is based on SHs with maximum degree  $n_{\text{max}} = 15$ , ‘othg’ provides significantly lower RMS values at all stations. ‘otlg’, on the

<sup>4</sup>Operational Tool for Ionosphere Mapping and Prediction, project financed by the Bundeswehr Geoinformation Centre.

Table 5.3: Results of the dSTEC analysis for 13 different stations, with the RMS in TECU values of  $dSTEC(t_s)$  for the different VTEC products.

	othg	otlg	othr	codg	uqrg	robr
ASPA	2.14	2.80		2.51	2.07	
BOGT	3.34	4.27		4.26	3.41	
DUBO	1.07	1.11		1.10	0.94	
MAC1	1.91	2.11		2.15	1.74	
PIMO	2.87	3.60		2.62	2.41	
URUM	0.77	1.33		1.01	0.78	
YKRO	2.13	2.33		2.67	2.11	
COCO	2.49	2.95		3.18	2.58	
	<b>2.09</b>	<b>2.6</b>		<b>2.43</b>	<b>2.01</b>	
CEBR	0.79	0.93	0.65	1.09	1.01	0.71
UZHL	0.70	0.70	0.56	0.67	0.83	0.61
HERT	0.84	0.87	0.68	0.90	0.98	0.82
WTZR	0.69	0.76	0.58	0.70	0.84	0.63
	<b>0.76</b>	<b>0.81</b>	<b>0.62</b>	<b>0.84</b>	<b>0.91</b>	<b>0.69</b>

other hand, has similar and occasionally lower or higher RMS values than ‘codg’, which allows for the consequence that ‘otlg’ and ‘codg’ are comparable in their accuracy with local differences. Assuming that the dSTEC analysis allows the assessment of GIMs with an accuracy of 0.1 TECU, the products ‘othg’ and ‘uqrg’ are also comparable with small local differences.

However, a clear trend can be seen that the global products ‘othg’ and ‘otlg’ are doing particularly well for Europe. The reason for this is the localizing feature of the B-spline basis functions, which have a strong advantage in regions with a high observation density.

A significant improvement in the representation of VTEC for specific regions is reflected in the RMS values of regional products. The products ‘othr’ and ‘robr’ have lower RMS values at the four regional stations than the global products. The RMS values of the product ‘othr’ especially are significantly smaller. In this particular case, the densification results in an improvement of about 18 % in the average values compared to the high-resolution global product.

As can be seen from the comparisons within the densification region, but also on a global scale, the model parts of the TSM based on B-splines set themselves apart from the models that are used for comparison. This means that both products have a particularly high quality, which enables an improved correction of the ionospheric disturbance for positioning. This test is carried out below.

### 5.3.2 Single-Frequency Positioning

To distribute the corrections to users for RT-applications, the SSR VTEC message described in Section 5.2.2 is used. However, the created B-spline products must first be transformed to a series expansion in terms of SH, as shown in Section 5.2.3. Since the SSR VTEC message is mainly used for the correction of GNSS signals in RT applications, a single-frequency Precise Point Positioning (PPP) is performed in the following.

The positioning by means of a single-frequency receiver was described in the publication **P-III** for two selected days in September 2017. The first day, 2 September 2017, was selected as a solar undisturbed day, whereas the second day, 8 September 2017, is known as a disturbed day with a solar event resulting in a geomagnetic storm. For these two days, the reconstructions coinciding

with the five cases from the assessment of the transformation methodology in Section 5.2.3 are used as ionosphere corrections for positioning. The different products are denoted according to the publication **P-III** as ‘othg’ for the original GIM and ‘o15g’, ‘o20g’, ‘o24g’, ‘o30g’, ‘o34g’ for the transformations. The numbers 15 to 34 provide the information about the cutoff frequency  $n_{max}$  used for the reconstruction.

The following part comprising the single-frequency positioning test is taken from the first-author publication **P-III**:<sup>5</sup>

We perform a Precise Point Positioning (PPP) for the stations BOGT, WTZR and ASPA using the open source software RTKLIB (Takasu and Yasuda, 2009; Prol et al., 2018). The selection of stations covers both mid- and low-latitudes, see Fig. 5.12, as well as regions with different characteristics for ionospheric modelling, i.e. either characterised with strong variations in VTEC (BOGT), dense observation distribution (WTZR) or low number of observations (ASPA). A kinematic processing mode is selected for each station to estimate the position for each epoch for which an observation was available. The VTEC values provided in the GIM are used to correct the ionospheric delay for each single-frequency observation of the stations. Positioning tests were performed for the days 2 September 2017 with moderate ionospheric activity and 8 September 2017 characterised by a geomagnetic storm.

The estimated coordinate components  $X_{est}(t_s)$ ,  $Y_{est}(t_s)$  and  $Z_{est}(t_s)$  are subtracted from the actual coordinates  $X(t_s)$ ,  $Y(t_s)$  and  $Z(t_s)$  provided by the IGS Dow et al. (2009) and the deviations of the 3D position are determined as

$$S(t_s) = \sqrt{(X(t_s) - X_{est}(t_s))^2 + (Y(t_s) - Y_{est}(t_s))^2 + (Z(t_s) - Z_{est}(t_s))^2}. \quad (5.24)$$

Figure 5.13 shows the time series of the differences  $S(t_s)$  for 2 September 2017 (upper panels) and 8 September 2017 (lower panels). A significant difference can be seen in  $S(t_s)$  between the two days. On 8 September 2017, due to the high geomagnetic activity the ionospheric corrections are more difficult to determine and thus, the positioning accuracy decreases and the deviations increase. This trend is especially noticeable for the stations BOGT and ASPA close to the equator. It can also be observed that their deviations increase during local noon, i.e., between 15:00 and 20:00 UT for BOGT and between 20:00 and 24:00 UT for ASPA. The large deviations of the position of BOGT and ASPA between 00:00 and 05:00 UT on 8 September are due to the high geomagnetic variations with increased geomagnetic index of  $Kp = 8$ . The variations are not as significant at the station WTZR, which was located on the night side of the Earth at that time. The daily variations of  $S$  in Fig. 5.13 show that ‘othg’, ‘o30g’ and ‘o34g’, in light green, blue and red, respectively, exhibit a similar variation. Stronger deviations and mostly larger values  $S(t_s)$  can be recognized for the GIMs ‘o15g’, ‘o20g’ and ‘o24g’ with the dashed lines. The GIM ‘codg’ shows a similar behaviour during the days. However, the ‘uqrg’ performs better in single frequency positioning and sometimes shows lower values than the ‘othg’, the ‘o30g’ and the ‘o34g’, except at local noon at station WTZR, where it shows large deviations.

A detailed evaluation of the performance of the different GIMs is performed using the respective RMS and the average  $\bar{S}$  values of the time series  $S(t_s)$ , which are depicted in Tab. 5.4.

The colour scheme in Tab. 5.4 implies the lowest and highest values of the RMS and  $\bar{S}$  in green and red, for the respective station and day. It can be seen that for all stations there are differences in the positioning accuracy between the two days examined. Hence, for DOY 251, the RMS and average values are increased. There is an additional trend which shows,

<sup>5</sup>The numbering of equations, figures and tables does not coincide with the numbering in the publication **P-III** Goss et al. (2020a) but are adapted to this thesis. Spelling and punctuation are corrected in the indented section. Abbreviations for equation, table and figure are used.

Table 5.4: RMS and  $\bar{S}$  values of deviations  $S(t_s)$  for September 2 (DOY 245) and 8 (DOY 251), 2017 at the stations BOGT, WTZR and ASPA. The maximum and minimum values of the RMS and  $\bar{S}$  are marked in red and green, respectively. The RMS and  $\bar{S}$  of the transformed versions are bold if they are lower than the values of the original GIM, ‘othg’.

	Value	DOY	othg	o15g	o20g	o24g	o30g	o34g	codg	uqrg
BOGT	RMS [m]	245	1.07	1.35	1.17	1.09	1.05	1.05	1.29	0.90
		251	2.91	3.19	3.12	3.03	2.91	2.86	3.14	2.98
	$\bar{S}$ [m]	245	0.90	1.13	1.00	0.92	0.89	0.89	1.05	0.77
		251	2.22	2.44	2.34	2.31	2.23	2.20	2.35	2.18
WTZR	RMS [m]	245	0.49	0.55	0.53	0.52	0.50	0.48	0.51	0.55
		251	0.49	0.90	0.57	0.54	0.50	0.49	0.51	0.62
	$\bar{S}$ [m]	245	0.45	0.50	0.49	0.48	0.46	0.44	0.46	0.50
		251	0.44	0.53	0.52	0.47	0.44	0.44	0.47	0.57
ASPA	RMS [m]	245	0.81	2.53	0.98	0.92	0.85	0.92	1.13	1.19
		251	2.18	3.12	2.59	2.67	2.17	2.11	2.65	1.80
	$\bar{S}$ [m]	245	0.69	1.37	0.86	0.79	0.73	0.77	0.95	0.94
		251	1.53	2.10	1.76	1.84	1.54	1.48	1.64	1.40

that for the selected stations and days the high resolution GIMs, ‘othg’ and ‘uqrg’ allow a correction of the ionospheric disturbances in a way that leads to a positioning with increased accuracy (see the green colours). Furthermore, the poor performance of the ‘o15g’ – which has mostly highlighted values in red – confirms the result from Section 5.3.1, that a transformed version with a higher degree of SH series expansion is necessary to achieve the quality of the original GIM. As the degree of SHs for the transformation increases, the accuracy of positioning increases when using their ionosphere corrections. The values written in bold in Tab. 5.4 allow the conclusion that a transformation with at least the maximum degree  $n_{max} = 30$  is necessary to achieve the quality of ‘othg’.

It should be pointed out, that the pure SH model, the ‘codg’, can correct the ionospheric disturbances for single-frequency positioning better than the transformed version ‘o15g’. However, in the example shown here, ‘codg’ cannot achieve accuracy of the ‘othg’, the ‘uqrg’ and the transformed versions ‘o30g’ and ‘o34g’.

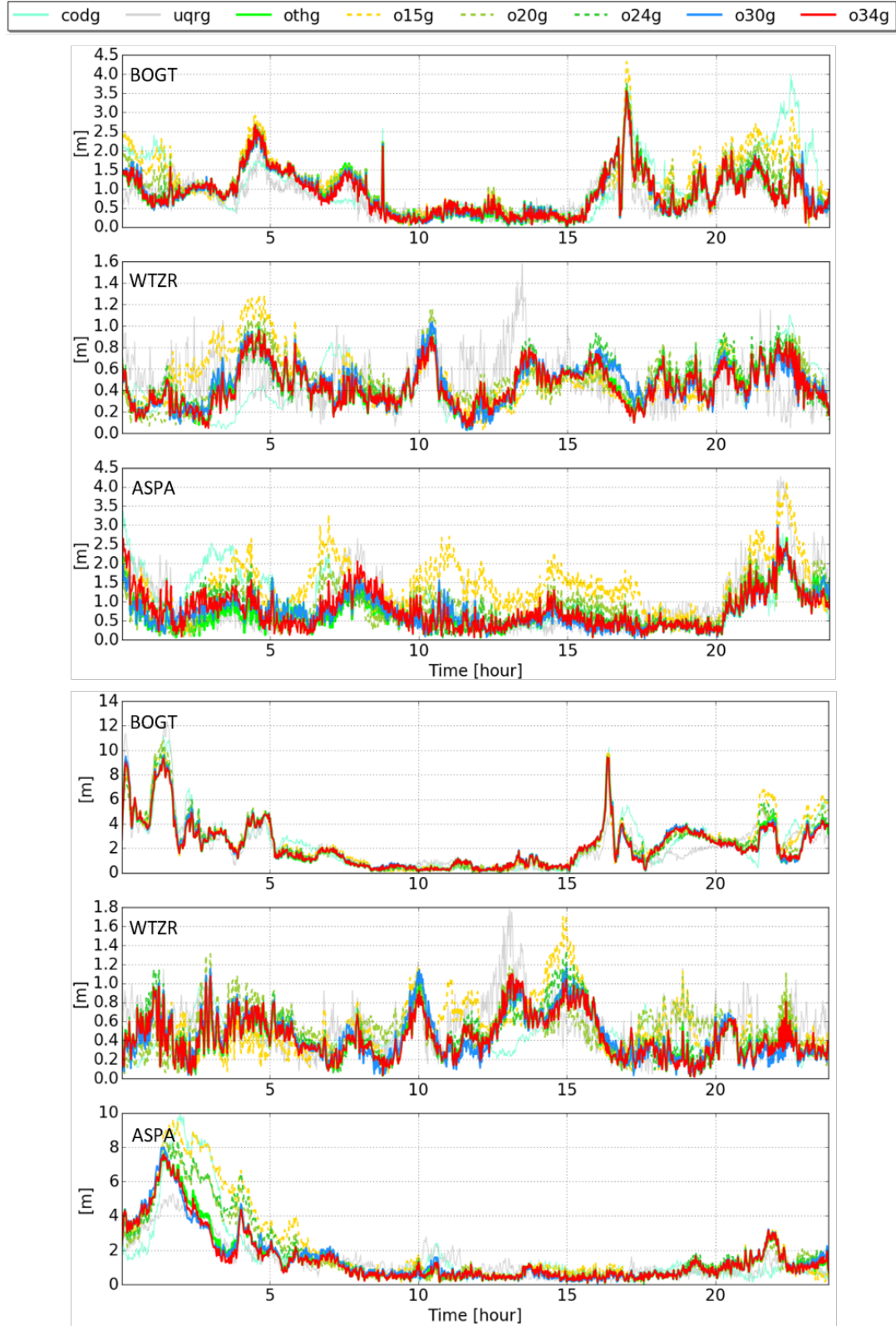


Figure 5.13: Differences  $S(t_s)$  in the 3D position between the position determined by Precise Point Positioning (PPP) and ionospheric corrections calculated by different GIMs and the actual position. The top three panels show the differences for the stations BOGT, WTZR and ASPA during the 2 September 2017 (Day Of Year 245) and the bottom three panels show the corresponding differences for 8 September 2017 (Day Of Year 251) with different scaling of the y-axis. On the x-axis, the time in Universal Time is depicted in hours.

## 6 Summary and Conclusions

The use of GNSS has become an indispensable part of our daily lives. While precise positioning with a smartphone is not particularly important, it is of great significance for autonomously guided platforms. The ionosphere has a great influence on the propagation of GNSS signals and thus degenerates the positioning accuracy. With the increasing demands on accuracy, the need for high-resolution corrections of the ionospheric delay is growing.

In this thesis, novel global and regional models for the high-resolution representation of VTEC based on low-latency GNSS data have been generated by means of series expansions in terms of tensor products of one-dimensional B-spline functions. These models allow for the dissemination of different VTEC products to the user within a short amount of time for correcting the ionospheric delay in positioning and navigation applications. In the following, the major results are summarised with regard to the research questions formulated in the introduction.

### 6.1 Primary Results of the Research Questions

All the research questions mentioned in the introduction were answered in the previous chapters, but not discussed in detail. The answers to the questions and an evaluation of the results of the thesis are put into context again in the following.

#### Development of a suitable algorithm for the data selection

##### Q-1 Selection of input data for global and regional high-resolution VTEC modelling

- a) How can a data selection be performed in order to serve both global and regional modelling procedures?
- b) What are the criteria for the input data to allow high-resolution ionosphere modelling?

Both questions have been answered in Sections 3.4 and 4.5.1. Thereby, the data selection is carried out on the basis of the stations from different networks. As described in the introduction and in Section 3.4, the GNSS networks include different sub-networks that combine stations providing observations with different latencies. In this thesis, data selection was applied to stations providing hourly observations.

With regard to question a):

In the presented B-spline adaptive selection (cf. Section 4.5.1), it is assumed that several observations are made in the vicinity of individual stations, i.e. IPPs are distributed in the near vicinity of individual stations. By selecting stations according to the location of the B-spline tensor products, it can be ensured that a sufficient number of observations are homogeneously distributed and that the sampling intervals  $\Delta\varphi$  and  $\Delta\lambda$  are present in compliance with the inequalities (4.15), (4.23). Therefore, the data set  $\mathcal{D}_1$  is only assigned to as many stations as are needed for the global model. In the following, the data separation is tested using the stations of the networks IGS, EUREF and UNAVCO for the period of October 2018. Figure 6.1 shows the distribution of all stations in panel a) and those from the station sets  $\mathcal{D}_1$  and  $\mathcal{D}_2$  in panel d) and g). The mid column shows the GIM generated with the observations of all stations (panel b))



and the GIM generated with the observations from stations set  $\mathcal{D}_1$  (panel e)). A B-spline model with level values  $J_1 = 4$  and  $J_2 = 3$  was used. Both GIMs show similar structures, but there are differences which are visible in the difference map in panel h). As can be seen, the differences mainly occur in regions where the standard deviation of the respective GIM changes due to the smaller number of stations (cf. panel c) and f)). A dSTEC analysis (5.23) by means of stations

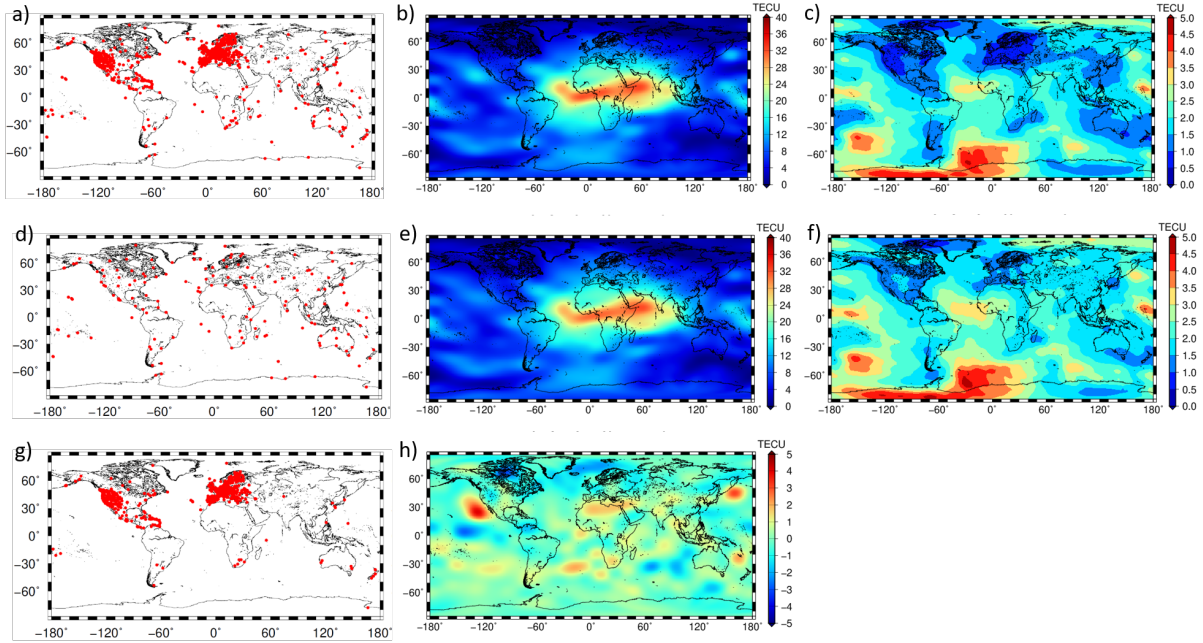


Figure 6.1: Panel a) show the distribution of stations providing hourly data to the networks IGS, EUREF and UNAVCO which are used for generating the GIM in panel b) with corresponding standard deviation map presented in panel c) by means of a B-spline expansion of level  $J_1 = 4$  and  $J_2 = 3$ . Panels d), e) and f) show the stations assigned to  $\mathcal{D}_1$  as well as the corresponding GIM and standard deviation map, respectively. Panel g) represents the stations assigned to  $\mathcal{D}_2$  and panel h) the differences between the GIMs shown in the panels b) and e).

used for both GIMs showed minor differences for the period from 5 October 2018 to 20 October 2018. The RMS value of 0.53 TECU for the GIM calculated from all stations and 0.57 TECU for the GIM calculated using the stations from  $\mathcal{D}_1$  shows that both GIMs are in a good agreement. Small differences are acceptable because

1. they are within the range of differences of several TECU that also arise between the different products of IAACs, (Roma-Dollase et al., 2017; Hernández-Pajares et al., 2017a).
2. higher resolutions can be created by densification in the sense of TSM over the regions with the greatest differences.

With regard to question b):

The data selection should be performed at regular intervals to redefine the station sets  $\mathcal{D}_1$  and  $\mathcal{D}_2$ , as it cannot be assumed that the stations will operate continuously. Thus, during the data selection, care is taken to ensure that only stations that provide data at the respective time interval are included in the selection algorithm. Furthermore, the requirements of the model in terms of sampling intervals  $\Delta\varphi$  and  $\Delta\lambda$  according to the inequalities (4.15) and (4.23) are considered.



**Achieved Goals:**

The data selection, as described in Section 4.5.1, allows downloading only observations of those stations that are used in the modelling process. Two main features of the described method are emphasized:

- By selecting individual stations in accordance to the inequalities (4.15) and (4.23), redundant stations can be eliminated and allow for a more homogeneous data distribution over the globe and a faster processing time.
- The data selection is an important part of the TSM, since by the requirement that the station lists  $\mathcal{D}_1$  and  $\mathcal{D}_2$  should not overlap, correlations of the observations for both model parts are prevented.

**Generation of high-resolution global VTEC products****Q-2 Global high-resolution modelling of the Vertical Total Electron Content**

- a) What is the advantage of using B-splines for sequential modelling of VTEC globally compared to traditional modelling methods on a sphere?
- b) How can the spectral resolution of the global B-splines series expansion be related to the maximum degree of a SH expansion?

The generation of high-resolution global VTEC products is subject to the three publications **P-I**, **P-II** and **P-III**. In all three publications B-spline models are used, which have proven to be suitable for the generation of GIMs and RIMs as it was published before, e.g. by Schmidt (2007); Schmidt et al. (2011, 2015a); Limberger (2015); Erdogan et al. (2017). A distinction is made between different latency types of GIMs. The most prominent VTEC products are those of the IAACs of the IGS, which are generated by different methods, including the choice of basis functions. The spatial and temporal resolution as well as the latency at which they can be disseminated depend on the respective algorithms for the generation of the GIMs.

With regard to question a):

The publication **P-I** presents an approach to model VTEC using hourly GNSS observations and a KF estimation procedure for the unknown series coefficients of the B-spline expansion (Erdogan et al., 2017, 2020). The IAACs generate GIM mostly as SH expansions with a maximum degree value  $n_{max} = 15$ . This value corresponds to a spatial resolution of  $12^\circ \times 12^\circ$  in latitude and longitude. B-spline expansions of VTEC offer a large number of advantages in comparison to SHs. Besides an appropriate handling of data gaps, the spatial resolution of the VTEC model can be adapted in latitude and longitude direction to both the data distribution and the signal structure. Since VTEC generally features finer structures in latitude than in longitude direction, level values are chosen accordingly with  $J_1 = 5$  and  $J_2 = 3$ , which correspond to a SH degree of  $n_{max} = 33$  in latitude direction and  $n_{max} = 12$  in longitude direction. Consequently, the usage of B-splines allows for generating GIMs which are characterised by a much higher spectral resolution in latitude direction as the aforementioned GIMs of the IAACs, which are based on SHs.

Furthermore, the B-spline approach allows for the generation of a MSA and thus multiple spectral resolution by means of the pyramid algorithm (4.49), as it is described in Section 4.6.1. The *Product Type 1a* und *Type 2a* as defined in the Sections 5.1.1 and 5.1.2 include both the high-resolution GIM, generated with B-spline levels  $J_1 = 5$  and  $J_2 = 3$ , as well as a smoothed version and a number of detail signals, as can be seen from Eq. (4.58).

Using the KF (4.61) to (4.62) for estimating the unknown B-spline coefficients, the temporal output sampling  $\Delta T$  of consecutive maps is defined by the KF step size  $t_{s+1} - t_s$ . Thus, the

VTEC maps are given at discrete time moments  $t_s$ . For time  $t$  with  $t_s < t < t_{s+1}$ , a linear interpolation (5.10) has to be applied, as described in the context with the IONEX format in Section 5.2. The accuracy of the interpolated values depends on the temporal sampling  $\Delta T$  as well as on the solar activity and varies with the time of the day and position on the globe (Li et al., 2020). For the global model, additionally to the usual values with  $\Delta T = 2\text{h}$ , the values  $\Delta T = 1\text{h}$  and  $\Delta T = 10\text{ min}$  were examined in the publication **P-I**. The increase of the temporal resolution from  $\Delta T = 2\text{h}$  to  $\Delta T = 10\text{ min}$  allows for an improvement of more than 20%. Hence, the temporal output sampling of  $\Delta T = 10\text{ min}$  is referred to as high temporal resolution for GIMs provided by means of IONEX. The spatial resolution concerns only the *Product of Type 2a* and corresponds to the spatial sampling intervals on a regular grid. Usually global VTEC maps are created with spatial output sampling intervals of  $\Delta\Phi = 2.5^\circ$  in latitude and  $\Delta\Lambda = 5^\circ$  in longitude direction. Higher resolutions of  $1^\circ \times 1^\circ$  are possible, but according to the publication **P-III** they increase the size of the dissemination files and are therefore inconvenient.

With regard to question b):

In the publication **P-I**, as well as in Section 4.6.1, the inequalities (4.40) have been derived. These allow the comparison of the spectral resolution generated by means of B-splines with the maximum degree of a SH expansion. It could be determined that a B-spline model with level values  $J_1 = 4$  and  $J_2 = 3$  generates GIMs, which are comparable to the GIMs of the IAACs generated by means of SHs with a maximum degree  $n_{max} = 15$ , cf. Tab. 4.2. A comparison of the high-resolution B-spline GIM based on  $J_1 = 5$  and  $J_2 = 3$  with the B-spline GIM based on  $J_1 = 4$  and  $J_3 = 3$  by means of the dSTEC analysis is shown in Tab. 5.3. As can be seen, significant improvements in terms of accuracy of the VTEC representation can be achieved by increasing the spectral resolution. In the publication **P-I** a similar comparison was made and an improvement of up to 11% could be shown.

#### **Achieved Goals:**

In fact, the developed approach for global modelling can handle data gaps appropriately by utilisation of the localising feature of the B-spline functions and allows for more precise GIMs. The main goals are emphasized:

- The global modelling procedure based on B-splines allows for generating high-spectral resolution models with a cutoff frequency  $n_{max} > 15$ .
- The increase of the values for the B-spline levels  $J_1$  and  $J_2$  allow for a more precise representation of the VTEC globally and yield an improvement of approximately 11% in accuracy.
- The temporal output sampling  $\Delta T$  between two estimated VTEC maps has a great influence on the accuracy of the VTEC values to be calculated. With the reduction from 2h to 10 min, improvements of more than 20% could be shown.

#### **Development of a regional densification by means of a regional B-spline expansion and a global background model**

##### **Q-3** Regional high-resolution modelling of the Vertical Total Electron Content

- a) What are the advantages of using RIMs compared to GIMs and which improvements in the representation of VTEC can be achieved?
- b) What is the scientific benefit of generating high-resolution regional models and what can they be used for?

These questions are subject to the publication **P-II**. Therein, the procedure of the TSM from Eq. (4.37) was developed. The TSM allows for the combination of a global background model representing the coarser structures and the regional densification accounting for the finer structures. The finer structures can only be generated where the sampling intervals  $\Delta\varphi$  and  $\Delta\lambda$  of the data are sufficiently small and allow the modelling of finer structures.

With regard to question a):

In Section 3.4, the distribution of GNSS networks and the distribution of the stations was discussed. Most of the continental regions are equipped with numerous GNSS observation stations, whereas in oceanic regions or at the polar caps stations are only sparsely located. Most of the continental stations provide their data operationally under the umbrella of global and regional networks, thus regional models can be set up. In the framework of the TSM, a densification is applied to those areas of dense data coverage. Considering the requirements on the region size (4.54), the regional densification model (4.52) can be set up. It is assumed that the observations within the region contain information which cannot be represented by the global model due to the truncation at a maximum level value for  $J_1$  and  $J_2$ . A higher resolution is generated by summing both models in the sense of the TSM from Section 4.6. By means of the inequalities (4.55) and by using the look-up table in Fig. 4.9, the approximate spectral resolution of the total VTEC within the region can be determined.

With regard to question b):

The use of high-resolution VTEC maps is of great importance to science, as it enables the investigation of small-scale variations such as TIDs and plasma bubbles. In general, different types of TIDs are distinguished on the basis of their spatial extent and their propagation velocity. In Section 2.2.2, TIDs are divided into LSTIDs with a wavelength of about 1000 km, i.e. about  $9^\circ$  extent, MSTIDs with a wavelength up to 300 km, i.e. about  $2.7^\circ$  extent and SSTIDs with a wavelength smaller than 50 km, i.e. smaller than  $0.5^\circ$  extent. These structures are only recognisable in VTEC maps if they have a correspondingly high spectral resolution. The regional VTEC products for Europe shown in Sections 5.1.1, 5.1.2 and 5.1.2 are in line with this resolution. Using the inequalities (4.55), a spectral resolution of  $n_{max} = 64$  in the latitude direction and  $n_{max} = 48$  in longitude direction can be calculated for the B-spline model with level values  $J_3 = 3$  and  $J_4 = 4$ , applied to a region of size  $25^\circ$  and  $35^\circ$  in latitude and longitude directions, respectively. This corresponds to the wavelengths of  $L_\varphi = 5.6^\circ$  and  $L_\lambda = 7.6^\circ$  and allows a representation of TIDs. In this context, the advantage of the MSA should also be mentioned. By using the pyramid algorithm (4.60), the signal can be split into a smoothed version and detail signals. Since the large variations must be eliminated in order to detect TIDs, the analysis of the detail signal enables the detection of the aforementioned LSTIDs and MSTIDs.

#### **Achieved Goals:**

The method for the regional densification was published in the first-author publication **P-II** and depends on a given global model in the sense of TSM. The following goals have been achieved:

- The global background map generated with a B-spline model with levels  $J_1 = 4$  and  $J_2 = 3$  is the first step of the TSM and represents the long-period signal structures, which are comparable to the GIMs with a SH model of maximum degree  $n_{max} = 15$ . In the second step, the regional B-spline model is exemplarily applied to Europe in **P-II**. The densification leads to an improved representation of VTEC with higher spectral resolution.
- In addition to the improved spectral resolution, the TSM enables the dissemination of both the global and the regional model. It is worth mentioning that the regional densification can be applied to different regions in parallel, as long as the criteria from the discussion of question a) are considered.

- By means of the TSM finer structures can be modelled, which allow the analysis of LSTIDs and MSTIDs, as described in the discussion of question b).

## Dissemination of high-resolution products

### Q-4 Strategy for the dissemination and use of high-resolution VTEC products

- Which different kinds of ionosphere products can be defined and what is the related appropriate dissemination strategy?
- How can the VTEC products be disseminated to users within the required time using typical data formats and what are the limitations in terms of accuracy?

These questions are subject to publication **P-III**. Therein, the last step in the processing chain in Fig. 5.7 was discussed in order to make the generated high-resolution products available to a user. For this purpose, given data formats must be used for dissemination and the estimated high-resolution VTEC products have to be adapted to satisfy the format specifications.

With regard to question a):

In the publications **P-I** and **P-II**, different global and regional ionospheric products were introduced. In general, a distinction is made between two different product types, namely (1) the coefficient-based products which are in Chapter 5 referred to as *Product Type 1* and (2) grid-based products referring to *Product Type 2*. The latter comprise evaluated values of VTEC on a regular grid with arbitrary spatial sampling intervals  $\Delta\Phi$  and  $\Delta\Lambda$ . *Product Type 1*, however, has the great advantage that VTEC values can be calculated at arbitrary points using the given coefficients, whereas by using *Product Type 2* an interpolation has to be performed, which may cause degeneration. The temporal resolution can be equally selected for both product types. This means that the coefficient values and the grid values can be estimated and disseminated with the same temporal sampling interval  $\Delta T$ .

Figure 6.2 shows in a flowchart how the different product types are connected. As can be seen, both product types comprise different sub-products. The *Product Type 1* is thus subdivided into the global *Product Type 1a* and the regional *Product Type 1b*. The coefficient-based products allow for a further division by means of the MSA, which is subject to **P-I** and repeated within this thesis in Section 4.6.1. As described, the MSA can be applied to both model steps of the TSM. As an example, the original global B-spline model  $(\hat{d}_{\text{glob}}^{J_1, J_2}, \hat{\sigma}_{d, \text{glob}}^{J_1, J_2})$  can be separated into a smoothed signal  $(\hat{d}_{\text{glob}}^{J'_1, J'_2}, \hat{\sigma}_{d, \text{glob}}^{J'_1, J'_2})$  and various detail signals  $(\hat{c}_{\text{glob}}^{J'_1, J'_2}, \hat{\sigma}_{c, \text{glob}}^{J'_1, J'_2})$ .

The *Product Type 2* comprises three sub-products, with the *Product Type 2a* defined as a VTEC grid on a global scale and the *Product Type 2b* as the regional detail signal, as well as *2c* as the total signal on a regional scale. In the publication **P-III**, different data formats are discussed, which fit to the defined products of *Product Type 1* and *Product Type 2*. The IONEX format is grid-based and includes snapshot maps for successive epochs with arbitrary sampling intervals  $\Delta T$ . With the IONEX format, the *Product Type 2a-c* can be disseminated. Since the file size of IONEX increases extremely with increasing spatial and temporal sampling intervals, they are usually used for post-processing applications. For the dissemination of RT information about the ionosphere, the so-called SSR VTEC message is typically used. The SSR VTEC message is a streaming format, with which a user can correct the ionospheric delay on positioning in RT applications. The SSR VTEC message supports coefficient-based products and it is therefore used for dissemination of *Product Type 1*.

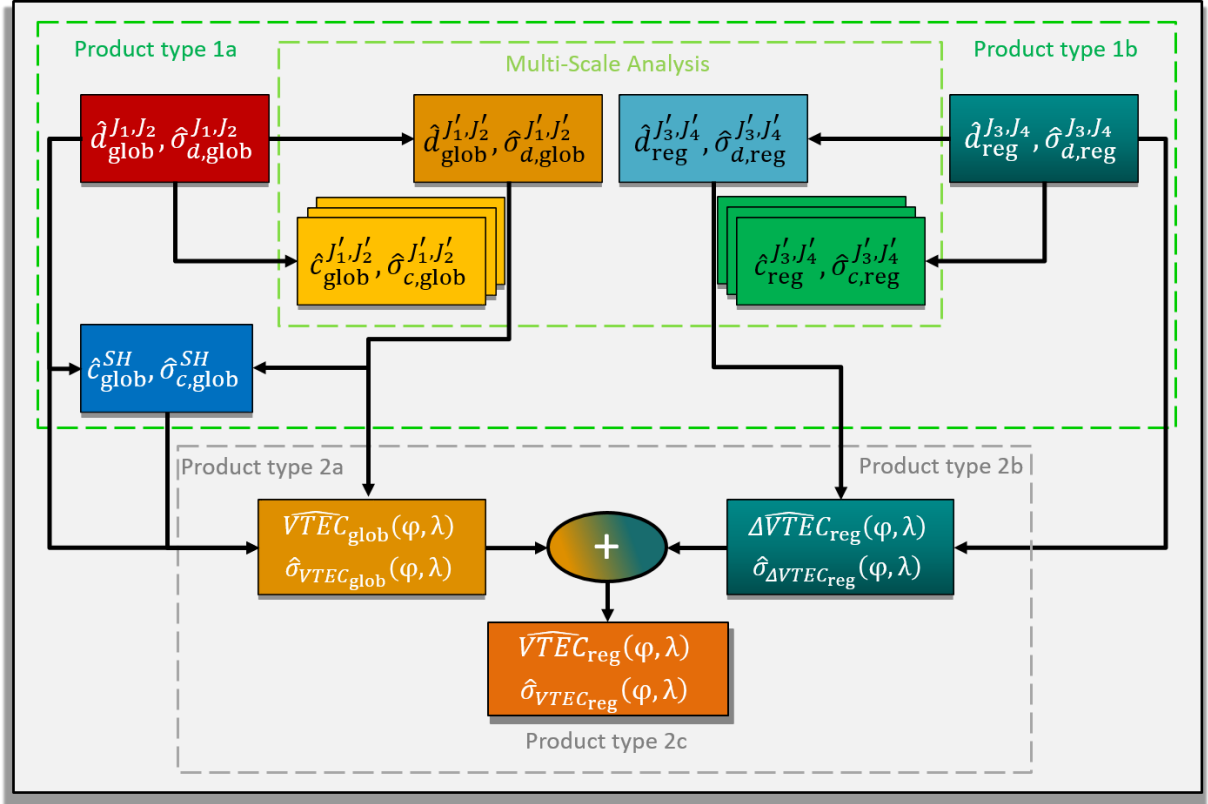


Figure 6.2: Defined *Product Type 1* and *Product Type 2* with the corresponding global and regional sub-products a), b) and c). By applying the pyramid algorithm (4.49) and (4.60) for the global and regional models, respectively, as well as by applying the transformation (5.19) from B-spline coefficients to coefficients of the SHs, further sub-products of *Product Type 1* are defined.

With regard to question b):

The high-resolution products developed within this thesis require an adequate data format for a dissemination in RT. The SSR VTEC message is not suitable because it only allows coefficients of SHs up to a maximum degree of  $n_{max} = 15$ . Therefore, the transformation (5.19) has been developed in **P-III**, which transforms the high-resolution global products into SHs coefficients ( $\hat{c}_{glob}^{SH}, \hat{\sigma}_{c, glob}^{SH}$ ). These coefficients correspond to the *Product Type 1* and listed in Fig. 6.2 accordingly. As shown in **P-III** and repeated in Section 5.2.3, a cutoff frequency of  $n_{max} = 34$  is needed to transform the high-resolution global map almost loss-free. The subsequent positioning test using single-frequency PPP shows that the positioning improves significantly with corrections of the transformed high-resolution map. Consequently, an enhancement of the maximum degree which is allowed by SSR VTEC message is required in order to meet the requirements of modern GNSS applications.

#### Achieved Goals:

- Definition of different product types for use for modern GNSS applications.
- Recommendation to modify the available formats for dissemination of high-resolution products, which allow a significant improvement in positioning compared to the conventionally used products

## 6.2 Outlook

As previously mentioned in the introduction, the number of different ionosphere models has increased in the last years. But what are the particular advantages of the different ionosphere models and what are they used for? In this thesis, the advantages of using B-splines to generate GIMs and RIMs were highlighted. It was shown that these models can be generated with high spectral, spatial and temporal resolution at low latency based on hourly GNSS data.

In the following a roadmap shows which further steps are necessary to make the developed products usable for modern GNSS applications. In addition, ideas are presented on how the methods described can be used and extended for scientific applications.

### Roadmap for the Use of High-Resolution VTEC Models for Modern GNSS Applications

A number of components along the processing chain for the generation of ionospheric products were examined and modified in detail in the last sections in order to generate high-resolution GIMs and RIMs with low latency. However, a further adaptation of the process is required when it comes to an operational use of the developed models for modern GNSS applications such as autonomous driving or precision agriculture. Two main topics are identified in this regard: (1) the decrease of the latency for the input data and (2) adaptation of the dissemination formats of RT products.

Regarding the first point, there are currently about 200 RT stations in the global IGS network that provide observations via streaming. Their global distribution is as inhomogeneous as the stations that provide hourly data. Further RT observations can be obtained from stations of regional networks via streaming, but the access is currently mostly limited. With the expansion of the GNSS networks and the improvements in the infrastructure there will be an increasing amount of stations in the future, which can provide their data via GNSS RT-data streams. Therefore, a reduction of the latency and a further development of the RT-GIM and RT-RIM can be carried out. According to Erdogan et al. (2021), however, various parameters in the KF procedure need to be adjusted, such as a more explicit treatment of DCBs and cycle slips in the estimation process.

Concerning the second aspect, a transformation has already been shown in this work that allows the developed global B-spline model to be made available to users in RT by means of the SSR VTEC message. However, there remains the problem of the limitation of the format to the maximum degree  $n_{max} = 16$  of the SHs. For the dissemination of high-resolution ionospheric corrections, the limitation of the degree needs to be changed in order to meet their requirements in accuracy. Since the new 5G standards allow higher bandwidths, larger amounts of data can be distributed via RT-streams for future applications, allowing the degree  $n_{max}$  to be increased within the SSR VTEC message. Nevertheless, this would only improve the spectral resolution of GIMs to be disseminated, but the limitation to a certain modelling approach remains. Therefore, a new specification of the data formats is necessary in the long run to ensure independence from the underlying processing methods for GIMs and RIMs. In this context, not only processing time for the transformation of non-SH models can be mitigated, but also regional products can be made available to users.

The approach based on MSA allows for a definition of a further B-spline based data format. By eliminating wavelet coefficients  $\tilde{c}_{glob}^{J'_1, J'_2}$  or  $\tilde{c}_{reg}^{J'_3, J'_4}$  of the detail signals, following certain significance criteria, data compression can be achieved. This enables high-resolution B-spline models to be disseminated to users in a compressed form via streaming. However, it is a prerequisite that users have an appropriate converter with which the compressed data can be read accordingly in order to extract high-resolution VTEC information for use.

### Roadmap for the Further use of High-Resolution VTEC Models in Science and Research

In sciences, VTEC maps serve as a basis for many applications. In this context, various focal points can be identified in which the VTEC maps developed within this dissertation are used. As mentioned in the introduction, the ionosphere is a manifestation of the space weather, i.e. the VTEC maps reflect the activity of the Sun. Two different phenomena must be distinguished:

1. The increase in electron density due to ionisation processes resulting from higher radiation activity (EUV, X-ray) of the Sun (cf. Tab. 2.1).
2. The injection of charged solar plasma into the Earth's atmosphere during a solar storm (cf. Tab. 2.2).

These phenomena mostly affect the day side of the ionosphere, but during extreme events, increased electron density values can also be seen on the night side of the Earth. By generating the GIMs with low latency, extreme changes can be detected at an early stage. However, in order to minimize the impact of space weather on the achievements of modern society, it is necessary to predict VTEC for time moments in the future. A considerable part of the scientific community is currently working on predicting the state of the ionosphere for future time moments. Often, forecast models are used in this context, which are developed and validated using time series of historical VTEC maps. In recent years, machine learning approaches such as neural networks have become more popular for predicting time series, which require a large amount of historical data to adjust their parameters accordingly. The B-spline models developed within this thesis are particularly suitable for the development of a forecast model, since the time series analysis can be based on the B-spline coefficients, thus, regional variations can also be taken into account, (Schmidt et al., 2017).

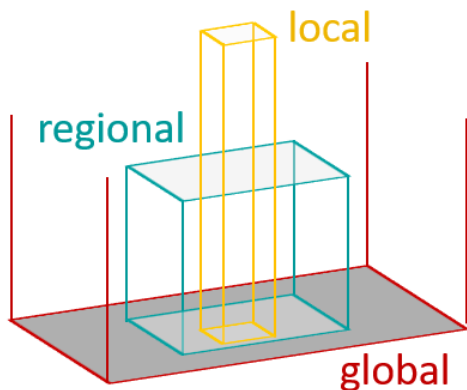


Figure 6.3: Schematic representation of a step model with three steps comprising a global model, a regional densification and a further densification for a local extend.

Another application of the developed VTEC models has already been discussed in connection with the research question **Q-4 b)**, where the use of high-resolution regional VTEC maps for the detection of small-scale ionospheric structures could be highlighted. Taking into account the corresponding spectral model resolution, it is possible to analyse the propagation of LSTIDs and MSTIDs. Indeed, in small areas over continents there is extremely dense coverage of stations where an extension of TSM is feasible. The extension by another level allows for creating the so-called local models for small areas, see Fig. 6.3. Assuming that the observations are available with sufficient accuracy, in a way that the satellite and receiver clocks as well as DCBs can be precisely determined, local models may even be able to take into account higher-order ionospheric effects.

As shown, the use of VTEC maps is diverse, yet the primary goal in ionospheric research is to model the structural changes in electron density and to understand physical relationships from them. It appears that using only GNSS observations is not sufficient for modelling electron density, since vertical variations cannot easily be determined by GNSS ground-based receivers. Ionosphere radio occultation (IRO) allows for determining the vertical structure of the electron density. Many other satellite missions, such as GRACE-FO and the MetOp satellites are equipped with occultation antennas and operate IRO. A larger



satellite-constellations performing IRO has to be mentioned in this context, namely the Formosat 3 /COSMIC I (2006-2015) constellation. A new edition of this constellation was launched in 2019 with the Formosat-7/COSMIC-2 satellites. Since the beginning of the year 2020, these satellites provide observations in the range between  $-40^\circ$  and  $40^\circ$  latitude with up to 19000 occultations per day. IRO is particularly advantageous because it not only provides information about the integrated effect of the ionosphere, i.e. the STEC, but also maps the vertical structure of the electron density. Information about the electron density retrieval can be found in Hernández-Pajares et al. (2000), Limberger et al. (2015). In order to be able to model the electron density

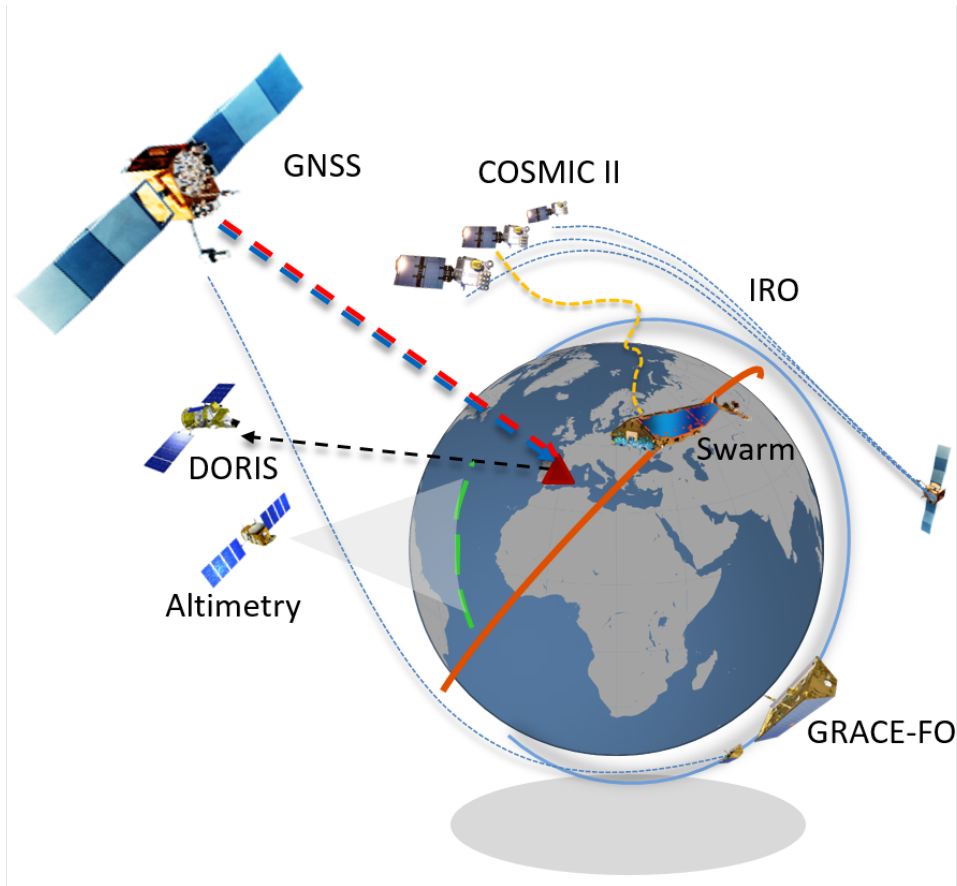


Figure 6.4: Schematic representation of different space geodetic observation techniques which can be used to improve the global data coverage.

with the highest possible resolution, it is necessary to combine as many different observations as possible, which are present at different altitudes and observed in different directions (Dettmering, 2003; Limberger, 2015), as shown in Fig. 6.4. It is worth mentioning the great advantage of using Altimetry and DORIS, which also provide observations over the oceans. To be more specific, Altimetry is mainly used for monitoring the oceans topography by measuring the distance between the ocean surface and the satellite by means of radio signals in nadir direction, whereas DORIS follows a similar measuring principle as GNSS and is intended to support methods for Precise Orbit Determination (POD). Thereby, the transmitting unit, the so-called DORIS-beacon, is mounted on the Earth's surface and the receiving unit on a satellite platform. Since DORIS beacons do not need a connection to the internet and only rely on electricity to transmit their signals, the beacons could be distributed homogeneously on a global scale, even on islands without connection to the internet. However, up to the present time, these observations can be used solely in post-processing approaches, since the observations have to be sent via downlink to



stations on the Earth's surface, which means that the observations can be made available for ionosphere modelling with a latency of several hours for Altimetry and even days for DORIS. Newest developments in the infrastructure intend to shorten the latency of these data allowing for a low-latency modelling of VTEC with higher accuracy over the oceans as well.

As long as all these observations are not available with sufficiently low latency, it is still necessary to use VTEC maps to represent the electron density with low latency in combination with information of the vertical structure of the ionosphere. To be more specific, the method of deriving the electron density from VTEC maps can be adapted from Aragon-Angel (2010) by dividing the electron density into a horizontal part, namely VTEC, and a vertical part using a height-dependent shape function; whereas the shape function can be obtained from any physical or empirical model, such as the International Reference Ionosphere (IRI).

In this thesis, the modelling by means of B-splines was applied primarily for VTEC. The time dependence of the VTEC products was modelled by a dynamical model relying on a random walk in the Sun-fixed coordinate system using a KF (Erdogan et al., 2017, 2020). Under the assumption that an optimal distribution of observations will be available in the future, the modelling approach using B-splines has particular advantages. To be more specific, B-splines are defined as 1-D functions and can be extended for several dimensions by multiplication and generation of multi-dimensional tensor products. By using the different types of B-spline, namely polynomial B-splines and trigonometric B-splines, global and regional or local models for the electron density can be developed. The modelling boundaries are therefore arbitrarily selectable for different temporal, latitudinal, longitudinal and altitude ranges. The flexible selection of the B-spline levels provides a further degree freedom, in a way that different spectral resolutions can be generated for different dimensions. B-splines provide the possibility to develop models which can be adapted temporally, spatially and spectrally to the type of target signal, such as TIDs and plasma bubbles. Hence, new generation of high-resolution ionosphere products can be expected in the future.



## 7 Content of the Publications

In the following, a short summary for each first-author publication and the co-author publication is given. Table 7.1 shows a classification of the contributions by A. Goss in percent for each publication.

Table 7.1: Contribution of the first Author to the publications

	first-author paper		
Paper	P-I	P-II	P-III
Idea and Paper Concept	70%	85%	90%
Computation and Realisation	80%	80%	90%
Analysis and Interpretation	85%	85%	90%
Figure and Table Compilation	95%	95%	95%
Manuscript Writing	85%	85%	90%
<b>Estimated Total Contribution</b>	<b>80%</b>	<b>85%</b>	<b>90%</b>

### 7.1 P-I

#### Reference

Andreas Goss, Michael Schmidt, Eren Erdogan, Barbara Görres, Florian Seitz (2019): **High-resolution vertical total electron content maps based on multi-scale B-spline representations** In: Annales Geophysicae 37(4), pp:699–717, DOI: 10.5194/angeo-37-699-2019

#### Copyright

This publication has originally been published in the open access journal ‘Annales Geophysicae’ and is available under the license of Creative Commons at <https://www.annales-geophysicae.net/>. The copyrights remain with the authors.

#### Summary Publication

The atmosphere and, in particular the electrons within the ionosphere, influence the propagation of electromagnetic waves in the atmosphere. For precise applications such as satellite-based navigation, i.e. GNSS positioning and navigation, it is necessary to correct the disturbances on the signal propagation. The International GNSS Service (IGS) and its Ionosphere Associated Analysis Centers (IAAC) routinely provide maps of the Vertical Total Electron Content (VTEC) of the ionosphere to correct for ionospheric delay. In general, the representation of a spherical function such as VTEC can be performed by means of a series expansion or by using a discretization technique. The selection of a suitable approach for ionosphere modelling means a trade-off between the distribution of available data and their possibility of representing ionospheric variations with high resolution and high accuracy. Thereby, a distinction must be made between spatial, temporal and spectral resolution.

Most of the IAACs generate VTEC maps based on a series expansion in terms of spherical harmonics (SH) up to the spectral degree  $n = 15$  and provide them with a spatial resolution of  $2.5^\circ \times 5^\circ$  with respect to the latitudinal and longitudinal directions, respectively, and a temporal sampling interval of 2 h. A SH series expansion with the degree  $n = 15$  allows a spatial resolution of  $12^\circ \times 12^\circ$ , hence, the higher spatial resolution is only possible by interpolation. Considering the accuracy requirements of modern GNSS applications, these models seem to be outdated and require an improvement in spectral resolution.

The modelling approach presented in this paper is based on localising basis functions, namely a series expansion in terms of polynomial and trigonometric B-splines. By applying the B-splines in the Sun-fixed geomagnetic (GSM) coordinate system, temporal variations, such as daily and sub-daily oscillations, are mitigated in VTEC. Thereby, the estimation of the unknown time-dependent coefficients is done by means of a Kalman filter (KF) with variable temporal step size. The procedure not only allows handling data gaps appropriately, it also sets up a multi-scale representation (MSR) to determine VTEC maps of different spectral resolution by applying the so-called pyramid algorithm. In a numerical example, the procedure is applied to data given in hourly data blocks. By means of the KF unknown series coefficients are estimated with a temporal sampling of 10 minutes and the MSR is applied in order to generate VTEC maps with different spectral resolutions.

## Declaration of Contribution

This paper has been published in the Journal 'Annales Geophysicae' and the content is based on the work carried out as part of the development process of the project OPTIMAP. OPTIMAP is a joint initiative of the Deutsches Geodätisches Forschungsinstitut der Technischen Universität München, Bundeswehr GeoInformation Centre (BGIC) and the German Space Situational Awareness Centre (GSSAC). The concept of the paper was proposed by A. Goss and discussed with the co-authors. The calculations are based on the software, partly developed by A. Goss in the project OPTIMAP. A. Goss performed the numerical investigations and compiled the figures and tables. The manuscript writing has been done by A. Goss and reviewed by all co-authors. **The overall own contribution of A. Goss for P-I is estimated at 80%**

We hereby confirm the correctness of the declaration of contribution and the reuse of the contents of the publication:

Andreas Goss, Michael Schmidt, Eren Erdogan, Barbara Görres, Florian Seitz (2019): High-resolution vertical total electron content maps based on multi-scale B-spline representations. In: Annales Geophysicae 37(4), pp:699–717, DOI: 10.5194/angeo-37-699-2019

apl. Prof. Dr. Michael Schmidt  
Deutsches Geodätisches Forschungsinstitut  
Technische Universität München, Germany

Signature: 

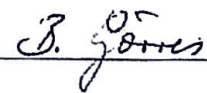
Date: 16.4.2021

Eren Erdogan  
Deutsches Geodätisches Forschungsinstitut  
Technische Universität München, Germany

Signature: 


Date: 16.04.2021

Dr. Barbara Görres  
Bundeswehr GeoInformation Centre (BGIC)  
Euskirchen, Germany

Signature: 

Date: 14.4.2021

Prof. Dr. Florian Seitz  
Deutsches Geodätisches Forschungsinstitut  
Technische Universität München, Germany

Signature:  Digital unterschrieben von Florian Seitz  
DN: cn=Florian Seitz, o=TUM, ou=DGFI-  
TUM, email=florian.seitz@tum.de, c=DE  
Date: 2021.04.09 14:32:04 +02'00'

Date: München, 9.4.2021



# High-resolution vertical total electron content maps based on multi-scale B-spline representations

Andreas Goss<sup>1</sup>, Michael Schmidt<sup>1</sup>, Eren Erdogan<sup>1</sup>, Barbara Görres<sup>2</sup>, and Florian Seitz<sup>1</sup>

<sup>1</sup>Deutsches Geodätisches Forschungsinstitut der Technischen Universität München,  
Arcisstraße 21, 80333 Munich, Germany

<sup>2</sup>Bundeswehr GeoInformation Centre (BGIC), Euskirchen, Germany

**Correspondence:** Andreas Goss (andreas.goss@tum.de)

Received: 28 February 2019 – Discussion started: 4 March 2019

Revised: 11 July 2019 – Accepted: 16 July 2019 – Published: 12 August 2019

**Abstract.** For more than 2 decades the IGS (International GNSS Service) ionosphere associated analysis centers (IAACs) have provided global maps of the vertical total electron content (VTEC). In general, the representation of a 2-D or 3-D function can be performed by means of a series expansion or by using a discretization technique. While in the latter case, pixels or voxels are usually chosen for a spherical function such as VTEC, for a series expansion spherical harmonics (SH) are primarily used as basis functions. The selection of the best suited approach for ionosphere modeling means a trade-off between the distribution of available data and their possibility of representing ionospheric variations with high resolution and high accuracy.

Most of the IAACs generate global ionosphere maps (GIMs) based on SH expansions up to the spectral degree  $n = 15$  and provide them with a spatial resolution of  $2.5^\circ \times 5^\circ$  with respect to the latitudinal and longitudinal directions, respectively, and a temporal sampling interval of 2 h. In recent years, it has frequently been claimed that the spatial resolution of the VTEC GIMs has to be increased to a spatial resolution of  $1^\circ \times 1^\circ$  and to a temporal sampling interval of about 15 min. Enhancing the grid resolution means an interpolation of VTEC values for intermediate points but with no further information about variations in the signal.  $n = 15$  in the SH case, for instance, corresponds to a spatial sampling of  $12^\circ \times 12^\circ$ . Consequently, increasing the grid resolution concurrently requires an extension of the spectral content, i.e., to choose a higher SH degree value than 15.

Unlike most of the IAACs, the VTEC modeling approach at Deutsches Geodätisches Forschungsinstitut der Technischen Universität München (DGFI-TUM) is based on local-

izing basis functions, namely tensor products of polynomial and trigonometric B-splines. In this way, not only can data gaps be handled appropriately and sparse normal equation systems be established for the parameter estimation procedure, a multi-scale representation (MSR) can also be set up to determine GIMs of different spectral content directly, by applying the so-called pyramid algorithm, and to perform highly effective data compression techniques. The estimation of the MSR model parameters is finally performed by a Kalman filter driven by near real-time (NRT) GNSS data.

Within this paper, we realize the MSR and create multi-scale products based on B-spline scaling, wavelet coefficients and VTEC grid values. We compare these products with different final and rapid products from the IAACs, e.g., the SH model from CODE (Berne) and the voxel solution from UPC (Barcelona). In contrast to the abovementioned products, DGFI-TUM's products are based solely on NRT GNSS observations and ultra-rapid orbits. Nevertheless, we can conclude that the DGFI-TUM's high-resolution product ("othg") outperforms all products used within the selected time span of investigation, namely September 2017.

## 1 Introduction

The properties of the atmosphere can be described by means of different variables, e.g., the temperature or the charge state. In the case of temperature, we distinguish between the troposphere (up to a height of about 15 km), the stratosphere (about 15 to 50 km), the mesosphere (about 50 to 90 km), the thermosphere (about 90 to 800 km) and the exosphere (above

800 km) using increasing height above the Earth's surface. In the case of the charge state, the atmosphere is split into the neutral atmosphere (up to a height of 80 km), the ionosphere (about 80 to 1000 km) and the plasmasphere (above 1000 km) (see, e.g., Limberger, 2015).

The ionosphere is mostly driven by the Sun; extreme UV (EUV), X-ray and solar particle radiation cause ionization processes. In geodesy, the main ionospheric impact is the influence of free electrons on radio wave propagation. This effect mainly depends on the signal frequency, i.e., the ionosphere is a dispersive medium (Schaer, 1999). Signals with frequencies lower than 30 MHz will be blocked and reflected by the ionosphere, whereas signals with shorter wavelengths penetrate the ionosphere but are affected with respect to speed and direction. The ionospheric influence on radio waves is twofold: the signal travel times are changed (delay) and the signal paths are modified (bending). While the latter effect can be neglected for most applications, the ionospheric delay

$$d_{\text{ion}} = \pm \frac{40.3}{f^2} \int_S^R N_e ds \quad (1)$$

depends directly on the electron density  $N_e$  along the signal path  $s$  between satellite  $S$  and receiver  $R$  and inversely on the carrier frequency  $f$ . Equation (1), which can be derived from dual-frequency measurements, is only an approximation as higher-order effects are neglected. These terms depend on the magnetic field, signal frequency, signal elevation, and ionospheric conditions and reach about 0.2 cm in zenith for GPS signals (Bassiri and Hajj, 1993). The sign on the right-hand side changes depending on whether it is applied for a carrier phase observation (“−”) or for a pseudorange measurement (“+”) (see, e.g., Langley, 1998).

Observations of space geodetic techniques, such as the global navigation satellite systems (GNSS) and the Doppler Orbitography and Radiopositioning Integrated by Satellite (DORIS) tracking system as well as satellite altimetry and ionospheric radio occultation (IRO) are based on electromagnetic signal propagation; thus, they are disturbed by the ionosphere. Most of the techniques are not directly sensitive to the electron density, but to the integrated effect along the ray path. In Eq. (1) the integral

$$\text{STEC}(\mathbf{x}^S, \mathbf{x}^R, t) = \int_S^R N_e(\mathbf{x}, t) ds \quad (2)$$

is called the slant total electron content (STEC). In Eq. (2), in addition to the time  $t$  we introduce the position vectors  $\mathbf{x}^S$   $\mathbf{x}^R$  and

$$\mathbf{x} = r [\cos \varphi \cos \lambda, \cos \varphi \sin \lambda, \sin \varphi]^T \quad (3)$$

of the satellite  $S$ , the receiver  $R$  and an arbitrary point  $P$  moving along the signal path  $s$ ; the coordinate triple  $(\varphi, \lambda, r)$

comprises latitude  $\varphi$ , longitude  $\lambda$  and radial distance  $r$  within a geocentric coordinate system  $\Sigma_E$ .

The vertical total electron content (VTEC),

$$\text{VTEC}(\varphi, \lambda, t) = \int_{h_l}^{h_u} N_e(\varphi, \lambda, h, t) dh, \quad (4)$$

is defined as the integration of the electron density in the vertical direction, i.e., along the height  $h$  above the Earth's surface, defined as  $h = r - R_E$ ;  $R_E$  refers to the radius of a spherical Earth. Furthermore, in Eq. (4)  $h_l$  and  $h_u$  are the respective heights of the lower and the upper boundary of the ionosphere (see, e.g., Dettmering et al., 2011, 2014; Limberger, 2015).

Equations (2) and (4) require a 3-D integration of the electron density. Often a simplification is preferred which is based on the so-called single-layer model (SLM). It assumes that all free electrons are concentrated in an infinitesimally thin shell, i.e., the sphere  $\Omega_H$  with radius  $R_H = R_E + H$  (Schaer, 1999), where  $H$  is the single-layer height. As a consequence of this assumption and according to

$$\text{STEC}(\mathbf{x}^S, \mathbf{x}^R, t) = M(z) \cdot \text{VTEC}(\mathbf{x}_{\text{IPP}}, t), \quad (5)$$

VTEC can be transformed into STEC by introducing a mapping function  $M(z)$  depending on the zenith angle  $z$  of the ray path between satellite  $S$  and receiver  $R$ . In Eq. (5) the position vector  $\mathbf{x}_{\text{IPP}}$ , i.e., the spherical coordinates  $(\varphi_{\text{IPP}}, \lambda_{\text{IPP}}, R_H)$  define the ionospheric pierce point (IPP), which refers to the geometrical piercing point of the straight line between  $S$  and  $R$  with the sphere  $\Omega_H$  of the SLM. This point denotes the reference point of an observation including the STEC, such as a GNSS measurement (see, e.g., Erdogan et al., 2017). Figure 1 shows, for instance, the global distribution of the IPPs from GNSS observations on 6 September 2017 between 12:55 and 13:05 UT. However, it must be pointed out that the introduction of a simple isotropic mapping function  $M(z)$ , depending solely on the zenith angle  $z$ , can only generate an approximation of STEC. Recently, more sophisticated approaches, e.g., the Barcelona ionospheric mapping function (BIMF), have been developed to improve the projection of VTEC on STEC (see, e.g., Lyu et al., 2018).

Combining Eqs. (1), (2) and (5) yields the relation

$$d_{\text{ion}}(\mathbf{x}^S, \mathbf{x}^R, t) = -\frac{40.3}{f^2} \cdot M(z) \cdot \text{VTEC}(\mathbf{x}_{\text{IPP}}, t) \quad (6)$$

between VTEC and the ionospheric delay  $d_{\text{ion}}$  in the case of a phase observation. Equation (6) can be interpreted and applied in two ways:

- if VTEC is given from an ionospheric model, the delay  $d_{\text{ion}}$  can be computed and used as a correction for GNSS observations;
- or if the delay  $d_{\text{ion}}$  can be derived from double-frequency GNSS measurements, it can be used as an observation to develop or improve VTEC models.



Applications, such as satellite navigation and positioning require high-precision and high-resolution VTEC models. For this purpose the correction  $d_{\text{ion}}$  could, according to Eq. (6), be derived from VTEC maps, usually the so-called global ionosphere maps (GIM). The most prominent GIM is provided by the International GNSS Service (IGS) (Feltens and Schaer, 1998; Hernández-Pajares et al., 2011) as a weighted combination product of VTEC maps from various IGS ionosphere associated analysis centers (IAACs), namely (1) the Jet Propulsion Laboratory (JPL), (2) the Center for Orbit Determination in Europe (CODE), (3) the European Space Operations Center of the European Space Agency (ESOC), (4) the Universitat Politècnica de Catalunya (UPC), (5) the Canadian Geodetic Survey of Natural Resources Canada (NRCan), (6) the Wuhan University (WHU) and (7) the Chinese Academy of Sciences (CAS). Recently, Roma-Dollase et al. (2017) published a review paper on these seven GIMs concerning their mapping techniques and their consistency during one solar cycle.

There are several modeling strategies for generating GIMs; the most prominent approach is based on spherical harmonics (SH) and was introduced by Schaer (1999). Further approaches include the tomographic approach based on voxels (Hernández-Pajares et al., 1999) and other approaches based on B-spline scaling functions and wavelets (Schmidt, 2007, 2015b; Schmidt et al., 2011), multivariate adaptive regression splines (MARS) and adaptive regression B-splines (BMARS) (Durmaz et al., 2010; Durmaz and Karslioglu, 2015), and polynomials (Komjathy and Langley, 1996).

Generally, we distinguish between GIMs provided as “final”, “rapid”, “near real-time” (NRT) or “real-time” (RT) products. This classification is based on the latency of the underlying input data. For final products, for instance, only post-processed observations and orbits are used, whereas NRT products are based on rapid orbits and observations with a latency of some minutes up to a few hours. GIMs are typically provided with a temporal resolution of 1 or 2 h and with a spatial resolution of  $2.5^\circ \times 5^\circ$  with respect to geographical latitude and longitude (Hernández-Pajares et al., 2017).

VTEC variations basically follow annual, seasonal, diurnal and semidiurnal periods. Earthquakes or incidental natural hazards can also cause small but visible signatures (Liu et al., 2004; Zhu et al., 2013). However, during space weather events, such as solar flares or coronal mass ejections (CME), the number of free electrons may drastically increase. In the latter case, solar plasma consisting of electrons, ions and photons may enter the Earth’s atmosphere and cause short period variations within the electron density distribution (see, e.g., Monte-Moreno and Hernández-Pajares, 2014; Wang et al., 2016; Tsurutani et al., 2006, 2009). As a consequence, the modeling of the disturbed ionosphere requires both a high temporal and a high spatial resolution. In 2012, during the IGS 2012 workshop in Olsztyn, Poland, it was recommended that high-resolution IGS combined GIMs be provided. The UPC and JPL IAACs agreed on disseminat-

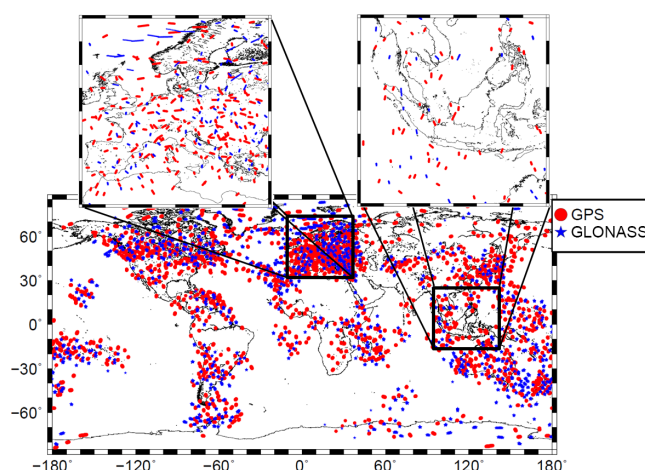


**Figure 1.** Global distribution of the IPPs from GPS (red dots) and GLONASS (blue stars) measurements for 6 September 2017 collected within a 10 min interval between 12:55 and 13:05 UT. The regional maps at the top are “zoom-ins” of Europe and Indonesia.

ing GIMs with a temporal resolution of 15 min and a spatial resolution of  $1^\circ \times 1^\circ$  with respect to latitude and longitude, respectively (Dach and Jean, 2013).

As already confirmed by Roma-Dollase et al. (2017), an increase in temporal resolution allows for an improvement in the overall accuracy of the GIMs. The authors compared the final products with a temporal resolution of 2 h with rapid products with a temporal resolution of 15 min using the dSTEC analysis, which is the most reliable method of assessing the accuracy of VTEC products (Hernández-Pajares et al., 2017). Following the results of their investigations, it can be stated that an increase in the temporal resolution yields better results in the dSTEC analysis.

To the knowledge of the authors, the spatial resolution of GIMs has not been investigated in detail to date. Most of the GIMs are based on series expansions in terms of SHs with a maximum degree of  $n_{\text{max}} = 15$ . This value fits to a block size of about  $12^\circ \times 12^\circ$  on the sphere  $\Omega_H$ . In contrast, a grid spacing of  $2.5^\circ \times 5^\circ$  corresponds to a maximum SH degree of around  $n = 36$ ; a  $1^\circ \times 1^\circ$  grid spacing, i.e., a spatial resolution of around 110 km along the Equator fits to a SH expansion up to degree  $n = 180$ . As a matter of fact, a reliable computation of the corresponding SH series coefficients requires a global input data coverage of the same spatial sampling. As the IAAC VTEC maps are based solely on GNSS observations with a rather inhomogeneous distribution (cf. Fig. 1 showing the IPPs of NRT observations with dense clusters over continents and large data gaps over oceans), finer ionospheric structures can only be monitored and modeled where high-resolution input data are available.

By increasing the temporal resolution of the GIMs, the number of observations supporting the individual maps decreases. The two “zoom-in” maps at the top of Fig. 1 show the strong incongruity between the data distribution and the



signal structure (cf. Fig. 9a, c). In areas with high-resolution data, such as Europe, the US or Australia, the VTEC signal is usually rather smooth. In areas with highly variable spatial and temporal signal structures such as in the equatorial belt, a much smaller number of observations is generally given. As a consequence, for global modeling we have to deal with a trade-off between signal structure and data resolution.

It is a well-known fact that SHs as global basis functions are not suitable for representing unevenly, globally distributed data. Consequently, in such cases, a series expansion in terms of localizing basis functions is more appropriate. In the following, we apply tensor products of polynomial and trigonometric B-splines as localizing 2-D basis functions. Besides the localizing features, B-splines additionally generate a multi-scale representation (MSR), also known as multi-resolution representation (MRR). The basic feature of a MSR is to split a target function into a smoothed, i.e., low-pass-filtered version, and a number of detail signals, i.e., band-pass-filtered versions via successive low-pass filtering (Mertins, 1999). Hence, a spatial MSR of VTEC adapts the model resolution to the data distribution and, thus, fulfills IGS' requirement of high-resolution VTEC modeling.

In this study, we compare global VTEC maps based on series expansions in terms of both globally defined SHs and localizing B-spline functions, including the MSR with respect to the spectral content. For this purpose, we use the SH degree as the common measure for the spectral content of a spherical signal. In detail, we study the interrelations between the SH degree, the spatial sampling intervals of the input data and the resolution levels of B-spline expansions. In addition, we discuss the influence of different temporal resolutions of the GIMs. For the estimation of the unknown series coefficients of the B-spline expansion, we use a Kalman filter (KF) procedure as explained by Erdogan et al. (2017). In order to assess the quality of the approach, we perform a dSTEC analysis (Hernández-Pajares et al., 2017).

The paper is outlined as follows: in Sect. 2 a description of VTEC modeling procedures based on both, SH and B-spline expansions are presented. In Sect. 2.3 we study the spectral resolution of global VTEC maps. Section 3 comprises a detailed description of the MSR and the estimation procedure. In Sect. 4 case studies are set up to verify the results of the previous sections numerically. Furthermore, this section provides a final assessment by means of a dSTEC validation. The final section provides conclusions and an outlook for future work.

## 2 VTEC modeling approaches

The 3-D signal  $VTEC(\varphi, \lambda, t) = f(\mathbf{x}, t)$ , introduced in Eqs. (4) and (5), can be modeled as series expansion

$$f(\mathbf{x}, t) = \sum_{k=0}^{\infty} c_k(t) \phi_k(\mathbf{x}) \quad (7)$$

in terms of given space-dependent basis functions  $\phi_k(\mathbf{x})$  and unknown time-dependent series coefficients  $c_k(t)$ .<sup>1</sup> Assuming that at discrete times  $t_s = t_0 + s \cdot \Delta t$  with  $s \in \mathbb{N}_0$  and sampling interval  $\Delta t$  the total number of  $I_s$  observations  $y(\mathbf{x}_{i_s}, t_s)$  of VTEC at IPP position  $P_{i_s} \in \Omega_H$  with  $i_s = 1, 2, \dots, I_s$  are given. Considering the measurement errors  $e(\mathbf{x}_{i_s}, t_s)$ , the observation equation follows from Eq. (7) and reads

$$\begin{aligned} y(\mathbf{x}_{i_s}, t_s) + e(\mathbf{x}_{i_s}, t_s) &= f_N(\mathbf{x}_{i_s}, t_s) = \\ &= \sum_{k=0}^N c_k(t_s) \phi_k(\mathbf{x}_{i_s}). \end{aligned} \quad (8)$$

Note, that we neglect the truncation error in the following

$$r_N(\mathbf{x}_{i_s}, t_s) = \sum_{k=N+1}^{\infty} c_k(t_s) \phi_k(\mathbf{x}_{i_s}) \quad (9)$$

and omit other unknown parameters such as the satellite and receiver differential code biases (DCB) for GNSS geometry-free observations on the right-hand side of Eq. (8) (see, e.g., Erdogan et al., 2017).

In the following (Sect. 2.1 and 2.2), the SH expansion – as likely the most frequently used approach in ionosphere modeling – and the 2-D B-spline tensor product approach are described.

### 2.1 Spherical harmonic expansion

In the SH approach, the observation equation, Eq. (8), can be rewritten as

$$\begin{aligned} y(\mathbf{x}_{i_s}, t_s) + e(\mathbf{x}_{i_s}, t_s) &= f_{n_{\max}}(\mathbf{x}_{i_s}, t_s) = \\ &= \sum_{n=0}^{n_{\max}} \sum_{m=-n}^n c_{n,m}(t_s) Y_{n,m}(\mathbf{x}_{i_s}), \end{aligned} \quad (10)$$

where the functions  $Y_{n,m}(\mathbf{x})$ , i.e., the SHs of degree  $n = 0, \dots, n_{\max}$  and order  $m = -n, \dots, n$ , are defined as

$$Y_{n,m}(\mathbf{x}) = P_{n,|m|}(\sin \varphi) \cdot \begin{cases} \cos m\lambda & \text{if } m \geq 0 \\ \sin |m|\lambda & \text{if } m < 0 \end{cases} \quad (11)$$

with  $P_{n,|m|}$  being the normalized associated Legendre functions of degree  $n$  and order  $m$ . The total  $(n_{\max}+1)^2$  quantities  $c_{n,m}(t)$  in Eq. (10) are the time-dependent SH coefficients. According to the sampling theorem on the sphere, the maximum degree  $n_{\max}$  is related to the sampling intervals  $\Delta\varphi$  and  $\Delta\lambda$  of the input data with respect to latitude  $\varphi$  and longitude  $\lambda$ , namely

$$\Delta\varphi < \frac{180^\circ}{n_{\max}} \quad \text{and} \quad \Delta\lambda < \frac{180^\circ}{n_{\max}}. \quad (12)$$

As can be seen from Eq. (11), SHs are basis functions of global support. This implies that each single SH function

<sup>1</sup>Note that we do not distinguish between geographical and geomagnetic spherical coordinates for latitude  $\varphi$  and longitude  $\lambda$ .

is different from zero almost everywhere on the sphere  $\Omega_H$ . Consequently, each coefficient  $c_{n,m}$  has to be recomputed if only one additional observation is considered in the set of observation Eq. (10).

As the VTEC observations  $y(\mathbf{x}_{i_s}, t_s)$  at the IPP positions will usually not be given on a spatial grid with constant mesh size, the sampling intervals  $\Delta\varphi$  and  $\Delta\lambda$  in the formulae of Eq. (12) have to be interpreted as global average values.

## 2.2 B-spline expansion

At DGFI-TUM we rely on B-splines as basis functions for ionosphere modeling, as they are (1) characterized by their localizing feature and (2) they can be used to generate a MSR. For VTEC modeling we rewrite Eq. (8) as

$$y(\mathbf{x}_{i_s}, t_s) + e(\mathbf{x}_{i_s}, t_s) = f_{J_1, J_2}(\mathbf{x}_{i_s}, t_s) = \sum_{k_1=0}^{K_{J_1}-1} \sum_{k_2=0}^{K_{J_2}-1} d_{k_1, k_2}^{J_1, J_2}(t_s) \phi_{k_1, k_2}^{J_1, J_2}(\varphi_{i_s}, \lambda_{i_s}) \quad (13)$$

with initially unknown time-dependent scaling coefficients  $d_{k_1, k_2}^{J_1, J_2}(t_s)$  and the 2-D scaling functions  $\phi_{k_1, k_2}^{J_1, J_2}(\varphi_{i_s}, \lambda_{i_s})$  of levels  $J_1$  and  $J_2$  with respect to  $\varphi$  and  $\lambda$ . The latter are defined as tensor products

$$\phi_{k_1, k_2}^{J_1, J_2}(\varphi, \lambda) = \phi_{k_1}^{J_1}(\varphi) \tilde{\phi}_{k_2}^{J_2}(\lambda) \quad (14)$$

of the 1-D scaling functions  $\phi_{k_1}^{J_1}(\varphi)$  and  $\tilde{\phi}_{k_2}^{J_2}(\lambda)$  depending on latitude  $\varphi$  and longitude  $\lambda$ , respectively. As the B-spline approach is not as well known as the SH approach, it will be described in more detail in the following; we further refer to Dierckx (1984); Stollnitz et al. (1995a, b); Lyche and Schumaker (2001); Jekeli (2005); Schmidt (2015b) and citations therein.

To decompose VTEC into its spectral components via the MSR in Sect. 3, Eqs. (13) and (14) need to be rewritten in vector and matrix notation. For this purpose we introduce the  $K_{J_1} \times 1$  vector

$$\boldsymbol{\phi}_{J_1}(\varphi) = [\phi_0^{J_1}(\varphi), \phi_1^{J_1}(\varphi), \dots, \phi_{K_{J_1}-1}^{J_1}(\varphi)]^T, \quad (15)$$

the  $K_{J_2} \times 1$  vector

$$\tilde{\boldsymbol{\phi}}_{J_2}(\lambda) = [\tilde{\phi}_0^{J_2}(\lambda), \tilde{\phi}_1^{J_2}(\lambda), \dots, \tilde{\phi}_{K_{J_2}-1}^{J_2}(\lambda)]^T \quad (16)$$

and the  $K_{J_1} \times K_{J_2}$  coefficient matrix

$$\mathbf{D}_{J_1, J_2} = \begin{bmatrix} d_{0,0}^{J_1, J_2} & d_{0,1}^{J_1, J_2} & \dots & d_{0, K_{J_2}-1}^{J_1, J_2} \\ d_{1,0}^{J_1, J_2} & d_{1,1}^{J_1, J_2} & \dots & d_{1, K_{J_2}-1}^{J_1, J_2} \\ \vdots & \vdots & \ddots & \vdots \\ d_{K_{J_1}-1,0}^{J_1, J_2} & d_{K_{J_1}-1,1}^{J_1, J_2} & \dots & d_{K_{J_1}-1, K_{J_2}-1}^{J_1, J_2} \end{bmatrix}. \quad (17)$$

Considering the computation rules for the Kronecker product “ $\otimes$ ” (cf. Koch, 1999), Eq. (13) can be written as

$$f(\varphi, \lambda, t) = (\tilde{\boldsymbol{\phi}}_{J_2}(\lambda) \otimes \boldsymbol{\phi}_{J_1}(\varphi))^T \text{vec} \mathbf{D}_{J_1, J_2}(t) = \boldsymbol{\phi}_{J_1}^T(\varphi) \mathbf{D}_{J_1, J_2}(t) \tilde{\boldsymbol{\phi}}_{J_2}(\lambda), \quad (18)$$

where “vec” refers to the vec operator.

### 2.2.1 Polynomial B-splines

In the following, we apply polynomial quadratic B-splines

$$\phi_{k_1}^{J_1}(\varphi) := N_{J_1, k_1}^{J_1}(\varphi) \quad (19)$$

of resolution level  $J_1 \in \mathbb{N}_0$  and shift  $k_1 = 0, 1, \dots, K_{J_1} - 1$  to represent the latitude-dependent variations of VTEC. To be more specific, a total of  $K_{J_1} = 2^{J_1} + 2$  B-splines are located along a meridian depending on the latitude  $\varphi \in [-90^\circ, 90^\circ]$ . To construct the  $K_{J_1}$  B-spline functions, the sequence

$$\begin{aligned} -90^\circ = \varphi_0^{J_1} = \varphi_1^{J_1} = \varphi_2^{J_1} < \varphi_3^{J_1} < \dots < \varphi_{K_{J_1}}^{J_1} = \\ = \varphi_{K_{J_1}+1}^{J_1} = \varphi_{K_{J_1}+2}^{J_1} = 90^\circ \end{aligned} \quad (20)$$

of knot points  $\varphi_{k_1}^{J_1}$  is established; the consideration of multiple knot points at the poles is called “endpoint-interpolating” and ensures the closing of the modeling interval. The constant distance between two consecutive knots  $\varphi_{k_1}^{J_1}$  and  $\varphi_{k_1+1}^{J_1}$  for  $k_1 = 2, \dots, K_{J_1} - 1$  amounts to  $180^\circ/2^{J_1}$ . Following Schumaker and Traas (1991) and Stollnitz et al. (1995b) the normalized quadratic polynomial B-splines can be calculated via the recursive relation

$$\begin{aligned} N_{J_1, k_1}^n(\varphi) &= \frac{\varphi - \varphi_{k_1}^{J_1}}{\varphi_{k_1+n}^{J_1} - \varphi_{k_1}^{J_1}} N_{J_1, k_1}^{n-1}(\varphi) \\ &+ \frac{\varphi_{k_1+n+1}^{J_1} - \varphi}{\varphi_{k_1+n+1}^{J_1} - \varphi_{k_1+1}^{J_1}} N_{J_1, k_1+1}^{n-1}(\varphi), \end{aligned} \quad (21)$$

with  $n = 1, 2$  from the initial values

$$N_{J_1, k_1}^0(\varphi) = \begin{cases} 1 & \text{if } \varphi_{k_1}^{J_1} \leq \varphi < \varphi_{k_1+1}^{J_1} \text{ and } \varphi_{k_1}^{J_1} < \varphi_{k_1+1}^{J_1} \\ 0 & \text{otherwise} \end{cases}.$$

Note, in Eq. (21) a factor is set to zero if the denominator is equal to zero.

As can be seen from Fig. 2, B-splines are characterized by their compact support or – in other words – they are different from zero only within a small subinterval of length  $\Delta_{J_1} \approx 3 \cdot h_{J_1}$ , where

$$h_{J_1} = \frac{180^\circ}{2^{J_1} + 1} \quad (22)$$

refers to the approximate distance between two consecutive B-splines along the meridian. As the total number  $K_{J_1}$  of B-splines depends on the level  $J_1$ , finer structures can be modeled by increasing  $J_1$ . The numerical value for the level  $J_1$  depends on the global average value  $\Delta\varphi$  for the input data sampling interval in the latitudinal direction according to

$$\Delta\varphi < h_{J_1} \quad (23)$$

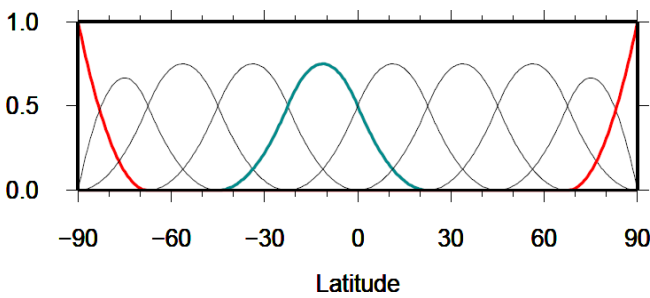


**Figure 2.** Polynomial B-splines of level  $J_1 = 3$  with a total number  $K_{J_1} = 2^3 + 2 = 10$  of B-splines along the meridian. The blue spline function  $N_{3,4}^2(\varphi)$  corresponds to the shift value  $k_1 = 4$  and covers a subinterval of length  $\Delta_3 \approx 3 \cdot 180^\circ / 9 = 60^\circ$ . The red spline functions  $N_{3,0}^2(\varphi)$  with shift value  $k_1 = 0$  and  $N_{3,9}^2(\varphi)$  with shift value  $k_1 = 9$  close the modeling interval at the poles.

(Schmidt et al., 2011). Solving Eq. (23), considering the level value  $J_1$  from Eq. (22), the inequality

$$J_1 \leq \log_2 \left( \frac{180^\circ}{\Delta\varphi} - 1 \right) \quad (24)$$

results.

### 2.2.2 Trigonometric B-splines

For modeling the longitudinal variations of VTEC trigonometric B-splines  $T_{J_2,k_2}^3(\lambda)$  of order 3 and, depending on the resolution level,  $J_2 \in \mathbb{N}_0$  and shift  $k_2 = 0, 1, \dots, K_{J_2} - 1$  are applied. As can be seen from Fig. 3, the total number  $K_{J_2} = 3 \cdot 2^{J_2}$  of trigonometric B-splines are located along the parallels of the chosen spherical coordinate system within the interval  $\lambda \in (0^\circ, 360^\circ)$ . Consequently, the first and the last two B-spline functions within the interval  $(0^\circ, 360^\circ)$  have to be completed by the so-called “wrapping around” effect. This constraint allows trigonometric B-splines to be defined in two different ways:

1. Following Schumaker and Traas (1991), Jekeli (2005) and Limberger (2015) periodic trigonometric B-splines can be calculated by means of a recurrence relation similar to Eq. (21). Thereby, additional constraints have to be introduced to force the periodicity of the series coefficients.
2. The second option was introduced by Lyche and Schumaker (2001) and used by Schmidt et al. (2011) and Schmidt (2015b). It will be described in the following in more detail.

To be more specific, the sequence of nondecreasing knot points

$$0^\circ = \lambda_0^{J_2} < \lambda_1^{J_2} < \dots < \lambda_{K_{J_2}-1}^{J_2} < 360^\circ, \quad (25)$$

with additional knots

$$\lambda_{K_{J_2}+i}^{J_2} = \lambda_i^{J_2} + 360^\circ \quad \text{for } i = 0, 1, 2 \quad (26)$$

for considering the periodicity is introduced. Similar to the polynomial B-splines, the distance between consecutive knots  $\lambda_{k_2}^{J_2}$  and  $\lambda_{k_2+1}^{J_2}$  for  $k_2 = 0, 1, \dots, K_{J_2} + 1$  is given as

$$h_{J_2} = \frac{360^\circ}{K_{J_2}} = \frac{120^\circ}{2^{J_2}}; \quad (27)$$

thus, the length of the nonzero subinterval of a trigonometric B-spline function  $T_{J_2,k_2}^3(\lambda)$  reads  $\Delta_{J_2} = 3 \cdot h_{J_2} = 360^\circ / 2^{J_2}$ . Following Lyche and Schumaker (2001) we define the functions

$$M_{J_2,k_2}(\lambda) = T_{J_2,k_2}^3(\lambda) = T_{h_{J_2}}^3(\lambda - \lambda_{k_2}^{J_2}). \quad (28)$$

Setting  $h_{J_2} = h$  and  $\lambda - \lambda_{k_2}^{J_2} = \Theta$  for the sake of simplification, the functions  $T_{h_{J_2}}^3(\lambda - \lambda_{k_2}^{J_2}) = T_h^3(\Theta)$  can be calculated via

$$T_h^3(\Theta) = \begin{cases} \frac{\sin^2(\Theta/2)}{\sin(h/2)\sin(h)} & \text{for } 0 \leq \Theta < h \\ \frac{1}{\cos(h/2)} - \frac{\sin^2((\Theta-h)/2) + \sin^2((2h-\Theta)/2)}{\sin(h/2)\sin(h)} & \text{for } h \leq \Theta < 2h \\ \frac{\sin^2((3h-\Theta)/2)}{\sin(h/2)\sin(h)} & \text{for } 2h \leq \Theta < 3h \\ 0 & \text{otherwise.} \end{cases} \quad (29)$$

Finally, we define the basis functions

$$\tilde{\phi}_{k_2}^{J_2}(\lambda) = \begin{cases} M_{J_2,k_2}(\lambda) & \text{for } k_2 = 0, \dots, K_{J_2} - 3 \\ M_{J_2,k_2}(\lambda) + M_{J_2,k_2}(\lambda - 360^\circ) & \text{for } k_2 = K_{J_2} - 2, K_{J_2} - 1 \end{cases} \quad (30)$$

introduced in Eq. (14). Figure 3 shows trigonometric B-splines of level  $J_2 = 2$ . With larger values for level  $J_2$  the splines become more narrow and finer structures can be modeled. The choice of the level value  $J_2$  again depends on the input data sampling interval. Analog to Eq. (23), the inequality

$$\Delta\lambda < h_{J_2} \quad (31)$$

has to be fulfilled, where  $\Delta\lambda$  denotes the global average value of the data sampling interval in the longitudinal direction. Finally, taking Eq. (27) into consideration, the inequality

$$J_2 \leq \log_2 \left( \frac{120^\circ}{\Delta\lambda} \right) \quad (32)$$

for the level value  $J_2$  is obtained.

### 2.3 Spectral resolution of global VTEC models

In Sect. 2.1 we derived the relations between the maximum degree  $n_{\max}$  of a SH expansion and the sampling intervals  $\Delta\varphi$  and  $\Delta\lambda$  of the input data. In Sect. 2.2 the corresponding relations between the level values  $J_1$  and  $J_2$  of a B-spline expansion and the data sampling intervals have been deduced.

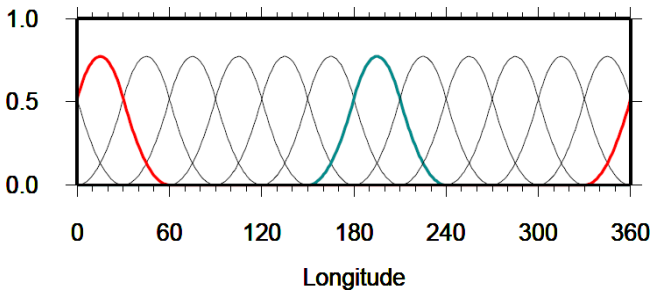


**Figure 3.**  $K_{J_2} = 3 \cdot 2^2 = 12$  trigonometric B-splines  $\tilde{\phi}_{k_2}^{J_2}(\lambda)$ , according to Eq. (30) for level  $J_2 = 2$ . The blue spline function  $\tilde{\phi}_5^2(\lambda)$  with shift value  $k_2 = 5$  is different from zero only in the subinterval of length  $\Delta J_2 = 360^\circ/4 \approx 90^\circ$ . The red basis function  $\tilde{\phi}_{11}^2(\lambda)$  shows the “wrapping-around” effect.

The substitution of the expression  $180^\circ/n_{\max}$  from the inequalities Eq. (12) into Eqs. (24) and (32) yields a total of six inequalities

$$\begin{aligned} J_1 &\leq \log_2\left(\frac{180^\circ}{\Delta\varphi} - 1\right) \leq \log_2(n_{\max} - 1), \\ J_2 &\leq \log_2\left(\frac{120^\circ}{\Delta\lambda}\right) \leq \log_2\left(\frac{2 \cdot n_{\max}}{3}\right). \end{aligned} \quad (33)$$

Given the numerical values 1 to 6 for the B-spline levels  $J_1$  and  $J_2$  Table 1 presents the corresponding largest numerical values for each, the SH degree  $n_{\max}$  and the sampling intervals  $\Delta\varphi$  and  $\Delta\lambda$  by evaluating the inequalities using Eq. (33).

From the spectral point of view the six inequalities from Eq. (33) comprise the following three scenarios:

1. If the global sampling intervals  $\Delta\varphi$  and  $\Delta\lambda$  are known, the mid parts of the inequalities from Eq. (33) are given. The maximum degree  $n_{\max}$  is calculable from the right-hand side inequalities and may be inserted into the SH expansion in Eq. (10). The left-hand side inequalities yield the two level values  $J_1$  and  $J_2$  which can be inserted into the B-spline expansion from Eq. (13).
2. With a specified numerical value for  $n_{\max}$  the right-hand parts of the inequalities from Eq. (33) are given. The data input sampling intervals  $\Delta\varphi$  and  $\Delta\lambda$  can be determined from the mid parts of the inequalities. Next, the two numerical values for the level values  $J_1$  and  $J_2$  can be calculated from the left-hand side inequalities and can be inserted into the B-spline expansion in Eq. (13).
3. If the processing time of VTEC maps has to be considered, the level values  $J_1$  and  $J_2$  are subject to certain restrictions; this is due to the fact that the number of numerical operations increases exponentially with the chosen numerical values for the levels. In this case, from the given left-hand side inequalities, the data sampling intervals  $\Delta\varphi$  and  $\Delta\lambda$  can be determined from the mid parts. Finally, the right-hand side inequalities yield numerical values for the maximum SH degree  $n_{\max}$ .

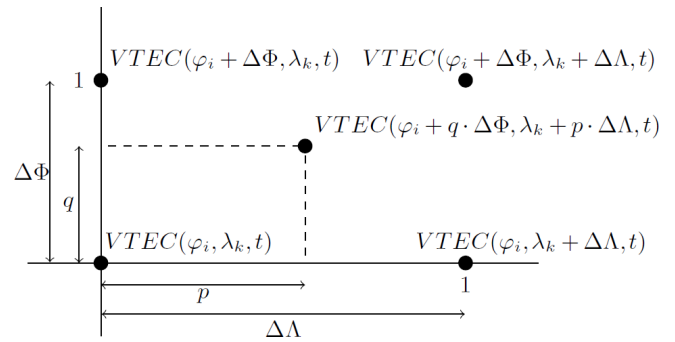


**Figure 4.** Schematic representation of the four-point spatial interpolation to calculate the VTEC value at  $P(\varphi_i + q \cdot \Delta\Phi, \lambda_k + p \cdot \Delta\Lambda)$  from the four corner points of the grid cell of interest.

As already mentioned in the introduction, most of the GIMs produced by the IAACs are based on series expansions in SHs up to a maximum degree of  $n_{\max} = 15$ . Following the abovementioned second strategy and Table 1, we obtain the approximations  $J_1 = 4$  (for  $n_{\max} = 17$ ) and  $J_2 = 3$  (for  $n_{\max} = 12$ ) for the two B-spline levels  $J_1$  and  $J_2$  for this example. Inserting these numbers into the B-spline expansion Eq. (13) yields the spectrally closest representation to the current IGS solutions. A numerical verification of this choice will be presented in Sect. 4.3.

## 2.4 VTEC output grids

The VTEC GIMs of the IAACs are usually provided with a spatial resolution of  $\Delta\Phi = 2.5^\circ$  in the latitudinal direction and  $\Delta\Lambda = 5^\circ$  in the longitudinal direction as well as a temporal sampling of  $\Delta T = 2$  h. Note, the resolution intervals  $\Delta\Phi$ ,  $\Delta\Lambda$  and  $\Delta T$  are usually distinct from the sampling intervals  $\Delta\varphi$ ,  $\Delta\lambda$  and  $\Delta t$  of the observations introduced in Sect. 2.1.

In order to calculate a VTEC value  $VTEC(\varphi, \lambda, t)$  at an arbitrary location  $P(\varphi = \varphi_i + q \cdot \Delta\Phi, \lambda = \lambda_k + p \cdot \Delta\Lambda)$  with  $0 \leq q \leq 1$  and  $0 \leq p \leq 1$  at an arbitrary time moment  $t$ , a simple bilinear spatial interpolation from the VTEC values of the four given corner points  $P(\varphi_i, \lambda_k)$ ,  $P(\varphi_i, \lambda_k + \Delta\Lambda)$ ,  $P(\varphi_i + \Delta\Phi, \lambda_k)$  and  $P(\varphi_i + \Delta\Phi, \lambda_k + \Delta\Lambda)$  is performed according to

$$\begin{aligned} VTEC(\varphi_i + q \cdot \Delta\Phi, \lambda_k + p \cdot \Delta\Lambda, t) &= (1 - q) \cdot (1 - p) \cdot VTEC(\varphi_i, \lambda_k, t) \\ &+ q \cdot (1 - p) \cdot VTEC(\varphi_i + \Delta\Phi, \lambda_k, t) \\ &+ p \cdot (1 - q) \cdot VTEC(\varphi_i, \lambda_k + \Delta\Lambda, t) \\ &+ q \cdot p \cdot VTEC(\varphi_i + \Delta\Phi, \lambda_k + \Delta\Lambda, t) \end{aligned} \quad (34)$$

(see, e.g., Schaer et al., 1998, Fig. 4 in this paper).

Note, by applying the interpolation formula (34), the quality of the calculated VTEC value decreases with increasing spatial resolution intervals  $\Delta\Phi$  and  $\Delta\Lambda$  and depends on the position within the grid cell. In order to improve the quality of the VTEC computation two methods can be used:

**Table 1.** Numerical values for the B-spline levels  $J_1$  and  $J_2$ , the maximum SH degree  $n_{\max}$  and the input data sampling intervals  $\Delta\varphi$  and  $\Delta\lambda$  by evaluating the inequalities from Eq. (33); the left part of the table presents the numbers along a meridian (upper inequalities in Eq. 33), and the right part represents the corresponding numbers along the Equator and its parallels according to the lower inequalities in Eq. (33).

Latitude							Longitude						
$J_1$	1	2	3	4	5	6	$J_2$	1	2	3	4	5	6
$n_{\max}$	3	5	9	17	33	63	$n_{\max}$	3	6	12	24	48	96
$\Delta\varphi$	60	36	20	10.5	5.45	2.85	$\Delta\lambda$	60	30	15	7.5	3.75	1.875

1. the chosen model approach, e.g., the SH or the B-spline expansion can be used directly to calculate VTEC values at any arbitrary point  $P(\varphi, \lambda)$ ;
2. the resolution intervals  $\Delta\Phi$  and  $\Delta\Lambda$  of the output grid can be set to smaller values, e.g., to  $1^\circ$ , as was proposed at the IGS workshop 2012.

For the calculation of a VTEC value  $\text{VTEC}(\varphi, \lambda, t)$  at an arbitrary time moment  $t = t_s + r \cdot \Delta T$  with  $0 \leq r \leq 1$  at a given spatial location  $P(\varphi, \lambda)$ , an interpolation with respect to time can be applied. Commonly, the linear interpolation

$$\text{VTEC}(\varphi, \lambda, t) = (1 - r) \cdot \text{VTEC}(\varphi, \lambda, t_s) + r \cdot \text{VTEC}(\varphi, \lambda, t_s + \Delta T) \quad (35)$$

between the two consecutive maps at epochs  $t_s$  and  $t_s + \Delta T$  is performed (see, e.g., Schaer et al., 1998).

The previously described interpolation methods allow for the calculation of VTEC values  $\text{VTEC}(\varphi, \lambda, t)$  at any spatial location  $P(\varphi, \lambda)$  and at any time  $t$ . However, for a more accurate calculation of VTEC an increase in the resolution is necessary for both domains. In the following, it is shown that the usage of a MSR based on the B-spline approach in combination with a KF estimation procedure provides the possibility to create VTEC maps of higher spatial and temporal resolution. Consequently, according to Table 1 the calculated VTEC maps cover a wider spectral band, i.e., the numerical value of  $n_{\max}$  becomes larger.

### 3 Multi-scale representation

The B-spline functions as introduced in Sect. 2.2.1 and 2.2.2 allow for the generation of a MSR. To be more specific, B-spline tensor product wavelet functions will be constructed which are intrinsically connected to the resolution levels of the MSR. Usually the MSR is interpreted as viewing a signal under different resolutions, as a microscope does (see, e.g., Schmidt, 2012; Schmidt et al., 2015a; Schmidt, 2015b; Liang, 2017). In all of the aforementioned studies, the MSR is based on a regional 2-D representation of VTEC in terms of tensor products of polynomial B-spline functions only. Within this study, however, we apply the MSR for a global 2-D representation of VTEC in terms of tensor products

of polynomial and trigonometric B-spline functions, as described by Lyche and Schumaker (2001) and Schumaker and Traas (1991).

#### 3.1 Pyramid algorithm

Neglecting the time dependency, the B-spline approach Eq. (18) reads

$$f_{J_1, J_2}(\varphi, \lambda) = \boldsymbol{\phi}_{J_1}^T(\varphi) \mathbf{D}_{J_1, J_2} \tilde{\boldsymbol{\phi}}_{J_2}(\lambda). \quad (36)$$

In the context of the MSR the vectors  $\boldsymbol{\phi}_{J_1}(\varphi)$  and  $\tilde{\boldsymbol{\phi}}_{J_2}(\lambda)$  are called scaling vectors, and the elements  $d_{k_1, k_2}^{J_1, J_2}$  of the matrix  $\mathbf{D}_{J_1, J_2}$  are denoted as scaling coefficients.

With  $J'_1 = J_1 - J$ ,  $J'_2 = J_2 - J$  and  $0 < J \leq \min(J_1, J_2)$  we obtain the 2-D MSR of the target function  $f(\mathbf{x})$  introduced in Eq. (7) as

$$f_{J_1, J_2}(\varphi, \lambda) = f_{J'_1, J'_2}(\varphi, \lambda) + \sum_{j=1}^J \sum_{\vartheta=1}^3 g_{J_1-j, J_2-j}^{\vartheta}(\varphi, \lambda). \quad (37)$$

Following the argumentation of Schmidt et al. (2015a) but considering the polynomial and the trigonometric B-spline functions the low-passed-filtered level  $(J'_1, J'_2)$  signal  $f_{J'_1, J'_2}(\varphi, \lambda)$  and the band-pass-filtered level  $(J_1 - j, J_2 - j)$  detail signals  $g_{J_1-j, J_2-j}^{\vartheta}(\varphi, \lambda)$  can be computed via the following relations:

$$\begin{aligned} f_{J'_1, J'_2}(\varphi, \lambda) &= \boldsymbol{\phi}_{J'_1}^T(\varphi) \mathbf{D}_{J'_1, J'_2} \tilde{\boldsymbol{\phi}}_{J'_2}(\lambda), \\ g_{j_1-1, j_2-1}^1(\varphi, \lambda) &= \boldsymbol{\phi}_{j_1-1}^T(\varphi) \mathbf{C}_{j_1-1, j_2-1}^1 \tilde{\boldsymbol{\psi}}_{j_2-1}(\lambda), \\ g_{j_1-1, j_2-1}^2(\varphi, \lambda) &= \boldsymbol{\psi}_{j_1-1}^T(\varphi) \mathbf{C}_{j_1-1, j_2-1}^2 \tilde{\boldsymbol{\phi}}_{j_2-1}(\lambda), \\ g_{j_1-1, j_2-1}^3(\varphi, \lambda) &= \boldsymbol{\psi}_{j_1-1}^T(\varphi) \mathbf{C}_{j_1-1, j_2-1}^3 \tilde{\boldsymbol{\psi}}_{j_2-1}(\lambda), \end{aligned} \quad (38)$$

where we introduced the definitions  $j_1 = J_1 - j + 1$  and  $j_2 = J_2 - j + 1$  for  $j = 1, \dots, J$ . Herein, the  $K_{j_1-1} \times 1$  and  $K_{j_2-1} \times 1$  scaling vectors  $\boldsymbol{\phi}_{j_1-1}(\varphi)$  and  $\tilde{\boldsymbol{\phi}}_{j_2-1}(\lambda)$  as well as the  $L_{j_1-1} \times 1$  and  $L_{j_2-1} \times 1$  wavelet vectors  $\boldsymbol{\psi}_{j_1-1}(\varphi)$  and  $\tilde{\boldsymbol{\psi}}_{j_2-1}(\lambda)$  can be calculated by means of the two-scale relations

$$\begin{aligned} \boldsymbol{\phi}_{j_1-1}^T(\varphi) &= \boldsymbol{\phi}_{j_1}^T(\varphi) \mathbf{P}_{j_1}, \\ \tilde{\boldsymbol{\phi}}_{j_2-1}^T(\lambda) &= \tilde{\boldsymbol{\phi}}_{j_2}^T(\lambda) \tilde{\mathbf{P}}_{j_2}, \\ \boldsymbol{\psi}_{j_1-1}^T(\varphi) &= \boldsymbol{\phi}_{j_1}^T(\varphi) \mathbf{Q}_{j_1}, \\ \tilde{\boldsymbol{\psi}}_{j_2-1}^T(\lambda) &= \tilde{\boldsymbol{\phi}}_{j_2}^T(\lambda) \tilde{\mathbf{Q}}_{j_2} \end{aligned} \quad (39)$$

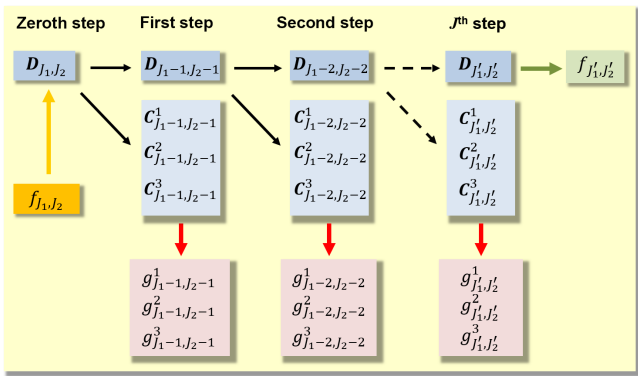


Figure 5. A 2-D MSR of the signal  $f_{J_1, J_2}(\varphi, \lambda)$ .

with  $L_{j_1-1} = K_{j_1} - K_{j_1-1}$  and  $L_{j_2} = K_{j_2} - K_{j_2-1}$ .

The numerical entries of the  $K_{j_1} \times K_{j_1-1}$  matrix  $\mathbf{P}_{j_1}$  and the  $K_{j_1} \times L_{j_1-1}$  matrix  $\mathbf{Q}_{j_1}$  can be taken from Stollnitz et al. (1995b) or Zeilhofer (2008); the corresponding entries of the  $K_{j_2} \times K_{j_2-1}$  matrix  $\tilde{\mathbf{P}}_{j_2}$  and the  $K_{j_2} \times L_{j_2-1}$  matrix  $\tilde{\mathbf{Q}}_{j_2}$  are provided by Lyche and Schumaker (2001).

In Eq. (38) we introduced the  $K_{j_1-1} \times K_{j_2-1}$  matrix  $\mathbf{D}_{j_1-1, j_2-1}$  of scaling coefficients  $d_{k_1, k_2}^{j_1-1, j_2-1}$  as well as the  $K_{j_1-1} \times L_{j_2-1}$  matrix  $\mathbf{C}_{j_1-1, j_2-1}^1$ , the  $L_{j_1-1} \times K_{j_2-1}$  matrix  $\mathbf{C}_{j_1-1, j_2-1}^2$  and the  $L_{j_1-1} \times L_{j_2-1}$  matrix  $\mathbf{C}_{j_1-1, j_2-1}^3$  of wavelet coefficients. These four matrices can be calculated via the 2-D downsampling equation

$$\begin{bmatrix} \mathbf{D}_{j_1-1, j_2-1} & \mathbf{C}_{j_1-1, j_2-1}^1 \\ \mathbf{C}_{j_1-1, j_2-1}^2 & \mathbf{C}_{j_1-1, j_2-1}^3 \end{bmatrix} = \begin{bmatrix} \mathbf{P}_{j_1} \\ \mathbf{Q}_{j_1} \end{bmatrix} \mathbf{D}_{j_1, j_2} \begin{bmatrix} \tilde{\mathbf{P}}_{j_2}^T & \tilde{\mathbf{Q}}_{j_2}^T \end{bmatrix}, \quad (40)$$

also known as the 2-D pyramid algorithm. The  $K_{j_1-1} \times K_{j_1}$  matrix  $\mathbf{P}_{j_1}$ , the  $K_{j_2-1} \times K_{j_2}$  matrix  $\tilde{\mathbf{P}}_{j_2}$ , the  $L_{j_1-1} \times K_{j_1}$  matrix  $\mathbf{Q}_{j_1}$  and the  $L_{j_2-1} \times K_{j_2}$  matrix  $\tilde{\mathbf{Q}}_{j_2}$  can be computed via the identities

$$\begin{bmatrix} \mathbf{P}_{j_1} \\ \mathbf{Q}_{j_1} \end{bmatrix} = \begin{bmatrix} \mathbf{P}_{j_1} & \mathbf{Q}_{j_1} \end{bmatrix}^{-1}, \quad (41)$$

$$\begin{bmatrix} \tilde{\mathbf{P}}_{j_2} \\ \tilde{\mathbf{Q}}_{j_2} \end{bmatrix} = \begin{bmatrix} \tilde{\mathbf{P}}_{j_2} & \tilde{\mathbf{Q}}_{j_2} \end{bmatrix}^{-1} \quad (42)$$

(see, e.g., Schmidt, 2007). The 2-D pyramid algorithm based on the decomposition Eq. (37) is visualized in Fig. 5. The “zeroth” step transforms the observations  $y(\mathbf{x}_{ij}, t_j)$  according to Eqs. (13) and (18) into the elements of the scaling matrix  $\mathbf{D}_{J_1, J_2}(t_j)$  as introduced in Eq. (17). The procedure applied will be explained in Sect. 3.2.

The previously described MSR refers to a successive low-pass filtering of the target function  $f(\varphi, \lambda, t)$  into two directions, namely latitude  $\varphi$  and longitude  $\lambda$ , in the same manner. If a signal  $f(\varphi, \lambda, t)$  is represented according to Eq. (18) up

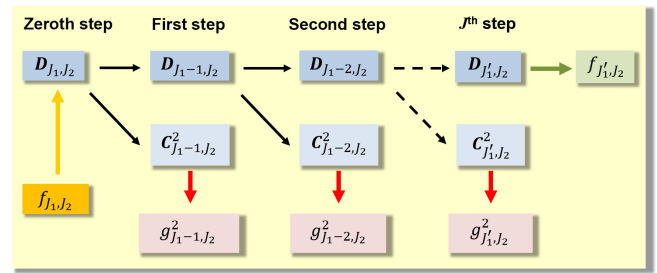


Figure 6. A 1-D MSR of the signal  $f_{J_1, J_2}(\varphi, \lambda)$  with respect to the latitude  $\varphi$ . The “zeroth” step on the left-hand side conforms with the one in Fig. 5.

to the level values  $J_1$  with respect to latitude and  $J_2$  with respect to longitude, i.e.,  $f(\varphi, \lambda, t) \approx f_{J_1, J_2}(\varphi, \lambda, t)$ , the application of the MSR Eq. (37) allows for the computation of low-pass-filtered signal approximations up to the level pairs  $(J_1-1, J_2-1), (J_1-2, J_2-2), \dots$ . The principal structures of the ionospheric key parameters such as VTEC, however, are usually parallel to the geomagnetic Equator. Consequently, we will additionally deal with a 1-D MSR of the signal  $f(\varphi, \lambda, t)$  with respect to the latitude. In this case Eq. (37) reduces to

$$f_{J_1, J_2}(\varphi, \lambda) = f_{J_1', J_2}(\varphi, \lambda) + \sum_{j=1}^J g_{J_1-j, J_2}(\varphi, \lambda). \quad (43)$$

Thus, signal approximations up to the level pairs  $(J_1-1, J_2), (J_1-2, J_2), \dots$  are obtained. From the four relations in Eq. (38) only the first and the third one have to be considered within the 1-D MSR Eq. (43), namely

$$\begin{aligned} f_{J_1', J_2}(\varphi, \lambda) &= \boldsymbol{\phi}_{J_1'}^T(\varphi) \mathbf{D}_{J_1', J_2} \tilde{\boldsymbol{\phi}}_{J_2}(\lambda), \\ g_{J_1-1, J_2}(\varphi, \lambda) &= \boldsymbol{\psi}_{j_1-1}^T(\varphi) \mathbf{C}_{j_1-1, J_2}^2 \tilde{\boldsymbol{\phi}}_{J_2}(\lambda) \end{aligned} \quad (44)$$

with  $j_1 = J_1 - j + 1$  for  $j = 1, \dots, J$ ,  $0 < J \leq J_1$  and  $J_1' = J_1 - J$ . The  $K_{j_1-1} \times K_{J_2}$  matrix  $\mathbf{D}_{j_1-1, J_2}$  of scaling coefficients and the  $L_{j_1-1} \times K_{J_2}$  matrix  $\mathbf{C}_{j_1-1, J_2}^2$  of wavelet coefficients can be calculated from the 1-D downsampling equation

$$\begin{bmatrix} \mathbf{D}_{j_1-1, J_2} \\ \mathbf{C}_{j_1-1, J_2}^2 \end{bmatrix} = \begin{bmatrix} \mathbf{P}_{j_1} \\ \mathbf{Q}_{j_1} \end{bmatrix} \mathbf{D}_{j_1, J_2}, \quad (45)$$

where the matrices  $\mathbf{P}_{j_1}$  and  $\mathbf{Q}_{j_1}$  can be computed via Eq. (41). The 1-D pyramid algorithm based on the decomposition Eq. (43) is visualized in Fig. 6.

Besides the representation of a signal, e.g., VTEC, by means of approximations on different resolution levels with respect to latitude and longitude, the MSR also allows for the utilization of a powerful “data compression procedure”, as the numerical value of a large number of wavelet coefficients is generally close to zero depending on the signal structure (see, e.g., Zeilhofer, 2008).

### 3.2 Estimation of unknown model parameters

To estimate the elements of the unknown  $K_{J_1} \times K_{J_2}$  matrix  $\mathbf{D}_{J_1, J_2}(t_s)$  from VTEC observations  $y(\mathbf{x}_{i_s}, t_s)$  (cf. Eq. 8) within the “zeroth” step of the MSR we apply Kalman filtering according to Erdogan et al. (2017).

In the linear formulation the Kalman filter consists (1) of the state equation

$$\boldsymbol{\beta}_s = \mathbf{F}_s \boldsymbol{\beta}_{s-1} + \mathbf{w}_{s-1} \quad (46)$$

and (2) of the system

$$\mathbf{y}_s + \mathbf{e}_s = \mathbf{A}_s \boldsymbol{\beta}_s \quad (47)$$

of observation equations. In Eq. (46) the  $u \times 1$  vector  $\boldsymbol{\beta}_s = \text{vec} \mathbf{D}_{J_1, J_2}(t_s)$  – known as the state vector – of the  $u = K_{J_1} \cdot K_{J_2}$  unknown scaling coefficients at time moment  $t_s$  is predicted from the state vector  $\boldsymbol{\beta}_{s-1}$  of the previous time moment  $t_{s-1}$  by means of the  $u \times u$  transition matrix  $\mathbf{F}_s$  and the  $u \times 1$  vector  $\mathbf{w}_{s-1}$  of the process noise. In Eq. (47)  $\mathbf{y}_s = (y(\mathbf{x}_{i_s}, t_s))$  and  $\mathbf{e}_s = (e(\mathbf{x}_{i_s}, t_s))$  are the  $I_s \times 1$  vectors of the observations and the measurement errors, respectively; the  $(i_s)$ th row vector  $\mathbf{a}_{i_s}^T$  of the  $I_s \times u$  coefficient matrix  $\mathbf{A}_s$  is given by the expression

$$\mathbf{a}_{i_s} = \tilde{\boldsymbol{\phi}}_{J_2}(\lambda_{i_s}) \otimes \boldsymbol{\phi}_{J_1}(\varphi_{i_s}), \quad (48)$$

as introduced in Eq. (18). The measurement error vector  $\mathbf{e}_s$  and the vector  $\mathbf{w}_s$  of the process noise are assumed to be white noise vectors with expectation values  $E(\mathbf{e}_s) = 0$  and  $E(\mathbf{w}_s) = 0$ , and fulfill the requirements

$$\begin{aligned} E(\mathbf{w}_s \mathbf{w}_1^T) &= \boldsymbol{\Sigma}_w \delta_{s,l}, \quad E(\mathbf{e}_s \mathbf{e}_1^T) = \boldsymbol{\Sigma}_y \delta_{s,l}, \\ E(\mathbf{w}_s \mathbf{e}_1^T) &= 0, \end{aligned} \quad (49)$$

where  $\delta_{s,l}$  is the delta symbol that equals 1 for  $s = l$  and 0 for  $s \neq l$ . In Eq. (49)  $\boldsymbol{\Sigma}_y$  and  $\boldsymbol{\Sigma}_w$  are given covariance matrices of the observations and the process noise, respectively.

The solution of the estimation problem as defined in Eqs. (46) and (47) generally consists of the sequential application of a prediction step (time update) and a correction step (measurement update). In the prediction step, the estimated state vector  $\hat{\boldsymbol{\beta}}_{s-1}$  and its covariance matrix  $\hat{\mathbf{D}}(\hat{\boldsymbol{\beta}}_{s-1}) = \hat{\boldsymbol{\Sigma}}_{\beta, s-1}$  are propagated from the time moment  $t_{s-1}$  to the next time moment  $t_s$  by means of

$$\boldsymbol{\beta}_s^- = \mathbf{F}_s \hat{\boldsymbol{\beta}}_{s-1}, \quad (50)$$

$$\boldsymbol{\Sigma}_{\beta, s}^- = \mathbf{F}_s \hat{\boldsymbol{\Sigma}}_{\beta, s-1} \mathbf{F}_s^T + \boldsymbol{\Sigma}_w, \quad (51)$$

where the symbol “ $-$ ” indicates the predicted quantities. The prediction step is followed by the measurement update

$$\hat{\boldsymbol{\beta}}_s = \boldsymbol{\beta}_s^- + \mathbf{K}_s (\mathbf{y}_s - \mathbf{A}_s \boldsymbol{\beta}_s^-), \quad (52)$$

$$\hat{\boldsymbol{\Sigma}}_{\beta, s} = (\mathbf{I} - \mathbf{K}_s \mathbf{A}_s) \boldsymbol{\Sigma}_{\beta, s}^-, \quad (53)$$

where  $\hat{\boldsymbol{\beta}}_s$  and  $\hat{\boldsymbol{\Sigma}}_{\beta, s}$  are the updated state vector and its covariance matrix, respectively. In Eqs. (52) and (53) the  $u \times I_s$

Kalman gain matrix

$$\mathbf{K}_s = \boldsymbol{\Sigma}_{\beta, s}^- \mathbf{A}_s^T (\mathbf{A}_s \boldsymbol{\Sigma}_{\beta, s}^- \mathbf{A}_s^T + \boldsymbol{\Sigma}_y)^{-1} \quad (54)$$

behaves as a weighting factor between the new measurements and the predicted state vector. The chosen step size  $t_s - t_{s-1}$  within the KF determines the maximum temporal resolution of the output.

Using the estimations  $\hat{\boldsymbol{\beta}}_s$  and  $\hat{\boldsymbol{\Sigma}}_{\beta, s}$  from Eqs. (52) and (53), a  $V \times 1$  vector  $\mathbf{f}_s$  of function values  $f(\varphi_i, \lambda_k, t_s)$  at arbitrary locations  $P(\varphi_i, \lambda_k)$  with  $i = 1, \dots, I$ ,  $k = 1, \dots, K$  and  $V = I \cdot K$  can be estimated by

$$\hat{\mathbf{f}}_s = \bar{\mathbf{A}}_s \hat{\boldsymbol{\beta}}_s, \quad (55)$$

$$\hat{\boldsymbol{\Sigma}}_{f, s} = \bar{\mathbf{A}}_s^T \hat{\boldsymbol{\Sigma}}_{\beta, s} \bar{\mathbf{A}}_s, \quad (56)$$

where  $\hat{\boldsymbol{\Sigma}}_{f, s}$  is the estimated  $V \times V$  covariance matrix of the estimation  $\hat{\mathbf{f}}_s$ . The  $V \times u$  matrix  $\bar{\mathbf{A}}_s$  is set up in a similar way to matrix  $\mathbf{A}_s$  in Eq. (47) with Eq. (48). In the following, we will interpret the function values  $f(\varphi_i, \lambda_k, t_s) = \text{VTEC}(\varphi_i, \lambda_k, t_s)$  as VTEC values.

### 3.3 B-Spline model output

The previously explained procedure allows for the dissemination of two products to the users:

- *Product 1*: a set of estimated scaling coefficients

$$\hat{d}_{k_1, k_2}^{J_1, J_2}(t_s) \big|_{k_1=0, \dots, K_{J_1}-1, k_2=0, \dots, K_{J_2}-1} \quad (57)$$

from Eq. (52) at time moments  $t_s$  for level values  $J_1$  and  $J_2$  at the spatial positions  $k_1$  in the latitudinal direction and  $k_2$  in the longitudinal direction, respectively, as well as their estimated standard deviations

$$\hat{\sigma}_{d; k_1, k_2}^{J_1, J_2}(t_s) \big|_{k_1=0, \dots, K_{J_1}-1, k_2=0, \dots, K_{J_2}-1} \quad (58)$$

extracted from the covariance matrix Eq. (53).

- *Product 2*: estimated VTEC values given as

$$\widehat{\text{VTEC}}_{J_1, J_2}(\varphi_i, \lambda_k, t_s) \big|_{i=1, \dots, I, k=1, \dots, K} \quad (59)$$

according to Eq. (55) at time moments  $t_s$  for level values  $J_1$  and  $J_2$  in the latitudinal and longitudinal direction, respectively, calculated at grid points  $P(\varphi_i, \lambda_k)$  as well as their estimated standard deviations

$$\hat{\sigma}_{\text{VTEC}}^{J_1, J_2}(\varphi_i, \lambda_k, t_s) \big|_{i=1, \dots, I, k=1, \dots, K}, \quad (60)$$

extracted from the covariance matrix Eq. (56).

According to Eq. (35), the time interval  $\Delta T$  between two consecutive maps of the coefficients Eq. (57) and their standard deviations Eq. (58) or the VTEC grid values Eq. (59) and their standard deviations Eq. (60) at times  $t_s$  and  $t_s + \Delta T$  can be chosen arbitrarily, e.g., as 10 or 15 min, 1 h or 2 h.



Following Eq. (34), the coordinates  $\varphi_i$  and  $\lambda_k$  of all of the  $V$  grid points  $P(\varphi_i, \lambda_k)$  are defined as  $\varphi_i = -90^\circ + (i-1) \cdot \Delta\Phi$  with  $\Delta\Phi = 180^\circ/(I-1)$  and  $\lambda_k = 0^\circ + (k-1) \cdot \Delta\Lambda$  with  $\Delta\Lambda = 360^\circ/K$ . As previously mentioned, the spatial resolution intervals  $\Delta\Phi$  and  $\Delta\Lambda$  are usually chosen as  $1^\circ$ ,  $2.5^\circ$  or  $5^\circ$ , i.e.,  $I = 181, 73, 37$  and  $K = 360, 144, 72$ .

The two products, i.e., the set of coefficients or the VTEC grid values reflect the two strategies of dissemination. In case of a SH expansion for RT applications as introduced in Sect. 2.1 the corresponding SH coefficients  $c_{n,m}$  from Eq. (10) can be transferred to the user by means of a RTCM (Radio Technical Commission for Maritime services) standard 1264 message. This message allows for the consideration of SH coefficients, but only up to degree  $n = 16$ . In the case of the B-spline expansion Eq. (13), however, an encoder procedure for the B-spline coefficients Eq. (57) is necessary, because the user has to evaluate the B-spline model just as in the SH case by substituting the B-spline tensor product Eq. (14) for the SHs Eq. (11). Due to the two restrictions, namely the sole use SH expansions and only up to a maximum degree  $n_{\max} = 16$ , the RTCM message format for data dissemination has to be urgently discussed and must be set up in a more flexible way (refer to the comments in Sect. 5). To apply the RTCM format in its current form, the VTEC grid values Eq. (59) can alternatively be used as observations  $y(\mathbf{x}_{i_s}, t_s)$  in Eq. (10) to calculate SH coefficients  $c_{n,m}(t_s)$  by means of a least-squares estimation. This way each GIM can be sent at a high update rate to the user for RT applications.

For Product 2, the VTEC grid values Eq. (59) as well as their standard deviations Eq. (60) are disseminated as VTEC and standard deviation maps, i.e., GIMs, with given spatial resolutions  $\Delta\Phi$  and  $\Delta\Lambda$  in the latitudinal and longitudinal direction, respectively, in IONEX format to the user.

## 4 Numerical investigations

In the following, the described modeling approach developed at DGFI-TUM is applied to real data. To be more specific, we use GPS and GLONASS NRT data in hourly blocks and apply ultra-rapid orbits. A detailed explanation of the data preprocessing and the setup of the full observation equations is presented by Erdogan et al. (2017). The IGS IAACs provide final products based on post-processed GNSS observations and orbits with a latency of more than 1 week. Several IAACs additionally provide rapid products with a latency of 1 d using rapid orbits. An overview on the products used in the this paper is given in Table 2.

For the evaluation of the data we have to define an appropriate coordinate system. Here we follow the standard procedure and use a sun-fixed geomagnetic coordinate system. To be more specific, we identify the coordinate system  $\Sigma_E$  introduced in the context of Eq. (3) with the Geocentric Solar Magnetic (GSM) coordinate system (see, e.g., Laundal and Richmond, 2017). Consequently, the SH and B-spline

**Table 2.** List of GIM products used in this paper. Information on names, types and latencies are taken from the following references: (1) Roma-Dollase et al. (2017), (2) Orus et al. (2005) and (3) this paper.

Institution	Product	Type	Latency	Reference
CODE	codg	Final	> 1 week	(1)
UPC	uqrg	Rapid	> 1 d	(2)
DGFI-TUM	oplg ophg	NRT	< 3 h	(3)

theory as presented in the previous sections is applied in the orthogonal GSM system. As diurnal variations of the ionosphere are mitigated in this coordinate system, the transition matrix  $\mathbf{F}_s$  introduced in the state Eq. (46) of the KF can be set to the identity matrix  $\mathbf{I}$ , i.e.,  $\mathbf{F}_s = \mathbf{I}$ . In other words, the dynamic system of the KF is set to a random walk process. Furthermore, for the time update in Eq. (46) we fix the step size  $t_s - t_{s-1}$  to 5 min.

While the scaling coefficients Eq. (57) and their standard deviations Eq. (58) of Product 1 are located within the GSM system, the VTEC values Eq. (59) and their standard deviations Eq. (60) of Product 2 are provided in the aforementioned IONEX format on a regular grid defined in a geographical geocentric Earth-fixed coordinate system. Thus, a coordinate system transformation has to be interposed.

### 4.1 Validation procedure

For validation purposes we rely on the dSTEC analysis which is currently regarded as the standard method for the quality assessment of VTEC models (see, e.g., Orus et al., 2007; Rovira-Garcia et al., 2015).

This analysis method is based on the calculation of the difference between STEC observations  $\text{STEC}(\mathbf{x}^S, \mathbf{x}_R, t_s)$  at discrete time moments  $t_s$  according to Eq. (2) and a reference observation  $\text{STEC}(\mathbf{x}^S, \mathbf{x}_R, t_{\text{ref}})$  along a specified satellite arc as

$$\text{dSTEC}_{\text{obs}}(t_s) = \text{STEC}(\mathbf{x}^S, \mathbf{x}_R, t_s) - \text{STEC}(\mathbf{x}^S, \mathbf{x}_R, t_{\text{ref}}). \quad (61)$$

The reference time moment  $t = t_{\text{ref}}$  is usually referred to the observation with the smallest zenith angle  $z = z_{\text{ref}}$ . In the same manner, the differences

$$\text{dSTEC}_{\text{map}}(t_s) = M(z_s) \cdot \text{VTEC}(\mathbf{x}_{\text{IPP}}, t_s) - M(z_{\text{ref}}) \cdot \text{VTEC}(\mathbf{x}_{\text{IPP}}, t_{\text{ref}}) \quad (62)$$

are calculated by means of Eq. (5) from the VTEC map to be validated. The quality assessment is performed by studying the differences

$$\text{dSTEC}(t_s) = \text{dSTEC}_{\text{obs}}(t_s) - \text{dSTEC}_{\text{map}}(t_s) \quad (63)$$

with expectation value  $E(\text{dSTEC}(t_s)) = 0$ .



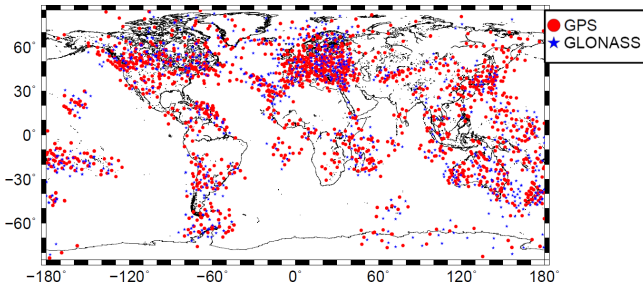


**Figure 7.** Global distribution of the IPPs from GPS (red dots) and GLONASS (blue stars) measurements for 6 September 2017, at 13:00 UT.

#### 4.2 Estimation of B-spline multi-scale products

Figure 7 shows the global distribution of the IPPs related to GNSS VTEC observations  $y(\mathbf{x}_{\text{IPP}}, t_s) = \text{VTEC}(\mathbf{x}_{\text{IPP}}, t_s)$  as introduced in Eq. (13) for 6 September 2017 at 13:00 UT. As the B-spline model is set up in the GSM coordinate system and the scaling coefficients are restricted to the state equation

$$d_{k_1, k_2}^{J_1, J_2}(t_s) = d_{k_1, k_2}^{J_1, J_2}(t_{s-1}) + w(t_{s-1}) \quad (64)$$

according to Eq. (46), we select  $\Delta\varphi = 5^\circ$  and  $\Delta\lambda = 10^\circ$  as appropriate values for the global average sampling interval of the input data as introduced at the end of Sect. 2.1. Consequently, the B-spline levels to  $J_1 = 5$  and  $J_2 = 3$  are taken from Table 1.

The covariance matrices  $\Sigma_y$  and  $\Sigma_w$  of the observations and the process noise, respectively, as defined in the formulae of Eq. (49), are set up according to Erdogan et al. (2017). In more detail,  $\Sigma_y$  consists of two diagonal block matrices related to GPS and GLONASS VTEC observations. The relative weighting between the blocks, i.e., between GPS and GLONASS, is performed by manually defined variance factors.

Figure 8a shows with  $J_1 = 5$ ,  $J_2 = 3$ ,  $K_{J_1} = 2^{J_1} + 2 = 34$  and  $K_{J_2} = 3 \cdot 2^{J_2} = 24$ , the numerical values of the total  $816 = 34 \cdot 24$  scaling coefficients are

$$\hat{d}_{k_1, k_2}^{5,3}(t_s) \big|_{k_1=0, \dots, 33, k_2=0, \dots, 23} \quad (65)$$

according to Eq. (57), estimated by means of Eq. (52). As the shift values  $k_1$  and  $k_2$  determine the location of the scaling coefficients, they can be plotted. Figure 8b shows the corresponding standard deviations as defined in Eq. (58). A test of significance is performed for each of the scaling coefficients according to Koch (1999).

While Fig. 8a and b show the results of Product 1 in the GSM system, Fig. 8c and d depict the corresponding results of Product 2 in a geographical geocentric coordinate system. With the choices  $\Delta\Phi = 2.5^\circ$  and  $\Delta\Lambda = 5.0^\circ$  for the grid spacing in the latitudinal and longitudinal directions, respectively, Product 2 provides the VTEC grid values

$$\widehat{\text{VTEC}}_{5,3}(\varphi_i, \lambda_k, t_s) \big|_{i=1, \dots, 73, k=1, \dots, 72} \quad (66)$$

and the corresponding standard deviations  $\hat{\sigma}_{\text{VTEC}}^{5,3}$  from Eqs. (59) and (60).

Note that for the visualization of VTEC and their standard deviations in Fig. 8c and d, we computed function values on a much denser grid using the interpolation formula (34).

From the comparison of Fig. 8a and c, it can be stated that the numerical values of the scaling coefficients directly reflect the signal structure, i.e., the signal energy. This fact is the consequence of the localizing character of the B-spline functions. Figure 8b and d reveal that the standard deviations are generally larger where no or only a few GNSS observations from IGS stations are available, namely over the oceans, e.g., the Southern Atlantic, but also over specific continental regions such as the Sahara and the Amazon region.

Figure 8a, i.e., the plot of the set of scaling coefficients  $\hat{d}_{k_1, k_2}^{5,3}$  in Eq. (65) can be interpreted as a visualization of the  $34 \times 24$  matrix  $\mathbf{D}_{5,3}$  defined in Eq. (17) and displayed in the top-left boxes of Figs. 5 and 6 for the 2-D and the 1-D MSR, respectively. Consequently, Fig. 8a and b are the results of the zeroth step within the pyramid algorithm, as explained in Sect. 3. Applying the first step of the 1-D pyramid algorithm, the downsampling Eq. (44) provides both the  $18 \times 24$  matrix  $\mathbf{D}_{4,3}$  of estimated scaling coefficients  $\hat{d}_{k_1, k_2}^{4,3}$  for the level values  $J_1 = 4$  and  $J_2 = 3$  as well as the  $16 \times 24$  matrix  $\mathbf{C}_{4,3}^2$  of estimated wavelet coefficients. Consequently, the definition of Product 2 in Sect. 3.3 can be extended to “Multi-Scale Products 2”:

- *ophg*: estimations with levels  $J_1 = 5$ ,  $J_2 = 3$

$$\widehat{\text{VTEC}}_{5,3}(\varphi_i, \lambda_k, t_s), \quad \hat{\sigma}_{\text{VTEC}}^{5,3}(\varphi_i, \lambda_k, t_s) \\ \Delta\Phi = 2.5^\circ, \quad \Delta\Lambda = 5.0^\circ; \quad (67)$$

- *oplg*: estimations with levels  $J_1 = 4$ ,  $J_2 = 3$

$$\widehat{\text{VTEC}}_{4,3}(\varphi_i, \lambda_k, t_s), \quad \hat{\sigma}_{\text{VTEC}}^{4,3}(\varphi_i, \lambda_k, t_s) \\ \hat{g}_{4,3}(\varphi_i, \lambda_k, t_s), \quad \hat{\sigma}_g^{4,3}(\varphi_i, \lambda_k, t_s) \\ \Delta\Phi = 2.5^\circ, \quad \Delta\Lambda = 5.0^\circ. \quad (68)$$

We denote the two Multi-Scale Products 2 as “ophg” and “oplg”, where the first symbols refer to the OPTIMAP processing software, which was developed within a third-party funded project (see Acknowledgements). The “p” is chosen according to the temporal output sampling  $\Delta T$  of maps, with “i” for  $\Delta T = 10$  min, “1” for  $\Delta T = 1$  h and “2” for  $\Delta T = 2$  h. The third symbol describes the spectral resolution and is selected as “l” for “low” and “h” for “high”. Finally, the last symbols indicates the model domain and is set to “g” for “global”. Furthermore, we want to mention again, that the “ophg” and “oplg” products are all presented in geographical coordinates.

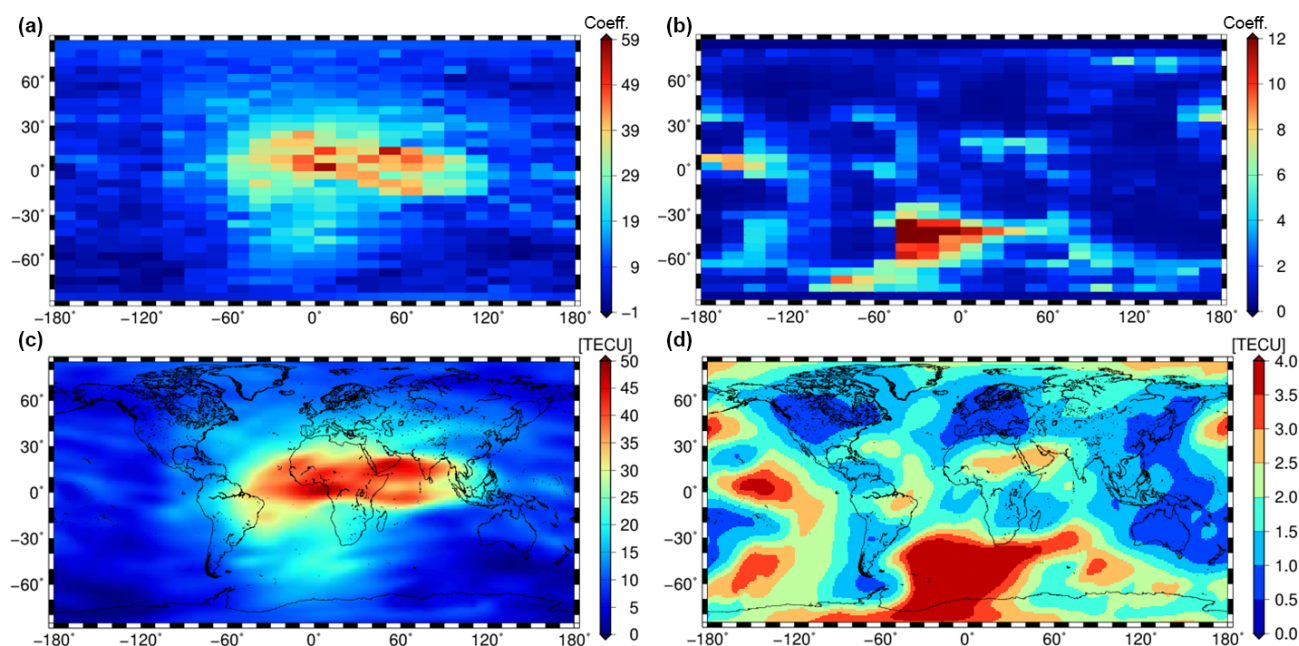


**Figure 8.** Estimated scaling coefficients (a) and their standard deviations (b) for level values  $J_1 = 5$  and  $J_2 = 3$  within the GSM coordinate system. Estimated VTEC values (c) and their standard deviations (d) as GIMs within a geographical coordinate system; all sets calculated for 6 September 2017 at 13:00 UT.

### 4.3 Comparison of VTEC maps from B-spline and spherical harmonic expansions

As mentioned in the context of Table 1, the B-spline levels  $J_1 = 4$  for latitude and  $J_2 = 3$  for longitude fit best to the highest degree  $n_{\max} = 15$  of a SH expansion Eq. (10). To be more specific, we compare the multi-scale product “o1lg” with the product “codg” provided by CODE. “codg” is characterized by a SH expansion up to degree  $n_{\max} = 15$  and a time interval  $\Delta T = 1$  h of two consecutive maps (Schaer, 1999).

Figure 9 shows the VTEC and standard deviation maps for 6 September 2017 at 13:00 UT as well as the difference map between “o1lg” and “codg”. Although the structures of the two VTEC maps are rather similar, the difference map shows deviations of up to  $\pm 6$  TECU. To judge this amount, a comparison of VTEC GIMs from different IAACs was performed (not shown here). This investigation stated that deviations between individual IAAC products can reach  $\pm 10\%$  or even more. Studying the structures within the difference map no larger systematic patterns are visible and, thus, justify our assumption that the quality of “o1lg” is comparable with the quality of the IAAC products. The standard deviation maps in Fig. 9b and d show different structures that are mainly caused by the application of the different estimation strategies, namely KF (“o1lg”) and least-squares estimation (“codg”).

To numerically assess the comparability we apply the dSTEC analysis described in Sect. 4.1. First we define a network of receiver stations which are used in Eq. (61).

The chosen set should not be used within the computation of the VTEC maps. Fulfilling both requirements at the same time is difficult and, thus, the set of stations shown in Fig. 10 contains both independent stations and stations used simultaneously in all VTEC models. As GNSS measurements are taken along the satellite arcs, the corresponding IPPs are located spatially within a grid cell and temporally between the discrete time moments of the “o1lg” and “codg” products. In order to calculate the VTEC values in Eq. (62), the spatial and temporal interpolation formulae (34) and (35) have to be applied. Figure 11 shows the RMS values of the differences Eq. (63) during the time span between 1 and 30 September 2017, at the chosen receiver stations.

As can be seen, the RMS values vary between 0.3 and 1.6 TECU. By comparing the RMS values of “o1lg” with a mean RMS value of 0.80 TECU and “codg” with a mean RMS of 0.77 TECU we can state that the quality of these two products is very close to each other.

The results indicate that the overall quality of the NRT product “o1lg” is comparable with that of the final product “codg” including the developed and implemented preprocessing strategies and steps of the GNSS data (see Table 2).

### 4.4 Assessment of the multi-scale VTEC products

The two multi-scale VTEC products “ophg” and “oplg” have been introduced in the two equation blocks Eqs. (67) and

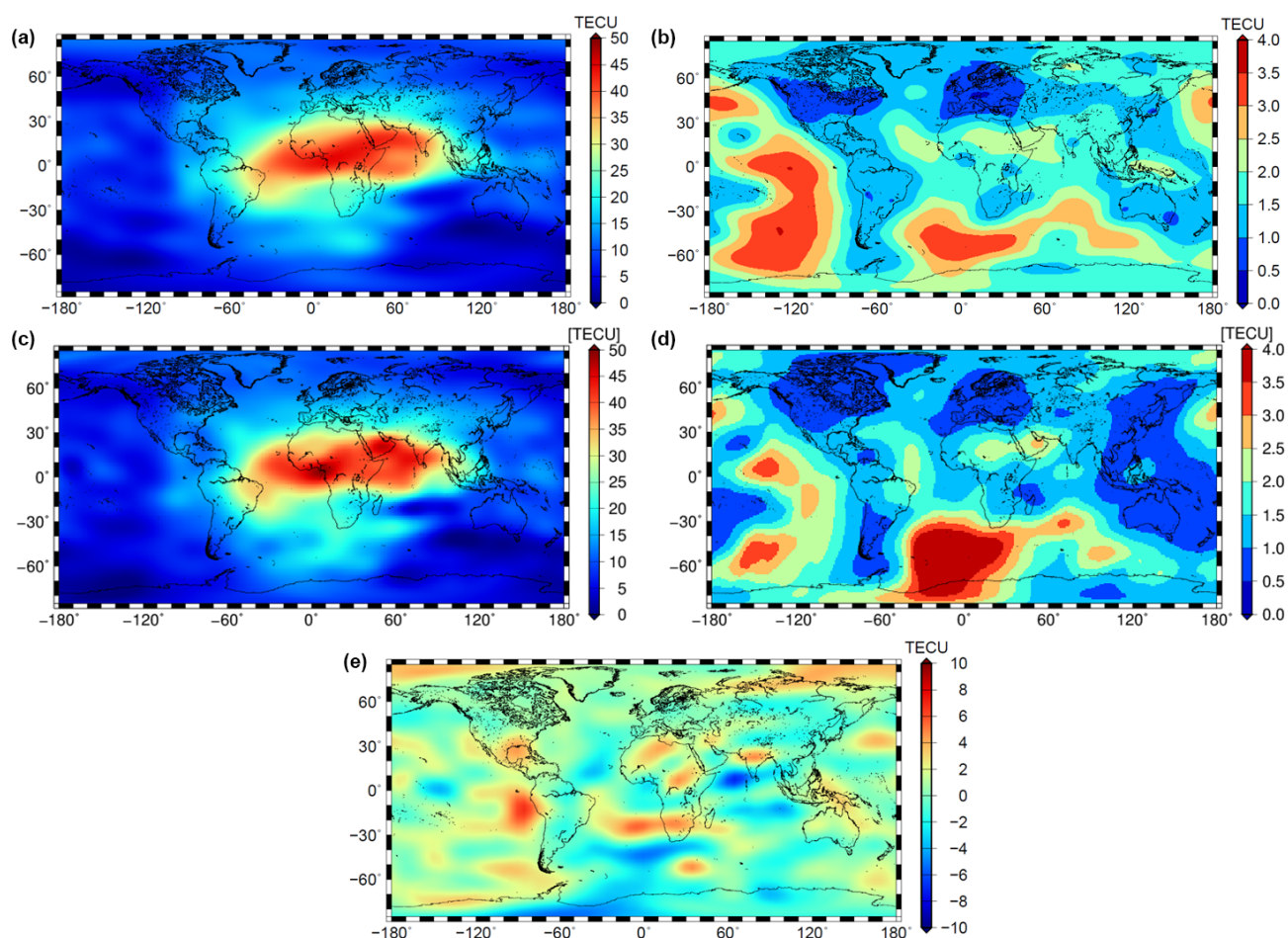


**Figure 9.** VTEC maps “codg” (a) and “o1lg” (c) as well as their standard deviation maps (b, d); difference map of the two VTEC maps (e); all data for 6 September 2017 at 13:00 UT.

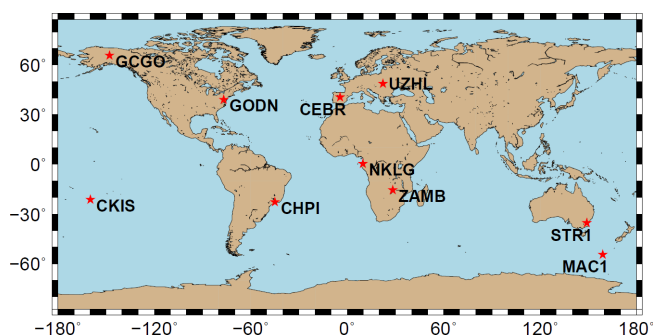


**Figure 10.** Distribution of the 10 IGS receiver stations used for the dSTEC analysis.

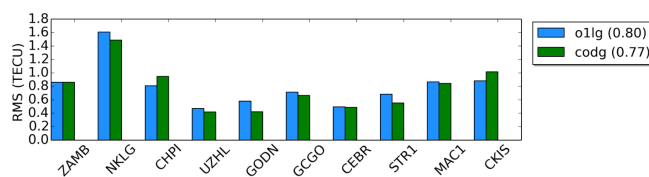


**Figure 11.** RMS values for the “codg” (green) and “o1lg” (blue) products computed at the 10 receiver stations shown in Fig. 10. The values in parentheses in the legend are the average RMS over all 10 receiver stations for the entire test period between 1 and 30 September 2017.

(68). In what follows, we study them during a solar storm of medium intensity on 8 September 2017 and during the strongest storm of the last 10 years, the prominent St. Patrick storm, which occurred on 17 March 2015. Figure 12a, c, and d show the results of the 8 September 2017 event at 19:00 UT

and Fig. 12b, d, and e display the corresponding maps for the St. Patrick storm event on 17 March 2015 at 19:00 UT.

As already mentioned in the context of Eq. (43), it is expected that the detail signal Eq. (44) is dominated by structures parallel to the geomagnetic Equator. The detail signal  $g_{4,3}(\varphi_i, \lambda_k, t_s)$  shown in Fig. 12e and f meets these expectations. Especially during the St. Patrick storm event, the detail signal shows strong signatures. It should be mentioned that



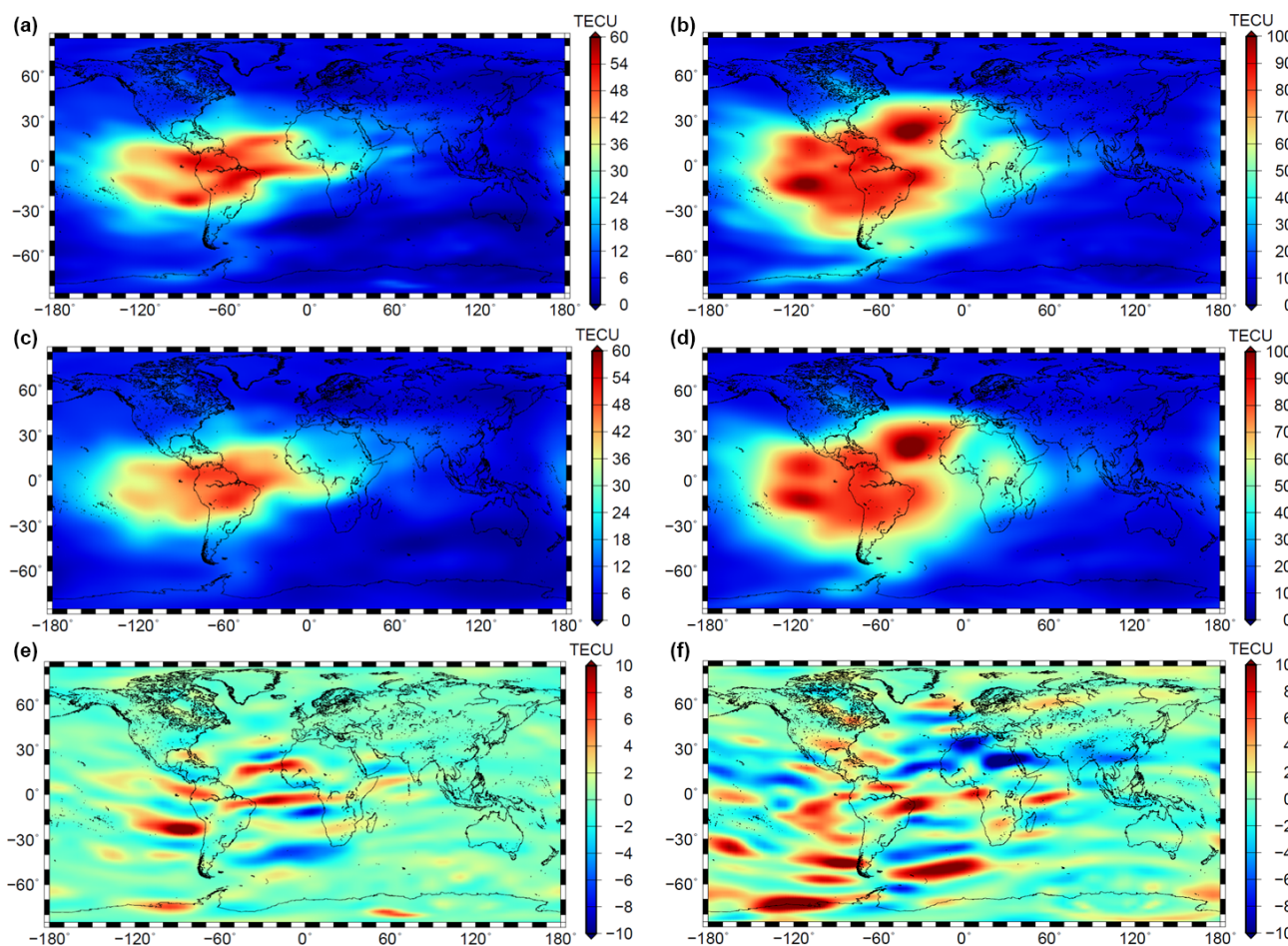


**Figure 12.** Multi-scale VTEC products for solar storm events: high-resolution VTEC map “ophg” for 8 September 2017 (a) and for 17 March 2015 (b); low-resolution VTEC map “oplq” for 8 September 2017 (c) and for 17 March 2015 (d); panels (e) and (f) show the detail signals introduced in equation block Eq. (68) and computed by means of Eq. (44) for the two solar events.

a large number of estimated wavelet coefficients collected in the matrix  $C_{4,3}^2$  are characterized by absolute values smaller than a given threshold. The neglect of these coefficients allows for a high data compression rate. Consequently, the number of significant coefficients as the outcome of a MSR would go drastically below the number of scaling coefficients within the set Eq. (57) of Product 1; the reader can get an impression of the number of neglected coefficients by paying attention to the light green and light blue colors in Fig. 12e and f. This advantageous feature of the MSR was not studied within this work but will be applied and published in the future.

Next, we focus on the solar storm during September 2017 and study the temporal sampling intervals of different GIMs. In summary, we distinguish between six products of different spectral content and different sampling intervals.

Figure 13 depicts the RMS values computed by the dSTEC analysis at the stations shown in Fig. 10. It is assumed that a product with a larger sampling interval  $\Delta T$  is less accurate than a product with a smaller sampling interval. Conse-

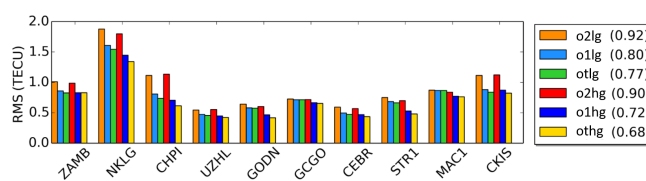


**Figure 13.** RMS values for the “o2hg”, “o1hg”, “othg”, “o2lg”, “o1lg” and “otlg” products computed at the 10 receiver stations shown in Fig. 10 during September 2017. The values in parentheses in the legend are the average RMS values over all 10 receiver stations for the entire test period between 1 and 30 September 2017.

quently, the average RMS values of “o2hg” and “o2lg” are larger than the corresponding values for a shorter sampling interval. Furthermore, it is assumed that RMS values for a product with higher B-spline levels, e.g., “othg”, are smaller than for the corresponding product with lower B-spline level values such as “otlg”. By comparing the corresponding color bars in Fig. 13, i.e., orange (“o2lg”) vs. red (“o2hg”), light

**Table 3.** Relative improvements (in percentage) for a downsizing of the sampling interval of the “o2lg”, “o1lg”, “otlg”, “o2hg”, “o1hg” and “otlg” products.

Product	RMS [TECU]	Percentage	Improvement
o2lg	0.92	100%	
o1lg	0.80	87.0%	13.0%
otlg	0.77	83.7%	16.3%
o2hg	0.90	100%	
o1hg	0.72	80.0%	20.0%
othg	0.68	75.6%	24.4%

**Table 4.** Results (in percentage) of the comparisons of the high-resolution products “ophg” with the low-resolution products “oplg”. Positive (bold) numbers mean an improvement, and negative (italic) values represent a reduction in the quality.

	o2lg	o1lg	otlg
o2hg	<b>2.2%</b>	<i>−12.5%</i>	<i>−16.9%</i>
o1hg	<b>21.7%</b>	<b>10.0%</b>	<b>6.5%</b>
othg	<b>26.1%</b>	<b>15.0%</b>	<b>11.7%</b>

blue (“o1lg”) vs. blue (“o1hg”) and green (“otlg”) vs. yellow (“othg”), the aforementioned assumptions are confirmed.

The differences in the RMS values of the first three products, “o2lg”, “o1lg” and “otlg”, are caused by their different sampling intervals. Comparing the mean RMS values of 0.92 and 0.80 TECU for “o2lg” and “o1lg”, respectively, we find a relative improvement of approximately 13.0 %. By decreasing the sampling from  $\Delta T = 2$  h to  $\Delta T = 10$  min, a further improvement of 16.3 % can be achieved.

Comparing the RMS values 0.90, 0.72 and 0.68 TECU of the “o2hg”, “o1hg” and “othg” products, respectively, we find relative improvements of 20 % and 24.4 % by downsizing the sampling interval from 2 to 1 h and finally to 10 min. A summary of the relative improvements is given in Table 3.

In the next step, we compare the quality of the multi-scale products “ophg” and “oplg” directly. First, we compare “o2lg” with “o2hg” and obtain an improvement of approximately 2.2 %. In the same manner, we compare “o1lg” with “o1hg” and “otlg” with “othg” and find that improvements of 10.0 % and 11.7 % can be achieved, respectively. Table 4 shows the results for the comparison of each pair of products; an improvement is indicated by numbers in bold font, and a deterioration is indicated by numbers in italic font. As a consequence, an increase of the numerical value for level  $J_1$ , i.e., the enhancement of the spectral resolution with respect to the latitude yields a significant improvement in the RMS values as long as the temporal sampling  $\Delta T$  is less than 2 h.

From the investigations in Sect. 4.3, it could be concluded that the quality of the “o2lg” product is comparable to the quality of the IAAC products. It can be seen from Table 4

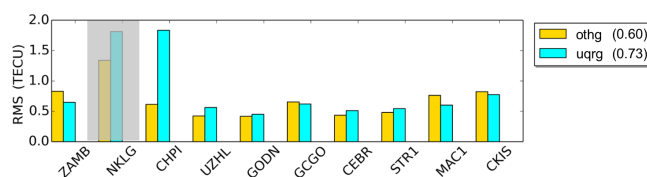


**Figure 14.** RMS values for the “uqrg” and “othg” products computed at 9 IGS receiver stations during September 2017. The values in parentheses in the legend are the average RMS values over all 9 receiver stations for the entire test period between 1 and 30 September 2017.

that there is a strong improvement of more than 26 % when using the “othg” product instead of the “o2lg” product. It is worth mentioning that both products are based on the same input data and are spatially related to each other by means of the MSR.

#### 4.5 Assessment of high-resolution VTEC models

As the “othg” product outperforms all other products used in the previous sections we now compare it with UPC’s “uqrg” product (Roma-Dollase et al., 2017) which provides smaller values in the relative standard deviation of their dSTEC analysis in comparison with the products of other IAACs. “uqrg” is a rapid product and is provided with a sampling interval  $\Delta T = 15$  min. As the “NKLG” station is not used in the calculation of “uqrg”, it is excluded from the calculation of the overall RMS value shown in the legend.

As can be seen, the RMS values vary between 0.5 and 1.8 TECU but are mostly below 1.0 TECU. The dominant RMS value of “uqrg” at the “CHPI” station reduces its quality significantly. If “CHPI” is neglected, the mean RMS value of “uqrg” decrease to 0.59 TECU. Summarizing these investigations, we can state that the overall quality of the two products is very similar. Considering the fact that “othg” is a NRT product with a latency of less than 3 h, it also outperforms “uqrg” which is a rapid product with a latency of around 1 d (see Table 2). However, for a final assessment, further validation studies have to be performed between the different products.

## 5 Conclusions and outlook

This paper presents an approach to model VTEC solely from NRT GNSS observations by generating a MSR based on B-splines; the unknown model parameters are estimated by means of an KF. Based on this approach, a number of products have been created which differ both in their spectral content and in their temporal resolution. From our investigations we state that the MSR provides B-spline models comparable to the standard GIMs of the IAACs, mostly based on SH expansions up to degree  $n_{\max} = 15$ . As the core of the numerical study we compare our results with the most prominent

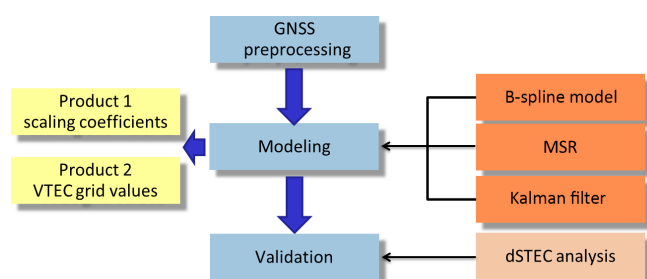


**Figure 15.** DGFI-TUM's processing modules, including (blue boxes) the download and preprocessing module for GNSS observations, the modeling module by means of B-splines, MSR and Kalman filtering (orange boxes) with possible output as Product 1 and Product 2 (yellow boxes) and the validation module.

VTEC maps of the IAACs to rate the quality. As the dSTEC analysis is the most frequently used validation method, we abandon a comparison with satellite altimetry products here. To summarize the validation studies, it can be stated that the high-resolution “othg” product outperforms all products used within the selected time span of investigation.

Besides the facts, that our models can handle data gaps due to the utilization of localizing basis functions, the application of a KF to include a dynamic prediction procedure and the use of the MSR to create products of different spectral content at the same time, it should be mentioned that DGFI-TUM's products

- are based on NRT GNSS observations only, i.e., are using input data with a latency of less than 3 h (in contrast, “codg” relies on post-processed data with a latency of larger than 3 weeks, and “uqrg” relies on rapid data with a latency of at least 1 d; cf. Table 2);
- rely on specially developed software modules (cf. Fig. 15), e.g., the preprocessing module using ultrarapid orbits;
- and can be disseminated to users with a delay of 2–3 h.

In general, the dissemination of these products to users can be undertaken in two different ways: based on estimated scaling coefficients (Product 1) or by calculated VTEC grid values (Product 2). For RT applications, however, the dissemination in terms of Product 1 is preferred, in particular the usage of the RTCM format. In the scope of the developments in the recent years, RT applications have become more important, e.g., in unmanned or autonomous vehicle development; thus, the restriction of the RTCM message to allow only for SH coefficients needs to urgently be discussed. Particularly from the point of view that there are also other modeling methods, a modification of the RTCM format would be appropriate. The MSR allows for significant data compression to be obtained due to the step-wise downsampling of the scaling coefficients according to the pyramid algorithm. Details

represented in the signal  $f_{J_1, J_2}$  of the zeroth step are stored in wavelet coefficients for the following steps (see Fig. 5). A large number of estimated wavelet coefficients are characterized by absolute values smaller than a given threshold and, thus, most of them can be neglected for the reconstruction of the original signal. Hence, the overall number of scaling and wavelet coefficients can be reduced drastically. Considering this powerful feature of data compression, we propose replacing the scaling coefficients of the highest levels with the significant wavelet coefficients of the lower levels for a definition of an alternative and more appropriate format for data dissemination in terms of Product 1.

The results presented encourage the further development of high accuracy VTEC maps. By extending the models by a fourth dimension, i.e., modeling of the electron density directly, inaccuracies due to the mapping function can be avoided. To model the vertical structure of the electron density, additional observations have to be incorporated, e.g., from DORIS, satellite altimetry and ionospheric radio occultations. This would mitigate the inhomogeneity of the data distribution and, in turn, even higher levels of the B-spline expansion can be chosen.

**Data availability.** The global VTEC maps in IONEX format used in the comparisons were acquired from the Crustal Dynamics Data Information System (CDDIS) data center by the following FTP server: <ftp://cddis.gsfc.nasa.gov/gnss/products/ionex/>. The hourly available GNSS data from IGS sites were operationally downloaded in real time through mirroring to the different IGS data centers, i.e., the CDDIS (<ftp://cddis.gsfc.nasa.gov/pub/gps/data/hourly/>), the Bundesamt für Kartographie und Geodäsie (BKG) (<ftp://igs.bkg.bund.de/IGS/nrt/>), the Institut Geographique National (IGN) (<ftp://igs.ensg.ign.fr/pub/igs/data/hourly/>) and the Korean Astronomy and Space Science Institute (KASI) (<ftp://nfs.kasi.re.kr/>). Furthermore, the ultrarapid orbits of GPS and GLONASS satellites utilized in the data preprocessing step can be accessed through FTP servers: for GPS via <ftp://cddis.gsfc.nasa.gov/pub/gps/products/>, and for GLONASS via <ftp://ftp.glonass-iac.ru/MCC/PRODUCTS/>.

**Author contributions.** The concept for the paper was proposed by AG and discussed with all co-authors. AG compiled the figures and wrote the paper with assistance from MS. The paper and figures were reviewed by all co-authors.

**Competing interests.** The authors declare that they have no conflict of interest.

**Acknowledgements.** We are grateful to the Bundeswehr GeoInformation Centre (BGIC) and the German Space Situational Awareness Centre (GSSAC) for funding the “Operational tool for ionosphere mapping and prediction” (OPTIMAP) project. The approach presented was developed within this framework.

The authors express their thanks to the following services and institutions for providing the input data: IGS and its data centers, the Center for Orbit Determination in Europe (CODE, Berne, Switzerland) and the Universitat Politècnica de Catalunya/IonSAT (UPC, Barcelona, Spain). Furthermore, the authors acknowledge the developers of the Generic Mapping Tools (GMT) which was primarily used for generating the figures in this work.

*Financial support.* This work was supported by the German Research Foundation (DFG) and the Technical University of Munich (TUM) in the framework of the Open Access Publishing Program.

*Review statement.* This paper was edited by Dalia Buresova and reviewed by Ilya Edemskiy and one anonymous referee.

## References

- Bassiri, S. and Hajj, G.: High-order ionospheric effects on the global positioning system observables and means of modeling them, *Manuscr Geodetica*, 18, 280–289, 1993.
- Bundesamt für Kartographie und Geodäsie, available at: <ftp://igs.bkg.bund.de/IGS/nrt/TS6/>, last access: 9 August 2019.
- CDDIS: GNSS data, available at: <ftp://cddis.gsfc.nasa.gov/pub/gps/data/hourly/TS5>, last access: 9 August 2019.
- Crustal Dynamics Data Information System: The global VTEC maps in IONEX format used in the comparisons, available at: <ftp://cddis.gsfc.nasa.gov/gnss/products/ionex/>, last access: 9 August 2019.
- Dach, R. and Jean, Y.: International GNSS Service – Technical Report 2012, Tech. Rep., available at: [ftp://igs.org/pub/resource/pubs/2012\\_techreport.pdf](ftp://igs.org/pub/resource/pubs/2012_techreport.pdf) (last access: 8 August 2019), 2013.
- Dettmering, D., Schmidt, M., Heinkelmann, R., and Seitz, M.: Combination of different space–geodetic observations for regional ionosphere modeling, *J. Geodesy*, 85, 989–998, 2011.
- Dettmering, D., Limberger, M., and Schmidt, M.: Using DORIS measurements for modeling the vertical total electron content of the Earth's ionosphere, *J. Geodesy*, 88, 1131–1143, <https://doi.org/10.1007/s00190-014-0748-2>, 2014.
- Dierckx, P.: Algorithms for smoothing data on the sphere with tensor products splines, *Computing*, 32, 319–342, 1984.
- Durmaz, M. and Karslioglu, M. O.: Regional vertical total electron content (VTEC) modeling together with satellite and receiver differential code biases (DCBs) using semi-parametric multivariate adaptive regression B-splines (SP-BMARS), *J. Geodesy*, 89, 347–360, 2015.
- Durmaz, M., Karslioglu, M. O., and Nohutcu, M.: Regional VTEC modeling with multivariate adaptive regression splines, *Adv. Space Res.*, 46, RSOD12, <https://doi.org/10.1016/j.asr.2010.02.030>, 2010.
- Erdogan, E., Schmidt, M., Seitz, F., and Durmaz, M.: Near real-time estimation of ionosphere vertical total electron content from GNSS satellites using B-splines in a Kalman filter, *Ann. Geophys.*, 35, 263–277, <https://doi.org/10.5194/angeo-35-263-2017>, 2017.
- Feltens, J. and Schaer, S.: IGS Products for the Ionosphere, Tech. Rep., European Space Operation Centre and Astronomical Institute of the University of Berne, 1–8, 1998.
- GPS, available at: <ftp://cddis.gsfc.nasa.gov/pub/gps/products>, last access: 9 August 2019.
- GLONASS, available at: <ftp://ftp.glonass-iac.ru/MCC/PRODUCTS/T>, last access: 9 August 2019.
- Hernández-Pajares, M., Juan, J. M., and Sanz, J.: New approaches in global ionospheric determination using ground GPS data, *J. Atmos. Sol.-Terr. Phys.*, 61, 1237–1247, [https://doi.org/10.1016/S1364-6826\(99\)00054-1](https://doi.org/10.1016/S1364-6826(99)00054-1), 1999.
- Hernández-Pajares, M., Juan, J. M., Sanz, J., Argón-Ángel, A., García-Rigo, A., Salazar, D., and Escudero, M.: The ionosphere: Effects, GPS modeling and benefits for space geodetic techniques, *J. Geodesy*, 85, 887–907, 2011.
- Hernández-Pajares, M., Roma-Dollase, D., Krankowski, A., García-Rigo, A., and Orús-Pérez, R.: Methodology and consistency of slant and vertical assessments for ionospheric electron content models, *J. Geodesy*, 19, 1405–1414, 2017.
- Institut Geographique National, available at: <ftp://igs.ensg.ign.fr/pub/igs/data/hourly>, last access: 9 August 2019.
- Jekeli, C.: Spline Representations of Functions on a Sphere for Geopotential Modeling, Tech. Rep., 475, 7–12, 2005.
- Korean Astronomy and Space Science Institute, available at: <ftp://nfs.kasi.re.kr/>, last access: 9 August 2019.
- Koch, K. R.: Parameter Estimation and Hypothesis Testing in Linear Models, Springer-Verlag Berlin Heidelberg, 1999.
- Komjathy, A. and Langley, R.: An assessment of predicted and measured ionospheric total electron content using a regional GPS network, Proceedings of the 1996 National Technical Meeting of The Institute of Navigation, 615–624, 1996.
- Langley, R. B.: Propagation of the GPS Signals, Springer Berlin Heidelberg, Berlin, Heidelberg, 111–149, [https://doi.org/10.1007/978-3-642-72011-6\\_3](https://doi.org/10.1007/978-3-642-72011-6_3), 1998.
- Laundal, K. and Richmond, A.: Magnetic Coordinate Systems, *Space Sci. Rev.*, 206, 27–59, 2017.
- Liang, W.: A regional physics-motivated electron density model of the ionosphere, Ph.D. thesis, Technical University of Munich, 2017.
- Limberger, M.: Ionosphere modeling from GPS radio occultations and complementary data based on B-splines, Ph.D. thesis, Technical University of Munich, 2015.
- Liu, J. Y., Chuo, Y. J., Shan, S. J., Tsai, Y. B., Chen, Y. I., Pulinets, S. A., and Yu, S. B.: Pre-earthquake ionospheric anomalies registered by continuous GPS TEC measurements, *Ann. Geophys.*, 22, 1585–1593, <https://doi.org/10.5194/angeo-22-1585-2004>, 2004.
- Lyche, T. and Schumaker, L.: A multiresolution tensor spline method for fitting functions on the sphere, *Siam J. Sci. Comput.*, 22, 724–746, 2001.
- Lyu, H., Hernández-Pajares, M., Nohutcu, M., García-Rigo, A., Zhang, H., and Liu, J.: The Barcelona ionospheric mapping function (BIMF) and its application to northern mid-latitudes, *GPS Solution*, 22, 724–746, 2018.
- Mertins, A.: Signal analysis: wavelets, filter banks, time-frequency transforms and applications, Wiley, Chichester, 1999.
- Monte-Moreno, E. and Hernández-Pajares, M.: Occurrence of solar flares viewed with GPS: Statistics and fractal nature, *J. Geophys. Res.*, 119, 9216–9227, 2014.



- Orus, R., Hernández-Pajares, M., Juan, J., and Sanz, J.: Improvement of global ionospheric VTEC maps by using kriging interpolation technique, *J. Atmos. Sol.-Terr. Phys.*, 67, 1598–1609, 2005.
- Orus, R., Cander, L., and Hernández-Pajares, M.: Testing regional vertical total electron content maps over Europe during 17–21 January 2005 sudden space weather event, *Radio Sci.*, 42, RS3004, <https://doi.org/10.1029/2006RS003515>, 2007.
- Roma-Dollase, D., Hernández-Pajares, M., Krankowski, A., Kotulak, K., Ghoddousi-Fard, R., Yuan, Y., Li, Z., Zhang, H., Shi, C., and Wang, C.: Consistency of seven different GNSS global ionospheric mapping techniques during one solar cycle, *J. Geodesy*, 92, 691–706, 2017.
- Rovira-Garcia, A., Juan, J., Sanz, J., and Gonzalez-Casado, G.: A Worldwide Ionospheric Model for Fast Precise Point Positioning, *IEEE T. Geosci. Remote Sens.*, 53, 4596–4604, 2015.
- Schaer, S.: Mapping and Predicting the Earth's Ionosphere Using the Global Positioning System, Ph.D. thesis, University of Berne, 1999.
- Schaer, S., Gurtner, W., and Feltens, J.: IONEX: The IONosphere Map EXchange Format Version 1, Tech. Rep., Astronomical Institute, University of Berne, Switzerland, 2–3, 1998.
- Schmidt, M.: Wavelet modelling in support of IRI, *Adv. Space Res.*, 39, 932–940, 2007.
- Schmidt, M.: Towards a multi-scale representation of multi-dimensional signals, VII Hotine-Marussi Symposium on Mathematical Geodesy, 137, 119–127, [https://doi.org/10.1007/978-3-642-22078-4\\_18](https://doi.org/10.1007/978-3-642-22078-4_18), 2012.
- Schmidt, M., Dettmering, D., Mößner, M., and Wang, Y.: Comparison of spherical harmonic and B-spline models for the vertical total electron content, *Radio Sci.*, 46, RS0D11, <https://doi.org/10.1029/2010RS004609>, 2011.
- Schmidt, M., Göttl, F., and Heinkelmann, R.: Towards the combination of data sets from various observation techniques, in: The 1st International Workshop on the Quality of Geodetic Observation and Monitoring Systems (QuGOMS'11), edited by: Kutterer, H., Seitz, F., Alkhatib, H., and Schmidt, M., 140, 35–43, 2015a.
- Schmidt M., Dettmering D., S. F.: Using B-spline expansions for ionosphere modeling, in: Handbook of Geomathematics, 2nd Edn., edited by: Freeden, W., Nashed, M. Z., and Sonar, T., Springer, 939–983, [https://doi.org/10.1007/978-3-642-54551-1\\_80](https://doi.org/10.1007/978-3-642-54551-1_80), 2015b.
- Schumaker, L. and Traas, C.: Fitting scattered data on spherelike surfaces using tensor products of trigonometric and polynomial splines, *Numerische Mathematik*, 60, 133–144, 1991.
- Stollnitz, E., DeRose, T., and Salesin, D.: Wavelets for computer graphics: a primer, Part I, *IEEE Comput. Graph.*, 3, 76–84, 1995a.
- Stollnitz, E., DeRose, T., and Salesin, D.: Wavelets for computer graphics: a primer, Part I and Part II, *IEEE Comput. Graph.*, 15, 75–85, 1995b.
- Tsurutani, B., Mannucci, A., Iijima, B., Guarnieri, F., Gonzalez, W., Judge, D., Gangopadhyay, P., and Pap, J.: The extreme Halloween 2003 solar flares (and Bastille Day, 2000 Flare), ICMs, and resultant extreme ionospheric effects: A review, *Adv. Space Res.*, 37, 1583–1588, 2006.
- Tsurutani, B., Verkhoglyadova, O. P., Mannucci, A., Lakhina, G. S., Li, G., and Zank, G. P.: A brief review of “solar flare effects” on the ionosphere, *Radio Sci.*, 44, RSOA17, <https://doi.org/10.1029/2008RS004029>, 2009.
- Wang, C., Rosen, I. G., Tsurutani, B. T., Verkhoglyadova, O. P., Meng, X., and Mannucci, A. J.: Statistical characterization of ionosphere anomalies and their relationship to space weather events, *J. Space Weather Space Clim.*, 6, A5, <https://doi.org/10.1051/swsc/2015046>, 2016.
- Zeilhofer, C.: Multi-dimensional B-spline Modeling of Spatio-temporal Ionospheric Signals, Series A, 123, 2008.
- Zhu, F., Yun, W., Yiyan, Z., and Gao, Y.: Temporal and spatial distribution of GPS-TEC anomalies prior to the strong earthquakes, *Astrophys. Space Sci.*, 345, 239–246, 2013.



## 7.2 P-II

### Reference

Andreas Goss, Michael Schmidt, Eren Erdogan, Florian Seitz (2020): **Global and Regional High-Resolution VTEC Modelling Using a Two-Step B-Spline Approach** In: Remote Sensing, 12, 1198, DOI: 10.3390/rs12071198

### Copyright

This publication has originally been published in the open access journal ‘Remote Sensing’ and is available under the license of Creative Commons at <https://www.mdpi.com/journal/remotesensing>. The copyrights remain with the authors.

### Summary Publication

Globally distributed GNSS stations of different networks, such as the network of the International GNSS Services (IGS), provide a large amount of multi-frequency observations which can be used to determine the state of the ionosphere. These data are used to generate Global Ionosphere Maps (GIM). Most of the Ionosphere Associated Analysis Centers (IAAC) of the IGS base their modelling strategies on series expansions in terms of spherical harmonics (SH). Due to the inhomogeneous global distribution of GNSS stations, and especially due to the large data gaps over oceanic areas, the global VTEC models are usually limited in their spatial and spectral resolution. Hence, the maximum degree of the SHs is chosen with  $n = 15$ .

Regional station networks such as the European Reference Frame (EUREF), the Australian Pacific Reference Frame (APREF) or the Sistema de Referencia Geocéntrico para las Américas (SIRGAS) are characterised by a dense station coverage over the continents and allow the generation of VTEC maps with higher resolution in the respective areas. A two-step modelling (TSM) approach is presented in this paper which takes advantage of these regional station networks in order to generate regional VTEC maps with higher spectral resolution accounting for the finer signal structures. The first step of the TSM comprises a global B-spline model with a series expansion of polynomial and trigonometric B-splines applied in latitude and longitude, respectively. The second step is solely based on polynomial B-splines in both directions for the regional densification of selected regions.

The TSM is integrated in a software package to provide VTEC maps using hourly GNSS data and ultra-rapid orbits. It allows for the dissemination of global and regional VTEC maps at once and with a latency of 2 to 3 hours. Within the numerical investigations, the TSM is applied to hourly data from 2015, including a geomagnetic storm on March 17. Validation with independent data shows that the generated regional high-resolution VTEC maps are of comparable accuracy to the regional maps provided by the Royal Observatory of Belgium (ROB). While the latter is provided with a latency of about one week, the developed approach allows disseminating the VTEC maps with low latency


## Declaration of Contribution

This paper has been published in the Journal 'Remote Sensing' and the content is based on the work carried out as part of the development process of the project OPTIMAP as well as in the context of the INSIGHT (Interactions of Low-orbiting Satellites with the Surrounding Ionosphere and Thermosphere) project. The latter was funded by the German Research Foundation (DFG) under the umbrella of the Special Priority Programme (SPP) 1788 Dynamic Earth with the grant number SCHM2433/10-2. OPTIMAP on the other hand is a joint initiative of the Deutsches Geodätisches Forschungsinstitut der Technischen Universität München, Bundeswehr GeoInformation Centre (BGIC) and the German Space Situational Awareness Centre (GSSAC). The concept of the paper was proposed by A. Goss and discussed with the co-authors. The calculations are based on the software, partly developed by A. Goss in the project OPTIMAP. A. Goss performed the numerical investigations, interpreted the results and compiled the figures and tables. The manuscript writing has been done by A. Goss and reviewed by all co-authors. **The overall own contribution of A. Goss for P-II is estimated at 85%**


We hereby confirm the correctness of the declaration of contribution and the reuse of the contents of the publication:

Andreas Goss, Michael Schmidt, Eren Erdogan, Florian Seitz (2020): Global and Regional High-Resolution VTEC Modelling Using a Two-Step B-Spline Approach. In: Remote Sensing, 12, 1198, DOI: 10.3390/rs12071198


apl. Prof. Dr. Michael Schmidt  
Deutsches Geodätisches Forschungsinstitut  
Technische Universität München, Germany

Signature:   
Date: 16.4.2021

Eren Erdogan  
Deutsches Geodätisches Forschungsinstitut  
Technische Universität München, Germany

Signature:   
Date: 16.04.2021




Prof. Dr. Florian Seitz  
Deutsches Geodätisches Forschungsinstitut  
Technische Universität München, Germany

Signature:   
Date: München, 9.4.21

Digital unterschrieben von Florian Seitz  
DN: cn=Florian Seitz, o=TUM, ou=DGFI-  
TUM, email=florian.seitz@tum.de, c=DE  
Datum: 2021.04.09 14:32:54 +02'00'

## Article

# Global and Regional High-Resolution VTEC Modelling Using a Two-Step B-Spline Approach

Andreas Goss , Michael Schmidt, Eren Erdogan  and Florian Seitz 

Deutsches Geodätisches Forschungsinstitut der Technischen Universität München, Arcisstraße 21, 80333 Munich, Germany; mg.schmidt@tum.de (M.S.); eren.erdogan@tum.de (E.E.); florian.seitz@tum.de (F.S.)

\* Correspondence: andreas.goss@tum.de

Received: 17 March 2020; Accepted: 3 April 2020; Published: 8 April 2020



**Abstract:** The ionosphere is one of the largest error sources in GNSS (Global Navigation Satellite Systems) applications and can cause up to several meters of error in positioning. Especially for single-frequency users, who cannot correct the ionospheric delay, the information about the state of the ionosphere is mandatory. Dual- and multi-frequency GNSS users, on the other hand, can correct the ionospheric effect on their observations by linear combination. However, real-time applications such as autonomous driving or precision farming, require external high accuracy corrections for fast convergence. Mostly, this external information is given in terms of grids or coefficients of the vertical total electron content (VTEC). Globally distributed GNSS stations of different networks, such as the network of the International GNSS Services (IGS), provide a large number of multi-frequency observations which can be used to determine the state of the ionosphere. These data are used to generate Global Ionosphere Maps (GIM). Due to the inhomogeneous global distribution of GNSS real-time stations and especially due to the large data gaps over oceanic areas, the global VTEC models are usually limited in their spatial and spectral resolution. Most of the GIMs are mathematically based on globally defined radial basis functions, i.e., spherical harmonics (SH), with a maximum degree of 15 and provided with a spatial resolution of  $2.5^\circ \times 5^\circ$  in latitude and longitude, respectively. Regional GNSS networks, however, offer dense clusters of observations, which can be used to generate regional VTEC solutions with a higher spectral resolution. In this study, we introduce a two-step model (TSM) comprising a global model as the first step and a regional model as the second step. We apply polynomial and trigonometric B-spline functions to represent the global VTEC. Polynomial B-splines are used for modelling the finer structures of VTEC within selected regions, i.e., the densification areas. The TSM provides both, a global and a regional VTEC map at the same time. In order to study the performance, we apply the developed approach to hourly data of the global IGS network as well as the EUREF network of the European region for St. Patrick storm in March 2015. For the assessment of the generated maps, we use the dSTEC analysis and compare both maps with different global and regional products from the IGS Ionosphere Associated Analysis Centers, e.g., the global product from CODE (Berne, Switzerland) and from UPC (Barcelona, Spain), as well as the regional maps from ROB (Brussels, Belgium). The assessment shows a significant improvement of the regional VTEC representation in the form of the generated TSM maps. Among all other products used for comparison, the developed regional one is of the highest accuracy within the selected time span. Since the numerical tests are performed using hourly data with a latency of one to two hours, the presented procedure is seen as an intermediate step for the generation of high precision regional real-time corrections for modern applications.

**Keywords:** ionosphere; vertical total electron content; B-splines; global navigation satellite systems; Kalman filter

## 1. Introduction

In the last decades, the use of GNSS for a broad range of commercial and scientific fields has significantly increased. Especially GNSS applications which rely on high precision positioning and navigation became more and more popular. With higher demands on accuracy, the requirements for detecting and correcting errors in the measurements increase. The main error sources in precise GNSS are the effects caused by the atmosphere. Whilst the tropospheric effects can yield approximately 1m error in positioning (in along range, i.e., the height), the ionosphere effects can vary between 1 m and even 100 m. The ionosphere is defined as the part of the upper atmosphere where the number of charged particles (electrons and ions) is high enough to induce significant changes in the propagation of radio waves. The effect mainly depends on the signal frequency; signals with frequencies lower than 30 MHz can be blocked and reflected, signals with a shorter wavelength, however, are affected in their travel times (delay) and their signal paths (bending). The delay of the signal between the satellite  $S$  and the receiver  $R$  defined as

$$d_{ion} = \pm \frac{40.3}{f^2} \int_S^R N_e ds \quad (1)$$

is only an approximation as higher-order effects are neglected. The sign on the right-hand side changes whether it is applied for carrier phase observations ('-') or for pseudorange measurements ('+') [1]. In geodesy the delay can be interpreted in two ways, namely as a

1. disturbing quantity which has to be corrected for precise applications or as a
2. target quantity.

In the latter case,  $d_{ion}$  can be used as observation to determine the electron density  $N_e$  as the ionospheric key parameter. Among many others, e.g., ionosondes and radio occultations, GNSS is the most prominent observation technique used to gain information about  $N_e$ . However, GNSS is not sensitive to the electron density directly, but on the integrated effect along the ray path. It is denoted as Slant Total Electron Content (STEC) and defined as

$$STEC(\mathbf{x}^S, \mathbf{x}_R, t) = \int_S^R N_e(\mathbf{x}, t) ds. \quad (2)$$

STEC depends on the electron density  $N_e(\mathbf{x}, t)$  along the ray path between the position  $\mathbf{x}^S$  of the satellite  $S$  and the position  $\mathbf{x}_R$  of the receiver  $R$  for time  $t$ . The position vector  $\mathbf{x}$  reads

$$\mathbf{x} = r [\cos \varphi \cos \lambda, \cos \varphi \sin \lambda, \sin \varphi]^T, \quad (3)$$

where  $\varphi$  and  $\lambda$  are latitude and longitude,  $r$  is the radial distance within a geocentric coordinate system  $\Sigma_E$ . Many ionosphere models rely on the assumption that all electrons in the ionosphere are concentrated on a spherical shell  $\Omega_H$  of infinitesimal thickness with fixed height  $H = r - R_e$  above the spherical Earth of radius  $R_e$ . It is denoted as single-layer model (SLM) and allows for the transformation of STEC into the vertical direction as

$$VTEC(\mathbf{x}_{IPP}, t) = \frac{STEC(\mathbf{x}^S, \mathbf{x}_R, t)}{M(z)} \quad (4)$$

by applying a mapping function  $M(z)$  depending on the zenith angle  $z$  [2]. It yields vertical total electron content (VTEC) referred to the Ionospheric Pierce Point (IPP), the intersection point of the ray-path with the shell  $\Omega_H$  at the position  $\mathbf{x}_{IPP}$ . Several approaches exist for the realization of the mapping function; recently UPC developed the Barcelona Ionospheric Mapping Function (BIMF) [3]. Besides the electron density VTEC means another ionospheric key parameter which can be represented as the integration,

$$VTEC(\varphi, \lambda, t) = \int_{h_l}^{h_u} N_e(\varphi, \lambda, h, t) dh, \quad (5)$$

of the electron density along the height between the lower boundary  $h_l$  and the upper boundary  $h_u$  of the ionosphere.

There are several approaches for representing VTEC globally by using input data from GNSS. The Ionospheric Associated Analysis Centers (IAAC) of the International GNSS Service (IGS), namely (1) the Jet Propulsion Laboratory (JPL), (2) the Center for Orbit Determination in Europe (CODE), (3) the European Space Operations Center of the European Space Agency (ESOC), (4) the Universitat Politècnica de Catalunya (UPC), (5) the Canadian Geodetic Survey of Natural Resources Canada (NRCAN), (6) the Wuhan University (WHU) and (7) the Chinese Academy of Sciences (CAS) routinely provide Global Ionosphere Maps (GIM) representing VTEC based on different mathematical approaches, namely the series expansion or the discretization technique. Whereas in the latter case, usually pixels or voxels are chosen [4], in the case of a series expansion spherical harmonics (SH) are mostly used. The GIM products of the IAACs are also used to generate an IGS GIM as a combined solution [5].

As a matter of fact, the representation of VTEC on a global scale suffers from the inhomogeneous distribution of the input data which does not allow a high-resolution representation on a global scale [6]. Capturing this inhomogeneity, the maximum degree of SHs is generally set to  $n = 15$ . The GIMs are usually provided in IONosphere Map EXchange (IONEX) format with a temporal resolution of 2 hours and a spatial sampling of  $2.5^\circ \times 5^\circ$  with respect to latitude and longitude and with a latency of more than one week [7,8].

Goss et al. [9] developed an approach based on B-spline basis functions and a Multi-Scale Representation (MSR) which allows to model VTEC globally with a higher spectral resolution. B-splines have already proven to be suitable basis function for representing global VTEC [10–12]. However, as a matter of fact, finer ionospheric structures can only be monitored and modeled where high-resolution input data are available, i.e., in continental regions such as Europe and North America, where a large number of stations of the global network of the IGS are located. Some of the continental regions are also covered with additional stations from regional networks, e.g., EUREF for Europe, AFREF for South Africa, ARGN and SPRGN for the Australian and Pacific region. Figure 1 shows all IPPs collected at 12:00 UT from the receiver stations of IGS and EUREF. Due to the coverage of observation stations over Europe, a dense cluster of observations is available.

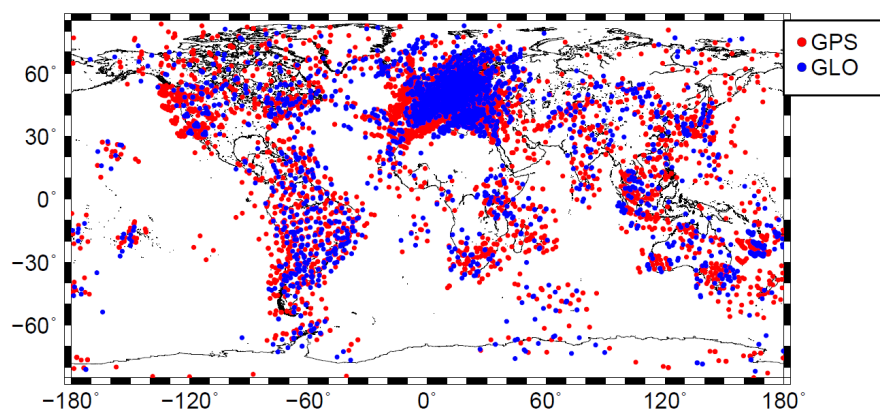


**Figure 1.** Distribution of IPPs collected from stations of the IGS and the EUREF network on 17 March 2015 at 12:00 UT. Blue colored dots indicate observations from GPS, red colored dots from GLONASS.

The Royal Observatory of Belgium (ROB) [13], for instance, provides Regional Ionospheric Maps (RIM) for the European region. Besides this, there are several approaches for the regional representation of VTEC, e.g., regional B-spline expansions [10,14–16], the thin plate spline (TPS) interpolation [17], the Taylor series [18] and the SH expansion using a spherical cap coordinate system [19].

In this paper, we describe a procedure to represent VTEC for regions with dense data coverage with high spatial and spectral resolution based on a two-step strategy using B-spline basis functions. In



the first step, we apply a global B-spline model with polynomial B-splines for latitude and trigonometric B-splines for longitude in order to represent the long-period VTEC part globally. In the second step, we perform a densification into regions with dense data coverage by using the global model as background and estimating B-spline coefficients of tensor products of polynomial B-splines representing the finer structures of VTEC. In combination, the model allows for a high-resolution VTEC representation within the densification regions. The developed approach is denoted as two-step model (TSM).

The paper is outlined as follows: in Section 2 a general description of the modelling of VTEC is given. Additionally in Section 2.1, the two-step model, based on B-spline basis functions and the connection between the two modelling steps is derived. Section 2.2 comprises a detailed description of the estimation of the unknown model parameters using a Kalman filter. Furthermore, in Section 2.3 the products of the TSM are defined. In Section 3 the TSM is applied to the European region during the St. Patrick storm days in March 2015 with a detailed validation in Section 4.

## 2. Modelling Strategies for the Regional VTEC Representation

A 3-D function  $VTEC(\varphi, \lambda, t) = f(\mathbf{x}, t)$ , as introduced in Equation (5), can be represented by means of a series expansion as

$$f(\mathbf{x}, t) = \sum_{k=0}^{\infty} c_k(t) \phi_k(\mathbf{x}), \quad (6)$$

wherein  $\phi_k(\mathbf{x})$  are given space-dependent basis functions and  $c_k(t)$  are the corresponding time-dependent series coefficients. Assuming that  $I_s$  observations  $y(\mathbf{x}_{i_s}, t_s)$  of VTEC are given at IPP positions  $P_{i_s} \in \Omega_H$  with  $i_s = 1, 2, \dots, I_s$  and discrete time moments  $t_s = t_0 + s \cdot \Delta t$  with  $s \in \mathbb{N}_0$  and  $\Delta t$  being a given temporal sampling interval, the observation equation can be written as

$$y(\mathbf{x}_{i_s}, t_s) + e(\mathbf{x}_{i_s}, t_s) = f_N(\mathbf{x}_{i_s}, t_s) = \sum_{k=0}^N c_k(t_s) \phi_k(\mathbf{x}_{i_s}), \quad (7)$$

with  $e(\mathbf{x}_{i_s}, t_s)$  being the measurement errors of the observations. Note, in the sequel of this paper, if not stated otherwise, we omit additional unknown parameters such as the satellite and receiver biases, i.e., Differential Code Biases (DCB) for the geometry free observations as on the right-hand side of Equation (7).

### 2.1. Two-Step B-Spline Expansion

At DGFI-TUM we rely on a two-step VTEC model (TSM) in terms of B-splines. The basic equation

$$VTEC_{\text{reg}}(\varphi, \lambda, t) = VTEC_{\text{glob}}(\varphi, \lambda, t) + \Delta VTEC_{\text{reg}}(\varphi, \lambda, t) \quad (8)$$

yields VTEC within the region of interest as the sum of the global model part  $VTEC_{\text{glob}}$  (first step) and the regional model part  $\Delta VTEC_{\text{reg}}$  (second step).

#### 2.1.1. Global B-spline Model

For global VTEC modelling we rewrite Equation (7) as

$$y(\mathbf{x}_{i_s}, t_s) + e(\mathbf{x}_{i_s}, t_s) = VTEC_{\text{glob}}(\mathbf{x}_{i_s}, t_s) = \sum_{k_1=0}^{K_{J_1}-1} \sum_{k_2=0}^{K_{J_2}-1} d_{k_1, k_2}^{J_1, J_2}(t_s) \phi_{k_1, J_1}(\varphi_{i_s}) \tilde{\phi}_{k_2, J_2}(\lambda_{i_s}), \quad (9)$$

with  $K_{J_1} \cdot K_{J_2}$  initially unknown time-dependent series coefficients  $d_{k_1, k_2}^{J_1, J_2}(t_s)$  and the tensor products

$$\phi_{k_1, J_1}(\varphi_{i_s}) \tilde{\phi}_{k_2, J_2}(\lambda_{i_s})$$

of polynomial B-spline functions  $\phi_{k_1, J_1}(\varphi)$  and trigonometric B-spline functions  $\tilde{\phi}_{k_2, J_2}(\lambda)$  representing VTEC w.r.t. latitude  $\varphi$  and longitude  $\lambda$ ; for more information see [9,20–23]. The shift parameters  $k_1 \in \{0, 1, \dots, K_{J_1} - 1\}$  and  $k_2 \in \{0, 1, \dots, K_{J_2} - 1\}$  for polynomial and trigonometric B-splines, define the position of the B-spline functions on the sphere  $\Omega_H$ . The total numbers  $K_{J_1} = 2^{J_1} + 2$  and  $K_{J_2} = 3 \cdot 2^{J_2}$  of B-spline functions depend on the B-spline levels  $J_1$  and  $J_2$ . In order to select appropriate numerical values for  $J_1$  and  $J_2$ , the two inequality chains

$$\begin{aligned} J_1 &\leq \log_2 \left( \frac{180^\circ}{\Delta\varphi} - 1 \right) \leq \log_2 (n_{max} - 1) \text{ and} \\ J_2 &\leq \log_2 \left( \frac{120^\circ}{\Delta\lambda} \right) \leq \log_2 \left( \frac{2 \cdot n_{max}}{3} \right), \end{aligned} \quad (10)$$

have been considered by Goss et al. [9] and relate  $J_1$  and  $J_2$  to the average global sampling intervals  $\Delta\varphi$  and  $\Delta\lambda$  of the input data, i.e., the GNSS measurements, and the maximum degree  $n_{max}$  of a SH expansion, which means the measure for the spectral content of a signal given on a sphere.

For the numerical values 1 to 6 for the B-spline levels  $J_1$  and  $J_2$ , Table 1 presents the corresponding largest numerical values for  $n_{max}$  as well as the corresponding sampling intervals  $\Delta\varphi$  and  $\Delta\lambda$  as already published in [9]. Additionally, the minimum wavelength  $L_\varphi = 2 \cdot \Delta\varphi$  and  $L_\lambda = 2 \cdot \Delta\lambda$  are given.

**Table 1.** Values for the B-spline levels  $J_1$  and  $J_2$ , the maximum spherical harmonics (SH) degree  $n_{max}$ , the input data sampling intervals  $\Delta\varphi$  and  $\Delta\lambda$ , as well as the minimum wavelengths  $L_\varphi$  and  $L_\lambda$ ; the left part presents the values along the meridian (upper inequalities in Equation (10)), the right part the corresponding values along the equator and its parallels (lower inequalities in Equation (10)).

Latitude							Longitude						
$J_1$	1	2	3	4	5	6	$J_2$	1	2	3	4	5	6
$n_{max}$	3	5	9	17	33	63	$n_{max}$	3	6	12	24	48	96
$\Delta\varphi$	60°	36°	20°	10.5°	5.45°	2.85°	$\Delta\lambda$	60°	30°	15°	7.5°	3.75°	1.875°
$L_\varphi$	120°	72°	40°	21°	10.9°	5.7°	$L_\lambda$	120°	60°	30°	15°	7.5°	3.75°

According to [9], the inequality chains (10) comprise two scenarios for determining  $J_1$  and  $J_2$ , depending on 1) the given sampling intervals  $\Delta\varphi$  and  $\Delta\lambda$  and 2) a given maximum degree  $n_{max}$  of the spectral content. As mentioned before, most of the GIMs of the IAACs are based on a SH expansion up to degree  $n_{max} = 15$ . Consequently, the level values  $J_1 = 4$  and  $J_2 = 3$  can be derived from Equation (10) [9]. Based on these values, average sampling intervals of approximately  $\Delta\varphi = 10^\circ$  and  $\Delta\lambda = 15^\circ$  are required.

### 2.1.2. Regional B-Spline Model

Most of the continental regions are characterized by a dense data coverage. Consequently, small values for the sampling intervals  $\Delta\varphi$  and  $\Delta\lambda$  can be chosen as shown, e.g., for the European continent, see Figure 1. For these regions a densification based on the principle of Equation (8) can be applied. Thereby, the global model from the previous section serves as background information for the regional model part. We rewrite Equation (7) as

$$y(x_{is}, t_s) + e(x_{is}, t_s) - VTEC_{glob}(x_{is}, t_s) = \Delta VTEC_{reg}(x_{is}, t_s) = \sum_{k_3=0}^{K_{J_3}-1} \sum_{k_4=0}^{K_{J_4}-1} d_{k_3, k_4}^{J_3, J_4}(t_s) \phi_{k_3, J_3}(\varphi) \phi_{k_4, J_4}(\lambda), \quad (11)$$

where we introduce tensor products of polynomial B-splines of level  $J_3$  and  $J_4$  with shift parameters  $k_3$  and  $k_4$  applied to both, latitude and longitude. The polynomial endpoint-interpolating B-splines ensure that the model intervals are closed in both directions at the region boundaries. Equation (11) applies for a rectangular area  $\Delta\Omega \in \Omega_H$  of size  $Y \times \Gamma$ . Herein,  $Y$  means the extension of the area  $\Delta\Omega$  with respect to the latitude  $\varphi$ ,  $\Gamma$  is the stretch of  $\Delta\Omega$  with respect to the longitude  $\lambda$ . The region size is

subject to restrictions: the smallest wavelength represented by the global background must be shorter or equal to the largest one of the regional model. Following this requirement, the inequalities

$$Y \geq L_\varphi \quad \text{and} \quad \Gamma \geq L_\lambda \quad (12)$$

can be set up. Similarly to the definition of the global level values, the inequality relations for the regional level values read

$$\begin{aligned} J_3 &\leq \log_2 \left( \frac{Y}{\Delta\varphi} - 1 \right) \leq \log_2 \left( \frac{Y \cdot n_{max}}{180^\circ} \right) \\ J_4 &\leq \log_2 \left( \frac{\Gamma}{\Delta\lambda} - 1 \right) \leq \log_2 \left( \frac{\Gamma \cdot n_{max}}{180^\circ} \right) \end{aligned} \quad (13)$$

in dependence of the average sampling intervals  $\Delta\varphi$  and  $\Delta\lambda$  of the observations within the region  $\Delta\Omega$ . Numerical values from the inequality chains (13) for a specified region can be found in Table 2.

Following this concept, the question remains, how to avoid correlations between the two parts of the TSM. To solve this problem we divide the set  $\mathcal{D}$  of all available observations into a subset  $\mathcal{D}_1$  of global observations  $y_{glob}$  and a subset  $\mathcal{D}_2$  of observations  $y_{reg}$  related to possible regional densification areas  $\Delta\Omega$ . In our current installation we determine the set  $\mathcal{D}_1$  by segmenting the Earth's surface into bins of a size related to the global sampling intervals  $\Delta\varphi$  and  $\Delta\lambda$  according to the Equations (10). For all bins in which more than two receiver stations of GNSS networks (e.g., IGS, EUREF, UNAVCO) are located, we select this receiver station which is the nearest one to the center of the bin. Then all observations of the chosen receiver station, related to the corresponding IPPs, are collected in the global set  $\mathcal{D}_1$ . The observations of the non-chosen stations within the bins are potential candidates for the regional data set  $\mathcal{D}_2$ . It should be noted that the densification data set  $\mathcal{D}_2$  may consist of several data sets  $\mathcal{D}_{2,a}, \mathcal{D}_{2,b}, \dots$  related to non-overlapping densification areas  $\Delta\Omega_A, \Delta\Omega_B, \dots$  such that  $\mathcal{D}_2 = \mathcal{D}_{2,a} \oplus \mathcal{D}_{2,b} \oplus \dots$

Note, the realization of the two data sets  $\mathcal{D}_1$  and  $\mathcal{D}_2$  is currently based on a preliminary procedure and will not be discussed in more detail. There are more sophisticated approaches, i.e., based on Voronoi diagrams considering also the station and receiver qualities [24].

## 2.2. Estimation of B-spline Coefficients

The Kalman-Filter (KF, Kalman, 1960) is a sequential estimator which yields the ionospheric parameters for both modelling steps (global and regional). In the KF the input data from the past have not to be stored and the current state is updated as soon as new observations are available [25]. It is an optimal recursive estimator in terms of minimum variance estimation including a time update (prediction step) and a measurement update (correction step); see e.g., [25–27]. The approach consists of a linear formulation of the state equations

$$\beta_s = F_s \beta_{s-1} + w_{s-1} \quad (14)$$

and of the observation equations

$$y_s + e_s = A_s \beta_s. \quad (15)$$

In Equation (14)  $\beta_s$  is the  $u \times 1$  vector of unknown series coefficients at time  $t_s$  predicted from the state vector  $\beta_{s-1}$  of the previous time step  $t_{s-1}$  by means of the  $u \times u$  transition matrix  $F_s$  and the  $u \times 1$  vector  $w_{s-1}$  of the process noise with  $u$  as the number of unknown series coefficients. Equation (15) consists of the  $I_s \times 1$  vector  $y_s = (y(x_{i_s}, t_s))$  of observations, the vector  $e_s = (e(x_{i_s}, t_s))$  of corresponding measurement errors and  $A_s$  the corresponding  $I_s \times u$  design matrix. The vectors  $e_s$  and  $w_s$  are characterized by the expectation vectors  $E(e_s) = \mathbf{0}$  and  $E(w_s) = \mathbf{0}$ , as well as the covariance matrices

$$E(w_s w_s^T) = \Sigma_w \delta_{s,l}, \quad E(e_s e_s^T) = \Sigma_y \delta_{s,l}, \quad E(w_s e_l^T) = \mathbf{0}, \quad (16)$$



where  $\delta_{s,l}$  is the delta symbol which equals to 1 for  $s = l$  and to 0 for  $s \neq l$ ; see [9,28].

### 2.2.1. Kalman Filter

The solution of the estimation problem as defined by the Equations (14) and (15) can be found by sequential application of the prediction step and the correction step. Hence, the state equation (14) is used to obtain the predicted ionospheric target parameter vector  $\beta_s^-$  and its covariance matrix  $\Sigma_{\beta,s}^-$  as

$$\beta_s^- = F_s \hat{\beta}_{s-1} \text{ and} \quad (17)$$

$$\Sigma_{\beta,s}^- = F_s \hat{\Sigma}_{\beta,s-1} F_s^T + \Sigma_w, \quad (18)$$

for details see [28]. Once the prediction of the state vector from time  $t_{s-1}$  to time  $t_s$  is given, the predicted state vector and its covariance matrix are updated with the new allocated measurements at time  $t_s$  by

$$\hat{\beta}_s = \beta_s^- + K_s (y_s - A_s \beta_s^-) \quad (19)$$

and

$$\hat{\Sigma}_{\beta,s} = (I - K_s A_s) \Sigma_{\beta,s}^-, \quad (20)$$

where  $\hat{\beta}$  and  $\hat{\Sigma}_{\beta,s}$  are the updated state vector and its covariance matrix. Thereby the so-called Kalman gain matrix

$$K_s = \Sigma_{\beta,s}^- A_s^T (A_s \Sigma_{\beta,s}^- A_s^T + \Sigma_y)^{-1} \quad (21)$$

behaves like a weighting matrix between the new measurements and the predicted state vector.

### 2.2.2. Coordinate System

VTEC exhibits a time-varying phenomenon. Therefore, a proper prediction model is required to take the time variation of the ionospheric parameters into account. Since  $VTEC_{\text{glob}}$  is represented in the geocentric solar magnetic (GSM) coordinate system which results in much slower variations of the B-spline coefficients in time, a random walk approach could be performed for all the unknown parameters of the global model part within the KF. In this case the transition matrix is defined as identity matrix, i.e.,  $F_s = I$ . Hence, the predicted state vector reads  $\beta_s^- = \hat{\beta}_{s-1}$ , according to Equation (17). Detailed information about the GSM coordinate system can be found, for instance, in [29,30]. The regional model, on the other hand, is set up in the Earth-fixed geographical coordinate system. Although VTEC varies significantly faster in this coordinates system, since it comprises the diurnal and shorter variations, too, the main part of VTEC is represented by the global background model  $VTEC_{\text{glob}}$ . Thus, the estimated differences  $\Delta VTEC_{\text{reg}}$  of  $VTEC_{\text{reg}}$  with respect to the background VTEC values exhibit small values. Thus, the random walk approach can also be used as a prediction model for the unknown regional B-spline coefficients.

### 2.2.3. Definition of the Global and the Regional Kalman Filter

Since both model parts are defined in different coordinate systems and based on different observation data sets, the estimation of their unknown parameters will be carried out separately. Therefore we rewrite the system of observation equations (15) for the global model as

$$y_{s,\text{glob}} + e_{s,\text{glob}} = A_{s,\text{glob}} \beta_{s,\text{glob}} \quad (22)$$

and for the regional model as

$$y_{s,\text{reg}} + e_{s,\text{reg}} = A_{s,\text{reg}} \beta_{s,\text{reg}} \quad (23)$$

in accordance to the different data sets  $D_1$  for the global model and  $D_2$  for the regional model. The global  $I_s^{D_1} \times 1$  observation vector  $y_{s, \text{glob}}$  consists of  $y(x_{i_s}, t_s) \in D_1$ , the regional  $I_s^{D_2} \times 1$  observation vector  $y_{s, \text{reg}}$  in Equation (23) consists of the values

$$\Delta VTEC_{\text{reg}}(x_{i_s}, t_s) = y(x_{i_s}, t_s) - VTEC_{\text{glob}}(x_{i_s}, t_s) \quad (24)$$

for all observations  $y(x_{i_s}, t_s) \in D_2$ . The vectors  $e_{s, \text{glob}}$  and  $e_{s, \text{reg}}$  are defined accordingly. The design matrices  $A_{s, \text{glob}}$  and  $A_{s, \text{reg}}$  are constructed by the tensor products of the B-spline functions according to the Equations (9) and (11). The state vector  $\beta_{s, \text{glob}}$  consists of the unknown B-spline coefficients  $d_{k_1, k_2}^{I_1, I_2}$  as well as the DCBs for satellites and the receivers of the stations assigned to  $D_1$ . The state vector  $\beta_{s, \text{reg}}$  consists of the unknown B-spline coefficients  $d_{k_3, k_4}^{I_3, I_4}$  and receiver DCBs of the receivers that are assigned to  $D_2$ , whereas the satellite DCBs can be omitted, since they are estimated within the global model part.

Since the estimation is performed for both model parts separately, we need to decompose the matrices  $\Sigma_y$  and  $\Sigma_w$  in the KF Equations (17) to (21) as well. The matrices  $\Sigma_{y, \text{glob}}$  and  $\Sigma_{y, \text{reg}}$  are set up in accordance to [28] and consist of two diagonal block matrices related to GPS and GLONASS observations of the data sets  $D_1$  and  $D_2$ . The relative weighting between the blocks is performed by adaptively defined variance factors, details can be found by [31]. The block matrices  $\Sigma_{w, \text{glob}}$  and  $\Sigma_{w, \text{reg}}$  are related to the process noise for the global and the regional model, respectively. They are adapted to the magnitude of the signal, i.e., we have to define different process noise for  $VTEC_{\text{glob}}$  and  $\Delta VTEC_{\text{reg}}$ . Additionally, the distribution of the observation data is considered for the calculation of the process noise. For more information see [31].

### 2.3. VTEC Model Output

By applying the KF procedure according to the Equations (17) to (20) to the global observations of data set  $D_1$  given in the GSM coordinate system in the first step and to the observations of the data set  $D_2$  given in the Earth-fixed geographical coordinate system for the regional densification step, we obtain the two estimations  $\hat{\beta}_{s, \text{glob}}$  and  $\hat{\beta}_{s, \text{reg}}$  for the unknown series coefficients as well as their estimated covariance matrices  $\hat{\Sigma}_{\beta, s, \text{glob}}$  and  $\hat{\Sigma}_{\beta, s, \text{reg}}$  successively. From these estimates we can evaluate the  $V \times 1$  vector

$$\hat{f}_{s, \text{glob}} = \bar{A}_s \hat{\beta}_{s, \text{glob}} \text{ and} \quad (25)$$

and the  $V \times V$  matrix

$$\hat{\Sigma}_{s, \text{glob}} = \bar{A}_s \Sigma_{\beta, s, \text{glob}} \bar{A}_s^T, \quad (26)$$

of VTEC values  $\widehat{VTEC}_{\text{glob}}(\varphi_v, \lambda_v, t_s)$  at arbitrary points  $P(\varphi_v, \lambda_v)$  on the sphere  $\Omega_H$  with  $v = 1, \dots, V$ , as well as the corresponding covariance matrix. The matrix  $\bar{A}_s$  is set up in a similar way as the matrix  $A_{s, \text{glob}}$  in the Equation (22). Accordingly, we can evaluate  $\Delta \widehat{VTEC}_{\text{reg}}(\varphi_w, \lambda_w, t_s)$  at points  $P(\varphi_w, \lambda_w)$  with  $w = 1, \dots, W$  within the region  $\Delta\Omega$  by

$$\hat{f}_{s, \text{reg}} = \bar{A}_s \hat{\beta}_{s, \text{reg}} \text{ and} \quad (27)$$

$$\hat{\Sigma}_{s, \text{reg}} = \bar{A}_s \Sigma_{\beta, s, \text{reg}} \bar{A}_s^T, \quad (28)$$

where  $\hat{f}_{s, \text{reg}}$  is a  $W \times 1$  vector and  $\hat{\Sigma}_{s, \text{reg}}$  the corresponding  $W \times W$  covariance matrix. Assuming both model parts are uncorrelated, the total VTEC within the region can finally be calculated by applying Equation (8) as

$$\widehat{VTEC}_{\text{reg}}(\varphi, \lambda, t_s) = \widehat{VTEC}_{\text{glob}}(\varphi, \lambda, t_s) + \Delta \widehat{VTEC}_{\text{reg}}(\varphi, \lambda, t_s) \quad (29)$$

for latitude  $\varphi = \varphi_v = \varphi_w$  and longitude  $\lambda = \lambda_v = \lambda_w$ . The same applies for the calculation of the standard deviation

$$\hat{\sigma}_{VTEC, \text{reg}}(\varphi, \lambda, t_s) = \sqrt{\hat{\sigma}_{s, \text{reg}}^2(\varphi, \lambda) + \hat{\sigma}_{s, \text{glob}}^2(\varphi, \lambda)}, \quad (30)$$

where the values  $\hat{\sigma}_{s,\text{reg}}^2(\varphi, \lambda)$  and  $\hat{\sigma}_{s,\text{glob}}^2(\varphi, \lambda)$  for each point  $P(\varphi, \lambda)$  at time moments  $t_s$  are given by the diagonal elements of  $\hat{\Sigma}_{s,\text{glob}}$  and  $\hat{\Sigma}_{s,\text{reg}}$ , respectively. A flowchart of the developed TSM approach is shown in Figure 2. Starting from global and regional GNSS station networks, the respective data sets  $\mathcal{D}_1$  and  $\mathcal{D}_2$  are defined. The left side of Figure 2 depicts the process chain for generating the global model part. The right-hand side of the flowchart shows the process for generating the regional densification. Here the extent of the densification area has to be chosen in dependency of the global levels  $J_1$  and  $J_2$  according to (12). Furthermore, the global model is required as a background for modelling the regional  $\Delta VTEC$ .

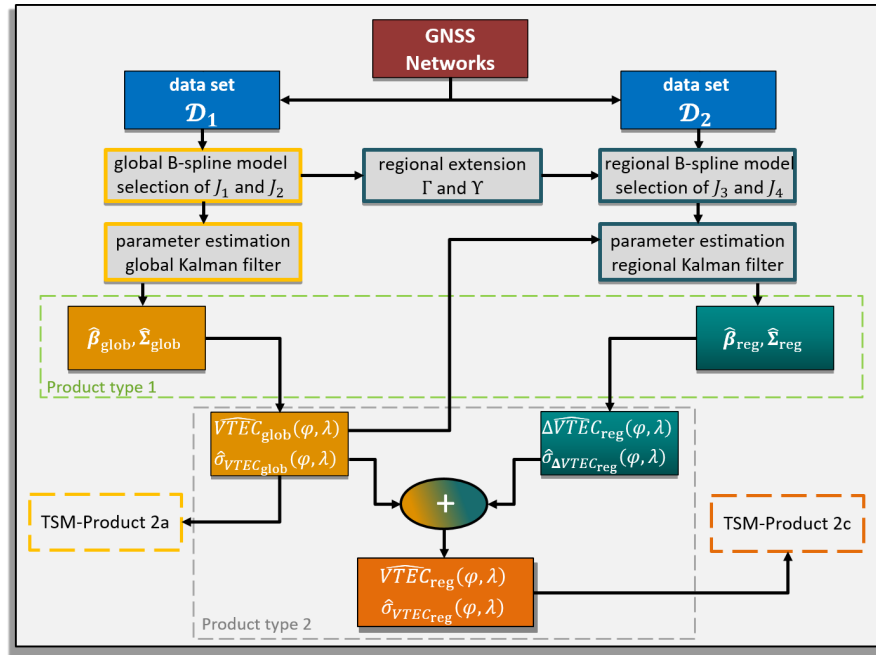


**Figure 2.** Flowchart of the two-step model (TSM), with the process chain for the first step—the global model—on the left side in yellow and the process chain for the second step—the regional densification—on the right side in green.

At the end of the process chain, the regional high-resolution  $VTEC_{\text{reg}}$  values are calculated by combining the estimated global and regional model parts according to the Equations (29) and (30).

#### VTEC Products

According to [9], the previously explained procedure allows for the dissemination of two types of products, namely

##### – Product type 1:

- estimated B-spline coefficients  $\hat{d}_{k_1, k_2}^{J_1, J_2}(t_s)$  and their standard deviations  $\hat{\sigma}_{d, k_1, k_2}^{J_1, J_2}(t_s)$  for the global model of levels  $J_1$  and  $J_2$  at time moments  $t_s$  as well as
- estimated B-spline coefficients  $\hat{d}_{k_3, k_4}^{J_3, J_4}(t_s)$  with their standard deviations  $\hat{\sigma}_{d, k_3, k_4}^{J_3, J_4}(t_s)$  for the regional model of levels  $J_3$  and  $J_4$  at time moments  $t_s$  and

##### – Product type 2

- estimated values  $\widehat{VTEC}_{\text{glob}}(\varphi_v, \lambda_v, t_s)$  and their standard deviations  $\hat{\sigma}_{VTEC_{\text{glob}}}(\varphi_v, \lambda_v, t_s)$  on a regular grid of the global model at time moments  $t_s$  taken from the Equations (25) and (26)

as well as

- b) estimated values  $\Delta \widehat{VTEC}_{reg}(\varphi_w, \lambda_w, t_s)$  and their standard deviations  $\widehat{\sigma}_{\Delta VTEC_{reg}}(\varphi_w, \lambda_w, t_s)$  from Equation (29) on a regular grid of the regional model at time moments  $t_s$  taken from the Equations (27) and (28) as well as
- c) estimated values  $\widehat{VTEC}_{reg}(\varphi_w, \lambda_w, t_s)$  and their standard deviation  $\widehat{\sigma}_{VTEC_{reg}}(\varphi_w, \lambda_w, t_s)$  on a regular grid of the regional model at time moments  $t_s$  taken from the Equation (29) and (30)

to the user. The two product types reflect the two strategies of dissemination. In terms of product type 2, VTEC is provided to users typically by means of the IONEX format, see [18]. Thereby, the sampling intervals  $\Delta\Phi$  in latitude and  $\Delta\Lambda$  in longitude between the grid points  $P(\varphi_v, \lambda_v)$  are usually chosen as  $1^\circ$ ,  $2.5^\circ$  or  $5^\circ$ . For the calculation of VTEC values at arbitrary points between the grid points an interpolation has to be applied which generally degenerates the quality of the calculated values [9]. In the case of product type 1, the VTEC values and the corresponding standard deviations can be calculated at arbitrary points with higher accuracy using the Equations (25) to (28) directly. However, then an encoder procedure for the estimated B-spline coefficients is necessary. In fact, the presented two-step approach described in Section 2.1 provides two products in terms of Product type 2, namely

- **TSM-Product 2a**  
the global model  $VTEC_{glob}(\varphi, \lambda, t)$  as well as the corresponding standard deviations  $\sigma_{glob}(\varphi, \lambda, t)$  for the representation of VTEC on a global scale and
- **TSM-Product 2c**  
the regional model  $VTEC_{reg}(\varphi, \lambda, t)$  and the corresponding standard deviations  $\sigma_{reg}(\varphi, \lambda, t)$  for the representation of VTEC with a higher spatial and spectral resolution within the selected region.

Due to the independent estimation of the coefficients  $d_{k_1, k_2}^{J_1, J_2}$  for the global and  $d_{k_3, k_4}^{J_3, J_4}$  for the regional model part, the global model is not affected by the densification step and can be disseminated as Product type 2a. The second step of the TSM, however, depends on the global background model. Hence, in this case both model steps have to be evaluated in order to provide the TSM-Product type 2c.

### 3. Two-Step Model for Europe

In the sequel, the developed approach is applied to real data collected during March 2015. This time span is selected because of the solar storm, the St. Patrick storm, happened on March 17. Thus, stronger spatial variations in VTEC can be observed and modeled. We apply the TSM with a densification for the European region. It is particularly suitable for the application of the TSM due to a dense coverage of receiver stations from both, the global IGS network and the regional EUREF network, which provides a dense observation distribution over Europe, see Figure 1. It shall be noted that the idea of the following investigation is the generation of a VTEC model defined within a region that is characterized by a high spatial and spectral resolution such that a TSM-Product 2c can be established. It is not our objective to create a VTEC model of the most highest spatial and spectral content for a given region.

#### 3.1. Global Model

We follow the workflow for the TSM procedure presented in Figure 2 and start with the definition of the different data sets  $\mathcal{D}_1$  for the global modelling part. Figure 3 shows in the left-hand panel all available stations from the global IGS network (red dots) and from the regional open network in Europe, EUREF (blue dots). The right-hand panel depicts the selected stations for creating the set  $\mathcal{D}_1$  with a more homogeneous distribution over the globe  $\Omega_H$ . The stations are selected by means of a

segmentation of the Earth's surface into bins of size  $10^\circ \times 10^\circ$  w.r.t. latitude and longitude, according to the inequality chains (10).

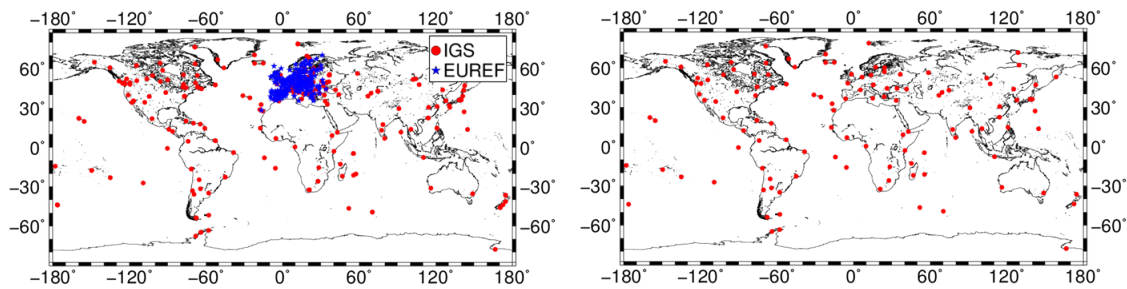


**Figure 3.** Receiver stations of the global IGS network (red dots) and the European EUREF network (blue dots), **left panel**; selected receiver stations which provide observations for the global data set  $\mathcal{D}_1$ , **right panel**.

The observations related to the IPPs of the chosen receiver stations define the data set  $\mathcal{D}_1$ . Figure 4 shows exemplarily the corresponding IPPs from GPS and GLONASS on 17 March 2015 at 12:00 UT with a less dense data coverage over the continental regions compared to the distribution of IPPs in Figure 1.

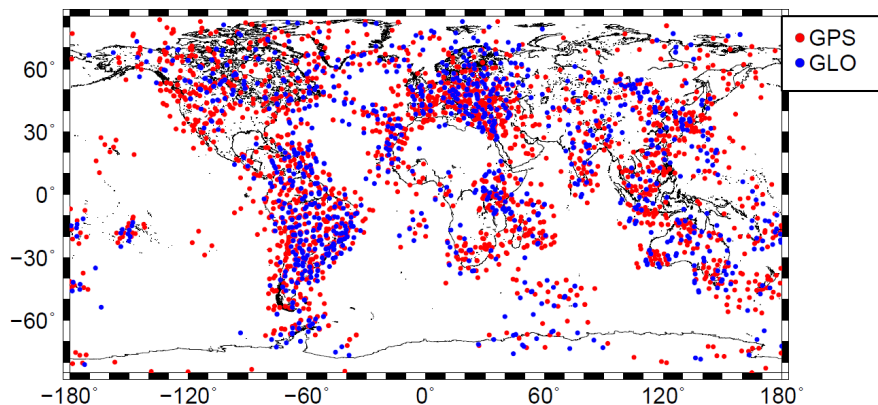


**Figure 4.** Observation distribution of GPS and GLONASS observations on 17 March 2015 at 12:00 UT, from the global data set  $\mathcal{D}_1$ .

According to the workflow in Figure 2 (left), the next step is to select the global B-spline levels  $J_1$  and  $J_2$ . As already mentioned in the context of Table 1 the levels  $J_1 = 4$  and  $J_2 = 3$  are chosen here. Given the vectors  $y_{s, \text{glob}}$ ,  $e_{s, \text{glob}}$ , the matrices  $\Sigma_{y, \text{glob}}$ ,  $\Sigma_{w, \text{glob}}$ , we run the Kalman filter for estimating the unknowns of the global model. We set the Kalman filter step size to  $\Delta t = t_s - t_{s-1} = 10$  minutes and estimate the  $18 \cdot 24 = 432$  global B-spline coefficients as well as the corresponding standard deviations

$$\begin{aligned} \hat{d}_{k_1, k_2}^{4,3}(t_s) \big|_{k_1=0, \dots, 17, k_2=0, \dots, 23} , \\ \hat{\sigma}_{d, k_1, k_2}^{4,3}(t_s) \big|_{k_1=0, \dots, 17, k_2=0, \dots, 23} \end{aligned} \quad (31)$$

with  $K_{J_1} = 2^4 + 2 = 18$  and  $K_{J_2} = 3 \cdot 2^3 = 24$ . The top left panel of Figure 5 shows the estimated coefficients and the top right panel the corresponding standard deviations from the Equations (19) and (20), respectively.

The estimated parameters are of Product type 1a as defined in Section 2.3. For the calculation of Product type 2a we select the output sampling intervals  $\Delta\Phi = 2.5^\circ$  and  $\Delta\Lambda = 5^\circ$  w.r.t. the geographical latitude and longitude, resp., as well as the temporal output sampling interval  $\Delta T = 10$  minutes. The estimated grid values  $\widehat{VTEC}_{\text{glob}}(\varphi_v, \lambda_v, t_s)$  and the corresponding standard deviations

$\hat{\sigma}_{VTEC_{glob}}(\varphi_v, \lambda_v, t_s)$  are shown in the lower panels of Figure 5. Note, here we applied a bi-linear interpolation according to [9,18] for visualization.

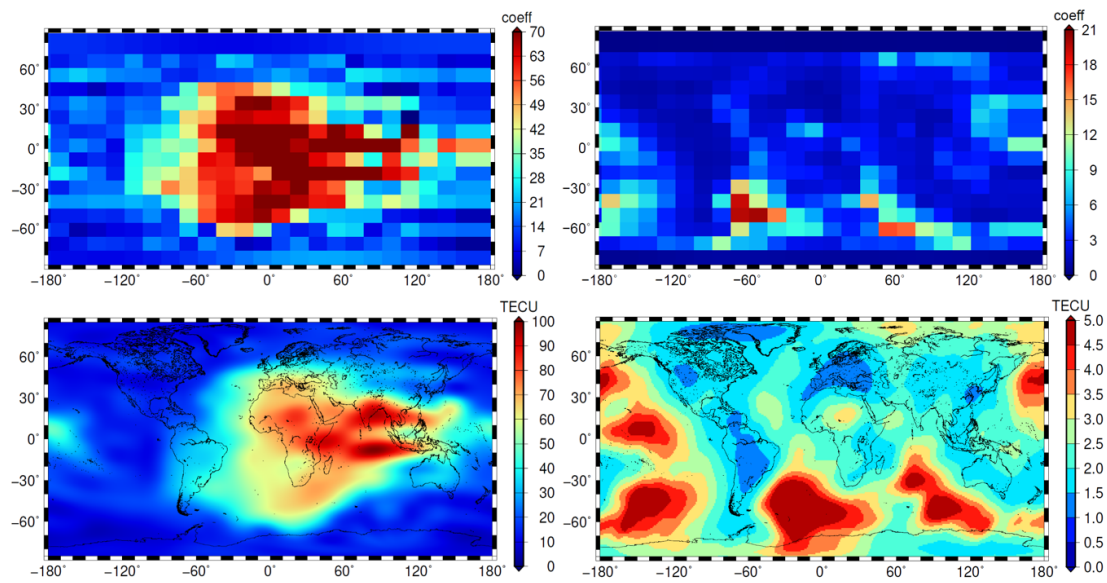


**Figure 5.** Estimated coefficients (**top left**) and their standard deviations (**top right**) for the level values  $J_1 = 4$  and  $J_2 = 3$  within the GSM coordinate system; estimated vertical total electron content (VTEC) values (**bottom left**) and their standard deviations (**bottom right**) as GIMs defined in the geographical coordinate system; all sets calculated for 17 March 2015 at 12:00 UT.

From the comparison of the two left-hand side panels, it can be stated that the numerical values of the estimated coefficients reflect the spatial signal structures in VTEC due to the localizing feature of the B-spline expansion. The standard deviations in the right-hand side panels reflect the data distribution. Hence, there are significantly larger standard deviations where only a few number of observations are available. This can be verified by comparing the standard deviations with the distribution of the IPPs shown in Figure 4.

### 3.2. Regional Model

As with the modelling of the global part, the first step for the regional model is to define the data set  $D_2$ . The method for this has already been described at the end of Section 2.1. Figure 6 depicts the receiver stations for both data sets  $D_1$  (red circles) and  $D_2$  (blue stars) within the European region.

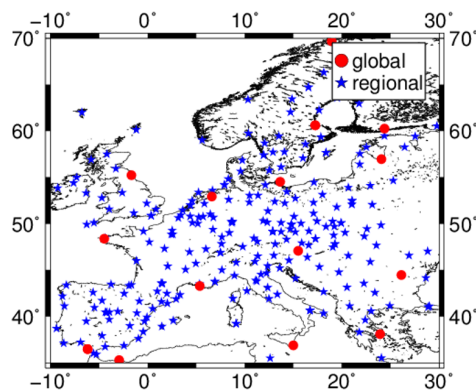


**Figure 6.** Receiver stations providing observations for the global data set  $D_1$  (red dots) and stations providing observations for the regional data set  $D_2$  (blue) within the European region.



The observations related to the IPPs of the receiver stations within the regional densification area are collected in the data set  $\mathcal{D}_2$  and exemplarily shown in Figure 7. Since the relation  $\mathcal{D}_1 \cap \mathcal{D}_2 = \emptyset$  holds, no observation can be a member of both data sets. Consequently, we assume negligible correlations between the two data sets.

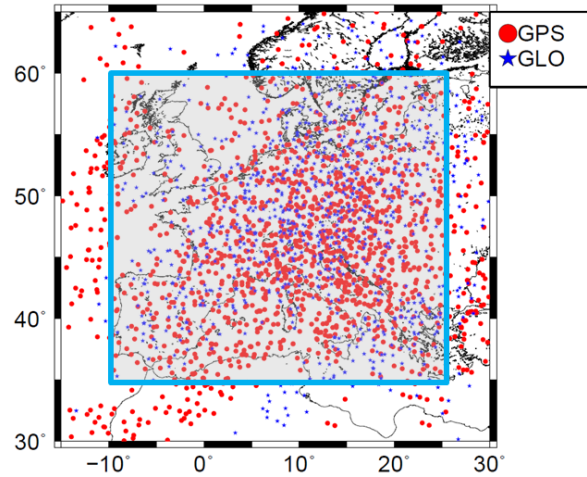


**Figure 7.** Distribution of the IPPs of the GPS and GLONASS observations from 17 March 2015 at 12:00 UT; the IPPs within the blue box are selected for the regional data set  $\mathcal{D}_2$ .

The regional model is set up after the definition of the size  $\Delta\Omega$  of the densification area. According to the inequalities (12) and (13) the regional levels  $J_3$  and  $J_4$  have to be defined independence of the observation distribution over Europe. We proceed as follows:

1. Selection of the regional extent

According to (12) the minimum wavelength represented by the global model must fit into the region. With the chosen level values  $J_1 = 4$  and  $J_2 = 3$  we obtain from Table 1  $L_\varphi = 21^\circ$  in latitude and  $L_\lambda = 30^\circ$  in longitude. The most homogeneous and dense distribution of IPPs of the data set  $\mathcal{D}_2$  is given between the latitudes  $\varphi \in [35^\circ, 60^\circ]$  and the longitudes  $\lambda \in [-10^\circ, 25^\circ]$ , this area is highlighted with the blue box in Figure 7. The densification area  $\Delta\Omega$  is chosen accordingly with a extension of  $Y = 25^\circ$  and  $\Gamma = 35^\circ$ , and thus fulfills the requirement (12).

2. Selection of the B-spline levels

Although the sampling intervals in the center of the defined region  $\Delta\Omega$  are particularly small, the average sampling intervals  $\Delta\varphi \leq 2.5^\circ$  and  $\Delta\lambda \leq 2.5^\circ$  are chosen due to the larger gaps at the boundaries. Substituting  $\Delta\varphi$ ,  $\Delta\lambda$ ,  $Y$  and  $\Gamma$  in the mid part of the chain (13) yields the maximum B-spline levels  $J_3 = 3$  and  $J_4 = 3$  from Table 2 which shows the numbers from the inequality chains (13) analog to Table 1 for the global case.

**Table 2.** Values for the B-spline levels  $J_3$  and  $J_4$ , the maximum SH degree  $n_{max}$ , the input data sampling intervals  $\Delta\varphi$  and  $\Delta\lambda$ , as well as the minimum wavelengths  $L_\varphi = 2 \cdot \Delta\varphi$  and  $L_\lambda = 2 \cdot \Delta\lambda$ ; the left part presents the numbers along the meridian (upper inequalities in Equation 13), the right part the corresponding numbers along the equator and its parallels (lower inequalities in Equation (13)).

Latitude					Longitude				
$J_3$	1	2	3	4	$J_4$	1	2	3	4
$n_{max}$	22	36	64	122	$n_{max}$	15	25	47	87
$\Delta\varphi$	$8^\circ$	$5^\circ$	$2.8^\circ$	$1.5^\circ$	$\Delta\lambda$	$11.6^\circ$	$7^\circ$	$3.8^\circ$	$2^\circ$
$L_\varphi$	$16^\circ$	$10^\circ$	$5.6^\circ$	$3^\circ$	$L_\lambda$	$23.2^\circ$	$14^\circ$	$7.6^\circ$	$4^\circ$

From Table 1 we identified the global level values  $J_1 = 4$  and  $J_2 = 3$  with the SH degrees value  $n_{max} = 17$  and  $n_{max} = 12$ , resp., as cutoff frequency of the spectral signal content of VTEC. From

Table 2 we obtain in the same manner for the B-spline levels  $J_3 = 3$  and  $J_4 = 3$  of the regional model. Consequently, our final regional VTEC model contains a spectral component up to the cutoff frequencies  $n_{max} = 64$  in latitude direction and  $n_{max} = 47$  in longitude direction.

With the chosen level values  $J_3 = 3$ ,  $J_4 = 3$ , the observation vector  $y_{s,reg}$ , the measurement error vector  $e_{s,reg}$ , the covariance matrix  $\Sigma_{y,reg}$  of the observations and the covariance matrix  $\Sigma_{w,reg}$  of the process noise, we perform the estimation of the regional B-spline coefficients by means of the Kalman filter. Its step size is set to  $\Delta t = 10$  minutes, as it was applied for the global model. We obtain the estimated coefficients and their standard deviations as

$$\begin{aligned} \hat{d}_{k_3,k_4}^{3,3}(t_s) \big|_{k_3=0,\dots,9, k_4=0,\dots,9} \\ \hat{\sigma}_{d,k_3,k_4}^{3,3}(t_s) \big|_{k_3=0,\dots,9, k_4=0,\dots,9} \end{aligned} \quad (32)$$

with  $K_{J_3} = 2^3 + 2 = 10$  and  $K_{J_4} = 2^3 + 2 = 10$  as the total number of B-spline coefficients. As for the global model part a test of significance was carried out for the estimated coefficients. From the 100 B-spline coefficients around 60 to 70 are significant during night time and 70 to 75 at local noon, with a  $\alpha$ -value of 0.01. During the storm time on March 17, the number of significant coefficients increases to 80, because of the stronger signal variations during that time.

For the example in Figure 8, we applied the Equations (27) and (28) to calculate  $\Delta VTEC$  and their corresponding standard deviations on a grid as Product type 2b introduced in Section 2.3. We chose the output sampling intervals  $\Delta\Phi = 1^\circ$  in latitude and  $\Delta\Lambda = 1^\circ$  in longitude. For the representation of the map in the upper panels of Figure 8 we use the bi-linear interpolation [9].

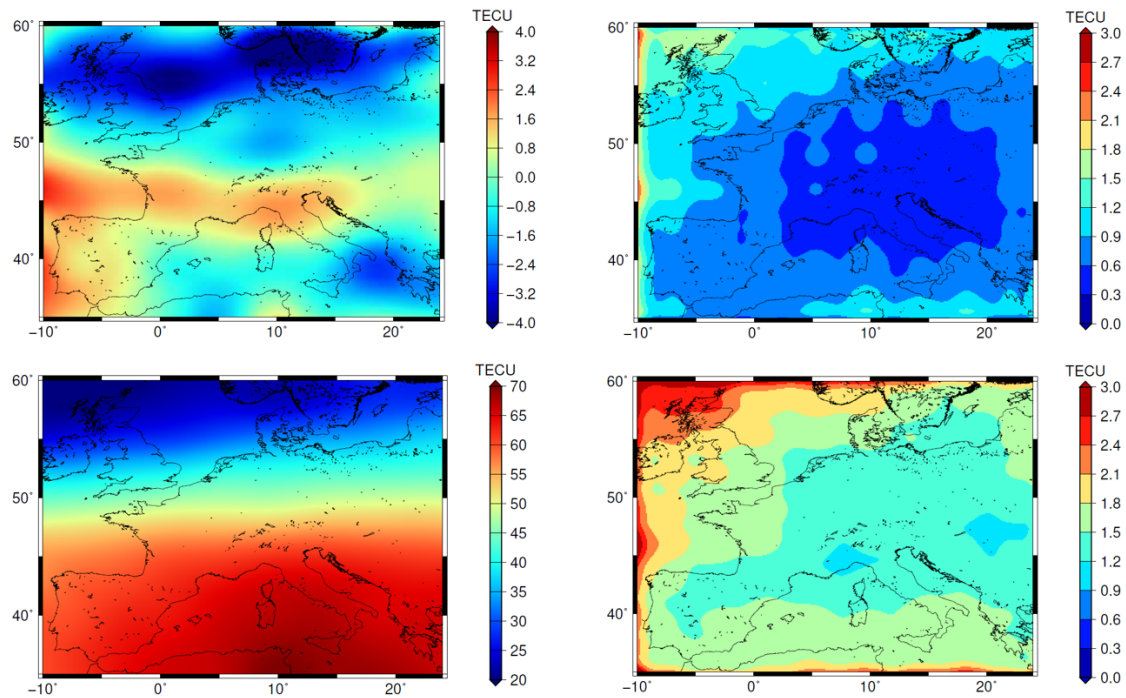


**Figure 8.** Estimated  $\Delta VTEC_{reg}$  values and their standard deviations (**upper panels**) for the selected B-spline levels  $J_3 = 3$  and  $J_4 = 3$ ; estimated  $VTEC_{reg}$  values (**bottom left**) and the corresponding standard deviation map (**bottom right**); all sets calculated for 17 March 2015 at 12:00 UT.

For the calculation of the total VTEC values and the corresponding standard deviations within the region  $\Delta\Omega$  we finally apply the Equations (29) and (30) using the estimated values – defined as Product type 2a –  $\widehat{VTEC}_{glob}(\varphi, \lambda, t)$  and  $\widehat{\sigma}_{VTEC_{glob}}(\varphi, \lambda, t)$  at the same grid points with sampling intervals  $\Delta\Phi = 1^\circ$  and  $\Delta\Lambda = 1^\circ$ . The lower panels represent finally the maps of Product type 2c



with  $\widehat{VTEC}_{reg}(\varphi, \lambda, t)$  as the total VTEC values (left) and  $\widehat{\sigma}_{VTEC_{reg}}(\varphi, \lambda, t)$ , the corresponding standard deviations (right) within the European region for 17 March 2015 at 12:00 UT.

Due to the absolute magnitude of the global signal values with up to 120 TECU, the detailed structures of the regional model with magnitudes of  $\pm 4$  TECU cannot be visualized appropriately in the bottom left panel of Figure 8. The standard deviation map on the bottom right panel shows larger values at the region boundaries and thus, reflects rather nicely the distribution of the observations, cf. Figures 4 and 7.

#### 4. Validation

In order to assess the VTEC TSM Products 2a and 2c as defined at the end of Section 2, we use the so-called dSTEC analysis. It is based on real GNSS observations for the comparison with the estimated VTEC maps and features an accuracy of less than 0.1 TECU, [8]. The differences

$$dSTEC_{obs}(t_s) = STEC(\mathbf{x}_s^S, \mathbf{x}_{s,R}, t_s) - STEC(\mathbf{x}_{ref}^S, \mathbf{x}_{ref,R}, t_{ref}) \quad (33)$$

between the observations  $STEC(\mathbf{x}_s^S, \mathbf{x}_{s,R}, t_s)$  according to Equation (2) at time moments  $t_s$  and the observation  $STEC(\mathbf{x}_{ref}^S, \mathbf{x}_{ref,R}, t_{ref})$  at the reference time moment  $t_{ref}$  along the same arc is compared with the differences

$$dSTEC_{map}(t_s) = M(z_s) \cdot VTEC(\mathbf{x}_{s,IPP}, t_s) - M(z_{ref}) \cdot VTEC(\mathbf{x}_{ref,IPP}, t_{ref}), \quad (34)$$

according to Equation (4). The reference time moment  $t = t_{ref}$  is usually referred to the observation with the smallest zenith angle  $z = z_{ref}$ , see Figure 9. The quality assessment is finally performed by evaluating the differences

$$dSTEC(t_s) = dSTEC_{obs}(t_s) - dSTEC_{map}(t_s) \quad (35)$$

with expectation value  $E(dSTEC(t_s)) = 0$ , for different products, e.g., the TSM-Products 2a and 2c, or the final GIMs of IGS [32], or its IAACs as it was done by Roma-Dollase et al. [7].

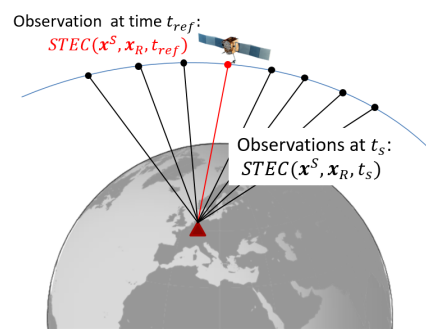


**Figure 9.** Schematic representation of the dSTEC analysis of one satellite-receiver pair.

Within the dSTEC analysis the difference (35) has to be calculated for a set of a number of selected receiver stations. For the choice of the receiver stations three strategies exist:

1. The observations of the selected receiver stations are used for the computation of all maps used in the analysis
2. No station of the selected receivers stations contributed to any of the different products, thus, the stations are independent from all products
3. A mixture of stations satisfying the items 1. and 2.

Since we define non-overlapping station lists providing observations to  $\mathcal{D}_1$  and  $\mathcal{D}_2$ , we follow the third strategy. Figure 10 shows the stations used in our dSTEC analysis. Note, we selected also stations that are located close to the boundaries of the region, to use their observations with IPPs located within the region.

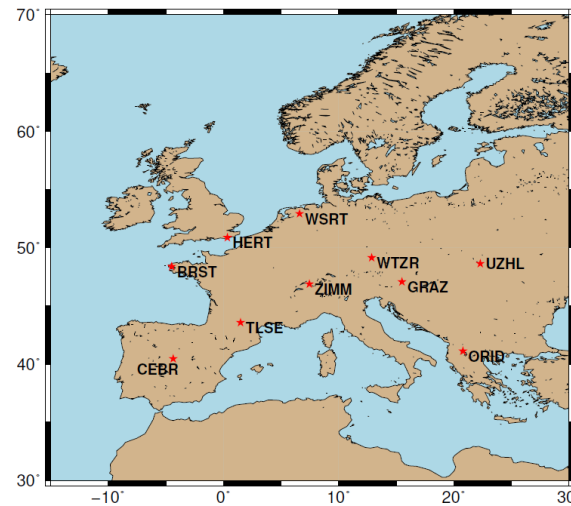


**Figure 10.** Distribution of 10 receiver stations within the densification area used for the dSTEC analysis.

For the assessment of the product quality we use the following TSM-Products (cf. Goss et al. [9]):

**TSM-Product 2a:**

- **otlg\_a:**  
the estimated  $\widehat{VTEC}_{glob}^{4,3}(\varphi, \lambda, t)$  with a grid resolution of  $\Delta\Phi = 2.5^\circ$ ,  $\Delta\Lambda = 5^\circ$  and  $\Delta T = 10$  minutes temporal sampling interval
- **otlg\_b:**  
the estimated  $\widehat{VTEC}_{glob}^{4,3}(\varphi, \lambda, t)$  with a grid resolution of  $\Delta\Phi = 1^\circ$ ,  $\Delta\Lambda = 1^\circ$  and  $\Delta T = 10$  minutes temporal sampling interval

**TSM-Product 2c:**

- **othr:**  
the estimated  $\widehat{VTEC}_{reg}^{3,3}(\varphi, \lambda, t)$  with a grid resolution of  $\Delta\Phi = 1^\circ$ ,  $\Delta\Lambda = 1^\circ$  and  $\Delta T = 10$  minutes temporal sampling interval.

We denote the global models as ‘otlg’ similar to Goss et al. [9]. The first letter ‘o’ refers to the OPTIMAP processing software, which was developed within a third-party project (see Acknowledgements) and means the basis of the presented study. The second letter indicates the chosen temporal output sampling interval with ‘t’ for  $\Delta T = 10$  minutes. The third letter denotes the spectral content of the output signal; it is chosen as ‘h’ for high and ‘l’ for low. The last letter indicates the model domain with ‘g’ for global and ‘r’ for regional. In the case of the global model we indicate two different grid resolutions with their endings ‘a’ and ‘b’, cf. Table 3.

For the validation of our TSM-Products we use other products listed in Table 3. They are characterized by different extents, latencies and output samplings  $\Delta\Phi$ ,  $\Delta\Lambda$  and  $\Delta T$ . We compare the global products ‘otlg\_a’, ‘otlg\_b’, ‘codg’ and ‘uqrg’, where ‘otlg\_a’ and ‘otlg\_b’ are based on ultra-rapid orbits and hourly GNSS observations with a latency of less than 3 hours [9]. The CODE product ‘codg’ is a final product and thus, based on post-processed data. UPC’s product, denoted as ‘uqrg’, is a rapid product and based on rapid GNSS data with a latency of approximately one day. Our regional product

‘othr’ is an ultra-rapid product, too. The only comparable external product for Europe is a final one provided by the Royal Observatory of Belgium (ROB) with a latency of approximately one week.

**Table 3.** Products used for validation; names, types and latencies are taken from the references listed in the last column.

Institution	Product	Extension	Latency	$\Delta\Phi$	$\Delta\Lambda$	$\Delta T$	Reference
DGFI-TUM	otlg_a	global	< 3 hours	2.5°	5°	10 min	[9]
DGFI-TUM	otlg_b	global	< 3 hours	1°	1°	10 min	[9]
DGFI-TUM	othr	regional	< 3 hours	1°	1°	10 min	this paper
ROB	rob主	regional	> 1 week	0.5°	0.5°	15 min	[13,33]
CODE	codg	global	> 1 week	2.5°	5°	1 h	[34]
UPC	uqrg	global	> 1 day	2.5°	5°	15 min	[7]

Figure 11 shows the RMS values of the differences (35) during the time span between 8 March and 23 March 2015 for each product at the 10 receiver stations shown in Figure 10.

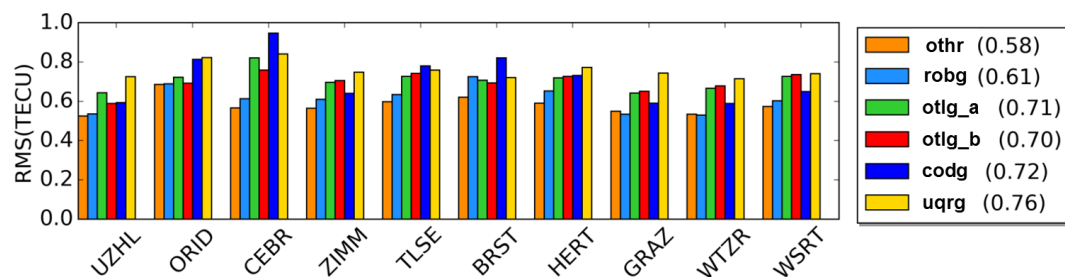


**Figure 11.** RMS values computed at the 10 stations shown in Figure 10 for the products listed in the legend; the two global products ‘otlg\_a’ and ‘otlg\_b’ as well as the regional product ‘othr’, the external regional product ‘rob主’ and the external global products ‘codg’ and ‘uqrg’ of the IAACs CODE and UPC are used for comparison. The values in the parantheses are the average RMS values over all 10 receiver stations for the entire test period between 8 March and 23 March 2015.

The RMS values at the different stations vary approximately between 0.5 TECU and 0.9 TECU. Note, during the geomagnetic storm on March 17, the RMS values for all products at all stations increase and can reach values of up to 4 TECU for a short time, but are averaged in Figure 11. In order to rate the RMS values at different station and for the TSM products appropriately, we need to distinguish the stations used in the assessment, which are assigned either to  $\mathcal{D}_1$  or to  $\mathcal{D}_2$ . Hence, the stations ‘BRST’, ‘HERT’, ‘GRAZ’, ‘WTZR’ and ‘WRST’ are stations which are used in the modelling procedure of the global VTEC maps, whereas ‘UZHL’, ‘ORID’, ‘CEBR’, ‘ZIMM’ and ‘TLSE’ are used for the regional model part. At a first step we compare the two global products of DGFI-TUM, ‘otlg\_a’ and ‘otlg\_b’ given with different spatial output sampling intervals  $\Delta\Phi$  and  $\Delta\Lambda$ . Consequently, different RMS values are obtained for both products at all stations. For the values  $VTEC(x_{s,IPP}, t_s)$  and  $VTEC(x_{ref,IPP}, t_{ref})$  in Equation (34) a bi-linear interpolation has to be applied between the given grid points. The quality of the interpolated VTEC decreases with an increasing spatial resolution and thus, we achieve a slightly smaller overall RMS value for the product ‘otlg\_b’. Comparing the bars for ‘otlg\_a’ and ‘otlg\_b’, we find larger differences in the RMS at the stations ‘UZHL’, ‘ORID’ and ‘CEBR’, which are independent stations for both models. The RMS values at all other stations are approximately equal.

In the next step, we compare the global product ‘otlg\_b’ and the regional product ‘othr’. Both are given with the same spatial and temporal sampling intervals. From the orange colored and the red colored bars for ‘othr’ and ‘otlg\_b’, respectively, we can conclude, that the regional model is of higher accuracy at all stations. This means, that we can achieve a significant improvement in the modelling accuracy within the region by applying the second step of the TSM. By comparing the overall RMS of

‘othr’ and ‘otlg\_b’, given in the parenthesis, we even find an increase in the accuracy of around 18.3% for ‘othr’.

In order to rate the TSM-Products 2a against products of the IAACs, we compare the overall RMS values, of ‘otlg\_a’ with 0.71 TECU, ‘otlg\_b’ with 0.70, ‘codg’ with 0.72 TECU and ‘uqrg’ with 0.76 TECU. Consequently, we find comparable results for the TSM products and ‘codg’ at all stations. However, when comparing the green and red color bars with the dark blue color bar for ‘codg’, for example at the stations ‘CEBR’ and ‘WTZR’, the differences are larger, so that local quality differences can be inferred. The product ‘uqrg’ performs slightly worse within the European region and for the selected time span, compared to the other global products.

Finally, we compare the regional TSM-Product 2b and the product ‘robg’. They are given with different spatial and temporal sampling, cf. Table 3, but the extension of the region covers with  $\varphi \in [35^\circ, 60^\circ]$  and  $\lambda \in [-10^\circ, 25^\circ]$  for ‘othr’ and with  $\varphi \in [35^\circ, 62^\circ]$  and  $\lambda \in [-15^\circ, 25^\circ]$  for ‘robr’ approximately the same area. However, ‘robg’ is a final product, whereas ‘othr’ is an ultra-rapid product. The product ‘othr’ shows a slightly higher accuracy than ‘robg’ of about 0.3 TECU in the overall RMS values. Nevertheless, both products are approximately of the same accuracy.

## 5. Summary and Conclusions

The presented approach aims at modelling VTEC with high spectral, spatial and temporal resolution for regions of dense data coverage. Compared to the GIMs provided by the IAACs, which are typically of lower spectral resolution, regional maps can represent finer structures. The global maps are usually provided with spatial output sampling intervals of  $\Delta\Phi = 2.5^\circ$  and  $\Delta\Lambda = 5^\circ$  and a temporal sampling interval of  $\Delta T = 2\text{h}$ . Regional maps, on the other hand, are usually provided with a finer grid resolution and a temporal sampling of  $\Delta T \leq 1\text{ hour}$ .

By means of the developed TSM, we generate both, a global model representing the coarser structures and a regional model representing the finer structures of VTEC. Both model parts are adapted optimally to the distribution of the independently defined data sets. The global data set consists of observations collected from selected receiver stations of the IGS network. To be more specific, the selection of these stations has to be adapted to the global situation. This means, that the observation sampling of the global data set has to fulfill the inequalities (10). Depending on the coverage the remaining receiver stations may provide dense clusters of observations within specific regions, cf. Figure 6. We performed numerical tests for Europe for March 2015, including the St-Patrick storm day, the strongest space weather event within the last decade. With the global resolution levels  $J_1 = 4$  and  $J_2 = 3$  we generate as the first step of the TSM the global VTEC model, comparable to the GIMs provided by the IAACs. In the second step, the regional VTEC model with resolution levels  $J_3 = 3$  and  $J_4 = 3$  is created. We apply the developed TSM to a densification area in Europe with cutoff frequencies of  $n = 64$  in latitude direction and  $n = 47$  in a longitude direction. Finally, the applied dSTEC validation shows that our generated regional ultra-rapid model with a latency of less than three hours is of higher accuracy than the global models and comparable to the regional final product of ROB.

Within this paper, we showed, that a higher spectral resolution and a higher accuracy can be achieved using appropriate regional modelling approaches. These high-resolution products can be used to study small scale and fast-changing variations of the ionosphere, e.g., traveling ionospheric disturbances (TID) [35,36], as well as plasma irregularities, such as plasma bubbles. For the use of the regional model in modern GNSS applications, such as autonomous driving or precision agriculture, the developed approach can be seen as an intermediate step towards the following developments:

- Since autonomous driving or precise navigation requires real-time information about the state of the ionosphere, the TSM approach must be adapted accordingly. For this purpose, the latency (see Table 3) of the TSM products must be reduced significantly. There are two ways, namely (1) transferring the products to real-time using a suitable forecast algorithm or (2)—which is more

preferably—directly applying real-time GNSS observations.

- There is also the question of how ionosphere information should be disseminated to the user in real-time. In general, the dissemination can be undertaken in two different ways: based on estimated series coefficients (Products type 1) or on estimated grid values (Product type 2). In the latter case, an interpolation of the grid values has to be performed to obtain VTEC information at any arbitrary point within the area on the investigation. In case of dissemination of estimated series coefficients, the Radio Technical Commission for Maritime Services (RTCM) message has to be mentioned, which allows us to transfer of the SHs coefficients up to degree 16 to the user. It is in the current form restricted to the sole use of SHs and thus, not suitable for the high-resolution products developed within this paper. Consequently, the dissemination of the products needs to be discussed urgently in order to provide highly precise information to the users.

In a further step, a validation method for ionospheric maps will be developed that is more suitable for navigation applications. A more sophisticated method will allow the determination of positioning accuracy using ionospheric corrections from different products.

**Author Contributions:** The concept of the paper was proposed by A.G. and discussed with M.S. and E.E. A.G. compiled the figures and wrote the text with assistance from M.S. M.S. and F.S. assume responsibility for the projects INSIGHT II and OPTIMAP for which significant contributions entered into this article. The paper and figures were reviewed from all authors. All authors have read and agreed to the published version of the manuscript.

**Funding:** This research was funded by the German Research Foundation (DFG) under grant number SCHM2433/10-2 (project INSIGHT II) and the Technical University of Munich (TUM) in the framework of the Open Access Publishing Program. The approach presented in this paper was to a large part developed in the framework of the project OPTIMAP ('Operational Tool for Ionospheric Mapping and Prediction') funded by the Bundeswehr GeoInformation Center (BGIC) and the German Space Situational Awareness Centre (GSSAC).

**Acknowledgments:** The authors thank the IGS and its IAACs, in particular the Center for Orbit Determination in Europe (CODE, Berne, Switzerland) and the Universitat Politècnica de Catalunya/IonSAT (UPC, Barcelona, Spain), for providing the data. Furthermore, the authors thank Nicolas Bergeot and the Royal Observatory of Belgium (ROB, Brussels, Belgium) for providing the regional VTEC maps for comparison. We acknowledge the Generic Mapping Tool (GMT), which was primarily used for generating the figures in this work.

**Conflicts of Interest:** The authors declare no conflict of interest

## References

1. Langley, R.B. Propagation of the GPS Signals. In *GPS for Geodesy*; Teunissen, P.J.G., Kleusberg, A., Eds.; Springer: Berlin/Heidelberg, Germany, 1998; pp. 111–149. [\[CrossRef\]](#)
2. Schaer, S. Mapping and Predicting the Earth's Ionosphere Using the Global Positioning System. Ph.D. Thesis, University of Bern, Bern, Switzerland, 1999.
3. Lyu, H.; Hernández-Pajares, M.; Nohutcu, M.; García-Rigo, A.; Zhang, H.; Liu, J. The Barcelona ionospheric mapping function (BIMF) and its application to northern mid-latitudes. *GPS Solut.* **2018**, *22*, 724–746. [\[CrossRef\]](#)
4. Hernández-Pajares, M.; Juan, J.M.; Sanz, J.; Argón-Àngel, A.; Garcia-Rigo, A.; Salazar, D.; Escudero, M. The ionosphere: Effects, GPS modeling and benefits for space geodetic techniques. *J. Geod.* **2011**, *85*, 887–907. [\[CrossRef\]](#)
5. Hernández-Pajares, M.; Juan, J.M.; Sanz, J.; Orus, R.; Garcia-Rigo, A.; Feltens, J.; Komjathy, A.; Schaer, S.C.; Krankowski, A. The IGS VTEC map: A reliable source of ionospheric information since 1998. *J. Geod.* **2009**, *83*, 263–275. [\[CrossRef\]](#)
6. Schmidt, M.; Dettmering, D.; Mößner, M.; Wang, Y. Comparison of spherical harmonic and B-spline models for the vertical total electron content. *Radio Sci.* **2011**, *46*, RS0D11. [\[CrossRef\]](#)
7. Roma-Dollase, D.; Hernandez-Pajares, M.; Krankowski, A.; Kotulak, K.; Ghoddousi-Fard, R.; Yuan, Y.; Li, Z.; Zhang, H.; Shi, C.; Wang, C. Consistency of seven different GNSS global ionospheric mapping techniques during one solar cycle. *J. Geod.* **2018**, *92*, 691–706. [\[CrossRef\]](#)



8. Hernández-Pajares, M.; Roma-Dollase, D.; Krankowski, A.; García-Rigo, A.; Orús-Pérez, R. Methodology and consistency of slant and vertical assessments for ionospheric electron content models. *J. Geod.* **2017**, *91*, 1405–1414. [\[CrossRef\]](#)
9. Goss, A.; Schmidt, M.; Erdogan, E.; Görres, B.; Seitz, F. High-resolution vertical total electron content maps based on multi-scale B-spline representations. *Ann. Geophys.* **2019**, *37*, 699–717. [\[CrossRef\]](#)
10. Schmidt, M. Wavelet modelling in support of IRI. *Adv. Space Res.* **2007**, *39*, 932–940. [\[CrossRef\]](#)
11. Schmidt, M. Towards a multi-scale representation of multi-dimensional signals. In *VII Hotine-Marussi Symposium on Mathematical Geodesy*; Springer: Berlin/Heidelberg, Germany, 2012; Volume 137, pp. 119–127. [\[CrossRef\]](#)
12. Dettmering, D.; Schmidt, M.; Heinkelmann, R.; Seitz, M. Combination of different space-geodetic observations for regional ionosphere modeling. *J. Geod.* **2011**, *85*, 989–998. [\[CrossRef\]](#)
13. Bergeot, N.; Chevalier, J.M.; Bruyninx, C.; Pottiaux, E.; Aerts, W.; Baire, Q.; Legrand, J.; Defraigne, P.; Huang, W. Near real-time ionospheric monitoring over Europe at the Royal Observatory of Belgium using GNSS data. *J. Space Weather Space Clim.* **2014**, *4*, A31. [\[CrossRef\]](#)
14. Nohutcu, M.; Karslioglu, M.O.; Schmidt, M. B-spline modeling of VTEC over Turkey using GPS observations. *J. Atmos. Sol. Terr. Phys.* **2010**, *72*, 617–624. [\[CrossRef\]](#)
15. Liang, W. A Regional Physics-motivated Electron Density Model of the Ionosphere. Ph.D. Thesis, Technical University of Munich, Munich, Germany, 2017. Available online: <http://mediatum.ub.tum.de/?id=1335966> (accessed on 24 March 2020).
16. Limberger, M. Ionosphere Modeling from GPS Radio Occultations and Complementary Data Based on B-splines. Ph.D. Thesis, Technical University of Munich, Munich, Germany, 2015.
17. Krypiak-Gregorczyk, A.; Wielgosz, P.; Borkowski, A. Ionosphere Model for European Region Based on Multi-GNSS Data and TPS Interpolation. *Remote Sens.* **2017**, *9*, 1221. [\[CrossRef\]](#)
18. Schaer, S.; Gurtner, W.; Feltens, J. IONEX: The IONosphere Map EXchange Format Version 1. In Proceedings of the IGS AC Workshop, Darmstadt, Germany, 9–11 February 1998.
19. Li, M.; Yuan, Y.; Wang, N.; Li, Z.; Zhang, X. Statistical comparison of various interpolation algorithms for reconstruction regional grid ionospheric maps over Cina. *J. Atmos. Sol. Terr. Phys.* **2018**, *89*, 331–345.
20. Lyche, T.; Schumaker, L. A multiresolution tensor spline method for fitting functions on the sphere. *SIAM J. Sci. Comput.* **2001**, *22*, 724–746. [\[CrossRef\]](#)
21. Stollnitz, E.; DeRose, T.; Salesin, D. Wavelets for computer graphics: A primer, part I. *IEEE Comput. Graph. Appl.* **1995**, *3*, 76–84. [\[CrossRef\]](#)
22. Stollnitz, E.; DeRose, T.; Salesin, D. Wavelets for computer graphics: A primer. Part I and Part II. *IEEE Comput. Graph. Appl.* **1995**, *15*, 75–85. [\[CrossRef\]](#)
23. Schmidt, M.; Dettmering, D.; Seitz, F. *Using B-Spline Expansions for Ionosphere Modeling*; Springer: Berlin, Germany, 2015; Volume 89, pp. 939–983. [\[CrossRef\]](#)
24. Lee, J.; Kim, M. Optimized GNSS Station Selection to Support Long-Term Monitoring of Ionospheric Anomalies for Aircraft Landing Systems. *IEEE* **2017**, *53*, 236–246. [\[CrossRef\]](#)
25. Gelb, A. *Applied Optimal Estimation*; The MIT Press: Cambridge, MA, USA, 1974.
26. Grewal, M.S.; Andrews, A.P. *Kalman Filtering: Theory and Practice Using MATLAB*, 2nd ed.; John Wiley & Sons, Inc.: Hoboken, NJ, USA, 2008; p. 416.
27. Simon, D. A game theory approach to constrained minimax state estimation. *IEEE Trans. Signal Process.* **2006**, *54*, 405–412. [\[CrossRef\]](#)
28. Erdogan, E.; Schmidt, M.; Seitz, F.; Durmaz, M. Near real-time estimation of ionosphere vertical total electron content from GNSS satellites using B-spline in a Kalman Filter. *Ann. Geophys.* **2017**, *35*, 263–277. [\[CrossRef\]](#)
29. Laundal, K.M.; Richmond, A. Magnetic Coordinate Systems. *Space Sci. Rev.* **2016**, *206*, 27–59. [\[CrossRef\]](#)
30. Komjathy, A.; Langley, R. An assessment of predicted and measured ionospheric total electron content using a regional GPS network. In *Proceedings of the 1996 National Technical Meeting of The Institute of Navigation*; Institute of Navigation: Alexandria, VA, USA, 1996; pp. 615–624.
31. Erdogan, E.; Schmidt, M.; Goss, A.; Görres, B.; Seitz, F. Adaptive Modeling of the Global Ionosphere Vertical Total Electron Content. *Geodyn. Model Dev.* **2020**. (close to submission).
32. Hernández-Pajares, M.; Juan, J.M.; Sanz, J. New approaches in global ionospheric determination using ground GPS data. *J. Atmos. Sol. Terr. Phys.* **1999**, *61*, 1237–1247. [\[CrossRef\]](#)

33. Bergeot, N.; Bruyninx, C.; Defraigne, P.; Pireaux, S.; Legrand, J.; Pottiaux, E.; Baire, Q. Impact of the Halloween 2003 ionospheric storm on kinematic GPS positioning in Europe. *GPS Solut.* **2011**, *15*, 171–180. [[CrossRef](#)]
34. Orus, R.; Cander, L.; Hernández-Pajares, M. Testing regional vertical total electron content maps over Europe during 17–21 January 2005 sudden space weather event. *Radio Sci.* **2007**, *42*, RS3004. [[CrossRef](#)]
35. Yang, H.; Monte-Moreno, E.; Hernández-Pajares, M. Multi-TID detection and characterization in a dense Global Navigation Satellite System receiver network. *J. Geophys. Res-Space* **2017**, *122*, 9554–9575. [[CrossRef](#)]
36. Hernández-Pajares, M.; Wielgosz, P.; Paziewski, J.; Krypiak-Gregorczyk, A.; Krukowska, M.; Stepniak, K.; Kaplon, J.; Hadas, T.; Sosnica, K.; Bosy, J.; et al. Direct MSTID mitigation in precise GPS processing. *Radio Sci.* **2017**, *52*. [[CrossRef](#)]



© 2020 by the authors. Licensee MDPI, Basel, Switzerland. This article is an open access article distributed under the terms and conditions of the Creative Commons Attribution (CC BY) license (<http://creativecommons.org/licenses/by/4.0/>).



## 7.3 P-III

### Reference

Andreas Goss, Manuel Hernández-Pajares, Michael Schmidt, David Roma-Dollase, Eren Erdogan, Florian Seitz (2020): **High-Resolution Ionosphere Corrections for Single-Frequency Positioning** In: Remote Sensing, 13(1), 12, 10.3390/rs13010012

### Copyright

This publication has originally been published in the open access journal ‘Remote Sensing’ and is available under the license of Creative Commons at <https://www.mdpi.com/journal/remotesensing>. The copyrights remain with the authors.

### Summary Publication

Ionospheric signal delay is one of the largest error sources in GNSS applications and can cause positioning errors in the order of several meters. External information about the state of the ionosphere is essential, especially for single-frequency users, who cannot correct for ionospheric signal delay. The International GNSS Service (IGS) and its Ionosphere Associated Analysis Centers (IAAC) routinely provide this information in terms of global ionosphere maps (GIM) representing the Vertical Total Electron Content (VTEC). However, these maps are mostly generated by series expansion in terms of spherical harmonics (SH) with a maximum degree of  $n = 15$  on the basis of post-processed observations. These so-called final GIMs are typically provided with a latency of several days up to weeks using the IONosphere EXchange (IONEX). For modern GNSS applications, the accuracy is too low and the latency too high.

Some of the IAACs generate the so-called RT-GIMs which represent the state of the ionosphere in real time. If they are generated by SHs they can be made available to users in real time via SSR VTEC message. However, the message only allows a maximum degree of  $n = 16$ . Beside the SHs, several alternative approaches, e.g. B-splines or Voxels, have proven to be appropriate basis functions for modelling the ionosphere with an enhanced resolution. Providing them using the SSR VTEC message requires a transformation to SHs.

This paper describes a method to transform B-spline based GIMs into SHs to meet the requirements of the SSR VTEC message. To maintain the quality of the high-resolution GIMs, a SH expansion with higher degrees  $n > 15$  must be used. Therefore, several cases are considered and compared in the numerical investigations. Compared to established final GIMs based on SHs of  $n = 15$ , the transformed GIMs of  $n > 15$  show a better performance for single-frequency positioning. Thus, it can be concluded that it is of high importance to change the dissemination strategies for ionosphere corrections to be applied to modern GNSS applications.

## Declaration of Contribution

This paper has been published in the Journal 'Remote Sensing' and the content is based on the work carried out as part of the development process of the project OPTIMAP as well as in the context of the INSIGHT project. The latter was funded by the German Research Foundation (DFG) under the umbrella of the Special Priority Programme (SPP) 1788 Dynamic Earth with the grant number SCHM2433/10-2.. OPTIMAP is a joint initiative of the Deutsches Geodätisches Forschungsinstitut der Technischen Universität München, Bundeswehr GeoInformation Centre (BGIC) and the German Space Situational Awareness Centre (GSSAC). The concept of the paper was proposed by A. Goss and discussed with the co-authors. A. Goss developed the software, performed the numerical investigations and compiled the figures. The interpretation of the results was carried out during a scientific visit to UPC as part of the internationalisation programme of the TUM Graduate School and in collaboration with H. Hernández-Pajares. The manuscript writing has been done by A. Goss and reviewed by all co-authors.

**The overall own contribution of A. Goss for P-III is estimated at 90%**

We hereby confirm the correctness of the declaration of contribution and the reuse of the contents of the publication:

Andreas Goss, Manuel Hernández-Pajares, Michael Schmidt, David Roma-Dollase, Eren Erdogan, Florian Seitz (2020): High-Resolution Ionosphere Corrections for Single-Frequency Positioning. In: Remote Sensing, 13(1), 12, 10.3390/rs13010012

Prof. Dr. Hernández-Pajares  
Technical University of Catalonia (UPC)  
Barcelona, Spain

Signature:

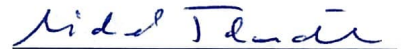


Date:

15-APRIL-2021

apl. Prof. Dr. Michael Schmidt  
Deutsches Geodätisches Forschungsinstitut  
Technische Universität München, Germany

Signature:



Date:

16. 4. 2021

Dr. David Roma-Dollase  
Institut de Ciències de l'Espai (IEEC-CSIC)  
Barcelona, Spain

Signature:



ROMA DOLLASE DAVID  
- 77915918Z  
2021.04.15 15:54:01  
+02'00'

Date:

Eren Erdogan  
Deutsches Geodätisches Forschungsinstitut  
Technische Universität München, Germany

Signature:



Date:

16.04.2021

Prof. Dr. Florian Seitz  
Deutsches Geodätisches Forschungsinstitut  
Technische Universität München, Germany

Signature:



Digital unterschrieben von Florian Seitz  
DN: cn=Florian Seitz, o=TUM, ou=DGFI-TUM, email=florian.seitz@tum.de, c=DE  
Datum: 2021.04.12 09:18:19 +02'00'

Date:

München, 12.4.2021

## Article

# High-Resolution Ionosphere Corrections for Single-Frequency Positioning

Andreas Goss <sup>1,\*</sup> , Manuel Hernández-Pajares <sup>2</sup> , Michael Schmidt <sup>1</sup>, David Roma-Dollase <sup>2,3</sup> , Eren Erdogan <sup>1</sup>  and Florian Seitz <sup>1</sup> 

- <sup>1</sup> Deutsches Geodätisches Forschungsinstitut der Technischen Universität München, Arcisstraße 21, 80333 Munich, Germany; mg.schmidt@tum.de (M.S.); eren.erdogan@tum.de (E.E.); florian.seitz@tum.de (F.S.)  
<sup>2</sup> UPC-IonSAT, Technical University of Catalonia (UPC), IEEC-UPC, 31. 08034 Barcelona, Catalonia, Spain; manuel.hernandez@upc.edu (M.H.-P.); roma@ieec.cat (D.R.-D.)  
<sup>3</sup> Institut de Ciències de l'Espai (IEEC-CSIC), Campus UAB, Carrer de Can Magrans s/n, 08193 Cerdanyola del Vallès, Spain  
 \* Correspondence: andreas.goss@tum.de

**Abstract:** The ionosphere is one of the main error sources in positioning and navigation; thus, information about the ionosphere is mandatory for precise modern Global Navigation Satellite System (GNSS) applications. The International GNSS Service (IGS) and its Ionosphere Associated Analysis Centers (IAAC) routinely provide ionospheric information in terms of global ionosphere maps (final GIM). Typically, these products are modeled using series expansion in terms of spherical harmonics (SHs) with a maximum degree of  $n = 15$  and are based on post processed observations from Global Navigation Satellite Systems (GNSS), as well as final satellite orbits. However, precise applications such as autonomous driving or precision agriculture require real-time (RT) information about the ionospheric electron content with high spectral and spatial resolution. Ionospheric RT-GIMs are disseminated via Ntrip protocol using the SSR VTEC message of the RTCM. This message can be streamed in RT, but it is limited for the dissemination of coefficients of SHs of lower degrees only. It allows the dissemination of SH coefficients up to a degree of  $n = 16$ . This suits to most the SH models of the IAACs, but higher spectral degrees or models in terms of B-spline basis functions, voxels, splines and many more cannot be considered. In addition to the SHs, several alternative approaches, e.g., B-splines or Voxels, have proven to be appropriate basis functions for modeling the ionosphere with an enhanced resolution. Providing them using the SSR VTEC message requires a transfer to SHs. In this context, the following questions are discussed based on data of a B-spline model with high spectral resolution; (1) How can the B-spline model be transformed to SHs in order to fit to the RTCM requirements and (2) what is the loss of detail when the B-spline model is converted to SHs of degree of  $n = 16$ ? Furthermore, we discuss (3) what is the maximum necessary SH degree  $n$  to convert the given B-spline model and (4) how can the transformation be performed to make it applicable for real-time applications? For a final assessment, we perform both, the dSTEC analysis and a single-frequency positioning in kinematic mode, using the transformed GIMs for correcting the ionospheric delay. The assessment shows that the converted GIMs with degrees  $n \geq 30$  coincide with the original B-spline model and improve the positioning accuracy significantly.

**Keywords:** ionosphere; GIM-products; vertical total electron content; global navigation satellite systems; B-splines; spherical harmonics



**Citation:** Goss, A.; Hernández-Pajares, M.; Schmidt, M.; Roma-Dollase, D. High-Resolution Ionosphere Corrections for Single-Frequency Positioning. *Remote Sens.* **2020**, *13*, 12. <https://dx.doi.org/10.3390/rs13010012>

Received: 16 November 2020

Accepted: 16 December 2020

Published: 22 December 2020

**Publisher's Note:** MDPI stays neutral with regard to jurisdictional claims in published maps and institutional affiliations.



**Copyright:** © 2020 by the authors. Licensee MDPI, Basel, Switzerland. This article is an open access article distributed under the terms and conditions of the Creative Commons Attribution (CC BY) license (<https://creativecommons.org/licenses/by/4.0/>).

## 1. Introduction

The delay on electromagnetic signals traveling through the atmosphere is mostly caused by free electrons which are available within the ionosphere between approximately 50 km to 1000 km. In fact, the so called ionospheric delay  $d_{ion}$ , which can be approximated better than 99.9%, affects the propagation of GNSS signals between a satellite  $S$  and a receiver  $R$ , and is one of the largest error sources in positioning and navigation [1]. It can

cause errors of several tens of meters in single frequency positioning for a frequency of  $f = 1575.42$  MHz ( $L_1$  GPS carrier frequency) [2–4]. The magnitude of the signal delay depends on the frequency  $f$  and on the number of free electrons  $N_e$ , which disturb the propagation of the signal. Using the ionospheric linear-combination (LC) [5], the user of a dual-frequency receiver can determine the so-called Slant Total Electron Content (STEC)

$$STEC(x^S, x_R, t) = \int_R^S N_e(x, t) ds, \quad (1)$$

as the integral of the total number of electrons acting on the signal at points  $P(x)$  along the ray-path, with position vector  $x = r [\cos \varphi \cos \lambda, \cos \varphi \sin \lambda, \sin \varphi]^T$ . Note that the coordinate triple  $(\varphi, \lambda, r)$  comprises the latitude  $\varphi$ , the longitude  $\lambda$  and the radial distance  $r$  within a geocentric coordinate system  $\Sigma_E$ . Single-frequency receivers, however, require external information about the state of the ionosphere to increase the accuracy in positioning. The International GNSS Service (IGS) routinely provides ionospheric delay corrections in terms of global ionosphere maps (GIM) representing the Vertical Total Electron Content (VTEC)

$$VTEC(\varphi, \lambda, t) = \int_{h_1}^{h_2} N_e(\varphi, \lambda, h, t) dh, \quad (2)$$

as the integrated electron density along the height  $h$  between the altitude boundaries  $h_1$  and  $h_2$  of the ionosphere. The GIMs are typically based only on GNSS observations and on the assumption of the Single Layer Model (SLM), which allows the transformation

$$VTEC(x_{IPP}, t) = \frac{STEC(x^S, x_R, t)}{M(z)}, \quad (3)$$

assuming a mapping function  $M(z)$ , which solely depends on the zenith angle  $z$  [6,7]. In the SLM, it is assumed that all electrons in the ionosphere are concentrated in an infinitesimal thin spherical layer of radius  $R = R_e + H$ , where  $R_e$  is the mean radius of the Earth and  $H$  is the layer height above the Earth's surface. In order to represent VTEC as a continuous function as in Equation (2), the mapped VTEC—given at the position  $x_{IPP}$  of the so called Ionosphere Pierce Points (IPP), as the intersection point of the ray-path and the single layer—is used as input to different modeling approaches for GIMs. The official IGS GIM is a combination of independent GIMs [3,8], provided by the Ionosphere Associated Analysis Centers (IAAC) [9]. The IAAC, the *Center for Orbit Determination in Europe* (CODE), the *European Space Operations Center of the European Space Agency* (ESOC/ESA), the *Chinese Academy of Sciences* (CAS), the *Canadian Geodetic Survey of Natural Resources Canada* (EMRG) and the *Wuhan University* (WHU) generate GIMs using spherical harmonic (SH) series expansions [8,10]. The GIM of the *Universitat Politècnica de Catalunya* (UPC) is based on a discretization technique in terms of voxels [11–13], whereas the GIM of the Jet Propulsion Laboratory (JPL) is based on a spline approach. The OPTIMAP group (see Acknowledgments) uses basis functions in terms of B-splines for the modeling of the GIMs [14–17].

It is necessary to distinguish between “final”, “rapid”, “ultra-rapid” or “real-time” GIMs. The classification is based on the underlying input data, see Table 1. Final GIMs, for instance, are usually based on post-processed observations, satellite orbits and receiver and satellite clocks, which are generally available after 2–3 weeks and the final GIMs can thus be provided with the corresponding product latency. In this regard, we classify rapid GIMs with a latency of one day, ultra-rapid GIM with a latency of 2–3 h, near real-time (NRT) with a latency of about 15 min and finally a real-time (RT) GIM—due to processing times—with a latency of some seconds. As it can be seen from Table 1, NRT and RT products are based on the same input data, but the distinction is based on product latency, which differs due to the computational burden.



**Table 1.** Definition of different latency types depending on the input data.

Latency Type	Final	Rapid	Ultra-Rapid	Near Real-Time	Real-Time
Data	post-processed	daily	hourly	data-streams	data-streams
Data Latency	2–3 weeks	>1 day	>1 h	real-time	real-time
Product Latency	2–3 weeks	>1 day	>1 h	<15 min	<1 min

The IAAC's GIMs are disseminated using the IONosphere map EXchange (IONEX) format. The ASCII-based IONEX format was developed and modified by Schaer et al. (1998) [6] and supports the dissemination of VTEC grids as epoch files or daily files. The spatial sampling of the grid points can be chosen arbitrarily but is typically fixed with sampling intervals of  $\Delta\Phi = 2.5^\circ$  and  $\Delta\Lambda = 5^\circ$  in latitude  $\varphi$  and longitude  $\lambda$  [18], respectively. The so-called epoch IONEX file contains one single VTEC map for an arbitrary epoch, while the daily IONEX file provides several VTEC maps at consecutive epochs with a temporal sampling of  $\Delta T = 2$  h, 1 h, 15 min or 10 min. The temporal sampling of consecutive maps within one IONEX file is typically fixed with 1–2 h for final products, up to 15 min for rapid- and 10 min for ultra-rapid products [15]. Since IONEX is a grid-based format, it is particularly flexible, allowing the maps to be provided without considering the underlying modeling approach, e.g., SHs, voxels or B-splines. However, with a spatial sampling of  $2.5^\circ \times 5^\circ$ , there are 5184 grid points to be calculated for each snapshot map and thus, with decreased temporal sampling intervals, the size of the IONEX file increases. For the dissemination of GIMs in RT, it is obvious that the calculation of such VTEC grids and thus, the creation of IONEX, even epoch IONEX is not adequate. The dissemination of GIMs in RT requires datastream-based formats, see for instance Caissy et al. [19].

A more convenient data format is provided by the Radio Technical Commission for Maritime Services (RTCM) and their Real-Time GNSS Data Transmission Standard RTCM 3.0. The format consists of individual State Space Representation (SSR) messages providing corrections of biases, orbits and clocks for each GNSS. The IM201 submessage type valid for all GNSS includes the SSR Ionosphere VTEC Spherical Harmonics corrections [20]. Centre national d'études spatiales (CNES), CAS and UPC developed an RT combination which is based on this SSR VTEC message for an experimental IGS RT-GIM [21]. The SSR VTEC message allows the transmission of SH coefficients up to a maximum degree of  $n = 16$ , by means of the Networked Transport of RTCM via Internet Protocol (Ntrip) to the user.

The SSR VTEC message has two drawbacks, namely, the restriction to coefficients of a series expansion in terms of SHs and their limitation to the maximum degree  $n_{max} = 16$ . Consequently, GIMs generated with alternative modeling approaches, such as B-splines or voxels, cannot be considered. However, B-splines and voxels have proven to be appropriate candidates for ionosphere modeling as well [11,22,23]. Roma-Dollase et al. (2017) [24] compared the performance of the GIMs of the IAACs and showed that the voxels-based GIM, the 'uqrg', provided by UPC has been performing with higher accuracy. Goss et al. (2019) [15] derived the relation between the B-spline approach and the SHs in the frequency domain and generated GIMs with different spectral resolutions based on a Multi Resolution Representation (MRR) in terms of B-splines. To be more specific, the maximum degree  $n_{max}$  of the SH series expansion defines its cutoff frequency and thus, the minimum wavelength which can be represented. In the B-spline case, the so-called levels define the corresponding minimum wavelength. A B-spline-based model was developed, generating high resolution GIMs with a cutoff frequency comparable to  $n_{max} = 33$ .

These high-resolution B-spline models do not coincide with the RTCM standards and has not yet been used for single-frequency positioning. Hence, it remains the question, how can high-resolution GIMs improve the positioning and how can they be made available to users.

This paper presents a study based on a ultra-rapid and high-resolution GIM, generated by a B-spline model. This GIM is transferred to an SH expansion considering the (1) spectral, spatial and temporal resolution as well as (2) the computational time, which is needed

for the transformation. An accuracy assessment based on the dSTEC analysis [24] and an assessment in terms of single-frequency positioning using the open source software RTKLIB [25] is performed.

The paper is outlined as follows; in Section 2, we introduce the different modeling approaches for GIMs. Section 2.4 gives an overview about the currently available data formats for the dissemination of GIMs. In Section 3, a methodology for the transfer is described considering the above mentioned two requirements about the resolutions and computational time. In this regard, we discuss in Sections 3.1 and 3.2 the usage of the so-called Reuter grid [26,27] to generate pseudo-observations for the estimation of SH coefficients in Section 3.3.

The developed approach is numerically tested and assessed in Section 4. A final summary about the applicability of the developed approach and the conclusions found are given in Section 5.

## 2. Global Ionosphere Map Generation

Representing the continuous 3-D function  $VTEC(\varphi, \lambda, t)$  as introduced in Equation (2) by means of a series expansion reads

$$VTEC(\varphi, \lambda, t) = f(\mathbf{x}, t) = \sum_{k=0}^{\infty} c_k(t) \phi_k(\mathbf{x}), \quad (4)$$

with the space-dependent basis functions  $\phi_k(\mathbf{x})$  and the unknown time-dependent series coefficients  $c_k(t)$ . Given the  $i_s = 1, 2, \dots, I_s$  observations  $y(\mathbf{x}_{i_s}, t_s)$  with observation errors  $e(\mathbf{x}_{i_s}, t_s)$  at discrete time moments  $t_s = t_0 + s \cdot \Delta t$  with  $s \in N_0$  and temporal sampling  $\Delta t$ , Equation (4) can be rewritten as

$$y(\mathbf{x}_{i_s}, t_s) + e(\mathbf{x}_{i_s}, t_s) = f(\mathbf{x}_{i_s}, t_s) = \sum_{k=0}^N c_k(t_s) \phi_k(\mathbf{x}_{i_s}). \quad (5)$$

Herein, the total number  $N + 1$  of terms depends, according to the sampling theorem on a sphere, on the spatial sampling intervals  $\Delta\varphi$  in latitude and  $\Delta\lambda$  in longitude for all observations at time  $t_s$ . The truncation error

$$r_N(\mathbf{x}, t) = \sum_{k=N+1}^{\infty} c_k(t) \phi_k(\mathbf{x}). \quad (6)$$

describes the higher order signal parts of  $VTEC(\mathbf{x}_{i_s}, t_s)$  which cannot be modeled by the series expansion (5) and is therefore neglected in the following.

### 2.1. Modeling Coordinate System

VTEC exhibits a strongly time-varying phenomenon. The ionosphere shows seasonal and annual, as well as daily and subdaily variations. These regular variations follow spatially the geomagnetic equator, therefore the modeling of the ionosphere is typically applied in the geocentric solar magnetic (GSM) coordinate system, which results in much slower variations of VTEC and allows for a more precise representation; detailed information about the GSM coordinate system can be found in [28]. Note, in the sequel of this paper, the models are set up in the GSM coordinate system, while plots and figures are represented in the Earth-fixed geographic coordinate system.

### 2.2. Spherical Harmonics Model

Using the SH approach, the observation Equation (5) can be rewritten as

$$y(\mathbf{x}_{i_s}, t_s) + e(\mathbf{x}_{i_s}, t_s) = f_{n_{\max}}(\mathbf{x}, t_s) = \sum_{n=0}^{n_{\max}} \sum_{m=-n}^n c_{n,m}(t_s) Y_{n,m}(\mathbf{x}_{i_s}) \quad (7)$$

where

$$Y_{n,m}(x_{i_s}) = P_{n,|m|}(\sin \varphi) \cdot \begin{cases} \cos m\lambda & \text{if } m \geq 0 \\ \sin |m|\lambda & \text{if } m < 0 \end{cases} \quad (8)$$

are the SHs of degree  $n = 0, \dots, n_{max}$  and order  $m = -n, \dots, n$ , with  $P_{n,|m|}(\sin \varphi)$  being the normalized associated Legendre functions. The maximum degree  $n_{max}$  represents the cutoff frequency of the model representation and is usually defined as a measure for the spectral content of a signal on a sphere. According to the sampling theorem on a sphere, the maximum degree  $n_{max}$  is determined from

$$n_{max} \leq \frac{180^\circ}{\Delta\varphi} \quad \text{and} \quad n_{max} \leq \frac{180^\circ}{\Delta\lambda} \quad (9)$$

and defines the total number  $N = (n_{max} + 1)^2$  of terms in Equation (7) and, thus, the total number of unknown series coefficients  $c_{n,m}(t)$ . The SHs are basis functions which are globally defined, as can be seen from Equation (8), this means that they are different from zero almost everywhere on the sphere and require a homogeneous distribution of observations [22]. However, the observations  $y(x_{i_s}, t_s)$  at the IPP positions are usually given with a globally inhomogeneous distribution with small sampling intervals over the continents and larger sampling intervals in oceanic regions, thus,  $\Delta\varphi$  and  $\Delta\lambda$  in (9) have to be interpreted as global average values.

### 2.3. B-Spline Model

For the series expansion in terms of B-splines, we rewrite Equation (5) as

$$y(x_{i_s}, t_s) + e(x_{i_s}, t_s) = f_{J_1, J_2}(x, t_s) = \sum_{k_1=0}^{K_{J_1}-1} \sum_{k_2=0}^{K_{J_2}-1} d_{k_1, k_2}^{J_1, J_2}(t_s) \phi_{k_1, k_2}^{J_1, J_2}(x_{i_s}) \quad (10)$$

with the time-dependent B-spline coefficients  $d_{k_1, k_2}^{J_1, J_2}(t_s)$  and the 2-D B-spline functions

$$\phi_{k_1, k_2}^{J_1, J_2}(x_{i_s}) = \phi_{k_1}^{J_1}(\varphi) \tilde{\phi}_{k_2}^{J_2}(\lambda) \quad (11)$$

of levels  $J_1$  and  $J_2$  with respect to  $\varphi$  and  $\lambda$ . The tensor product (11) consists of so-called endpoint interpolating polynomial B-spline functions  $\phi_{k_1}^{J_1}(\varphi)$ , which are used for the representation of the latitudinal dependencies. The trigonometric B-splines  $\tilde{\phi}_{k_2}^{J_2}(\lambda)$  in longitude direction ensure a continuous representation of VTEC along the circles of latitudes [29]. The B-spline levels  $J_1$  and  $J_2$  define the total number  $K_{J_1} = 2^{J_1} + 2$  and  $K_{J_2} = 3 \cdot 2^{J_2}$  of B-spline functions  $\phi_{k_1}^{J_1}(\varphi)$  and  $\tilde{\phi}_{k_2}^{J_2}(\lambda)$  and the shift parameters  $k_1 = 0, 1, \dots, K_{J_1} - 1$  and  $k_2 = 0, 1, \dots, K_{J_2} - 1$  are their position along the latitude and the longitude. Figure 1 shows the polynomial B-spline functions of level  $J_1 = 3$  (left) where the first and the last two splines indicate the endpoint interpolating feature. The right panel in Figure 1 shows the trigonometric B-splines of level  $J_2 = 2$  with two splines crossing the  $360^\circ$  meridian. This feature allows for a continuous representation around the globe; more information can be found in [15,22,23,29].



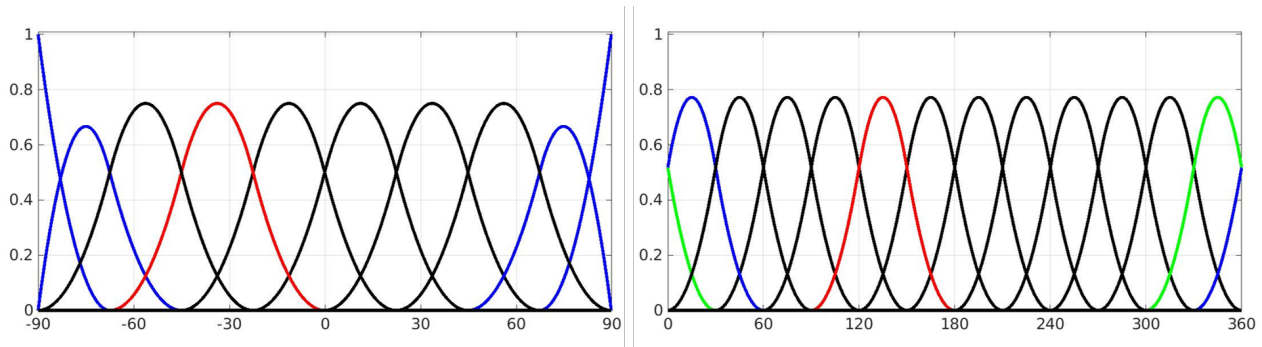


**Figure 1.** Polynomial B-spline of level  $J_1 = 3$  (left). The blue-colored splines indicate the endpoint interpolating feature at the boundaries of the interval. In the right panel, the trigonometric B-spline of level  $J_2 = 2$  are represented. Here, the blue-colored spline as well as the green-colored spline indicate the wrapping around at the boundaries of the  $0^\circ$  and  $360^\circ$  meridian. The red-colored B-spline functions are of shift parameters  $k_1 = 3$  and  $k_2 = 3$  for the polynomial and trigonometric B-splines, respectively.

In contrast to SHs, B-splines are localizing basis functions, i.e., they are different from zero only in small intervals, see the red colored B-spline functions in Figure 1. This means that for the estimation of unknown series coefficients, each tensor product (11) must be supported by observations to avoid singularities, [14–17]. In this regard, the B-spline levels  $J_1$  and  $J_2$  have to be chosen carefully. Similar to the calculation of the maximum degree (9), the levels depend on the mean sampling intervals  $\Delta\varphi$  and  $\Delta\lambda$  and the inequalities

$$J_1 \leq \log_2 \left( \frac{180^\circ}{\Delta\varphi} \right) \quad \text{and} \quad J_2 \leq \log_2 \left( \frac{120^\circ}{\Delta\lambda} \right), \quad (12)$$

have to be fulfilled, see [15,22,23]. Note, the higher the levels are chosen, the more spline functions are distributed along the latitude  $\varphi$  and the longitude  $\lambda$  and the finer are the structures in terms of wavelengths  $L_\varphi = 2 \cdot \Delta\varphi$  in latitude and  $L_\lambda = 2 \cdot \Delta\lambda$  in longitude that can be represented [15,16].

#### 2.4. VTEC Products

Given the  $(N + 1) \times 1$  vector  $\hat{\mathbf{c}}_s = [\hat{c}_0, \hat{c}_1, \dots, \hat{c}_N]^T$  of estimated series coefficients  $\hat{c}_k(t_s)$  for a time moment  $t_s$ , the estimated values  $\widehat{VTEC}(\varphi_v, \lambda_v, t_s)$  at arbitrary points with latitudes  $\varphi_v$  and longitudes  $\lambda_v$ , with  $v = 1, \dots, V$ , can be calculated by

$$\hat{\mathbf{f}}_s = \mathbf{A}_s \hat{\mathbf{c}}_s. \quad (13)$$

Therein,  $\hat{\mathbf{f}}_s$  is the  $V \times 1$  vector of the values  $\widehat{VTEC}(\varphi_v, \lambda_v, t_s)$ , the  $V \times (N + 1)$  matrix  $\mathbf{A}_s$  comprises the underlying basis functions  $\phi_k(\mathbf{x})$  as shown in Equation (4).

Consequently, two strategies for disseminating ionospheric corrections can be set up. For each one, an appropriate product type is defined, which provides the information about the state of the ionosphere, namely

- *Product type 1:* estimated series coefficients  $\hat{c}_k(t_s)$  with  $k = 0, \dots, N$ . It is assumed that a user has an appropriate converter for evaluating the respective series expansion (4). In that way, the corrections can directly be calculated by the user.
- *Product type 2:* VTEC grid values  $\widehat{VTEC}(\varphi_l, \lambda_r, t_s)$  for  $l = 1, \dots, L$  latitudes  $\varphi_l$  and  $r = 1, \dots, R$  longitudes  $\lambda_r$ , where  $L$  is the number of points along the meridians and  $R$  is the number of grid points along the circles of latitudes with arbitrary sampling  $\Delta\Phi = \varphi_{l+1} - \varphi_l$  and  $\Delta\Lambda = \lambda_{r+1} - \lambda_r$ , respectively. This implies that a user has to interpolate between the provided grid points in order to obtain the required correction.

In the following, we distinguish between grid-based *Product type 2* formats (Section 2.5.1) and coefficient-based *Product type 1* formats (Section 2.5.2).

## 2.5. Dissemination Formats for Positioning

To improve positioning by GNSS, ionospheric effects on the signals have to be corrected. Ionospheric corrections are therefore typically provided in terms of VTEC maps. The type of application (real-time, post-processing) determines the *Product type* to be used. For a proper application of the corrections, the preliminary position of the receiver  $x_R$  and the position of the GNSS satellites  $x^S$  are required. These allow the determination of the position vector  $x_{IPP}$  of the IPP and subsequently the determination of the ionospheric correction either from *Product type 1* or from *Product type 2*.

### 2.5.1. IONEX Format

The IONEX format was introduced by Schaer et al. in 1998 [6] and is up to now commonly used for the dissemination of GIMs of any type of latency. The format is particularly advantageous, because it allows for provision of additional information such as used receiver stations as well as DCBs. Usually, the VTEC values are given in an Earth-fixed geographic coordinate system on grids with a spatial sampling of  $\Delta\Phi = 2.5^\circ$  in latitude and  $\Delta\lambda = 5^\circ$  in longitude for snapshot maps with a temporal sampling of  $\Delta T = 2$  h.

When providing corrections using grid-based formats, the user must first perform an interpolation between the grid points and the temporal snapshot maps [6,15]. In order to calculate the values  $VTEC(\varphi_{IPP} = \varphi_l + q \cdot \Delta\Phi, \lambda_{IPP} = \lambda_r + p \cdot \Delta\lambda)$  for the position of the IPPs with  $0 \leq q \leq 1$  and  $0 \leq p \leq 1$  for time  $t_s$ , the simple bilinear spatial interpolation from VTEC values of the surrounding four points, as well as the temporal interpolation for any arbitrary time  $t = t_s + \tau \cdot \Delta T$  with  $0 \leq \tau \leq 1$  according to Schaer et al. (1998) [6] can be applied. By applying the interpolation, the quality of the calculated VTEC values depends on the position of  $VTEC(\varphi_l + q \cdot \Delta\Phi, \lambda_r + p \cdot \Delta\lambda, t)$  within the grid cell, on the spatial sampling intervals  $\Delta\Phi$  and  $\Delta\lambda$ , as well as the temporal sampling  $\Delta T$ . The interpolation is applied in Sun-fixed coordinate system in order to take into account the Earth's rotation, see [6].

### 2.5.2. Coefficient Based Format

The currently preferred method for dissemination of ionospheric corrections for RT positioning is based on SH coefficients, follows *Product type 1* and is based on RTCM streams. The SSR VTEC message allows the dissemination of estimated coefficients  $\hat{c}_{n,m}(t_s)$  of a SH model with additional information about degree  $n$  and order  $m$  of the underlying SH model, as well as the time moments  $t_s$  and the height  $H$  of the single layer model for which the coefficients are valid. According to the message specifications the coefficients must be provided in Sun-fixed longitude with a phase shift of 2 h to the approximate VTEC maximum at 14:00 local time. This means that a coordinate transformation must be carried out for the values  $VTEC(\varphi_{IPP}, \lambda_{IPP}, t_s)$ , which first provides a transformation from GSM to the Sun-fixed geographic coordinate system and then a rotation around the spin-axis of the Earth by 2 h. The SSR VTEC message is designed for the dissemination of SH coefficients and allows them only up to degree and order  $n = 16$ . This means that higher resolution models cannot be distributed via the SSR VTEC message. Another restriction of the message is that models not based on SHs require always a transformation to SHs.

### 2.5.3. Requirements for GIM Formats

The strategy for the dissemination and thus the choice of *Product type 1* or *Product type 2* of the estimated VTEC information is subject to certain restrictions, depending on their further use, namely:

- ... For precise positioning in post processing mode: to be more specific, as long as the data are not immediately used by a user, the size of the data is less important and the transformation may take longer. Which means, the VTEC information can be prepared with high resolution and quality and be provided to the user. It does not

- matter which dissemination strategy is chosen and through which platform (FTP, streaming) the information reaches the user.
- ... For precise navigation and positioning in RT: in this case, the selection of possible dissemination formats is limited. Hence, the user must receive the ionospheric information within seconds and with high precision, in order to correct the GNSS measurements used for positioning. Currently, only the SSR VTEC message is used for this purpose. Consequently, the dissemination strategy with *Product type 1* has to be chosen.

### 3. Methodology

For the dissemination of a B-spline-based RT ionospheric correction to a user by means of *Product type 1* and the currently intended data format, i.e., the SSR VTEC message, a transformation of the B-spline model into SH coefficients is required. For the transformation of the B-spline model, it must be considered that:

1. The transformation should be done with high precision, i.e., since B-splines and SHs are characterized by different features, a high degree  $n_{max}$  of the SH expansion needs to be considered.
2. The time which is needed for the transformation is limited. Hence, the processing time including the generation of pseudo-observations—the evaluation of Equation (18)—and the estimation of the SH coefficients (cf. Equation (20)) should be completed within seconds.

#### 3.1. Point Distribution on a Sphere

The transformation of the B-spline model to SHs requires input data generated by the B-spline model which reflect the variations in the GIM globally, i.e., VTEC values given as pseudo-observations on a global grid. As a matter of fact, a reliable computation of SH series coefficients requires homogeneously distributed input data. Since a regular grid as described in Section 2.5 does not fulfill this criterion, a Reuter grid is used instead [26]. The Reuter grid provides equi-distributed points  $P(\varphi_l, \lambda_{l,r})$  on the sphere with spherical coordinates

$$\varphi_0 = -90^\circ \quad \text{and} \quad \lambda_{0,0} = 0^\circ, \quad (14)$$

$$\varphi_l = -90^\circ + l \Delta\varphi_l \quad \text{and} \quad \lambda_{l,r} = r \frac{360^\circ}{\gamma_l}, \quad (15)$$

$$\varphi_\gamma = 90^\circ \quad \text{and} \quad \lambda_{\gamma,0} = 0^\circ \quad (16)$$

for  $r = 0, \dots, \gamma_l - 1$  and  $l = 1, \dots, \gamma - 1$  with  $\gamma \in \mathbb{N}$  and the sampling intervals  $\Delta\varphi_l = \frac{180^\circ}{\gamma}$  in latitude direction. Furthermore,

$$\gamma_l = \lfloor 360^\circ / \arccos((\cos \Delta\varphi_l - \sin^2 \varphi_l) / \cos^2 \varphi_l) \rfloor \quad (17)$$

means the total number of grid points along the circle of latitude  $\varphi_l$ . Reforming of Equation (17) results in the sampling interval  $\Delta\lambda_l$  of the grid points in longitude direction. For  $\varphi_l = 0$ , it applies  $\Delta\varphi_l = \Delta\lambda_l$ . More information about the Reuter grid can be found in [27,30].

The left part of the Table 2 shows for different values of  $\gamma$  the values of the spatial sampling intervals  $\Delta\varphi_l$  along the meridian and  $\Delta\lambda_l$  at the equator, as well as the total number  $V$  of Reuter grid points. The right part of Table 2 provides, for each degree  $n_{max}$ , the necessary mean sampling intervals  $\Delta\varphi$  and  $\Delta\lambda$  from Equation (9) and the corresponding total number of coefficients  $N$ .

The Reuter grid is particularly advantageous for the RT conversion of the B-spline model to SHs, because it provides a homogeneous distribution of the pseudo-observations and fulfills at the same time the conditions of the inequalities (9). Furthermore, a small number  $V$  of pseudo observations allows a transformation with short processing time. The values  $\Delta\varphi_l$  and  $\Delta\lambda_l$  for Reuter grids of  $\gamma = 16, 21, 25, 31, 35$  in the left part of Table

2 fulfill the conditions (9) for SHs with maximum degrees  $n_{max} = 15, 20, 24, 30, 34$  in the right part.

**Table 2.** Sampling intervals  $\Delta\varphi_l$  and  $\Delta\lambda_l$  of the Reuter grid points for different values of  $\gamma$  and the corresponding number  $V$  of Reuter grid points. Required max. sampling intervals  $\Delta\varphi_{SH}$  and  $\Delta\lambda_{SH}$  and the number of unknown coefficients of spherical harmonics (SHs) with different values for  $n_{max}$ .

Reuter Grid						Spherical Harmonics					
$\gamma$	16	21	25	31	35	$n_{max}$	15	20	24	30	34
$\Delta\varphi_l, \Delta\lambda_l$	11.25°	8.57°	7.2°	5.8°	5.14°	$\Delta\varphi, \Delta\lambda$	12	9	7.5	6	5.3
$V$	317	563	797	1225	1561	$N$	256	441	625	961	1224

Figure 2 shows the distribution of Reuter grid points with different values for  $\gamma$ . Due to the projection in the map, the Reuter grid points diverge with increasing latitude.

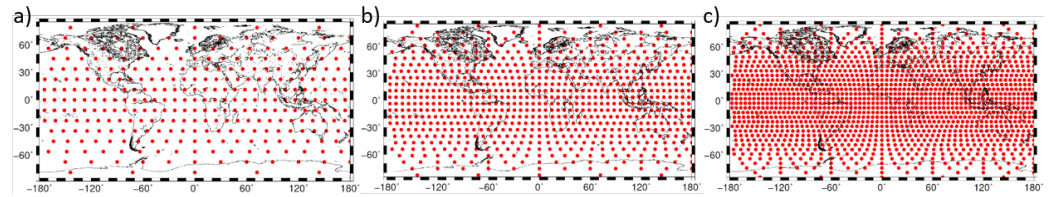


**Figure 2.** Reuter grids with values  $\gamma = 16$  in panel (a),  $\gamma = 25$  in panel (b) and  $\gamma = 35$  in panel (c).

### 3.2. Pseudo Observations from B-spline Model Output

The pseudo observations are generated by means of the given  $u \times 1$  vector  $\hat{\beta}_s = [\hat{d}_{0,1}^{J_1, J_2}(t_s), \hat{d}_{0,2}^{J_1, J_2}(t_s), \dots, \hat{d}_{K_{J_1}-1, K_{J_2}-1}^{J_1, J_2}(t_s)]$  of estimated B-spline coefficient  $\hat{d}_{k_1, k_2}^{J_1, J_2}(t_s)$  of levels  $J_1$  and  $J_2$  with  $u = K_{J_1} \cdot K_{J_2}$  for the time moment  $t_s$ . We rewrite Equation (13) for the B-spline case as

$$\hat{f}_s = A_s \hat{\beta}_s \quad (18)$$

with the  $V \times u$  design matrix  $A_s$  consisting B-spline tensor products according Equation (11).  $\hat{f}_s$  is a  $V \times 1$  vector comprising the values  $\widehat{VTEC}_R(\varphi_l, \lambda_r, t_s)$ , with the index  $R$  indicating the VTEC values on a Reuter grid.

### 3.3. Estimation of SH Coefficients from Reuter Grid

The series coefficients  $c_{n,m}$  are estimated by parameter estimation from  $V > N$  pseudo observations  $\hat{f}_s$ . By rewriting the observation Equation (7), the linear equation system

$$\hat{f}_s + e_s = X_s c_s \quad (19)$$

can be established, with the  $V \times 1$  consistency vector  $e_s$ , the  $(N+1) \times 1$  vector  $c_s = [c_{0,0}, c_{1,0}, \dots, c_{N,N}]^T$  of series coefficients, as well as the  $V \times (N+1)$  design matrix  $X_s$  comprising the functions  $Y_{n,m}(\varphi_l, \lambda_r)$  according to (8). In case of a matrix  $X_s$  with full column rank, the problem can be solved by

$$\hat{c}_s = [X_s^T P_s X_s]^{-1} X_s^T P_s \hat{f}_s. \quad (20)$$

Substituting Equation (18) for the observations vector  $\hat{f}_s$  the transformation between the B-spline and the SH coefficients is established and reads

$$\hat{c}_s = [X_s^T P_s X_s]^{-1} X_s^T P_s A_s \hat{\beta}_s = T_s \hat{\beta}_s, \quad (21)$$

with the  $(N+1) \times u$  transformation matrix  $T_s$ .

With the estimated coefficients  $\hat{c}_s$ , the *Product type 1* and *Product type 2* can be distributed to users (cf. Section 2.4). Figure 3 shows a flowchart on the methodology of the previously derived transformation method. Thereby the generation of pseudo-observations

$\widehat{VTEC}_R(\varphi_l, \lambda_r, t_s)$  on a Reuter grid by means of given B-spline coefficients  $\hat{\beta}_s$  is followed by the estimation of the SH coefficients. The different sets  $\hat{\beta}_s$  and  $\hat{c}_s$  of coefficients can be considered for the dissemination in terms of *Product type 1*, however, only the set  $\hat{c}_s$  can be disseminated by means of the SSR VTEC message. Furthermore, both sets allow the generation of *Product type 2*. The two versions  $\widehat{VTEC}(\varphi_l, \lambda_r, t_s)$  generated by B-splines and  $\widehat{VTEC}_{SH}(\varphi_l, \lambda_r, t_s)$  generated by means of the transformation method are depicted on the right hand side of the flowchart in Figure 3. Both grids can be disseminated by means of the IONEX file format.

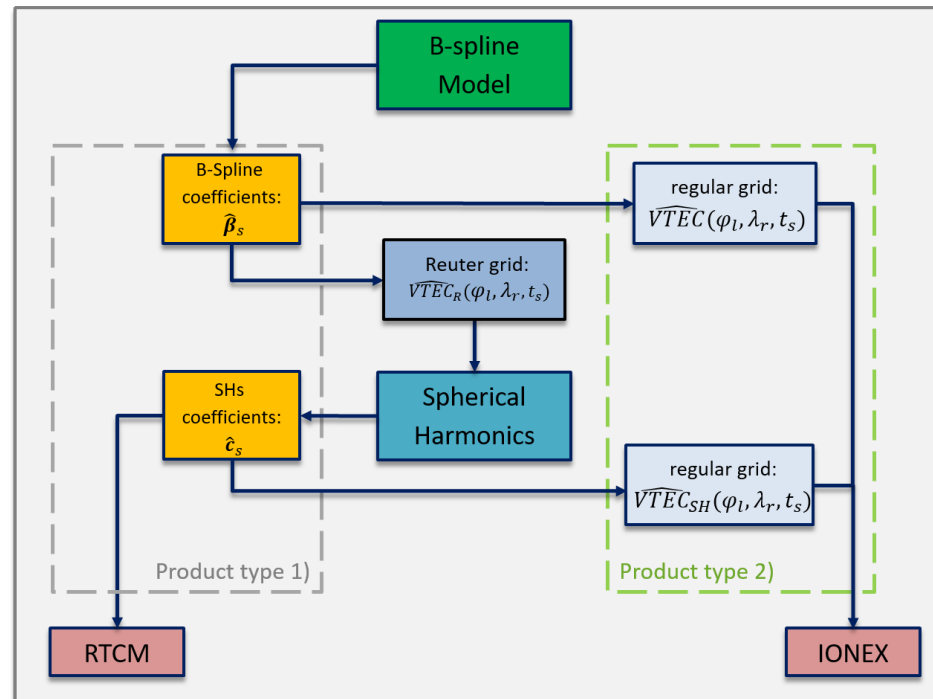


**Figure 3.** Schematic representation of the transformation and the following generation of the products of type 1 and 2 and the typically used data formats SSR VTEC message and IONEX, respectively.

#### 4. Results and Discussion

Subsequently, the developed approach will be applied for the period from 2 September 2017 to 12 September 2017. This period was chosen because of the varying ionospheric activity. Hence, the period is in the decreasing phase of the last solar cycle with a moderate number of sunspots. In addition, solar flares occurred between September 4 to September 8 with the consequence of a geomagnetic storm and increased values for the Kp index up to the value 8.

Given are the B-spline coefficients in the Sun-fixed coordinate system of the B-spline series expansion with the levels  $J_1 = 5$  and  $J_2 = 3$  for the mentioned period. At this stage, it should be mentioned that the present B-spline model according to Goss et al. [15] and Erdogan et al. [17] was generated by means of hourly GNSS observations and ultra-rapid GNSS orbits and that it is classified as an ultra-rapid GIM according to the definition from the introduction.

According to [15] and to Table 3, an expansion in terms of polynomial B-splines with the level  $J_1 = 5$  can be identified by a cutoff frequency of  $n_{max} = 33$  in SHs. An expansion in terms of trigonometric B-splines with the level  $J_2 = 3$  corresponds to a cutoff frequency  $n_{max} = 12$ . The ionosphere usually shows structures that follow the geomagnetic equator and thus, stronger variations occur in latitude direction. Therefore, a higher spectral resolution is chosen in the latitude direction and a lower spectral resolution in the longitude direction. Since the spectral representation in latitude and longitude directions are very



different for the given B-spline model, different cases are considered in the following to test and validate the determined approach.

**Table 3.** Different values for B-spline levels  $J_1$  and  $J_2$  with their corresponding values for the cutoff frequency  $n_{max}$  and the minimum wavelengths  $L_\varphi$  and  $L_\lambda$  (see Goss et al., 2019 and 2020 [15,16]).

Polynomial B-Splines							Trigonometric B-Splines						
$J_1$	1	2	3	4	5	6	$J_2$	1	2	3	4	5	6
$n_{max}$	3	5	9	17	33	63	$n_{max}$	3	6	12	24	48	96
$L_\varphi$	120°	72°	40°	21°	10.9°	5.7°	$L_\lambda$	120°	60°	30°	15°	7.5°	3.75°

Following Sections 3.1 and 3.2, we generate the pseudo-observations on Reuter grids for different values of  $\gamma$ . Figure 4 shows an example for September 8, at 12:00 UT with the VTEC map and modeled with B-splines in the left column. The right column depicts the pseudo-observation on the Reuter grid with  $\gamma = 21$ .

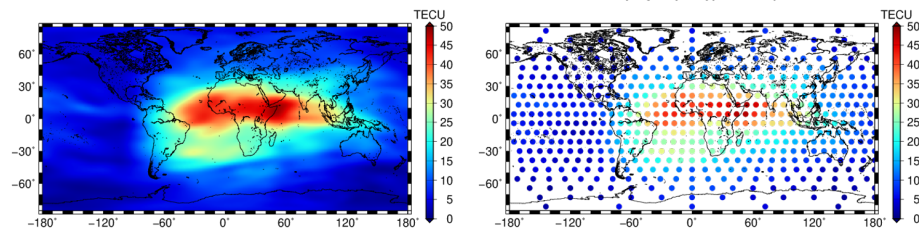


**Figure 4.** Original global ionosphere map (GIM) generated by the B-spline model with levels  $J_1 = 5$  and  $J_2 = 3$  in the left column. In the right column are the pseudo observations on a Reuter grid with  $\gamma = 21$ .

Thereafter, five different transformation cases are considered and the SH coefficients are estimated by the parameter estimation as described in Section 3.3. Thereby, the requirements for the transformation, which were defined in the beginning of Section 3 were taken into account. The values for  $\gamma$ , as well as for the highest degree  $n_{max}$  of the SH series expansion were used according to Section 3.1 and Table 2. Table 4 presents the five cases, which are analyzed in the following for their quality and feasibility. For quality estimation we follow the flowchart shown in Figure 3 and generate both the original B-spline GIM for  $\widehat{VTEC}(\varphi_l, \lambda_r, t_s)$  and the transformed version  $\widehat{VTEC}_{SH}(\varphi_l, \lambda_r, t_s)$  on a regular grid. The quality characteristics, RMS (%), mean value  $\delta_{mean}$ , maximum value  $\delta_{max}$  and minimum value  $\delta_{min}$  are determined based on the deviations, i.e., the differences  $\delta(\varphi_l, \lambda_r, t_s) = \widehat{VTEC}(\varphi_l, \lambda_r, t_s) - \widehat{VTEC}_{SH}(\varphi_l, \lambda_r, t_s)$  between the original GIM and the SH GIM. The applicability of the approach is executed on the basis of the necessary processing time  $\widehat{\Delta t}$  per epoch, which is needed for the transformation. For comparison reasons, the transformations have been computed on a workstation with 64 GB RAM, and a 8 core processor of 3.2 GHz clock rate. Thereby  $\widehat{\Delta t}$  comprises the evaluation time for the pseudo-observations as well as the estimation of the SH coefficients. All values given in Table 4 are averages obtained from transformed version computed with a  $\Delta T = 10$  min temporal sampling within the designated time span.

In the following, we discuss the given cases in more detail. In the first case, with  $V = 317$  pseudo-observations given on a Reuter grid with  $\gamma = 16$ , an SH series expansion with degree  $n_{max} = 15$  and  $N = 256$  coefficients has to be estimated. The average processing time for the transformation took  $\widehat{\Delta t} = 1.43$  s. However, the transformed version with degree  $n_{max} = 15$  produces systematic errors compared to the original GIM. The RMS value of the deviations shows with 1.31 TECU significant differences. The relative RMS value

$$rel. \text{ RMS}[\%] = 100 \cdot \sqrt{\frac{\sum_{l=1}^L \sum_{r=1}^R (\delta(\varphi_l, \lambda_r, t_s))^2}{\sum_{l=1}^L \sum_{r=1}^R (\widehat{VTEC}(\varphi_l, \lambda_r, t_s))^2}} \quad (22)$$

provides the RMS in percentage with 9.23% for the first case. The first column in Figure 5 shows the SH GIM in the top panel and the deviation map in the bottom panel. The deviation map represents mainly stripes in east–west direction, which indicate the difference in the spectral resolution for latitude direction between the original GIM corresponding to  $n_{max} = 33$  and representing the minimum wavelengths of  $L_{\varphi} = 10.9^{\circ}$  and the SH GIM of  $n_{max} = 15$ , representing minimum of wavelengths  $L_{\varphi} = 24^{\circ}$  (cf. Table 3). Visible are deviations with maximum values of  $\delta_{max} = 8.22$  TECU and minimum  $\delta_{min} = -8.06$  TECU, whereas the average  $\delta_{mean}$  is close to 0 TECU. In the second case, both the grid resolution and the degree of the SH expansion are increased to  $\gamma = 21$  and  $n_{max} = 20$ , respectively. This causes an insignificant increase in computation time to  $\Delta t = 1.85$  s, but a significant improvement in the transformation accuracy to a relative RMS of 5.83% (cf. Table 4). For the third case, the processing time doubles compared to the first case with  $\Delta t = 3.12$  s, but the error of the transformation is reduced by a half and a relative RMS of 4.19% can be achieved. This improvement is also visible in the second column of Figure 5. Due to the increased degree of the SHs, finer structures in latitude direction can be represented better than in the first case. Therefore, the stripes in east–west direction in the deviation map show a smaller extension in latitude direction and occur with decreased magnitude of  $\delta_{max} = 5.23$  TECU and  $\delta_{min} = -4.21$  TECU.

**Table 4.** Numerical and statistical results to estimate the quality and feasibility for the different cases.

	1. Case	2. Case	3. Case	4. Case	5. Case
$\gamma$	16	21	25	31	35
$V$	317	563	797	1225	1561
$n_{max}$	15	20	24	30	34
$N$	256	441	625	961	1224
$\Delta t$	1.43 s	1.85 s	3.12 s	4.99 s	8.23 s
rel. RMS [%]	9.23	5.83	4.19	2.54	1.83
RMS [TECU]	1.31	0.83	0.60	0.36	0.26
$\delta_{max}$ [TECU]	8.22	5.91	5.23	2.22	1.79
$\delta_{min}$ [TECU]	−8.06	−6.29	−4.21	−2.23	−1.9
$\delta_{mean}$ [TECU]	0.016	0.0012	0.014	0.0033	0.003

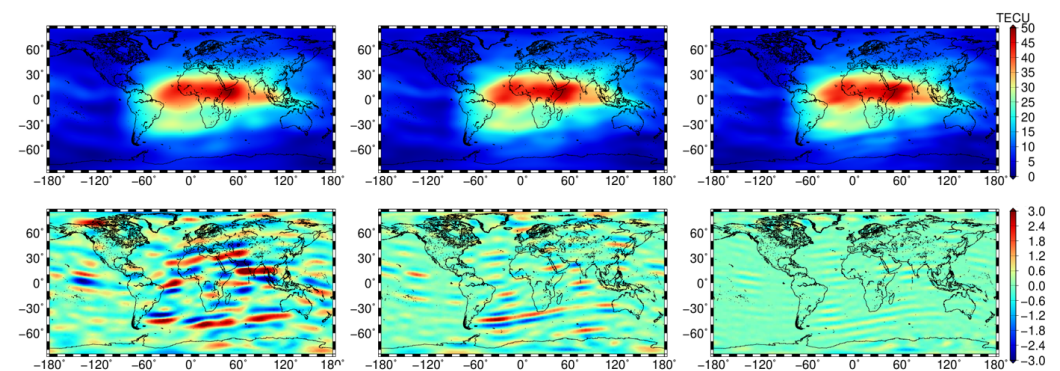


**Figure 5.** SH GIM (top panels) and deviation maps (bottom panels) of the 1. (left column), 3. (middle column) and 5. (right column) test case from Table 4 for September 8, at 12:00 UT.

Further improvements can be achieved by increasing the degree of the SH expansion for the transformation, but with a further extension of the processing time per epoch. The transformation using  $n_{max} = 34$  needs an average transformation time of  $\Delta t = 8.23$  s per epoch. The corresponding SH GIM is shown in the top right panel in Figure 5. The east–west stripes in the deviation map below are mainly visible in the area of the equatorial anomaly with maximum values of  $\delta_{max} = 1.79$  TECU and minimum values of  $\delta_{min} = -1.9$  TECU. The SH GIM describes a relative RMS of 1.83% compared to the original GIM. For



these five cases, it can be concluded that the quality of the transformation improves with increasing degree  $n_{max}$  for the SH series expansion.

Accordingly, Figure 6 shows on the left the relative RMS values and on the right the RMS values of the deviations for the period from 2 September 2017 and 12 September 2017 with decreasing magnitude.

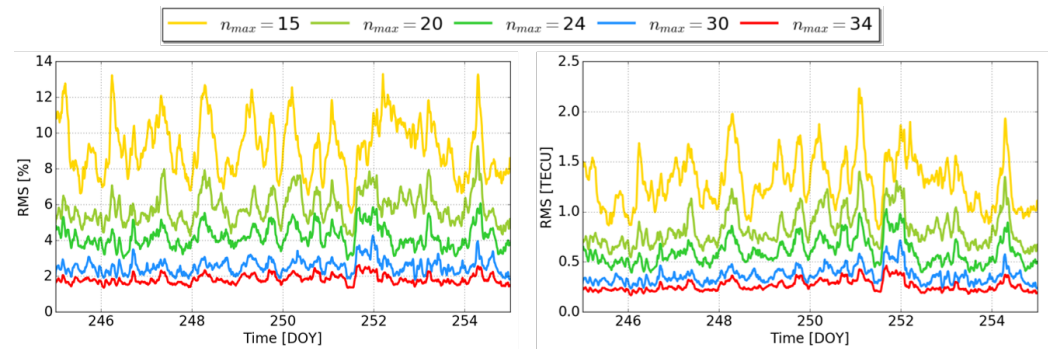


**Figure 6.** Change in relative RMS values (**left**) and RMS values (**right**), for the period from 2 September 2017 (DOY 245) to 12 September 2017 (DOY 255); temporal sampling intervals of 10 min.

#### 4.1. Validation

Subsequently, the original B-spline GIM and its transformed versions are validated using the dSTEC analysis and tested for their ability to correct the ionospheric disturbances in single frequency positioning. Additionally, the GIMs of the IAACs CODE from Berne, Switzerland and UPC from Barcelona, Spain are used for comparison.

##### 4.1.1. dSTEC Analysis

The dSTEC analysis is one of the most commonly used validation method for GIMs. It is based on the comparison of differenced STEC observations  $dSTEC_{obs}$  of a receiver and satellite pair along its phase-continuous arc, with the differenced STEC values  $dSTEC_{map}$  computed from the GIM to be validated as

$$dSTEC(t_s) = dSTEC_{obs}(t_s) - dSTEC_{map}(t_s), \quad (23)$$

with expectation value  $E(dSTEC(t_s)) = 0$ . Note, the STEC values from the GIMs are obtained by applying the mapping from Equations (3) and by the applying the interpolations from Section 2.5.1 according to Schaer et al. (1998) [6] for the position and time of the IPP of the observations along the satellite arc. More detailed information on the dSTEC analysis can be found in [15,18,24].

For the calculation of  $dSTEC_{obs}$ , the receiver stations shown in Figure 7 are used. These are either independent of the GIMs to be validated or have contributed to all of their calculations. Table 5 provides a summary of the results of the dSTEC analysis. The original B-spline GIM of DGFI-TUM is called ‘othg’. The naming follows the definition in [15], where ‘o’ stands for the OPTIMAP processing software, which was developed in a third-party project (see Acknowledgments). The second digit describes the temporal output sampling with ‘t’ for ten minutes. The ‘h’ describes the high spectral resolution and the ‘g’ the global expansion. The transformed versions of the ‘othg’, coinciding with the different cases of the previous section are named accordingly, but with the respective degree of SHs used for the transformation in the second and third digit. The last two columns in Table 5 show the results for the GIMs ‘codg’ and ‘uqrg’ provided by CODE and UPC, respectively. All GIMs used in the dSTEC analysis are given in IONEX format with spatial sampling of  $\Delta\varphi = 2.5^\circ$  in latitude and  $\Delta\lambda = 5^\circ$  in longitude. All other specifications for the different GIMs are depicted in Table 5.

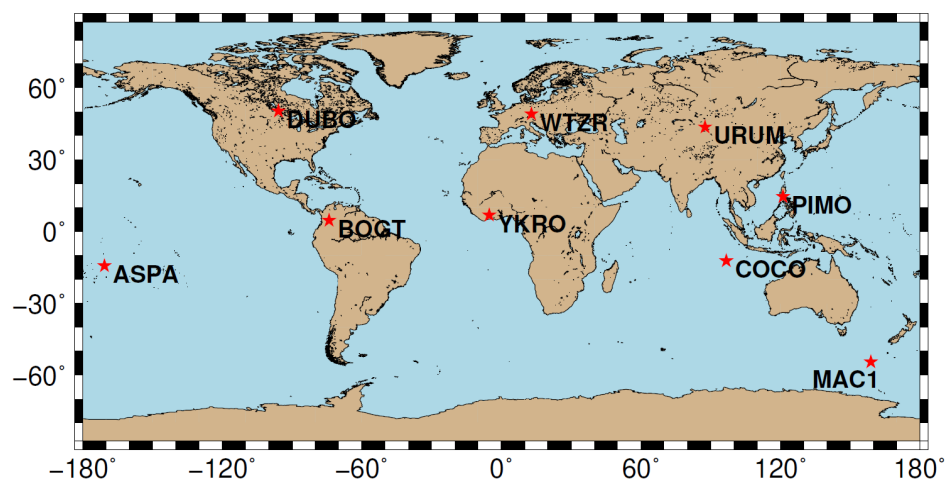


**Figure 7.** Global distribution of 9 receiver stations that are used for the dSTEC validation and for comparison of the generated GIMs.

**Table 5.** Comparison of GIMs with different characteristics, i.e., model type, degree of series expansion ( $J_1, J_2, n_{max}$ ), temporal output sampling intervals ( $\Delta T$ ) and latency until provision. For each of the investigated GIMs, the RMS of the dSTEC analysis is given.

GIM	othg	o15g	o20g	o24g	o30g	o34g	codg	uqrg
Model	B-splines	SHs	SHs	SHs	SHs	SHs	SHs	Voxel & Kriging
$n_{max}$		15	20	24	30	34	15	n.a.
$J_1/J_2$	5/3							
$\Delta T$	10 min	10 min	10 min	10 min	10 min	10 min	60 min	15 min
Latency	<3 h	<3 h	<3 h	<3 h	<3 h	<3 h	>1 week	>1 day
Reference	[15]	Section 3	Section 3	Section 3	Section 3	Section 3	[31]	[13]
RMS [TECU]	0.91	1.18	1.05	1.00	0.93	0.92	1.01	0.85

The last row shows the RMS values of  $dSTEC(t_s)$ , Equation (23), for each GIM given as the average over all stations and all observations during the period in September 2017. They indicate the performance of the individual GIMs during the designated period and for the selected stations. As usual the ‘uqrg’ performs best in the selection of GIMs with an RMS of 0.85 TECU, followed by ‘othg’ with an RMS of 0.91 TECU. The transformed versions show a trend that was already shown in Figure 6; the RMS values of transformed versions with larger  $n_{max}$  approach the value of the original ‘othg’. With an RMS of 0.92 TECU, the ‘o34g’ has a negligible difference in the accuracy to ‘othg’. This confirms their approximate agreement in the spectral resolution with  $n_{max} = 34$  for ‘o34g’ and the cutoff frequency of  $n_{max} = 33$  (cf. Table 3) in the latitude direction of ‘othg’. A comparison of the GIMs ‘o15g’ and ‘codg’, both based on an SH series expansion of  $n_{max} = 15$ , shows that a higher degree for the transformation is necessary, since the original GIM ‘othg’ provides a higher and ‘o15g’ a less quality than the ‘codg’ during the period of investigation.

#### 4.1.2. GIM Performance in Single-Frequency PPP

We perform a Precise Point Positioning (PPP) for the stations BOGT, WTZR and APSA using the open source software RTKLIB [25,32]. The selection of stations covers both mid and low latitudes, see Figure 7, as well as regions with different characteristics for ionospheric modeling, i.e., either characterized with strong variations in VTEC (BOGT), dense observation distribution (WTZR) or low number of observations (APSA). A kinematic processing mode is selected for each station to estimate the position for each epoch for which an observation was available. The VTEC values provided in the GIM are used to correct the ionospheric delay for each single frequency observation of the stations. Positioning tests were performed for the days 2 September 2017 with moderate ionospheric activity and 8 September 2017 characterized by a geomagnetic storm.

The estimated coordinate components  $X_{est}(t_s)$ ,  $Y_{est}(t_s)$  and  $Z_{est}(t_s)$  are subtracted from the actual coordinates  $X(t_s)$ ,  $Y(t_s)$  and  $Z(t_s)$  provided by the IGS [33] and the deviations of the 3D position are determined as

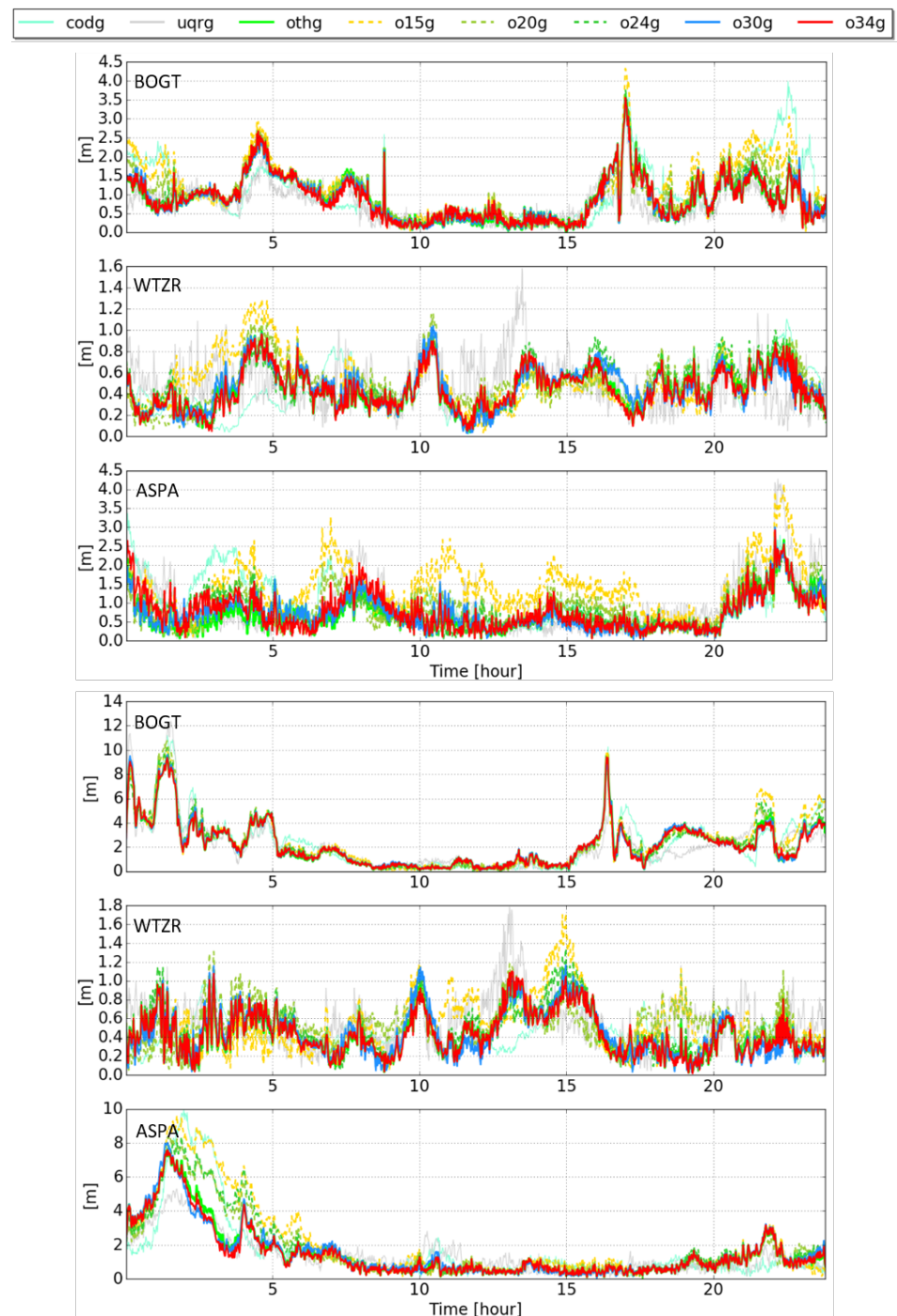
$$S(t_s) = \sqrt{(X(t_s) - X_{est}(t_s))^2 + (Y(t_s) - Y_{est}(t_s))^2 + (Z(t_s) - Z_{est}(t_s))^2}. \quad (24)$$

Figure 8 shows the time series of the differences  $S(t_s)$  for 2 September 2017 (left) and 8 September 2017 (right). A significant difference can be seen in  $S(t_s)$  between the two days. On 8 September 2017, due to the high geomagnetic activity the ionospheric corrections are more difficult to determine and thus, the positioning accuracy decreases and the deviations increase. This trend is especially noticeable for the stations BOGT and ASPA close to the equator. It can also be observed that their deviations increase during local noon, i.e., between 15:00 and 20:00 UT for BOGT and between 20:00 and 24:00 UT for ASPA. The large deviations of the position of BOGT and ASPA between 00:00 and 05:00 UT on September 8 are due to the high geomagnetic variations with increased geomagnetic index of  $Kp = 8$ . The variations are not as significant at the station WTZR, which was located on the night side of the Earth at that time. The daily variations of  $S$  in Figure 8 show that ‘othg’, ‘o30g’ and ‘o34g’, in light green, blue and red, respectively, exhibit a similar variation. Stronger deviations and mostly larger values  $S(t_s)$  can be recognized for the GIMs ‘o15g’, ‘o20g’ and ‘o24g’ with the dashed lines. The GIM ‘codg’ shows a similar behavior during the days. However, the ‘uqrg’ performs better in single frequency positioning and sometimes shows lower values than the ‘othg’, the ‘o30g’ and the ‘o34g’, except at local noon at station WTZR, where it shows large deviations.

A detailed evaluation of the performance of the different GIMs is performed using the respective RMS and the average  $\bar{S}$  values of the time series  $S(t_s)$ , which are depicted in Table 6.

**Table 6.** RMS and  $\bar{S}$  values of deviations  $S(t_s)$  for September 2 (DOY 245) and 8 (DOY 251), 2017 at the stations BOGT, WTZR and ASPA. The maximum and minimum values of the RMS and  $\bar{S}$  are marked in red and green, respectively. The RMS and  $\bar{S}$  of the transformed versions are bold if they are lower than the values of the original GIM, ‘othg’.

	Value	DOY	othg	o15g	o20g	o24g	o30g	o34g	codg	uqrg
BOGT	RMS [TECU]	245	1.07	1.35	1.17	1.09	1.05	1.05	1.29	0.90
		251	2.91	3.19	3.12	3.03	2.91	2.86	3.14	2.98
	$\bar{S}$ [TECU]	245	0.90	1.13	1.00	0.92	0.89	0.89	1.05	0.77
		251	2.22	2.44	2.34	2.31	2.23	2.20	2.35	2.18
WTZR	RMS [TECU]	245	0.49	0.55	0.53	0.52	0.50	0.48	0.51	0.55
		251	0.49	0.90	0.57	0.54	0.50	0.49	0.51	0.62
	$\bar{S}$ [TECU]	245	0.45	0.50	0.49	0.48	0.46	0.44	0.46	0.50
		251	0.44	0.53	0.52	0.47	0.44	0.44	0.47	0.57
ASPA	RMS [TECU]	245	0.81	2.53	0.98	0.92	0.85	0.92	1.13	1.19
		251	2.18	3.12	2.59	2.67	2.17	2.11	2.65	1.80
	$\bar{S}$ [TECU]	245	0.69	1.37	0.86	0.79	0.73	0.77	0.95	0.94
		251	1.53	2.10	1.76	1.84	1.54	1.48	1.64	1.40



**Figure 8.** Differences  $S(t_s)$  in the 3D position between the position determined by Precise Point Positioning (PPP) and ionospheric corrections calculated by different GIMs and the actual position. Left side shows the differences for the stations BOGT, WTZR and ASPA during the 2 September 2017 (DOY 245) and the right side the corresponding differences for 8 September 2017 (DOY 251) with different scaling of the y-axis. On the x-axis, the time in UT is depicted in hours.

The color scheme in Table 6 implies the lowest and highest values of the RMS and  $\bar{S}$  in green and red, for the respective station and day. It can be seen that for all stations there are differences in the positioning accuracy between the two days examined. Hence, for DOY 251, the RMS and average values are increased. There is an additional trend which shows, that for the selected stations and days the high resolution GIMs, ‘othg’ and ‘uqrg’ allow a correction of the ionospheric disturbances in a way that leads to a positioning with increased accuracy (see the green colors). Furthermore, the poor performance of the

‘o15g’—which has mostly highlighted values in red—confirms the result from Section 4.1.1, that a transformed version with a higher degree of SH series expansion is necessary to achieve the quality of the original GIM. As the degree of SHs for the transformation increases, the accuracy of positioning increases when using their ionosphere corrections. The values written in bold in Table 6 allow the conclusion that a transformation with at least the maximum degree  $n_{max} = 30$  is necessary to achieve the quality of ‘othg’.

It should be pointed out, that the pure SH model, the ‘codg’, can correct the ionospheric disturbances for single frequency positioning better than the transformed version ‘o15g’. However, in the example shown here, ‘codg’ cannot achieve accuracy of the ‘othg’, the ‘uqrg’ and the transformed versions ‘o30g’ and ‘o34g’.

## 5. Summary and Conclusions

The dissemination of RT ionosphere information is currently based on the RTCM message 1264, which can provide SH coefficients up to a maximum degree of  $n_{max} = 16$ . The IGS started to provide a combined RT-GIM, collecting the GIMs from CAS, CNES and UPC using Ntrip protocol and the SSR VTEC message [21]. Since the SSR VTEC message is currently the only format type for dissemination the RT-GIMs of the IAAcs, only SH models can be considered. Other models which are not based on SHs need to be converted and suffer from degeneration in the accuracy of the GIMs. Especially, high-resolution models cannot be converted appropriately to SHs when a low degree  $n_{max} = 16$  is used in the transformation. This means that an adaptation or extension of the existing dissemination formats, as already objected by Goss et al. (2019) and (2020) [15,16], must be carried out.

This paper presents a novel approach on the transformation of GIMs modeled by means of a B-spline series expansion to SH coefficients. It should be noted that the developed method can also be applied to models based on voxels or alternative basis functions.

The developed approach is setup in a way that the processing time during transformations are acceptable for RT applications and the transformed SH GIMs maintain the quality of the original GIM.

However, the numerical investigations are based on ultra-rapid GIMs modeled by a B-spline series expansion according to [15]. The given ultra-rapid GIMs only serve to test the developed approach and to assess the accuracy and quality of the transformations and the latency can further be decreased. The investigation period covers the days 2 September to 12 September 2017 with a geomagnetic storm on September 8. In a first step, a case study considering five cases with different degrees  $n_{max}$  for the transformation to SH is shown. It was found that with an increased value  $n_{max} \geq 30$ , the transformations converge sufficiently with the original B-spline model. However, for a transformation of the given B-spline model with level values of  $J_1 = 5$  and  $J_2 = 3$  a degree of  $n_{max} > 34$  is required.

In the assessment comprising a dSTEC analysis and a single-frequency PPP, the models of CODE (SHs of  $n_{max} = 15$ —‘codg’) and UPC (voxel and Kriging model—‘uqrg’) were used for comparison with the B-spline GIM ‘othg’ and its transformed versions. For both assessment methods, the high-resolution GIMs ‘othg’ and ‘uqrg’ as well as the transformed versions with degrees  $n_{max} \geq 30$  performed the best. The single-frequency PPP shows a discrepancy between the transformed SH GIMs of lower degree  $n_{max}$  and the original GIM ‘othg’, but also between ‘codg’ and the high-resolution solutions ‘othg’ and ‘uqrg’.

Finally, it can be concluded that for a transformation of the B-spline model to SHs, the maximum degree  $n_{max}$  has to be adapted accordingly. In this way, high quality ionospheric corrections can be provided to single-frequency users for the correction of positioning and navigation. This means that for the dissemination of high-resolution GIMs, an extension of the limited degree of the SH coefficients which is allowed by SSR VTEC message is required and accomplished urgently.

**Author Contributions:** The concept of the paper was proposed by A.G. and discussed with M.H.-P. and M.S., A.G. compiled the figures and wrote the text. The paper was reviewed by M.H.-P., M.S.,



D.R.-D., E.E., F.S., M.S. and F.S. assume responsibility for the projects INSIGHT II and OPTIMAP for which significant contributions entered into this article. The paper and figures were reviewed by all authors. All authors have read and agreed to the published version of the manuscript.

**Funding:** This research was funded by the German Research Foundation (DFG) under grant number SCHM2433/10-2 (project INSIGHT II) and the Technical University of Munich (TUM) in the framework of the Open Access Publishing Program. The approach presented in this paper was to a large part developed in the framework of the project OPTIMAP (‘Operational Tool for Ionospheric Mapping and Prediction’) funded by the Bundeswehr GeoInformation Center (BGIC) and the German Space Situational Awareness Centre (GSSAC).

**Data Availability Statement:** The data presented in this study are openly available in <ftp://cddis.gsfc.nasa.gov/>.

**Acknowledgments:** The authors thank the IGS and its IAAcs, in particular the Center for Orbit Determination in Europe (CODE, Berne, Switzerland) and the Universitat Politècnica de Catalunya/IonSAT (UPC, Barcelona, Spain), for providing the data. We acknowledge the Generic Mapping Tool (GMT), which was primarily used for generating the figures in this work.

**Conflicts of Interest:** The authors declare no conflict of interest.

## References

1. Klobuchar, J.A. Ionospheric Time-Delay Algorithm for Single-Frequency GPS Users. *IEEE Trans. Aerospace Electron. Syst.* **1987**, AES-23, 325–331.
2. Petit, G.; Luzum, B. IERS Conventions. Technical Report. 2010. Available online: [www.iers.org](http://www.iers.org) (accessed on 21 December 2020).
3. Hernández-Pajares, M.; Juan, J.M.; Sanz, J.; Argón-Àngel, A.; Garcia-Rigo, A.; Salazar, D.; Escudero, M. The ionosphere: Effects, GPS modeling and benefits for space geodetic techniques. *J. Geod.* **2011**, *85*, 887–907. [\[CrossRef\]](#)
4. Langley, R.B. Propagation of the GPS Signals. In *GPS for Geodesy*; Teunissen, P.J.G., Kleusberg, A., Eds.; Springer: Berlin/Heidelberg, Germany, 1998; pp. 111–149. [\[CrossRef\]](#)
5. Ciraolo, L.; Azpilicueta, F.; Brunini, C.; Meza, A.; Radicella, S. Calibration errors on experimental slant total electron content (TEC) determined with GNSS. *J. Geod.* **2007**, *81*, 111–120. [\[CrossRef\]](#)
6. Schaer, S.; Gurtner, W.; Feltens, J. *IONEX: The IONosphere Map EXchange Format Version 1*; Technical Report; Astronomical Institute, University of Berne: Bern, Switzerland, 1998.
7. The International GPS Service (IGS): An interdisciplinary service in support of Earth sciences. *Adv. Space Res.* **1999**, *23*, 631–653. [\[CrossRef\]](#)
8. Feltens, J.; Schaer, S. *IGS Products for the Ionosphere*; Technical report; European Space Operation Centre and Astronomical Institute of the University of Berne: Bern, Switzerland, 1998.
9. Villiger, A. (Ed.) *International GNSS Service Technical Report 2018*; Technical report, IGS Central Bureau and University of Bern; Bern Open Publishing: Bern, Switzerland, 2018.
10. Li, Z.; Yuan, Y.; Wang, N.; Hernández-Pajares, M.; Huo, X. SHPTS: Towards a new method for generating precise global ionospheric TEC map based on spherical harmonic and generalized trigonometric series functions. *J. Geod.* **2015**, *89*, 331–345. [\[CrossRef\]](#)
11. Hernández-Pajares, M.; Juan, J.M.; Sanz, J. New approaches in global ionospheric determination using ground GPS data. *J. Atmos. Sol. Terr. Phys.* **1999**, *61*, 1237–1247. [\[CrossRef\]](#)
12. Hernández-Pajares, M.; Juan, J.M.; Sanz, J.; Orus, R.; Garcia-Rigo, A.; Feltens, J.; Komjathy, A.; Schaer, S.C.; Krankowski, A. The IGS VTEC map: A reliable source of ionospheric information since 1998. *J. Geod.* **2009**, *83*, 263–275. [\[CrossRef\]](#)
13. Orus, R.; Hernández-Pajares, M.; Juan, J.; Sanz, J. Improvement of global ionospheric VTEC maps by using kriging interpolation technique. *J. Atmos. Sol.-Terr. Phys.* **2005**, *67*, 1598–1609. [\[CrossRef\]](#)
14. Erdogan, E.; Schmidt, M.; Seitz, F.; Durmaz, M. Near real-time estimation of ionosphere vertical total electron content from GNSS satellites using B-spline in a Kalman Filter. *Ann. Geophys.* **2017**, *35*, 263–277. [\[CrossRef\]](#)
15. Goss, A.; Schmidt, M.; Erdogan, E.; Görres, B.; Seitz, F. High-resolution vertical total electron content maps based on multi-scale B-spline representations. *Ann. Geophys.* **2019**, *37*, 699–717. [\[CrossRef\]](#)
16. Goss, A.; Schmidt, M.; Erdogan, E.; Seitz, F. Global and Regional High-Resolution VTEC Modelling Using a Two-Step B-Spline Approach. *Remote Sens.* **2020**, *12*, 1198, doi:10.3390/rs12071198. [\[CrossRef\]](#)
17. Erdogan, E.; Schmidt, M.; Goss, A.; Görres, B.; Seitz, F. Adaptive Modeling of the Global Ionosphere Vertical Total Electron Content. *Remote Sens.* **2020**, *12*, 1822. [\[CrossRef\]](#)
18. Hernández-Pajares, M.; Roma-Dollase, D.; Krankowski, A.; García-Rigo, A.; Orús-Pérez, R. Methodology and consistency of slant and vertical assessments for ionospheric electron content models. *J. Geod.* **2017**, *19*, 1405–1414. [\[CrossRef\]](#)
19. Caissy, M.; Agrotis, L.; Weber, G.; Pajares, M.; Hugentobler, U. The international GNSS real-time service. *GPS World* **2012**, *23*, 52–58.

20. RTCM. IGS State Space Representation (SSR). Technical Report. 2020. Available online: [https://files.igs.org/pub/data/format/igs\\_ssr\\_v1.pdf](https://files.igs.org/pub/data/format/igs_ssr_v1.pdf) (accessed on 21 December 2020).
21. Li, Z.; Wang, N.; Hernández-Pajares, M.; Yuan, Y.; Krankowski, A.; Liu, A.; Zha, J.; García-Rigo, A.; Roma, D.; Yang, H.; et al. IGS real-time service for global ionospheric total electron content modeling. *J. Geod.* **2020**, *94*, 1–16, doi:10.1007/s00190-020-01360-0. [[CrossRef](#)]
22. Schmidt, M.; Dettmering, D.; Mößmer, M.; Wang, Y. Comparison of spherical harmonic and B-spline models for the vertical total electron content. *Radio Sci.* **2011**, *46*, RS0D11. [[CrossRef](#)]
23. Schmidt, M.; Dettmering, D. Using B-spline expansions for ionosphere modeling. In *Handbook of Geomathematics*, 2nd ed.; Freeden, W., Nashed, M.Z., Sonar, T., Eds.; Springer: Berlin/Heidelberg, Germany, 2015; pp. 939–983. 80. [[CrossRef](#)]
24. Roma-Dollase, D.; Hernández-Pajares, M.; Krankowski, A.; Kotulak, K.; Ghoddousi-Fard, R.; Yuan, Y.; Li, Z.; Zhang, H.; Shi, C.; Wang, C. Consistency of seven different GNSS global ionospheric mapping techniques during one solar cycle. *J. Geod.* **2017**, *92*, 691–706. [[CrossRef](#)]
25. Takasu, T.; Yasuda, A. Development of the low-cost RTK-GPS receiver with an open source program package RTKLIB. In *International Symposium on GPS/GNSS*; International Convention Center: Jeju, Korea, 2009.
26. Reuter, R. Über Integralformeln der Einheitsphäre und Harmonische Splinefunktionen. Ph.D. Thesis, RWTH Aachen, Aachen, Germany, 1982.
27. Freeden, W.; Grevens, T.; Schreiner, M. *Constructive Approximation on the Sphere*; Oxford University Press: Oxford, UK, 1998.
28. Laundal, K.; Richmond, A. Magnetic Coordinate Systems. *Space Sci. Rev.* **2017**, *206*, 27–59. [[CrossRef](#)]
29. Lyche, T.; Schumaker, L. A multiresolution tensor spline method for fitting functions on the sphere. *SIAM J. Sci. Comput.* **2001**, *22*, 724–746. [[CrossRef](#)]
30. Eicker, A. Gravity Field Refinement by Radial Basis Functions from In-situ Satellite Data. Ph.D. Thesis, Rheinische Friedrich-Wilhelms-Universität Bonn, Bonn, Germany, 2008.
31. Schaer, S. Mapping and Predicting the Earth's Ionosphere Using the Global Positioning System. Ph.D. Thesis, University of Berne, Bonn, Germany, 1999.
32. Prol, F.; Camargo, P.; Monico, J.; Muella, M. Assessment of a TEC calibration procedure by single-frequency PPP. *GPS Solut.* **2018**, *22*, 35. [[CrossRef](#)]
33. Dow, J.; Neilan, R.E.; Rizos, C. The International GNSS Service in a changing landscape of Global Navigation Satellite Systems. *J. Geod.* **2009**, *83*. [[CrossRef](#)]



## 7.4 Co-Author Publications

### C-I

Erdogan, E. and Schmidt, M. and Goss, A. and Görres, B. and Seitz, F. (2020): **Adaptive Modeling of the Global Ionosphere Vertical Total Electron Content** In: Remote Sensing, 12(11), 1822, DOI: 10.3390/rs12111822

For the generation of ionosphere products with low latency, a suitable estimator is required which can process incoming observations soon after their acquisition. In this context, the Kalman filter (KF) as a recursive estimator is often applied. In the **C-I**, an adaptive KF is applied for estimating the unknown B-spline coefficients. One part of the adaptive KF is to implement a Variance Component Estimation (VCE) to compute the VTEC by assimilation of observations from different GNSS. The second part takes advantage of the localising B-spline basis functions, i.e. the coefficients, which are assigned to a specific region. This means that the B-splines reflect the variations in VTEC. In this context, the prediction model of the target parameters (coefficients) is adapted to the structure of the B-spline coefficients and to the number of supporting observations.

The adaptive KF was developed within the framework of the project OPTIMAP in order to take into account the different accuracies of different observations in the estimation by means of VCE. In the framework of OPTIMAP, the TSM model was developed, modelling both VTEC on a global scale and  $\Delta$ VTEC on a regional scale. This required an adaptation of the dynamical model to the signal to be modelled in order to control the sensitivity of the observations to the estimation. The contribution of A. Goss to the publication **C-I** was mainly through discussion of the approach in the adaptation of KF, as well as the contribution to the interpretation, analysis and presentation of the results in the context of the project OPTIMAP.

### C-II

Qi Liu, Manuel Hernández-Pajares, Haixia Lyu, Andreas Goss (2021): **Influence of temporal resolution on the performance of global ionospheric maps** In: Journal of Geodesy, 95(3), 1–16, 10.1007/s00190-021-01483-y

There are significant differences in the temporal sampling of successive VTEC maps when generating and providing GIMs in post-processing by means of IONEX. In order to extract VTEC values for arbitrary points in time, the interpolation (5.10) is used. It seems obvious that the goal is to generate GIMs with the highest possible temporal resolution to avoid interpolation errors. In **C-II**, the 15-minute resolution GIM 'uqrg' of UPC (Barcelona, Spain) was sampled at different time intervals to investigate the need for high temporal resolution. By means of a comparison with observations of altimetry over the oceans and with independent observations of GNSS, these GIMs were analysed. The influence of temporal sampling on the accuracy of the calculated VTEC is particularly crucial during the top phase of the solar cycle. Further differences could be observed by investigation of different latitude bands. The influence of temporal sampling on the accuracy of the VTEC is less in the mid and high latitudes than at the equator. From the investigations, it could be concluded that the temporal sampling has a significant influence on the accuracy of the retrieved VTEC values, if it is greater than 1 hour. A concrete recommendation can be made to provide GIMs with the shortest possible temporal sampling.

In the context of a research visit at UPC, A. Goss participated in the discussions of the study there and contributed to the interpretations of the results. The main contribution to the manuscript is the review with recommendations and comments.



# List of Figures

1.1	Relation between ionospheric key-quantities; the left part presents the integration of $N_e$ along the ray path of a signal which leads to the STEC. The right part indicates a projection of the STEC into the vertical direction by means of a mapping function, leading to the VTEC. . . . .	2
1.2	Flowchart for the generation of ionosphere products with reference to the three publications and to the respective sections that represent the individual contents. .	3
1.3	Distribution of the stations of the global IGS and the regional EUREF and UN-AVCO networks providing hourly data. . . . .	4
2.1	Schematic representation of the structuring of the atmosphere in the temperature domain on the left side and the ionisation domain on the right side. Known geodetic space techniques, as well as their observation geometry are represented in the middle. In the temperature domain, the structuring of the neutral atmosphere depends on the temperature as represented with the dashed line on the left. The charged atmosphere is defined in the ionisation domain and thus depends on the number of charged particles. The red dashed line shows the idealised profile of the electron density distribution starting with the ionosphere from 50 km up to approximately 1000 km with the transition to the charged plasmasphere. . . . .	9
2.2	Scheme of the SLM mapping. . . . .	15
3.1	Schematic representation of the GPS constellation with six orbital planes of $55^\circ$ inclination. The satellites are placed along the orbital plane with an altitude of 20,200 km. . . . .	18
3.2	Schematic representation of the GLONASS constellation with three orbital planes of $64.8^\circ$ inclination. Eight satellites are placed with an angular distance of $45^\circ$ along the orbital plane with an altitude of 19,100 km. . . . .	19
3.3	Schematic representation of the satellite constellation of Galileo in panel a) and of BeiDou in panel b) . . . . .	21
3.4	Distribution of GNSS stations that make their data available under the umbrella of various global and regional networks. . . . .	22
3.5	Distribution of stations that deliver data to the different networks in hourly intervals. . . . .	22
4.1	The schematic representation of the GSM coordinate system. . . . .	24
4.2	Polynomial B-splines of different levels $J_\Phi = 0, 1, 2, 3$ with the corresponding total numbers $K_{J_\Phi} = 3, 4, 6, 10$ of B-splines along the unit interval $[0, 1]$ from the top left to the bottom right. The red-coloured spline functions $N_{2,3}^2(x)$ (left) and $N_{3,3}^2(x)$ (right) in the bottom panels correspond to the shift value $k_\Phi = 3$ . The blue-coloured spline functions in the bottom panels ensure the closure of the modelling interval at the boundaries. . . . .	27

4.3	Trigonometric B-splines $\tilde{\phi}_{k_T}^{J_T}(\lambda)$ of different level $J_T = 1, 2, 3, 4$ from the top left panel to the bottom right with increasing total number of B-splines distributed on the circle $[0^\circ, 360^\circ)$ . The red-coloured spline function $\tilde{\phi}_3^{J_T}(\lambda)$ with shift value $k_T = 3$ in each panel is different from zero only in the sub-interval of length $\Delta_{J_T} = 360^\circ/2^{J_T}$ . The green- and blue-coloured B-spline functions $\tilde{\phi}_{K_{J_T}}^{J_T}(\lambda)$ show the effect of the continuous modelling around the equator. . . . .	29
4.4	<i>Processing chain</i> : Flowchart of the processing chain, including the steps to be followed within the data acquisition level. . . . .	30
4.5	Schematic representation of the B-spline adapted station selection with the distribution of knot points $\nu_{k_\phi}^{J_\phi}$ along the latitudes and knot points $\lambda_{k_T}^{J_T}$ for B-spline expansions of level $J_\phi = 4$ and $J_T = 3$ . The left panel a) shows the global map with the grid and the stations, and panels b) and c) consider two specific cases which need to be taken into account within the third step of the selection procedure. . . . .	33
4.6	The stations assigned to the global station set $\mathcal{D}_1$ in panel a), as well as the station assigned to the station set $\mathcal{D}_2$ in panel b), based on the total number of stations providing hourly data, which are shown in 3.4. . . . .	33
4.7	<i>Processing chain</i> : Flowchart of the processing chain, including the data acquisition level (cf. Section 4.5) and the modelling level with the TSM comprising the global and the regional modelling modules. . . . .	37
4.8	2-D MSR of the signal $f_{J_1, J_2}(\varphi, \lambda)$ . . . . .	41
4.9	Look-up table to determine regional B-spline levels $J_3$ and $J_4$ and the corresponding spektral resolution. . . . .	43
5.1	Distribution of observations provided by the stations of set $\mathcal{D}_1$ in a) and provided by the stations of set $\mathcal{D}_2$ in b) for 17 March 2015 at 12:00 UT. . . . .	51
5.2	<i>Product Type 1a</i> : Estimated coefficients and standard deviations of the B-spline series expansion for 17 March 2015 at 12:00 UT. Panels a) and b) show the high-resolution product generated with level values $J_1 = 5$ and $J_2 = 3$ and panels c) and d) show its smoothed version of levels $J'_1 = 4$ and $J_2 = 3$ . . . . .	53
5.3	<i>Product Type 1b</i> : Estimated coefficients of the regional B-spline series expansion for $\Delta VTEC$ for 17 March 2015 at 12:00 UT. In a) the B-spline coefficients and in b) the corresponding standard deviations for a B-spline expansion of level $J_3 = 3$ and $J_4 = 3$ are shown. c) and d) show the smoothed version of level $J'_3 = 2$ and $J'_4 = 2$ . . . . .	54
5.4	<i>Product Type 2a</i> : Estimated values of $\widehat{VTEC}_{\text{glob}}(\varphi_l, \lambda_r, t_s)$ in panels a) and c) and $\widehat{\sigma}_{VTEC_{\text{glob}}}(\varphi_l, \lambda_r, t_s)$ in b) and d), for 17 March 2015 at 12:00 UT. The values are given on a grid with sampling intervals of $\Delta\Phi = 2.5^\circ$ and $\Delta\Lambda = 5^\circ$ . . . . .	55
5.5	<i>Product Type 2b</i> : Values of $\widehat{\Delta VTEC}_{\text{reg}}$ in a) and c) and the corresponding standard deviation $\widehat{\sigma}_{\Delta VTEC_{\text{reg}}}$ in b) and d). . . . .	56
5.6	<i>Product Type 2c</i> : Evaluated values $\widehat{VTEC}_{\text{reg}}(\varphi_l, \lambda_r, t_s)$ in a) and the corresponding standard deviations $\widehat{\sigma}_{VTEC_{\text{reg}}}(\varphi_l, \lambda_r, t_s)$ in panel b), as the final map of the TSM. . . . .	56
5.7	<i>Processing chain</i> : Flowchart of the processing chain including the data acquisition level (cf. Section 4.5), the modelling level with the TSM (cf. Section 4.6) and the product level comprising different format types to be used for data dissemination of ionosphere products. . . . .	57
5.8	Schematic representation of the 4-point spatial interpolation to calculate the VTEC value at $P(\varphi_l + q \cdot \Delta\Phi, \lambda_r + p \cdot \Delta\Lambda)$ from the four corner points of the grid cell of interest. . . . .	59

5.9	Reuter grids with values $\gamma = 16$ in panel (a), $\gamma = 25$ in panel (b) and $\gamma = 35$ in panel (c). . . . .	61
5.10	SH GIM ( <b>top panels</b> ) and deviation maps ( <b>bottom panels</b> ) of the 1. ( <b>left column</b> ), 3. ( <b>middle column</b> ) and 5. ( <b>right column</b> ) test case from Tab. 5.2 for September 8, at 12:00 UT. . . . .	64
5.11	Change in relative RMS values ( <b>left</b> ) and RMS values ( <b>right</b> ), for the period from 2 September 2017 (Day Of Year 245) to 12 September 2017 (Day Of Year 255); temporal sampling intervals of 10 min. . . . .	64
5.12	Stations used in the dSTEC analysis, selected according to criteria 3). . . . .	66
5.13	Differences $S(t_s)$ in the 3D position between the position determined by Precise Point Positioning (PPP) and ionospheric corrections calculated by different GIMs and the actual position. The top three panels show the differences for the stations BOGT, WTZR and ASPA during the 2 September 2017 (Day Of Year 245) and the bottom three panels show the corresponding differences for 8 September 2017 (Day Of Year 251) with different scaling of the y-axis. On the x-axis, the time in Universal Time is depicted in hours. . . . .	70
6.1	Panel a) show the distribution of stations providing hourly data to the networks IGS, EUREF and UNAVCO which are used for generating the GIM in panel b) with corresponding standard deviation map presented in panel c) by means of a B-spline expansion of level $J_1 = 4$ and $J_2 = 3$ . Panels d), e) and f) show the stations assigned to $\mathcal{D}_1$ as well as the corresponding GIM and standard deviation map, respectively. Panel g) represents the stations assigned to $\mathcal{D}_2$ and panel h) the differences between the GIMs shown in the panels b) and e). . . . .	72
6.2	Defined <i>Product Type 1</i> and <i>Product Type 2</i> with the corresponding global and regional sub-products a), b) and c). By applying the pyramid algorithm (4.49) and (4.60) for the global and regional models, respectively, as well as by applying the transformation (5.19) from B-spline coefficients to coefficients of the SHs, further sub-products of <i>Product Type 1</i> are defined. . . . .	77
6.3	Schematic representation of a step model with three steps comprising a global model, a regional densification and a further densification for a local extend. . . .	79
6.4	Schematic representation of different space geodetic observation techniques which can be used to improve the global data coverage. . . . .	80



# List of Tables

1.1	Product types defined by means of the latency of the input data adapted from <b>P-III</b> . . . . .	4
2.1	The influence of solar radiation on the neutral particles in the atmosphere. . . . .	11
2.2	Phenomenon of solar wind and CME interacting with the ionosphere . . . . .	12
3.1	GPS observation codes for determining the ionospheric observable. . . . .	19
3.2	Currently operational GLONASS satellites and the related channel numbers taken from <a href="https://www.glonass-iac.ru/en/guide/navfaq.php">https://www.glonass-iac.ru/en/guide/navfaq.php</a> . . . . .	20
4.1	Errors in [m] in the pseudorange related to different error sources. . . . .	30
4.2	Numerical values for the B-spline levels $J_1$ and $J_2$ , the maximum SH degree $n_{max}$ and the input data sampling intervals $\Delta\varphi$ and $\Delta\lambda$ by evaluating the inequalities (4.40); the left part of the table presents the numbers along a meridian (upper inequalities in Eq. (4.40)), the right part the corresponding numbers along the equator and its parallels according to the lower inequalities in Eq. (4.40). . . . .	39
5.1	Sampling intervals $\Delta\varphi_l$ and $\Delta\lambda_l$ of the Reuter grid points for different values of $\gamma$ and the corresponding number $V$ of Reuter grid points. Required max. sampling intervals $\Delta\varphi_{SH}$ and $\Delta\lambda_{SH}$ and the number of unknown coefficients of SHs with different values for $n_{max}$ . . . . .	61
5.2	Numerical and statistical results to estimate the quality and feasibility for the different cases. . . . .	63
5.3	Results of the dSTEC analysis for 13 different stations, with the RMS in TECU values of $dSTEC(t_s)$ for the different VTEC products. . . . .	67
5.4	RMS and $\bar{S}$ values of deviations $S(t_s)$ for September 2 (DOY 245) and 8 (DOY 251), 2017 at the stations BOGT, WTZR and ASPA. The maximum and minimum values of the RMS and $\bar{S}$ are marked in red and green, respectively. The RMS and $\bar{S}$ of the transformed versions are bold if they are lower than the values of the original GIM, ‘othg’. . . . .	69
7.1	Contribution of the first Author to the publications . . . . .	83





# Acronyms

**APREF** Asia Pacific Reference Frame

**CAS** Chinese Academy of Science

**CME** Coronal Mass Ejection

**CODE** Center for Orbit Determination

**CPB** Carrier Phase Bias

**DCB** Differential Code Bias

**DGFI-TUM** Deutsches Geodätisches Forschungsinstitut der Technischen Universität München

**DORIS** Doppler Orbitography and Radiopositioning Integrated by Satellite

**EIA** Equatorial Ionization Anomaly

**ESA** European Space Agency

**ESM** Extended Slab Model

**ESOC-ESA** European Space Operation Center of the European Space Agency

**EUREF** European Reference Frame

**EUV** Extreme Ultraviolet

**FTP** File Transfer Protocol

**GIM** Global Ionospheric Map

**GLONASS** GLObal'naya Navigatsionnaya Sputnikovaya Sistema

**GNSS** Global Navigation Satellite Systems

**GPS** Global Positioning Systems

**GRACE-FO** Gravity Recovery and Climate Experiment-Follow-On Mission

**GSM** Global Solar Geomagnetic

**IAAC** Ionosphere Associated Analysis Center

**IGS** International GNSS Service

**IONEX** Ionosphere Exchange Format

**IPP** Ionospheric Pierce Point

**IRI** International Reference Ionosphere

<b>IRNSS</b>	Indian Regional Navigation Satellite Systems
<b>IRO</b>	Ionosphere Radio Occultation
<b>JPL</b>	Jet Propulsion Laboratory
<b>KF</b>	Kalman Filter
<b>LEO</b>	Low Earth Orbiting
<b>LSTID</b>	Large-Scale Traveling Ionospheric Disturbances
<b>MetOp</b>	Meteorological Operational Satellite
<b>MRR</b>	Multi-Resolution Representation
<b>MSA</b>	Multi-Scale Analysis
<b>MSLM</b>	Modified Single Layer Mapping
<b>MSR</b>	Multi-Scale Representation
<b>MSTID</b>	Medium-Scale Traveling Ionospheric Disturbances
<b>NAVSTAR-GPS</b>	NAVigational Satellite Timing And Ranging – Global Positioning System
<b>NRCan</b>	Canadian Geodetic Survey of Natural Resources Canada
<b>OPTIMAP</b>	Operational Tool for Ionosphere Mapping and Prediction
<b>POD</b>	Precise Orbit Determination
<b>PPP</b>	Precise Point Positioning
<b>PRN</b>	Pseudo Random Noise
<b>QZSS</b>	Quasi Zenith Satellite System
<b>RBMC</b>	Brazilian Network for Continuous Monitoring of the GNSS Systems in real time
<b>RIM</b>	Regional Ionosphere Map
<b>RINEX</b>	Receiver Independent Exchange Format
<b>RMS</b>	Root Mean Square
<b>RNSS</b>	Regional Navigation Satellite Systems
<b>ROB</b>	Royal Observatory of Belgium
<b>RT</b>	Real-Time
<b>RTCM</b>	Radio Technical Commission for Maritime Services
<b>SH</b>	Spherical Harmonic
<b>SLM</b>	Single Layer Model
<b>SoL</b>	Safety of Life

---

**SSR** State Space Representation

**SSTID** Small-Scale Traveling Ionospheric Disturbances

**STEC** Slant Total Electron Content

**TEC** Total Electron Content

**TECU** Total Electron Content Unit

**TID** Traveling Ionospheric Disturbances

**TSM** Two-Step Model

**UNAVCO** UNAVCO is a non-profit university-governed consortium that facilitates geoscience research and education using Geodesy

**UPC** Universitat Politècnica de Catalunya

**VCE** Variance Component Estimation

**VTEC** Vertical Total Electron Content

**WHU** Wuhan University



# Bibliography

- Aragon-Angel, A. (2010). *Contributions to ionospheric electron density retrieval*. PhD thesis, Research Group of Astronomy and Geomatics (gAGE), Technical University of Catalonia (UPC).
- Astafyeva, E., Rolland, L., Lognonné, P., Khelifi, K., and Yahagi, T. (2013). Parameters of seismic source as deduced from 1 hz ionospheric GPS data: Case study of the 2011 Tohoku-oki event. *Journal of Geophysical Research: Space Physics*, 118(9):5942–5950.
- Bassiri, S. and Hajj, G. (1993). High-order ionospheric effects on the global positioning system observables and means of modeling them. *Manuscr Geodetica*, 18:280–289.
- Belehaki, A., I.Tsagouri, Altadill, D., Blanch, E., Borries, C., Buresova, D., Chum, J., I.Galkin, Miguel, J. J., Segarra, A., C.C. Timoté, C. C., Tziotziou, K., Verhulst, T., and Watermann, J. (2020). An overview of methodologies for real-time detection, characterisation and tracking of traveling ionospheric disturbances developed in the TechTIDE project. *J. Space Weather Space Clim.*, 10:42.
- Bergeot, N., Bruyninx, C., Defraigne, P., Pireaux, S., Legrand, J., Pottiaux, E., and Baire, Q. (2011). Impact of the Halloween 2003 ionospheric storm on kinematic GPS positioning in Europe. *GPS Solutions*, 15(2):171–180.
- Bergeot, N., Chevalier, J.-M., Bruyninx, C., Pottiaux, E., Aerts, W., Baire, Q., Legrand, J., Defraigne, P., and Huang, W. (2014). Near real-time ionospheric monitoring over Europe at the Royal Observatory of Belgium using GNSS data. *Journal of Space Weather and Space Climate*, 4:A31.
- Beutler, G., Rothacher, M., Schaer, S., Springer, T., Kouba, J., and Neilan, R. (1999). The International GPS service (IGS): An interdisciplinary service in support of Earth sciences. *Advances in Space Research*, 23(4):631–653.
- Bothmer, V. and Daglis, I. (2007). *Space Weather: Physics and Effects*. Springer Praxis Books. Springer Berlin Heidelberg.
- Ciraolo, L., Azpilicueta, F., Brunini, C., Meza, A., and Radicella, S. (2007). Calibration errors on experimental slant total electron content (TEC) determined with GNSS. *Journal of Geodesy*, 81:111–120.
- Cliver, E. and Dietrich, W. (2013). The 1859 space weather event revisited: limits of extreme activity. *J. Space Weather Space Clim.*, 3:A31.
- Dach, R. and Jean, Y. (2013). International GNSS Service - Technical report 2012. Technical report.
- Dach, R., Lutz, S., Walser, P., and Fridez, P. (2015). Bernese GPS Software Version 5.2. Technical report.
- Dettmering, D. (2003). *Die Nutzung des GPS zur dreidimensionalen Ionosphärenmodellierung*. PhD thesis, University of Stuttgart.

- Dettmering, D., Limberger, M., and Schmidt, M. (2014). Using doris measurements for modeling the vertical total electron content of the earth’s ionosphere. *Journal of Geodesy*, 88(12):1131–1143.
- Dettmering, D., Schmidt, M., Heinkelmann, R., and Seitz, M. (2011). Combination of different space-geodetic observations for regional ionosphere modeling. *Journal of Geodesy*, 85(12):989–998.
- Dierckx, P. (1984). Algorithms for smoothing data on the sphere with tensor products splines. *Computing*, 32(4):319–342.
- Dow, J., Neilan, R. E., and Rizos, C. (2009). The international GNSS Service in a changing landscape of Global Navigation Satellite Systems. *Journal of Geodesy*, 83(3).
- Eicker, A. (2008). *Gravity Field Refinement by Radial Basis Functions from In-situ Satellite Data*. PhD thesis, Rheinische Friedrich-Wilhelms-Universität Bonn.
- Erdogan, E., Schmidt, M., Goss, A., Görres, B., and Seitz, F. (2020). Adaptive Modeling of the Global Ionosphere Vertical Total Electron Content. *Remote Sensing*, 12(11):1822.
- Erdogan, E., Schmidt, M., Goss, A., and Seitz, F. (2021). Real-time ionosphere VTEC modeling with B-splines using Multi-GNSS carrier-phase observations. *submitted to Space Weather*.
- Erdogan, E., Schmidt, M., Seitz, F., and Durmaz, M. (2017). Near real-time estimation of ionosphere vertical total electron content from GNSS satellites using B-spline in a Kalman Filter. *Annales Geophysicae*, 35:263–277.
- Feltens, J. and Schaer, S. (1998). IGS Products for the Ionosphere. Technical report. European Space Operation Centre and Astronomical Institute of the University of Berne.
- Freedman, W., Greven, T., and Schreiner, M. (1998). *Constructive Approximation on the Sphere*. Oxford University Press.
- Gelb, A. (1974). Applied optimal estimation. *The MIT Press, Cambridge*.
- Goss, A., Hernández-Pajares, M., Schmidt, M., Roma-Dollase, D., Erdogan, E., and Seitz, F. (2020a). High-Resolution Ionosphere Corrections for Single-Frequency Positioning. *Remote Sensing*, 13(1):12.
- Goss, A., Schmidt, M., Erdogan, E., Görres, B., and Seitz, F. (2019). High-resolution vertical total electron content maps based on multi-scale b-spline representations. *Annales Geophysicae*, 37(4):699–717.
- Goss, A., Schmidt, M., Erdogan, E., and Seitz, F. (2020b). Global and Regional High-Resolution VTEC Modelling Using a Two-Step B-spline Approach. *Remote Sensing*, 12(7):1198.
- Grejner-Brzezinska, D., Kashani, I., and Wielgosz, P. (2005). On accuracy and reliability of instantaneous network RTK as a function of network geometry, station separation, and data processing strategy. *GPS Solutions*, 9(3):212–225.
- Grewal, M. S. and Andrews, A. P. (2008). *Kalman Filtering : Theory and Practice Using MATLAB*. John Wiley & Sons, Inc., Hoboken, New Jersey, 2 edition.
- Hapgood, M. A. (1992). Space Physics Coordinate Transformations: A User Guide. *Planetary and Space Science*, 50(5):711–717.



- Heelis, R. A. (2014). *Aspects of Coupling Processes in the Ionosphere and Thermosphere*, chapter ca14, pages 161–169. Ltd.
- Heise, S. (2002). *Rekonstruktion dreidimensionaler Elektronendichteverteilungen basierend auf CHAMP-GPS-Messungen*. PhD thesis, Freie Universität Berlin.
- Hernández-Pajares, M., García-Rigo, A., Juan, J. M., Sanz, J., Monte, E., and Argón-Àngel, A. (2012a). GNSS measurement of EUV photons flux rate during strong and mid solar flares. *Space Weather*, 10(12):S12001.
- Hernández-Pajares, M., Juan, J. M., and Sanz, J. (1999). New approaches in global ionospheric determination using ground GPS data. *Journal of Atmospheric and Solar-Terrestrial Physics*, 61(16):1237–1247.
- Hernández-Pajares, M., Juan, J. M., and Sanz, J. (2000). Improving the Abel inversion by adding ground GPS data to LEO radio occultations in ionospheric sounding. *Geophysical Research Letters*, 27(16):2473–2476.
- Hernández-Pajares, M., Juan, J. M., and Sanz, J. (2006). Medium-scale traveling ionospheric disturbances affecting GPS measurements: Spatial and temporal analysis. *Journal of Geophysical Research*, 111(A7).
- Hernández-Pajares, M., Juan, J. M., Sanz, J., and Argón-Àngel, A. (2012b). Propagation of medium scale traveling ionospheric disturbances at different latitudes and solar cycle conditions. *Radio Science*, 47(06):1–22.
- Hernández-Pajares, M., Juan, J. M., Sanz, J., Argón-Àngel, A., Garcia-Rigo, A., Salazar, D., and Escudero, M. (2011). The ionosphere: Effects, GPS modeling and benefits for space geodetic techniques. *Journal of Geodesy*, 85:887–907.
- Hernández-Pajares, M., Juan, J. M., Sanz, J., Orus, R., Garcia-Rigo, A., Feltens, J., Komjathy, A., Schaer, S. C., and Krankowski, A. (2009). The IGS VTEC map: a reliable source of ionospheric information since 1998. *Journal of Geodesy*, 83(3):263–275.
- Hernández-Pajares, M., Roma-Dollase, D., Krankowski, A., García-Rigo, A., and Orús-Pérez, R. (2017a). Methodology and consistency of slant and vertical assessments for ionospheric electron content models. *Journal of Geodesy*, 19(12):1405–1414.
- Hernández-Pajares, M., Wielgosz, P., Paziewski, J., Krypiak-Gregorczyk, A., Krukowska, M., Stepniak, K., Kaplon, J., Hadas, T., Sosnica, K., Bosy, J., Orus-Perez, R., Monte-Moreno, E., Yang, H., Garcia-Rigo, A., , and Olivares-Pulido, G. (2017b). Direct MSTID mitigation in precise GPS processing. *Radio Science*, 52(3).
- Jacobi, C., Jakowski, N., Schmidtke, G., and Woods, T. N. (2016). Delayed response of the global total electron content to solar EUV variations. *Advances in Radio Science*, 14:175–180.
- Jekeli, C. (2005). Spline Representations of Functions on a Sphere for Geopotential Modeling. Technical Report 475.
- Kim, M., Lee, J., Pullen, S., and Gillespie, J. (2013). Optimized gnss network station selection to support the development of ionospheric threat models for gabs. *International Technical Meeting of the Institute of Navigation*, pages 559–570.
- Kim, M., Seo, J., and Lee, J. (2014). A Comprehensive Method for GNSS Data Quality Determination to Improve Ionospheric Data Analysis. *Sensors*, 14(8):14971–14993.

- Klobuchar, J. A. (2013). Ionospheric Time-Delay Algorithm for Single-Frequency GPS Users. *International Technical Meeting of the Institute of Navigation*, AES-23(3):325–331.
- Koch, K. R. (1999). *Parameter Estimation and Hypothesis Testing in Linear Models*. Springer-Verlag Berlin Heidelberg.
- Krypiak-Gregorczyk, A., Wielgosz, P., and Borkowski, A. (2017). Ionosphere Model for European Region Based on Multi-GNSS Data and TPS Interpolation. *Remote Sensing*, 9(1221).
- Langley, R. B. (1998). *Propagation of the GPS Signals*, pages 111–149. Springer Berlin Heidelberg, Berlin, Heidelberg.
- Laundal, K. and Richmond, A. (2017). Magnetic Coordinate Systems. *Space Sci Rev*, 206(1):27–59.
- Lee, J. and Kim, M. (2017). Optimized GNSS Station Selection to Support Long-Term Monitoring of Ionospheric Anomalies for Aircraft Landing Systems. *IEEE*, 53(1):236–246.
- Li, M., Yuan, Y., Wang, N., Li, Z., and Zhang, X. (2018). Statistical comparison of various interpolation algorithms for reconstruction regional grid ionospheric maps over China. *Journal of Atmospheric and Solar-Terrestrial Physics*, 172:129–137.
- Li, Z., Wang, N., Hernández-Pajares, M., Yuan, Y., Krankowski, A., Liu, A., Zha, J., García-Rigo, A., Roma-Dollase, D., Yang, H., Laurichesse, D., and Bolt, A. (2020). IGS real-time service for global ionospheric total electron content modeling. *Journal of Geodesy*, 94(32).
- Li, Z., Yuan, Y., Wang, N., Hernández-Pajares, M., and Huo, X. (2015). SHPTS: towards a new method for generating precise global ionospheric TEC map based on spherical harmonic and generalized trigonometric series functions. *Journal of Geodesy*, 89(4):331–345.
- Liang, W. (2017). *A regional physics-motivated electron density model of the ionosphere*. PhD thesis, Technical University of Munich.
- Liang, W., Limberger, M., Schmidt, M., Dettmering, D., and Hugentobler, U. (2016). Combination of ground- and space-based GPS data for the determination of a multi-scale regional 4-d ionosphere model. In: *Rizos C., Willis P. (Eds.) IAG 150 Years, IAG Symposia*, 143:751–758.
- Limberger, M. (2015). *Ionosphere modeling from GPS radio occultations and complementary data based on B-splines*. PhD thesis, Technical University of Munich.
- Limberger, M., Hernández-Pajares, M., Aragón-Ángel, A., Altadill, D., and Dettmering, D. (2015). Long-term comparison of the ionospheric f2 layer electron density peak derived from ionosonde data and formosat-3/cosmic occultations. *Journal of Space Weather and Space Climate*, 5(A21).
- Liu, J., Chen, R., Wang, Z., and Zhang, H. (2010). Spherical cap harmonic model for mapping and predicting regional TEC. *GPS Solutions*, 15(2):109–119.
- Liu, J. Y., Chuo, Y. J., Shan, S. J., Tsai, Y. B., Chen, Y. I., Pulinets, S. A., and Yu, S. B. (2004). Pre-earthquake ionospheric anomalies registered by continuous GPS TEC measurements. *Annales Geophysicae*, 22(5):1585–1593.
- Liu, Q., Hernández-Pajares, M., Lyu, H., and Goss, A. (2021). Influence of temporal resolution on the performance of Global Ionospheric Maps. *Journal of Geodesy*, 95(3):34.

- Lyche, T. and Schumaker, L. (2001). A multiresolution tensor spline method for fitting functions on the sphere. *SIAM J. SCI. COMPUT.*, 22(2):724–746.
- Lyu, H., Hernández-Pajares, M., Nohutcu, M., García-Rigo, A., Zhang, H., and Liu, J. (2018). The Barcelona ionospheric mapping function (BIMF) and its application to northern mid-latitudes. *GPS Solution*, 22(67):724–746.
- Mannucci, A. J., Wilson, B., Yuan, D., C.H.Ho, Lindqwister, U., and Runge, T. (1998). A global mapping technique for GPS derived ionospheric total electron content measurements. *Radio Science*, 33(3):565–582.
- Mannucci, A. J., Wilson, B. D., and Edwards, C. D. (1993). A New Method for Monitoring the Earth’s Ionospheric Total Electron Content Using the GPS Global Network. In *Proceedings of the 6th International Technical Meeting of the Satellite Division of The Institute of Navigation (ION GPS 1993)*, pages 1323 – 1332, Salt Lake City, UT.
- Mason, S. (2017). Adaptive modelling of the vertical total electron content of the earth’s ionosphere.
- Mertins, A. (1999). *Signal analysis: wavelets, filter banks, time-frequency transforms and applications*. Wiley.
- Möbmer, M. (2009). Globale drei-dimensionale Ionosphaerenmodellierung des VTEC (in german).
- Moldwin, M. (2008). *An Introduction to Space Weather*. Cambridge University Press.
- Monte-Moreno, E. and Hernández-Pajares, M. (2014). Occurrence of solar flares viewed with GPS: Statistics and fractal nature. *Journal of Geophysical Research*, 119(11):9216–9227.
- Nohutcu, M., Karslioglu, M. O., and Schmidt, M. (2010). B-spline modeling of VTEC over Turkey using GPS observations. *Journal of Atmospheric and Solar-Terrestrial Physics*, 72(7):617–624.
- Orus, R., Cander, L., and Hernández-Pajares, M. (2007). Testing regional vertical total electron content maps over europe during 17-21 January 2005 sudden space weather event. *Radio Science*, 42(3):RS3004.
- Orus, R., Hernández-Pajares, M., Juan, J., and Sanz, J. (2005). Improvement of global ionospheric VTEC maps by using kriging interpolation technique. *Journal of Atmospheric and Solar-Terrestrial Physics*, 67(16):1598–1609.
- Oughton, E., Skelton, A., Horne, B., Thomson, A., and Gaunt, C. (2017). Quantifying the daily economic impact of extreme space weather due to failure in electricity transmission infrastructure. *Space Weather*, 15(1):65–83.
- Petit, G. and Luzum, B. (2010). IERS Conventions (2010). Technical report, [www.iers.org](http://www.iers.org).
- Prol, F., Camargo, P., Monico, J., and Muella, M. (2018). Assessment of a TEC calibration procedure by single-frequency PPP. *GPS Solutions*, 22(35).
- Reischung, P., Griffiths, J., Ray, J., and R. Schmid, X. C. . B. G. (2012). IGS08: the IGS realization of ITRF2008. *GPS Solutions*, 16(4):483–494.
- Reuter, R. (1982). *Über Integralformeln der Einheitsphäre und harmonische Splinefunktionen*. PhD thesis, RWTH Aachen.

- Rolland, L., Lognonné, P., Astafyeva, E., Kherani, E. A., Kobayashi, N., Mann, M., and Munekane, H. (2011). The resonant response of the ionosphere imaged after the 2011 off the Pacific coast of Tohoku Earthquake. *Earth Planets and Space*, 63(7):853–857.
- Roma-Dollase, D., Hernández-Pajares, M., Krankowski, A., Kotulak, K., Ghoddousi-Fard, R., Yuan, Y., Li, Z., Zhang, H., Shi, C., and Wang, C. (2017). Consistency of seven different GNSS global ionospheric mapping techniques during one solar cycle. *Journal of Geodesy*, 92(6):691–706.
- Rovira-Garcia, A., Juan, J., Sanz, J., and Gonzalez-Casado, G. (2015). A Worldwide Ionospheric Model for Fast Precise Point Positioning. *IEEE T. Geoscience Remote Sensing*, 53(8):4596–4604.
- Schaer, S. (1999). *Mapping and Predicting the Earth’s Ionosphere Using the Global Positioning System*. PhD thesis, University of Berne.
- Schaer, S., Gurtner, W., and Feltens, J. (1998). IONEX: The IONosphere Map EXchange Format Version 1. Technical report. Astronomical Institute, University of Berne, Switzerland.
- Schmidt, M. (2007). Wavelet modelling in support of IRI. *Advances in Space Research*, 39(5):932–940.
- Schmidt, M. (2012). Towards a Multi-Scale Representation of Multi-Dimensional Signals. In Sneeuw, N., Novák, P., Crespi, M., and Sansò, F., editors, *VII Hotine-Marussi Symposium on Mathematical Geodesy*, pages 119–127, Berlin, Heidelberg. Springer Berlin Heidelberg.
- Schmidt, M., Bilitza, D., Shum, C., and Zeilhofer, C. (2008). Regional 4-d modeling of the ionospheric electron density. *Advances in Space Research*, 42(4):782–790.
- Schmidt, M., Dettmering, D., Mößner, M., and Wang, Y. (2011). Comparison of spherical harmonic and B-spline models for the vertical total electron content. *Radio Science*, 46(6):RS0D11.
- Schmidt, M., Dettmering, D., and Seitz, F. (2015a). *Using B-Spline Expansions for Ionosphere Modeling*, pages 939–983. Springer Berlin Heidelberg, Berlin, Heidelberg.
- Schmidt, M., Erdogan, E., Goss, A., Hernández-Pajares, M., Rigo, A. G., and Lyu, H. (2017). Development and validation of sequential UBS and NABS models. Technical report, ACORDE Technologies.
- Schmidt, M., Göttl, F., and Heinkelmann, R. (2015b). Towards the Combination of Data Sets from Various Observation Techniques. In Kutterer, H., Seitz, F., Alkhatib, H., and Schmidt, M., editors, *The 1st International Workshop on the Quality of Geodetic Observation and Monitoring Systems (QuGOMS’11)*, pages 35–43, Cham. Springer International Publishing.
- Schrijver, C. J., Kauristie, K., Aylward, A. D., Denardini, C. M., Gibson, S. E., Glover, A., Gopalswamy, N., Grande, M., Hapgood, M., Heynderickx, D., Jakowski, N., Kalegaev, V. V., Lapenta, G., Linker, J. A., Liu, S., Mandrini, C. H., Mann, I. R., Nagatsuma, T., Nandy, D., Obara, T., O’Brien, T. P., Onsager, T., Opgenoorth, H. J., Terkildsen, M., Valladares, C. E., and Vilmer, N. (2015). Understanding space weather to shield society: A global road map for 2015–2025 commissioned by COSPAR and ILWS. *Advances in Space Research*, 55(12):2745–2807.
- Schumaker, L. and Traas, C. (1991). Fitting scattered data on spherelike surfaces using tensor products of trigonometric and polynomial splines. *Numerische Mathematik*, 60(1):133–144.

- Schunk, R. W. and Nagy, A. F. (2009). *Ionosphere: Physics, Plasma Physics and Chemistry*. Cambridge University Press.
- Seeber, G. (1989). *Satellitengeodäsie: Grundlagen, Methoden und Anwendungen*. Walter de Gruyter.
- Simon, D. (2006). *Optimal state estimation: Kalman, H infinity, and nonlinear approaches*. John Wiley & Sons.
- Stollnitz, E., DeRose, T., and Salesin, D. (1995a). Wavelets for computer graphics: a primer, Part I. *IEEE Computer Graphics and Applications*, 15(3):76–84.
- Stollnitz, E., DeRose, T., and Salesin, D. (1995b). Wavelets for computer graphics: a primer, Part I. *IEEE Computer Graphics and Applications*, 15(4):75–85.
- Takasu, T. and Yasuda, A. (2009). Development of the low-cost RTK-GPS receiver with an open source program package RTKLIB. Technical report.
- Tsurutani, B. and Gonzalez, W. (1997). The interplanetary causes of magnetic storms: A review. *Washington DC American Geophysical Union Geophysical Monograph Series*, 98:77–89.
- Tsurutani, B., Mannucci, A., Iijima, B., Guarnieri, F., Gonzalez, W., Judge, D., Gangopadhyay, P., and Pap, J. (2006). The extreme Halloween 2003 solar flares (and Bastille Day, 2000 Flare), ICMEs, and resultant extreme ionospheric effects: A review. *Advances in Space Research*, 37(8):1583–1588.
- Tsurutani, B., Verkhoglyadova, O. P., Mannucci, A., Lakhina, G. S., Li, G., and Zank, G. P. (2009). A brief review of solar flare effects on the ionosphere. *Radio Science*, 44(1):1–14.
- Villiger, A. and Dach, R. (2018). International GNSS Service - Technical report 2018. Technical report. compiled in May 2019, available at: [ftp://ftp.igs.org/pub/resource/pubs/2018\\_techreport.pdf](ftp://ftp.igs.org/pub/resource/pubs/2018_techreport.pdf) (last access: March 30, 2020).
- Wang, C., Rosen, I. G., Tsurutani, B. T., Verkhoglyadova, O. P., Meng, X., and Mannucci, A. J. (2016a). Statistical characterization of ionosphere anomalies and their relationship to space weather events. *Journal of Space Weather and Space Climate*, 6(A5):A5.
- Wang, N., Yuan, Y., Li, Z., Montenbruck, O., and Tan, B. (2016b). Determination of different code biases with multi-gnss observations. *Journal of Geodesy*, 90(3):209–228.
- Wanninger, L. (1994). *Der Einfluss der Ionosphäre auf die Positionierung mit GPS*. Fachrichtung Vermessungswesen: Wissenschaftliche Arbeiten der Fachrichtung Vermessungswesen der Universität Hannover. Univ. Hannover.
- Zeilhofer, C. (2008). Multi-dimensional B-spline Modeling of Spatio-temporal Ionospheric Signals.
- Zhu, F., Yun, W., Yihan, Z., and Gao, Y. (2013). Temporal and spatial distribution of GPS-TEC anomalies prior to the strong earthquakes. *Astrophysics and Space Science*, 345:239–246.
- Zolesi, C. and Cander, L. R. (2007). *Ionosphere Prediction and Forecasting*. Springer Geophysics. Springer Berlin Heidelberg.



# Acknowledgements

The completion of this thesis would not have been possible without the support of many people. Therefore, I would like to take this opportunity to thank those who have accompanied me on this journey.

First of all, I would like to thank Michael Schmidt for giving me the opportunity to write this thesis in the first place. In particular, I would like to thank you for the close guidance, lots of advice and discussions, even on non-scientific topics.

Additionally I would like to thank Manuel Hernández-Pajares for giving me the opportunity of a research stay in Barcelona. I am grateful for all the help and input I received from him. Many thanks to Urs Hugentobler, who reviewed my work and also contributed to its success through discussions in previous years.

Many thanks to my mentor Georg Lothar, who has supported me throughout my studies up to this point and has always been there for me with his advice.

A significant part of this work is based on developments in many different projects, in which many colleagues were involved. I would like to thank everyone for the good collaboration. Most of all, I would like to thank Eren Erdogan, who worked with me on the projects at DGFI-TUM and without whom this work would not have been possible.

My thanks goes to all former and current colleagues at DGFI-TUM for the pleasant working atmosphere and the interdisciplinary discussions during the numerous events at the institute. I appreciated the support and open doors of all colleagues for various questions and discussions. I would like to thank Florian Seitz for the opportunity to write my doctoral thesis at DGFI-TUM and for being a co-author of my publications.

Finally, I would like to thank my parents Angelika and Josef Goss, my brother Sebastian and especially my girlfriend Franziska, who have always encouraged me along the way and without whom this would certainly not have been possible. Thank you for all your support and for always believing in me.